

Copyright is owned by the Author of the thesis. Permission is given for a copy to be downloaded by an individual for the purpose of research and private study only. The thesis may not be reproduced elsewhere without the permission of the Author.

MATHEMATICAL MODELLING OF
GRANULATION PROCESSES

A THESIS PRESENTED IN PARTIAL
FULFILMENT OF THE REQUIREMENTS
FOR THE DEGREE OF

DOCTOR OF PHILOSOPHY
IN
MATHEMATICAL PHYSICS

AT MASSEY UNIVERSITY, PALMERSTON NORTH,
NEW ZEALAND.

PATRICK REUBEN RYNHART
NOVEMBER 2004

Abstract

Granulation is an industrial process where fine particles are bound together into larger granules. The process has numerous applications including the manufacture of pharmaceuticals and the production of cosmetics, chemicals, detergents and fertilisers. This thesis studies aspects of wet granulation which involves the application of a viscous binder, usually in the form of a spray, to an agitated bed of powder particles. Individual powder particles may adhere together, joined by small quantities of binder fluid called liquid bridges. By a process of collision and adherence additional particles may join the newly formed agglomerates. Agglomerates may also coalesce together which is a process that leads to granule formation. On the completion of this process, granules are typically dried.

This thesis studies wet granulation on three different levels. First, micro-level investigations of liquid bridges between two and three particles are performed. For the two-particle case, the fluid profile of static (stationary) and dynamic (moving) liquid bridges is investigated. For the static case, a numerical solution to the Young-Laplace equation is obtained; this relates the volume of binder fluid to liquid bridge properties such as the inter-particle force. An analytic solution is also obtained, providing the liquid bridge profile in terms of known mathematical functions. For both solutions, the radii of the (spherical) primary particles may be different. The dynamic case is then studied using the Navier-Stokes equations with the low Reynolds number approximation. The motion of the approaching particles is shown to be damped by the viscosity of the liquid bridge. Static liquid bridges between three equally sized primary particles are then studied. Symmetry of the problem is used to obtain a numerical solution to the Young-Laplace equation. Liquid bridge properties are calculated in terms of the binder fluid volume. Experimental agreement is provided.

Secondly, a model to estimate the stickiness (fractional wet surface area) of agglomerates is proposed. Primary particles are approximated as spheres and are added one at a time in a closely packed arrangement. The model includes parameters to control the inter-particle separation distance and the fluid saturation state. Computational geometry is used to obtain results which relate the number of particles and the volume of binder fluid to the stickiness of the agglomerates.

Finally, a population balance model for wet granulation is developed by extending an earlier model to incorporate the effects of binder fluid. Functions for the inter-particle collision rate and drying rate are proposed, including functions which are derived from the geometric model, described above, for the case of maximum particle consolidation. The model is solved numerically for a range of coalescence kernels and results are presented which show the effect of binder volume and the drying rate.

Acknowledgements

Firstly I would like to express my sincere thanks to my chief supervisor Professor Robert McKibbin. I have always appreciated your encouragement, leadership, friendly manner and teaching skill.

Special thanks to my supervisor Professor Robert McLachlan. It is due to your mathematical knowledge and skill that this project has been a success.

Thank you Dr Jim Jones for your knowledge, enthusiasm and optimism as a supervisor. I appreciated your friendship, your investment of time, and your encouragement to publish and attend international conferences. Thank you for your careful reading and attention to detail which has been invaluable.

Special thanks to my long-time friend Jonathan Marshall. Thank you for writing the ‘C++ toolbox’ which was used in this thesis. Best wishes to Keren and yourself for working in the U.K. Thanks to Dr Tammy Smith and Associate Professor Bruce Van Brunt for brightening up the mathematics department. Thanks to Tim White, my ‘open-source’ neighbour Brett Ryland and Paul (Petal) Gardner for the fun and friendship over the years. To Avi Shalav, thanks for your friendship, enthusiasm and for filling my whiteboard with your fantastic cartoons whenever you visit.

Thanks to my family for regularly checking up on me and for always welcoming me back home to Napier. To my brother Kieran, it has been great fun flatting with you and I wish you every success in the future with your graphics design work. To my brother John it has been great to get to know you. Keep up the skating, music and gaming! Thanks Mum for your continued love and support. Thanks Da for your many interesting day tramps and for the games of pool.

I am very grateful to the following sources of financial assistance: Massey University Doctoral Scholarship, the Institute of Fundamental Sciences Graduate Research Fund, the Royal Society of New Zealand, the New Zealand Vice-Chancellors’ Committee and Studylink.

This thesis is dedicated to Georgie Milne who will be Georgie Rynhart by the time this thesis goes to print. Your daily love, support, encouragement and patience has been an amazing blessing. Thank you for bringing your bright happy smile into my life. I look forward to spending the rest of our lives together ö ö ö.

Nomenclature

Constants and variables are defined when they first appear in the text. Commonly used variables from Chapters 2 to 5 are listed below.

Chapter 2 Variables (Liquid Bridges Between Two Particles)

Static

Variable	Description
H_0	Mean curvature
Δp	Pressure difference
γ_{lv}	Fluid surface tension
r	Vertical coordinate
x	Horizontal coordinate
r_1	Radii of curvature in the $r - x$ plane
r_2	Radii of curvature in the $r - y$ plane
r_0	Bridge height at $x = 0$
θ	Contact angle
α	Half angle for particle 'A'
β	Half angle for particle 'B'
σ	Scaling variable
R	Non-dimensional bridge vertical coordinate
X	Non-dimensional bridge horizontal coordinate
R_0	Non-dimensional bridge height at $X = 0$
ΔP	Non-dimensional pressure difference
S	Non-dimensional inter-particle separation distance
V	Non-dimensional liquid bridge volume
A	Non-dimensional liquid bridge surface area
F	Non-dimensional inter-particle binding force
E	Non-dimensional Gibbs free surface energy
C	Non-dimensional normalised force ($C = \frac{F}{2\pi}$)

Dynamic

Variable	Description
t	time
r	Vertical coordinate
R	Sphere radius
z	Vertical Coordinate
h	Separation function

Variables used in Chapter 2 (continued)

h_0	Closest separation
\vec{v}	Velocity vector
ρ	Fluid density
g	Acceleration due to gravity
μ	Dynamic Viscosity
P	Pressure within liquid bridge
P_{amb}	Ambient pressure
\bar{P}	Vertically averaged pressure
Re	Reynolds number
F_{bridge}	Force
V_0	Constant bridge volume

Chapter 3 Variables (Static Liquid Bridges Between Three Particles)

Variable	Description
H_0	Mean curvature
Δp	Pressure difference
γ	Fluid surface tension
(X, Y, Z)	Cartesian coordinates
(r, θ)	Cylindrical coordinates
z	Liquid bridge surface in cylindrical coordinates
\mathbf{Z}	Liquid bridge surface in Cartesian coordinates
α	Contact angle
δ	Half-filling angle
r_0	Central point of liquid bridge
r_s	Intersection between the sphere and fluid
r_p	Intersection between the symmetry plane and fluid
C_1	Contour of the three-phase contact line
C_2	Contour of the symmetry plane
a	Sphere radius
S	Inter-particle separation distance
n_{surface}	Fluid surface outward pointing normal vector
n_{sphere}	Sphere outward pointing normal vector
n_{sym}	Symmetry plane outward pointing normal vector
\hat{z}	Mesh approximation to z
V	Liquid bridge volume

Variables used in Chapter 3 (continued)

S	Liquid bridge surface area
F	Inter-particle binding force

Chapter 4 Variables (Modelling the Agglomeration Process)

Variable	Description
S	Matrix containing coordinates of primary particles
σ	Minimum separation distance between sphere centres
δ	Fluid saturation parameter
T	Tetrahedra matrix
F	Face matrix
κ	Skewness number
Ξ	Objective function for optimisation
\mathbf{S}_i	Polyhedron representation of the sphere centred at S_i
\mathbf{T}_i	Polyhedron representation of the expanded tetrahedron centred at T_i
V_{binder}	Binder volume
A_{binder}	Agglomerate wet surface area
A_{particle}	Agglomerate dry surface area
W	Surface wetness
V^*	Fluid-to-solid volume ratio
N	Agglomerate size (number of primary particles)
V_{solid}	Volume of a primary particle
A_{solid}	Surface area of a primary particle

Chapter 5 Variables (Population Balance Modelling)

Variable	Description
N	Total number of particles
i, j	Particle size
n_i	Number of particles of size i
$K_{i,j}$	Coalescence kernel (in the absence of binder)
K_0	Size independent component of the coalescence kernel
M	Total mass of particles
m_i	Mass of particles of size i
N_0	Initial number of particles

Variables used in Chapter 5 (continued)

t	Time
\bar{i}	Mean particle size
σ	Variance
b_i	Wet binder mass for all particles of size i
B_i	Wet binder mass of a particle of size i
\bar{B}	Total wet binder mass
$\Phi_{i,j}$	Sticking efficiency function
Φ_0	Size independent component of the sticking efficiency function
$\hat{K}_{i,j}$	Coalescence kernel (in the presence of binder)
D_i	Drying rate of particles of size i
D_0	Drying rate constant
$\frac{D_0}{K_0}$	Collision-to-drying ratio
s_{\max}	Maximum particle size

Contents

Abstract	i
Acknowledgements	iii
Nomenclature	v
1 Introduction	1
1.1 Granulation	1
1.2 Growth Mechanisms	4
1.2.1 Wetting and Nucleation	7
1.2.2 Growth and Consolidation	12
1.2.3 Attrition and Breakage	14
1.3 Micro-level Models for Granulation	15
1.3.1 Saturation States	15
1.3.2 Static Liquid Bridges	16
(i) Toroidal approximation	19
(ii) Liquid bridge stability	20
(iii) Larger arrangements	22
1.3.3 Dynamic Liquid Bridges	23
1.4 Granulation Simulations	33
1.5 Thesis Preview	35
2 Liquid Bridges Between Two Particles	39
2.1 Introduction	39
2.2 The Young-Laplace Equation	39
2.3 Numerical Solution	41

2.3.1	Liquid Bridge Properties	45
	(i) Separation distance	45
	(ii) Surface area	46
	(iii) Volume	46
	(iv) Inter-particle binding force	47
	(v) Gibbs free surface energy	47
2.3.2	Summary of the solution technique	48
2.4	Numerical Results	49
2.5	Analytic Solution	58
2.5.1	Phase Portrait	61
2.6	Dynamic Liquid Bridges	66
2.6.1	Balance Equations	67
2.6.2	Velocity Profile	67
2.6.3	Determining the pressure	70
2.6.4	Force	71
2.6.5	Numerical Solution	72
2.6.6	Example	73
3	Static Liquid Bridges Between Three Particles	75
3.1	Introduction	75
3.2	Derivation of the Equations	78
3.2.1	Mean Curvature	78
3.2.2	Boundary conditions	79
	(i) Fluid contact angle	79
	(ii) Symmetry Plane	80
3.3	Numerical Solution	81
3.3.1	Constant Mean Curvature (CMC)	82

3.3.2	Boundary conditions	83
	(i) Fluid/sphere intersection	83
	(ii) Symmetry plane	83
3.3.3	Complete System of Equations	84
3.3.4	Liquid Bridge Properties	85
	(i) Volume	85
	(ii) Surface Area	87
	(iii) Inter-particle binding force	88
3.3.5	Solving the System using Matlab	88
	(i) Convergence and Solution Checks	89
3.4	Results	91
	3.4.1 Agreement with Experiment	91
4	Modelling the Agglomeration Process	97
4.1	Introduction	97
4.2	Adding Particles	100
4.3	Examples of Particle Placement	103
4.4	Defining the Fluid Surface	104
4.5	Agglomerate Properties	108
4.6	Half-space Intersections with the Tetrahedra	112
4.7	Calculating Agglomerate Properties	115
4.8	Solving the Model	117
4.9	Results of the Model	118
4.10	Fitting Functions for $s = 0$	126
4.11	Future Work	130

5	Population Balance Modelling	131
5.1	Introduction	131
5.2	Modelling the Effects of Binder Fluid	142
5.3	Numerical Solution	148
5.4	Model Results	150
5.4.1	Recommendations for verifying the model	158
6	Summary, Conclusions and Suggestions for Future Work	159
6.1	Summary and Conclusions	159
6.2	Suggestions for Future Work	160
	Bibliography	163

Introduction

1.1 Granulation

Granulation is a process where fine particles are bound together into larger granules. A list of the processes by which granulation can be achieved is given in Figure 1.1 [1]. In all of these processes, the objective is the formation of permanent bonds between particles. Figure 1.2 shows images of lactose granules taken under microscope. Primary applications of granulation include the manufacture of pharmaceuticals and the production of cosmetics, chemicals, detergents, and fertilisers [2,3]. Advantages of granulation include improved product flow (flowability), uniform product composition, increased shelf-life and improved compressibility. Ingredient segregation is also prevented which is advantageous for shipping and handling. In chemical applications granulation is frequently used for the production of raw ceramic mixes and the preparation of detergent and surfactant components.

This thesis concentrates on aspects of granulation by agglomeration (see Figure 1.1) which involves applying a binder to a bed of moving particles, either as a dry powder which melts as the powder is heated, or as a liquid binder. Through a combination of surface tension, capillary forces, and viscous dissipation, the binder allows agglomerates to coalesce and to grow in size [4]. Coalescence occurs when permanent liquid bridges form between particles. The liquid bridges eventually form solid bridges by solidification, crystallisation, mechanical interlocking of particles within agglomerates, and glass transition upon drying.

In this thesis wet granulation is studied on three different levels. First, micro-level investigations of liquid bridges between two and three particles are presented. Secondly, a separate geometric model is provided to estimate the wet fractional surface area (or stickiness) of moderately large agglomerates. Finally, a population balance model for modelling wet granulation is developed. This model incorporates functions that are de-

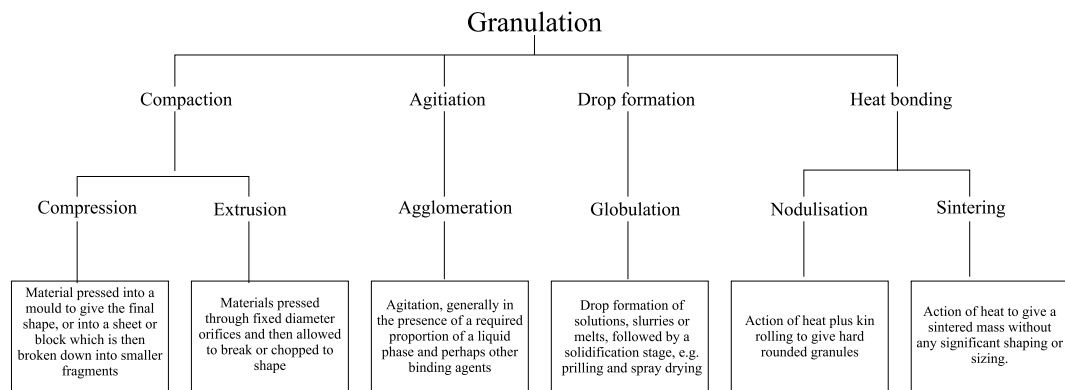


Figure 1.1: Classification of granulation processes. This figure is adopted from Sherrington and Oliver [1].

rived from the geometric agglomerate model. The motivation for this thesis is to gain insight into the micro-level profile and properties of liquid bridges and to develop a simulation of granulation that relates the stickiness of agglomerates to the probability of coalescence.

General background on granulation

A typical granulation circuit used in tablet making is shown in Figure 1.3. Production can be maximised by operating the process semi-continuously. In such a cycle, bulk raw ingredients are blended before being loaded into a granulator, which typically operates batchwise, although Leuenberger [5] has developed a semi-continuous process with a continuous granulator and batchwise drying. On completion of granulation, an end-point decided by the operator, the agglomerates are typically dried. A classifier may then sort particles for suitability in a tableting press by removing fines (under-sized particles) and over-sized particles. The accepted product is used to make tablets while the rejected product is ground up using a mill and fed back as an ingredient. The circuit shown in Figure 1.3 is representative of the process; additional steps such as cooling or additional pharmaceutical processes may also be included. Laboratory-scale granules may take product loads as small as several litres while commercial systems may granulate up to 600 litres of product per batch. In tableting it is common to mix active and filling ingredients and then granulate the blend to ensure uniform dosage of active ingredients. Kristensen *et al.* [3] provides a comprehensive review on pharmaceutical wet granulation.

Granulation systems can be low, medium or high-shear, referring to the magnitude of the agitation forces exerted on the particles during granulation. High-shear systems have a large overall intensity of agitation and the granules they produce are hard, dense, spherical and have low porosities [6, 7]. They have shorter process times compared to low-shear systems. Low-shear systems use a relatively small mechanical force to combine



(a) Lactose granules formed using Polyethylene glycol (PEG) as the binder.

(b) Lactose granules formed using Urea as the binder.

Figure 1.2: Images of granules taken under microscope. (Photographed using imaging equipment at the Horticulture and Food Research Institute of New Zealand.)

powders, relying instead on properties of the powder and binder to obtain coalescence. Granules produced by these systems are less dense, softer, more porous and less spherical than high-shear granules. They offer better compaction and are generally preferred for tableting [8].

The Würster fluidised bed is the industry standard for low-shear granulation and is illustrated in Figure 1.4(a). It uses a rapid flow of gas to transform solid particles into a fluid-like state by forcing air up through an initially stationary bed of particles [9]. Particles are recirculated by being propelled upward into a turbulent zone where inter-particle collisions occur. The particles then fall back to the bed under gravity. Usually the fluidising air is heated which allows inter-particle bonds to dry and for excess binder to evaporate. This reduces the likelihood of the bed binding together as a cohesive mass.

The Lödige mixer granulator, illustrated schematically in Figure 1.4(b), is a high-shear system with rotating blades, also called an impeller, that continually mixes particles. The impeller blades may rotate about a vertical or a horizontal axis [10]. It is also usual for a chopper blade to be present to control the maximum size of granules. Typical rotation speeds for the impeller blade are between 100 and 1000 rpm and typical speeds of the chopper are between 1000 and 5000 rpm. Continuous systems may have more than one impeller and more than one chopper and sometimes these systems also include some degree of fluidisation [11].

The medium-shear drum or pan granulator is illustrated in Figure 1.4(d). In this system particles recirculate and segregate by means of a rotating drum [11]. The granule density produced by this system is between that of the fluidised bed and the Lödige mixer

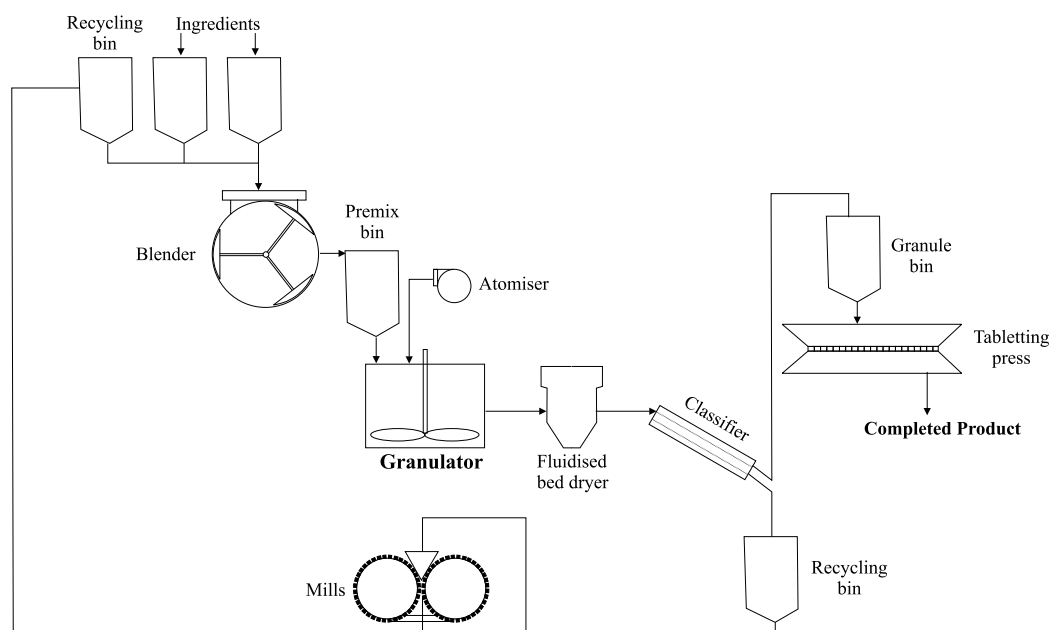


Figure 1.3: Schematic diagram of the granulation cycle. Industrial granulation systems operate on a continuous cycle to maximise production. Adapted from the 7th Edition of Perry's Chemical Engineers' Handbook [11].

granulator.

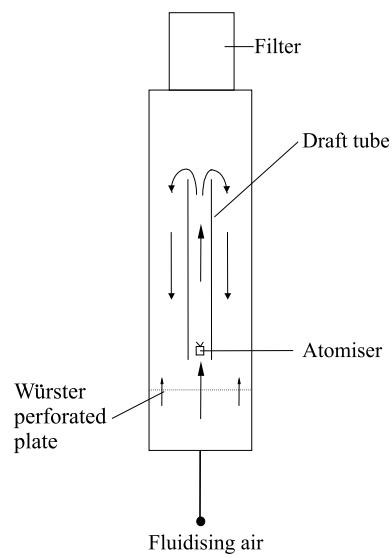
Binder choice is important in the production of granules. Liquid binders can be either aqueous or solvent based although aqueous solutions are more commonly used due to safety. The binder must have sufficient viscosity to promote agglomeration and growth but also provide sufficient strength to hold dried granules together as they become increasingly brittle as the inter-particle bonds dry. Normally an eight to twenty-four hour drying process is used.

End-product characteristics of granules, such as the mean particle size, granule strength, porosity and particle size distribution, are dependent on the type of granulator, the fill level, agitation intensity and the properties of the powder, binder and the delivery of binder [2, 11–13].

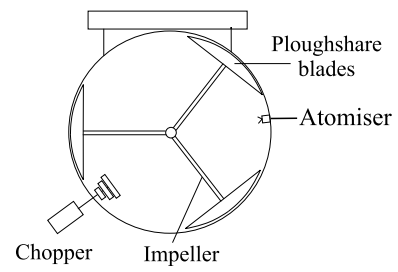
Granulation is a complex function of various stages of growth which are discussed in the following section.

1.2 Growth Mechanisms

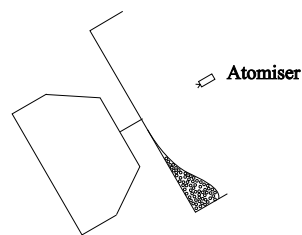
The mechanisms of wet granulation may be classified into the following stages: (i) wetting and nucleation, (ii) growth and consolidation and (iii) attrition and breakage [11]. Figure 1.5 provides an overview of these mechanisms.



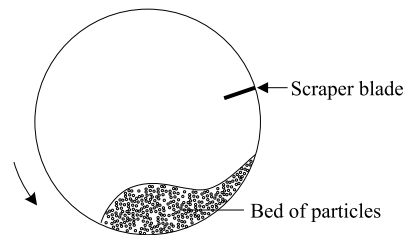
(a) Würster fluidised bed granulator



(b) Lödige high-shear mixer granulator.



(c) Side-on view of a drum granulator.



(d) End-on view of a drum granulator.

Figure 1.4: The Würster low-shear fluidised bed granulator, the high-shear Lödige system and the medium-shear drum (pan) granulator.

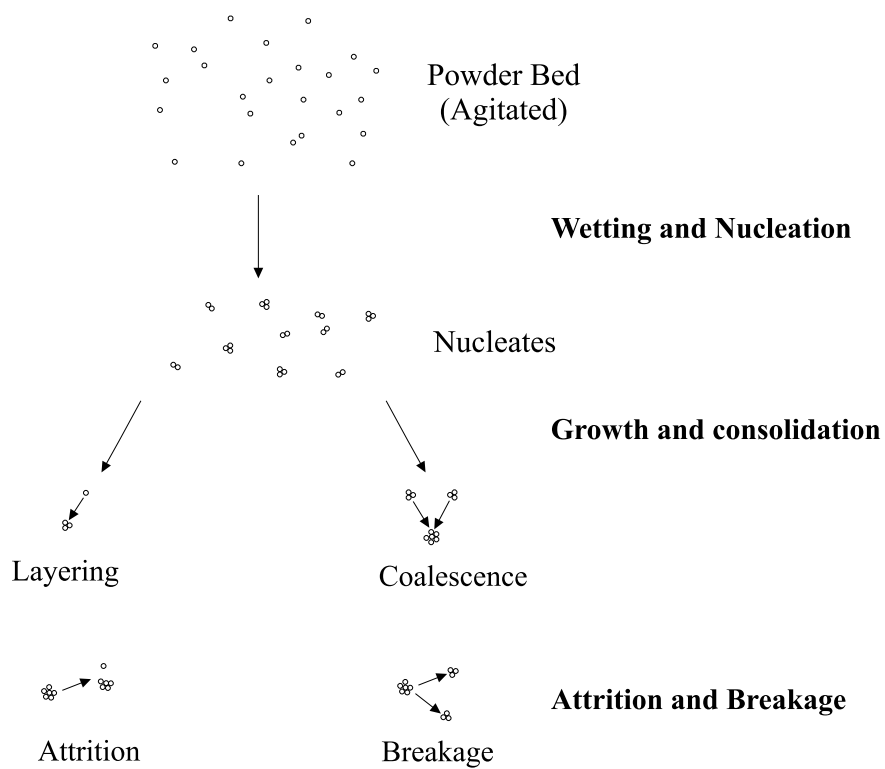


Figure 1.5: Overview of granulation mechanisms. Application of a binder to a moving bed of particles causes nucleates to form. As nucleates become surface wet, by consolidation, granules may form by layering and coalescence mechanisms. Attrition and breakage represent the reverse processes of layering and coalescence respectively.

Sections 1.2.1-1.2.3 below provide a summary of the research that has been completed in this area. Although this research is not directly related to the material in Chapters 2-5, it is included here to place our work in context.

1.2.1 Wetting and Nucleation

Nucleation refers to the period of initial contact between powder and binder. The objective of wetting, also known as binder dispersion, is to distribute binder liquid evenly throughout the powder to result in the formation of small nuclei [2].

Schæfer and Mathiesen [14] classify wetting and nucleation by comparing the relative size of powder particles and binder droplets. If liquid droplets are large in comparison to the diameter of powder particles, nucleation is said to occur by immersion. In this case, powder particles penetrate into larger liquid droplets to produce saturated nuclei which coalesce rapidly. Distribution refers to the converse situation where small binder droplets attach to the surface of powder particles to produce highly porous agglomerates. In practise a balance between these limiting cases is desired.

Binder can be delivered as a spray, using an atomiser, or by pouring or melting binder directly onto a moving bed of particles. Well-dispersed binder produces a narrow, well controlled nuclei size distribution [15]. The rate of nucleate formation and size distribution may be controlled by atomiser spray characteristics such as the spray flux, powder flux and droplet size distribution [15,16]. Fine droplets result in improved wetting [11,15]. Increasing the spray flux has been observed to increase the mean granule size, although high spray rates combined with large droplet sizes can result in poor quality spray characteristics due to droplet overlap. Increasing the spray angle (the angle through which the spray is dispersed) decreases the mean particle size and narrows the nuclei size distribution. This occurs because decreasing the spray density causes particles to be locally less surface wet. Increasing the agitation intensity increases the flux of powder (passing by the atomiser) which improves binder dispersion. Experimental studies have shown that delivering binder as a melt or by pouring often leads to inconsistent wetting. Downstream, this results in preferential growth, where regions of the bed are both under- and over-granulated. This causes end-product variation and a wide particle size distribution [15].

Thermodynamic properties

Thermodynamic properties of the powder and binder also influence wetting [15]. The contact angle θ , a fluid property, illustrated in Figure 1.6 for a stationary fluid, is the angle formed between solid and liquid at the three-phase contact line [17]. Perfect wetting has a contact angle of 0° and is achieved only in the case of an ideal fluid. This corresponds

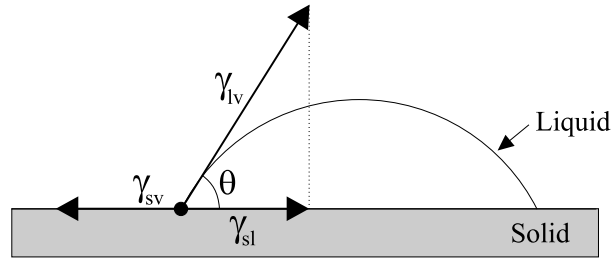


Figure 1.6: The contact angle θ for a stationary droplet in contact with a solid. The dot represents the three-phase contact line which is the intersection of the three interfaces. Subscripts on the surface tension γ refer to solid, liquid and vapour interfaces.

to the fluid spreading uniformly over a solid to create a thin, continuous layer of liquid. Partial wetting occurs for $\theta < 90^\circ$. Non-wetting fluids occur for $90^\circ \leq \theta < 180^\circ$ where a fluid contacts but does not spread. Complete non-wetting, where liquid and solid contact only at a single point, occurs for $\theta = 180^\circ$.

When fluid and solid are in equilibrium contact, as in Figure 1.6, the Young-Dupr e equation applies,

$$\gamma_{sv} - \gamma_{sl} = \gamma_{lv} \cos \theta. \quad (1.1)$$

The subscripts refer to the interfaces as shown in Figure 1.6. (For example γ_{lv} is the surface tension of the liquid-vapour interface.) The term $\gamma_{lv} \cos \theta$ is called the adhesion tension. Maximising this term results in improved wetting uniformity [11]. Low contact angles increase the adhesion tension and are associated with improved spreading of fluid over solid [15]. The adhesion tension may also be increased by using a different binder or by adjusting the surfactant concentration. Increasing the binder concentration also increases the contact angle θ although Ayala *et al.* [18] report that an optimum solution can be obtained. Granulation involves dynamic wetting on a short time scale where powder and fluid are not in equilibrium contact due to particle agitation. However, experimental studies have verified that the results discussed above also apply in the dynamic case [2].

Thermodynamics may be used to study the spread of a fluid over a solid [15]. The work required to divide a material is called the work of cohesion. Figure 1.7(a) illustrates the separation of a liquid and Figure 1.7(b) the separation of a solid. The area of the interfaces formed is A . The work of cohesion for the liquid is $W_{cl} = 2\gamma_{lv}A$ because two liquid-vapour interfaces are formed. Similarly, the work of cohesion for the solid is $W_{cs} = 2\gamma_{sv}A$. The work required to separate two different materials is called the work of adhesion. The separation of a liquid and solid is illustrated in Figure 1.7(c). Following separation, a liquid-vapour and solid-vapour interface is formed and a liquid-solid interface is destroyed. The work of adhesion is therefore $W_a = (\gamma_{sv} + \gamma_{lv} - \gamma_{ls})A$.

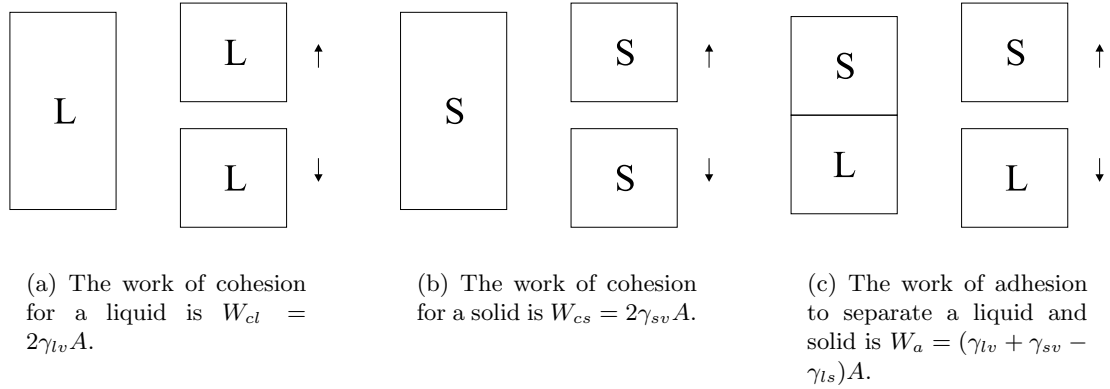


Figure 1.7: Figure (a) shows the separation of a liquid, (b) the separation of a solid and (c) the separation of liquid and solid (cited in [15]).

The definitions provided above are now used to study the spreading of a droplet over a solid. Figure 1.8 shows the initial position of a droplet as a solid outline. It later spreads to the position marked by the dotted outline. Following spreading, a liquid-vapour surface of area A_1 is formed and a solid-liquid interface of area A_2 is exchanged for a solid-vapour interface. The work of spreading is therefore

$$W_{ls} = \gamma_{lv} A_1 + (\gamma_{sl} - \gamma_{sv}) A_2. \quad (1.2)$$

Assuming that $A_1 \approx A_2 = A$, Equation (1.2) may be written using the works of cohesion and adhesion as

$$W_{ls} = W_{cl} - W_a. \quad (1.3)$$

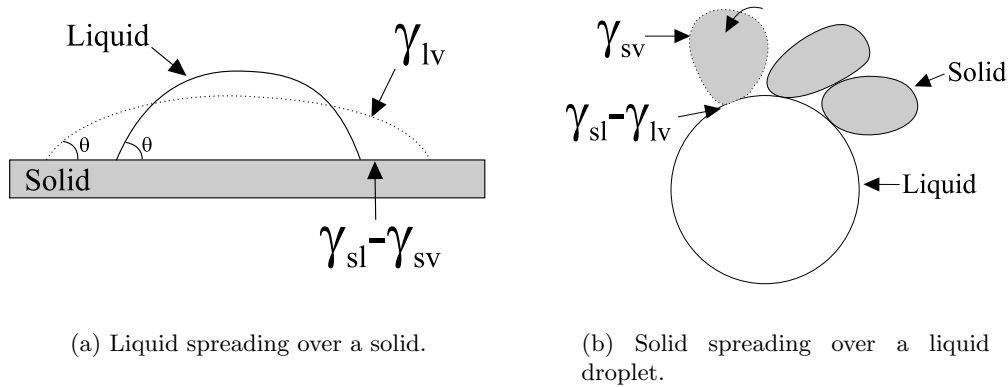
Spreading occurs if $W_{ls} < 0$ because the energy change is exothermic. For $W_{ls} > 0$ the droplet contracts. For $W_{ls} = 0$ the fluid is stationary and is in thermodynamic equilibrium.

Conditions are also derived for the solid to spread over the liquid. This is to be avoided in granulation because it results in poor wetting. If the solid spreads, as illustrated in Figure 1.8(b), then a solid-vapour interface of area A_1 is formed and a solid-liquid interface of area A_2 is exchanged for a liquid-vapour interface. The work of the solid spreading is thus

$$W_{sl} = \gamma_{sv} A_1 + (\gamma_{ls} - \gamma_{lv}) A_2. \quad (1.4)$$

As above, assuming that $A_1 \approx A_2 = A$, the work of spreading may be written as

$$W_{sl} = W_{cs} - W_a. \quad (1.5)$$



(a) Liquid spreading over a solid.

(b) Solid spreading over a liquid droplet.

Figure 1.8: If $W_{ls} < 0$ then the liquid spreads over the solids as shown in (a). If $W_{sl} < 0$ then the solid spreads of the liquid as shown in (b).

The solid spreads over the liquid for $W_{sl} < 0$ and recedes for $W_{sl} > 0$. For $W_{sl} = 0$ the arrangement is in thermodynamic equilibrium and is stationary.

If $W_{cl} > W_a$ and $W_{cs} > W_a$ then $W_{ls} > 0$ and $W_{sl} > 0$. This case corresponds to non-wetting where the liquid and the solid make contact at a single point.

Figure 1.9 illustrates nucleation by distribution and immersion and the influence that the works of spreading W_{ls} and W_{sl} have on granulation.

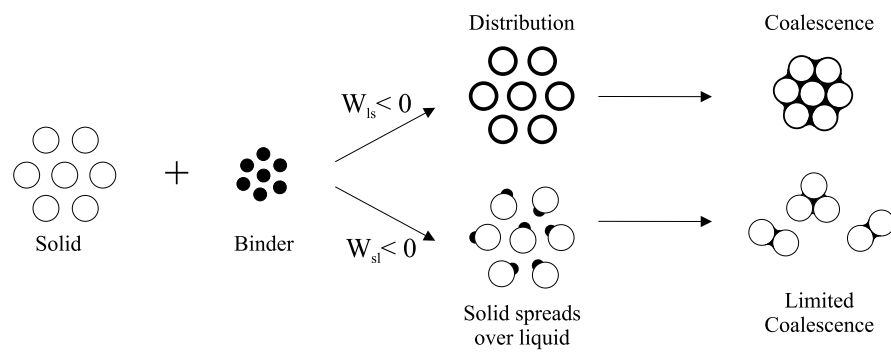
Viscous properties

The viscosity of the binder is a further consideration for wetting and later growth. Decreasing the binder viscosity enhances atomisation because finer droplets are created, allowing nucleation to enter the drop controlled regime described by Hapgood [15]. Wetting is also affected by spreading, either by impact of droplets on a powder surface or by smearing as powder surfaces are sheared. Both processes are affected by viscosity.

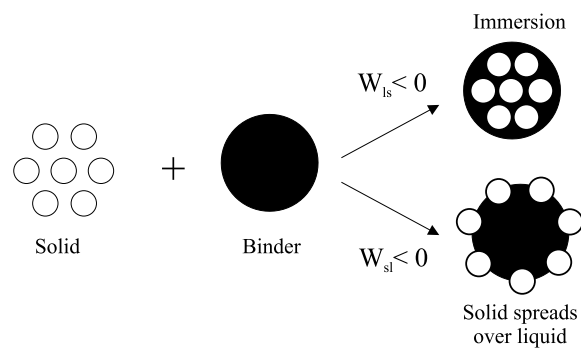
Initial growth is enhanced by low binder viscosity and later growth by higher binder viscosity [19]. Viscous binders are slow to flow through the powder pores to form saturated nuclei. Increasing the binder viscosity generally inhibits both atomisation and binder dispersion. Hence a viscous binder will often form large initial nuclei but will take a long time to uniformly disperse throughout the powder. This may delay on the onset of uniform growth but can also cause preferential growth.

Binder dispersion

Litster *et al.* [20] model the dispersion of binder from an atomiser. Droplets are produced at a volumetric flow-rate of \dot{V} and have an average droplet diameter of d . Binder is delivered to the powder bed with cross-sectional area A . The dimensionless spray flux



(a) Nucleation by distribution.



(b) Nucleation by immersion.

Figure 1.9: The effect of W_{ls} and W_{sl} on nucleation for (a) distribution and (b) immersion.

provides a measure of binder coverage on the powder surface and is defined by

$$\Psi = \frac{3\dot{V}}{2\dot{A}d} \quad (1.6)$$

where $\dot{A} = \frac{dA}{dt}$. For $\Psi \gg 1$ the volume of binder added per unit powder bed is large. In this case droplet coalescence occurs due to droplet overlap. Controlled nucleation, with a narrow size distribution, occurs for $\Psi < 1$. Litster *et al.* [20] report that optimal results are achieved for $\Psi \lesssim 0.1$.

1.2.2 Growth and Consolidation

Following nucleation, particles are sufficiently surface wet to form agglomerates. Layering is the term used to describe growth whereby primary particles or nuclei attach to larger agglomerates. Coalescence refers to the union of two similarly sized nucleates or granules [11].

Layering has been described by Wauters *et al.* [21] as the appearance of wet spots on the surface of granules, due to consolidation, and the adherence of fine particles to these regions. Induction, also known as densification, refers to growth where layering is the dominant mechanism and continues until the supply of fines is exhausted. The length of the induction period decreases with increasing liquid content [22]. Following induction, agglomerates increase in surface wetness which allows the particles to undergo growth by coalescence [16]. As the mass of an incident particle is typically much less than that of an agglomerate, layering is assumed to be successful if a wet region exists.

Coalescence has been identified as a more complex interaction than layering because the particles involved have similar masses and because the liquid bridges become dynamic. Following a collision several outcomes are possible: (i) the particles coalesce, (ii) the particles rebound or (iii) one or both of the particles break into fragments. A number of models exist in the literature to predict whether coalescence will occur following a binary collision [4, 23–27]. Of these, the models that are suitable for modelling wet granulation are those developed by Ennis *et al.* [4] and Liu *et al.* [26]. Both models consider a binary collision where the particles are coated with a uniform layer of liquid. The dissipation of the impact kinetic energy within the fluid layer is considered. Ennis *et al.* [4] assume that no permanent deformation of the granule surfaces occur, which allows the model to be applied, as an approximation, to coalescence in low-shear systems. Liu *et al.* [26] extend the model of Ennis *et al.* [4] to account for plastic deformation which is significant in high-shear systems. Both models are discussed in more detail in Section 1.3.3.

Consolidation occurs when external compressive or shear forces are applied to particles. In granulation this is caused by agitation forces, inter-particle collisions and collisions between the particles and the walls of the granulator [2]. Consolidation causes the porosity of granules to decrease and for the binder to migrate towards the surface of the particles. If the binder viscosity is increased then the rate of consolidation is slowed because strong particles, resistant to deformation, are formed. If the highly viscous binder is able to migrate to the surface, however, the fluid can dissipate more kinetic energy of the incident particles to increase the probability of coalescence. Thus, high-viscosity binders have been observed to have slow initial growth but rapid long-term growth [22].

Iveson *et al.* [28] studied the evolution of granule size distributions obtained from low, medium and high-shear experiments. Their analysis has identified the following classifications for growth: wetting and nucleation, induction, steady growth and rapid growth. Iveson *et al.* [28] present their findings as a growth regime map for granulation which is illustrated in Figure 1.10. This map defines approximate boundaries for the various growth types. For fixed binder viscosity they postulate that granule growth is a function of the Stokes deformation number St_{def} and the maximum granule pore saturation s_{max} . The Stokes deformation number is defined as

$$St_{\text{def}} = \frac{\frac{1}{2}\tilde{m}(2u_0)^2}{32\tilde{a}^3Y} \quad (1.7)$$

which is the ratio of the impact kinetic energy, resulting from a head-on binary collision at a relative speed $2u_0$, to the energy loss incurred by the plastic deformation of granules. In Equation (1.7) \tilde{m} denotes the harmonic mean mass

$$\tilde{m} = \frac{m_1m_2}{m_1 + m_2}, \quad (1.8)$$

\tilde{a} the harmonic mean radius

$$\tilde{a} = \frac{a_1a_2}{a_1 + a_2} \quad (1.9)$$

and Y the granule dynamic yield stress. For the regime map u_0 is taken as some representative collision velocity for the ensemble. The maximum pore saturation s_{max} is defined as the ratio of the liquid-to-void mass when the voids are filled with liquid,

$$s_{\text{max}} = \frac{w\rho_s(1 - \epsilon_{\text{min}})}{\rho_l\epsilon_{\text{min}}}, \quad (1.10)$$

where w is the mass ratio of liquid to solid, ρ_s is the density of the solid particles, ρ_l is the liquid density and ϵ_{min} is the minimum porosity achieved by the granules in the ensemble. s_{max} increases with residence time in the granulator because of consolidation.

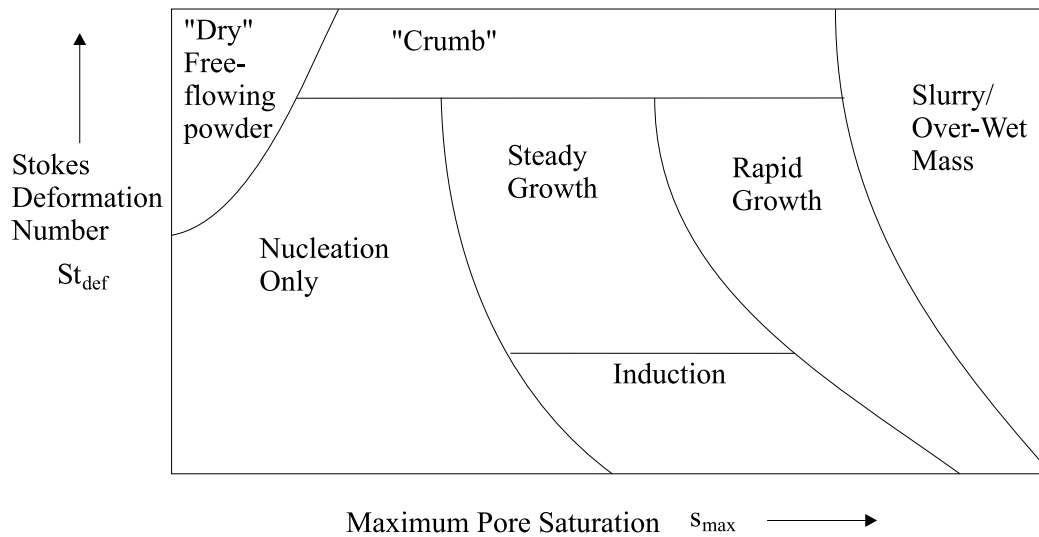


Figure 1.10: Growth regime map for granulation from Iveson *et al.* [28] showing the dominant growth mechanisms in terms of the Stokes deformation number St_{def} and the maximum pore saturation s_{max} .

Steady growth occurs when granules are weak and deformable and a large contact area is formed between the particles upon collision. Liquid is squeezed onto the surface of particles which promotes particle coalescence. Growth is approximately linear with respect to time for steady growth and occurs for low viscosity binder fluids. Rapid growth is coalescence that occurs when particles become surface saturated with liquid and tends to occur in systems that have strong, slowly consolidating granules which are formed following a period of induction. The high surface wetness of these particles enables them to undergo coalescence easily [28].

As may be inferred from the map, the “Dry” free flowing powder occurs in the presence of large deformation forces but with minimal binder. The “crumb” area occurs when there is sufficient liquid but high impact forces causing attrition and breakage (which is discussed below). The slurry/over-wet condition occurs when the system is saturated with binder resulting in the formation of a cohesive mass.

1.2.3 Attrition and Breakage

Attrition and layering are inverse processes. Attrition occurs when individual or small clusters of primary particles break away from an agglomerate. Breakage refers to the inverse mechanism of coalescence where an agglomerate fractures into two or more similarly sized segments [11].

The mechanisms of attrition and breakage occur when an external shear force is applied to particles. The primary cause of breakage in high-shear systems is the contact of particles

with the impeller and chopper blades. Attrition and breakage also result from inter-particle collisions and collisions between the particles and the walls of the granulator. Breakage is more common in high-shear systems [11].

Tardos *et al.* [29] define a simple model for the attrition and breakage of particles in wet granulation systems. (A limitation of the model, however, is that it does not differentiate between the mechanisms of attrition and breakage individually.) The model is based on the work of Ennis *et al.* [4] and uses analogies between layering and attrition and coalescence and breakage. Tardos *et al.* [29] consider an agglomerate of mass m , travelling at speed u_0 where a shear force of magnitude τ is applied. The Stokes deformation number for attrition and breakage is defined as

$$\text{St}_{\text{break}} = \frac{\frac{1}{2}mu_0^2}{V\tau} \quad (1.11)$$

where V denotes the volume of the agglomerate. St_{break} is equal to the ratio of the particle kinetic energy to the internal energy of the particle available to resist deformation before fracture occurs. It is assumed that the shear-stress propagates uniformly throughout the particle. A critical Stokes number $\text{St}_{\text{break}}^*$ is defined where breakage and attrition occurs for $\text{St}_{\text{break}} > \text{St}_{\text{break}}^*$. Unlike the Ennis model, a theoretical value for $\text{St}_{\text{break}}^*$ is not provided and therefore this value is determined experimentally. Tardos *et al.* [29] propose that the granule will behave as a Herschel-Bulkley fluid under stress as given by the condition

$$\tau(\dot{\gamma}) = \tau_0 + k\dot{\gamma}^n \quad (1.12)$$

where τ denotes the shear stress, τ_0 is the yield stress, k is an apparent viscosity, $\dot{\gamma} = \frac{d\gamma}{dt}$ is the shear-rate and n is a power law exponent. Herschel-Bulkley fluids respond to shear by requiring a minimum stress τ_0 to initiate flow but have the property that the shear-stress decreases with increasing shear-rate $\dot{\gamma}$.

It is likely that future research will develop more detailed models that will distinguish between the mechanisms of attrition and breakage.

1.3 Micro-level Models for Granulation

1.3.1 Saturation States

For agglomeration, three states define the amount of binder internally contained in a granule. The pendular, funicular, and capillary states refer, in increasing order, to the fraction of internal pore space that is occupied by fluid [30]. The pendular state describes

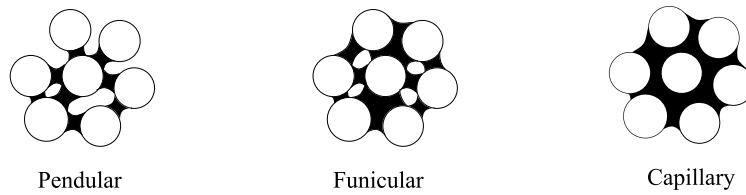


Figure 1.11: Pendular, funicular and capillary saturation states.

neighbouring particles that are joined together by individual pendular liquid bridges while the capillary state refers to an agglomerate where the inter-particle voids are completely filled with binder. The transition between these cases is known as the funicular saturation state. During granulation it is usual for the saturation state to increase due to consolidation. Classifications of saturation states higher than capillary also exist such as droplet. This, however, refers to an overly-saturated state where the primary particles are contained within a droplet. Since this saturation state leads directly to over-wetting it is not preferred for granulation.

The work discussed in Section 1.3.2 and Chapter 2 considers the pendular saturation state for liquid bridges between two particles, Chapter 3 considers the funicular saturation state for liquid bridges between three particles and the capillary saturation state is assumed for the geometric agglomerate model which is detailed in Chapter 4.

1.3.2 Static Liquid Bridges

Physical models of liquid bridges formed between the contact points on solid particles are fundamental to modelling wet granulation. Historically, this problem dates to 1873 with the work of Plateau in adsorption thermodynamics. In the work presented below, primary particles are approximated by spheres. This approach is valid provided the particles are approximately spherical and the surface asperities are small compared to the radius of the primary particles. The profile of static liquid bridges formed between two spheres are known as the nodoid of Plateau [31]. The term static implies that the fluid surface is stationary.

Figure 1.12 illustrates a cross-section of a pendular static liquid bridge formed between two spheres of radius a . Models of this arrangement consider liquid bridges attached to small, rigid particles where the weight of the fluid is small compared to the surface tension force. This allows the gravitational force to be neglected [31–35]. External forces, such as electrostatic and Van der Waals forces, are assumed to be absent. The binder fluid is assumed to be uniform, incompressible and in thermodynamic equilibrium with ambient

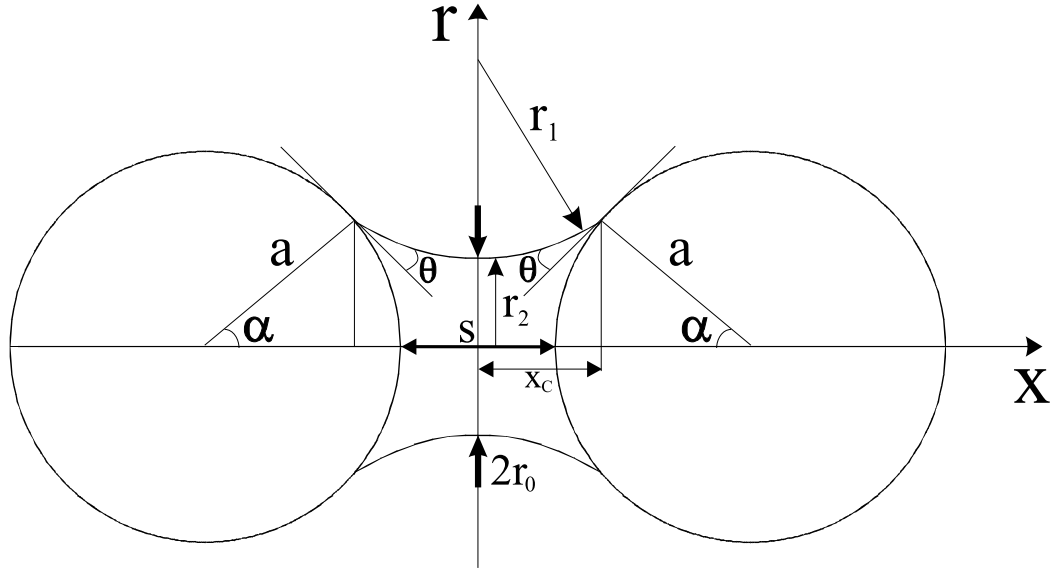


Figure 1.12: Static liquid bridge drawn in the $x - r$ plane between particles of radius a . The principal radii of curvature are denoted by r_1 and r_2 . The angle between the tangent plane to the spheres and the fluid surface is equal to the fluid contact angle θ . The height of the bridge at $x = 0$ is r_0 and the half-filling angle is α .

conditions.

For the conditions described above, the relevant geometric equation, for static liquid bridges, is the Young-Laplace equation, derived by Batchelor [17], as

$$H_0 = \frac{\Delta p}{2\gamma_{lv}}. \quad (1.13)$$

In Equation (1.13), H_0 denotes the mean curvature of the liquid bridge surface, γ_{lv} the fluid surface tension and Δp the capillary pressure difference (or jump) caused by the presence of the fluid. When Δp is positive the internal bridge pressure is higher than the external (or ambient) pressure. For static liquid bridges Δp is constant and therefore H_0 is constant.

The coordinates r and x in Figure 1.12 define the height and position of the fluid surface. The x -axis passes through the centre of the primary particles and the origin is defined as the point where the tangent $r'(x)$ to the bridge surface is horizontal and the height of the bridge is r_0 . The angle between the fluid surface and the horizontal x axis is given by ψ so that $r'(x) = \tan \psi$. The bridge is rotationally symmetric about the x -axis and therefore $r = r(x)$. The separation distance between the particles is s and the distance between the origin and the contact point of the fluid with the spheres is x_c . From Figure 1.12, it can be shown that $s = 2[x_c - a(1 - \cos \alpha)]$.

Equation (1.13) may be solved by rewriting it in terms of $r(x)$ and the derivatives of $r(x)$. The principal radii of curvatures in the $r - x$ and $r - y$ planes are respectively denoted by r_1 and r_2 . In terms of r_1 and r_2 the mean curvature is

$$H_0 = \frac{1}{2} \left(\frac{1}{r_1} + \frac{1}{r_2} \right) \quad (1.14)$$

where the curvature in the $r - x$ plane is $1/r_1$ and the curvature in the $r - y$ plane is $1/r_2$. Substituting Equation (1.14) into Equation (1.13) gives [31–35]

$$\gamma_{lv} \left(\frac{1}{r_1} + \frac{1}{r_2} \right) = \Delta p. \quad (1.15)$$

The liquid bridge is a surface of revolution about the x -axis. This allows vector calculus results to be applied (see [36] for details) to write Equation (1.15) as

$$\gamma_{lv} \left(\frac{r''}{(1+r'^2)^{3/2}} - \frac{1}{r(1+r'^2)^{1/2}} \right) = \Delta p \quad (1.16)$$

where $r = r(x)$, $r' = \frac{dr}{dx}$ and $r'' = \frac{d^2r}{dx^2}$.

At $x = x_C$, the three-phase contact line, the angle between the fluid and the tangent plane to the spheres is equal to the contact angle θ . Figure 1.13 shows an enlarged view of the fluid surface and sphere for $x \geq 0$ and $r \geq 0$. At $x = x_C$, using Figure 1.13,

$$\psi \Big|_{x=x_C} = \frac{\pi}{2} - (\alpha + \theta). \quad (1.17)$$

(For concave liquid bridges $\psi > 0$ and for convex liquid bridges $\psi < 0$.) From Equation (1.17) the boundary condition at x_C is

$$\begin{aligned} r'(x_C) &= \tan \psi \Big|_{x=x_C} \\ &= \tan \left(\frac{\pi}{2} - (\alpha + \theta) \right) \\ &= \cot(\alpha + \theta). \end{aligned} \quad (1.18)$$

For fixed contact angle θ , Lian [35] integrates Equation (1.16) subject to the boundary conditions and treats the mean curvature and half-filling angle α as parameters. Liquid bridge properties are calculated including the volume, surface area, separation distance and the Gibbs' free surface energy. The maximum inter-particle distance corresponding to rupture is also calculated in terms of the liquid bridge volume.

Chapter 2 of this thesis extends the work of Lian [35] by calculating liquid bridge properties where the radii of the primary particles may be different. (Lian [35] assumes both

Geometrically, from Figure 1.14,

$$r_1 \cos(\alpha + \theta) = \frac{s}{2} + r_A(1 - \cos \alpha) \quad (1.20)$$

$$r_1 + r_2 = r_1 \sin(\alpha + \theta) + r_A \sin \alpha \quad (1.21)$$

where s denotes the separation distance between the closest edges of the primary particles.

By rearrangement of Equations (1.20) and (1.21), the radii of the circular arcs is given by

$$r_1 = \frac{\frac{s}{2} + r_A(1 - \cos \alpha)}{\cos(\alpha + \theta)} \quad (1.22)$$

$$r_2 = r_1 [\sin(\alpha + \theta) - 1] + r_A \sin \alpha. \quad (1.23)$$

For a zero degree contact angle (perfect wetting), Lian [35] finds that the toroidal approximation gives errors of less than 10 % when compared to the true profile provided that the half-filling angle $\alpha \leq 45^\circ$.

Simons *et al.* [24] used Equations (1.22) and (1.23) to obtain expressions for the inter-particle binding force in terms of the rupture energy of static liquid bridges assuming perfect wetting ($\theta = 0^\circ$). The following relationship was obtained between the dimensionless rupture energy E^* and the dimensionless rupture volume V^* ,

$$E^* = 1.8\sqrt{V^*}. \quad (1.24)$$

Equation (1.24) was derived by evaluating the axial surface tension force and the hydrostatic force at $x = 0$. (An alternative approach is to use the method of Hotta *et al.* [34] to evaluate these forces at the three-phase contact line.)

(ii) Liquid bridge stability

De Bisschop and Rigole [31] take a fundamental approach to studying static liquid bridges between two particles. Instead of beginning with the Young-Laplace equation they find the surface with minimum Gibbs free surface energy for a given volume of binder fluid v . The solution to this isoperimetric problem is obtained using the calculus of variations [37]. The approach taken is now outlined. The Gibbs free energy E of a liquid bridge surface is equal to the sum of (i) the free surface energy due to the liquid-vapour interface and (ii) the free surface energy due to the liquid-solid interface [31]. For primary particles of

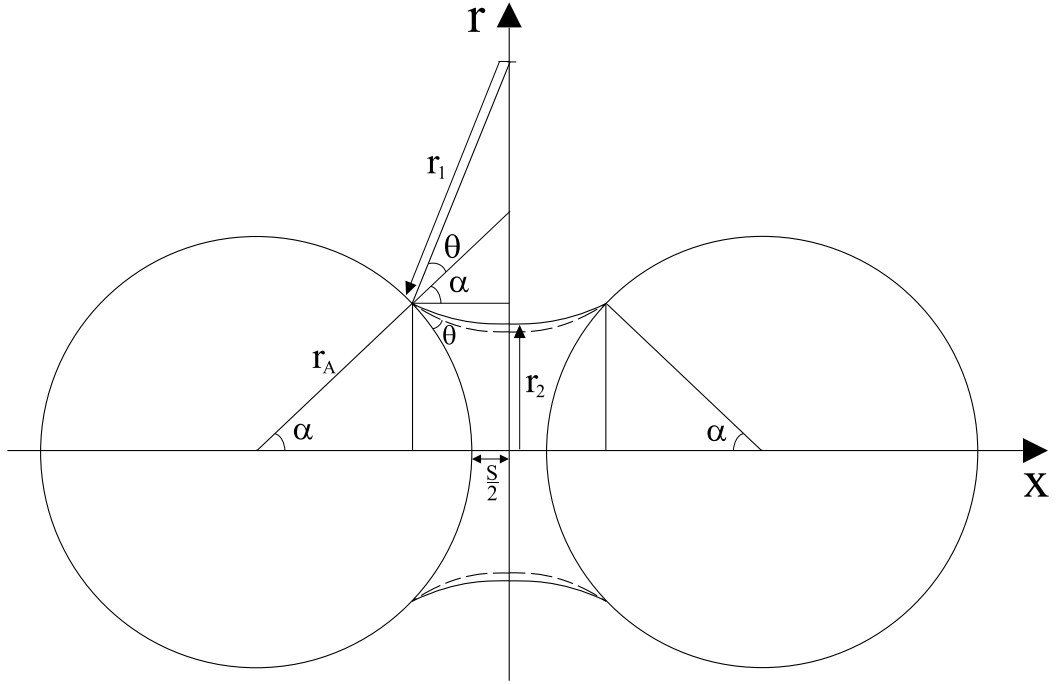


Figure 1.14: Liquid bridge geometry using the toroidal approximation with circular arcs of radii r_1 and r_2 . The dotted line represents the true profile of the liquid bridge.

equal radii a the Gibbs free surface energy is given by

$$E = 2 \int_0^{x_B} \left[2\pi\gamma_{lv} r \sqrt{1 + \left(\frac{dr}{dx}\right)^2} + 2\pi(\gamma_{sl} - \gamma_{sv}) u_c \sqrt{1 + \left(\frac{du_c}{dx}\right)^2} \right] dx, \quad (1.25)$$

where γ denotes the respective surface tensions, as defined in Equation (1.1), $r(x)$ denotes the liquid bridge profile and $u_c(x)$ is the profile of a primary particle of radius a as given by

$$u_c(x) = \begin{cases} \sqrt{a^2 - (x_c + a \cos \alpha)^2} & \frac{s}{2} \leq x \leq x_c \\ 0 & x < \frac{s}{2} \end{cases} \quad (1.26)$$

Equation (1.25) may be simplified, using the Young-Dupré equation from Equation (1.1), to give

$$E = 2 \times 2\pi\gamma_{lv} \int_0^{x_B} \left[r \sqrt{1 + \left(\frac{dr}{dx}\right)^2} - \cos \theta u_c \sqrt{1 + \left(\frac{du_c}{dx}\right)^2} \right] dx. \quad (1.27)$$

The isoperimetric constraint on Equation (1.25) is a fixed volume of fluid v as given by

$$v = 2\pi \left[\int_0^{x_C} (r^2 - u_c^2) dx \right]. \quad (1.28)$$

The integrand of Equation (1.25) is denoted by I and the integrand of Equation (1.28) by J . According to the calculus of variations, the expression

$$F = I - \lambda J \quad (1.29)$$

is formed where λ is a constant called the Lagrange multiplier. The liquid bridge profile is then obtained by solving the Euler-Lagrange equations

$$\frac{\partial F}{\partial r} - \frac{d}{dx} \left(\frac{\partial F}{\partial r'} \right) = 0. \quad (1.30)$$

Upon solving Equation (1.30), De Bisschop and Rigole [31] find that

$$\lambda - p_a = \gamma_{lv} \left[\frac{r''}{(1 + r'^2)^{\frac{3}{2}}} - \frac{1}{r(1 + r'^2)^{\frac{1}{2}}} \right] \quad (1.31)$$

where p_a denotes the external (ambient) pressure. Equation (1.31) is the Young-Laplace equation where the parameter λ is equal to the pressure within the liquid phase (since the right-hand side of Equation (1.31) is equal to Δp from Equation (1.16).) This independently confirms the requirement for static liquid bridges to have constant mean curvature.

The results presented in Chapter 2, along with the results obtained by Lian [35] and De Bisschop and Rigole [31], show that for a fixed inter-particle separation distance s and contact angle θ , it is possible for two distinct liquid bridge arrangements to be obtained for a given fluid volume v . In theory, the calculus of variations may be used to address this stability issue. However, the second variational problem of the Gibbs free surface energy has not been solved analytically [35]. The Gibbs free surface energy is therefore calculated numerically. In cases where two liquid bridge configurations are possible, for a given volume v , the stable arrangement, which occurs physically, is that which has minimum Gibbs free surface energy.

(iii) Larger arrangements

Provided the fluid surface is static, the Young-Laplace equation from Equation (1.13) applies to agglomerates containing an arbitrary number of particles. The fluid surface is required to have constant mean curvature H_0 and the contact angle θ occurs at the contact points between the primary particles and the fluid. For particles in the capillary saturation state the pressure difference Δp is uniform throughout the fluid. For particles

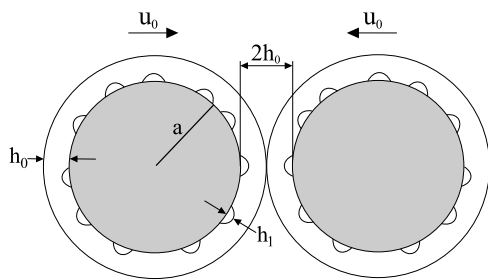
in the pendular and funicular saturation state Δp may differ between each continuous portion of fluid.

Fisher [32] models liquid bridges between a collection of mono-sized particles assuming that pendular liquid bridges occur between neighbouring particles and that individual fluid segments do not overlap. For this simplified arrangement, the model discussed in Section 1.3.2 may be applied repeatedly to each portion of fluid. For the more general case, where the fluid portions merge, Fisher [32] remarks, “After the coalescence of the separate portions of liquid into a continuous body, the problem of the nature of the liquid surface, and of the force produced by it, in relation to the total volume of water present, becomes one of great complexity, which has I believe never been even cursorily examined.” Chapter 3 makes progress on this formidable problem by solving the Young-Laplace equation for capillary state static liquid bridges between three particles. The method used may also be extended to solve for four and five particle arrangements.

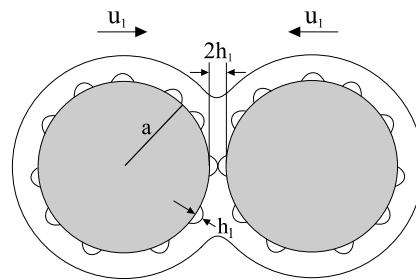
Urso *et al.* [38] recently provided classifications of liquid bridges between three particles. These workers do not solve Young-Laplace equation but instead approximate liquid bridges by using circular arcs in two dimensions which is an extension of the toroidal approximation discussed in Section 1.3.2.

1.3.3 Dynamic Liquid Bridges

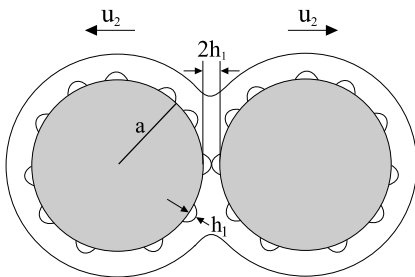
Ennis *et al.* [4] consider two particles, each of radius a and mass m , approaching at a relative speed of $2u_0$ in a head-on (or normal) collision as shown in Figure 1.15(a). Capillary and surface tension forces are neglected; only the viscous force is considered. The h -axis measures the separation distance between the particles. Both particles are assumed to be coated with a uniform layer of liquid of thickness h_0 . They also have surface asperities of height h_1 . Figure 1.15(a) shows the initial contact between the liquid layers where the particles are separated by a distance $2h_0$. Due to viscous dissipation, the fluid is squeezed outward from the gap and, as shown in Figure 1.15(b), the particles make contact at $h = 2h_1$ at speed u_1 . This causes an increase in hydrodynamic pressure resulting in the particles deforming elastically, about their axis of symmetry, according to the theory of linear elasticity [39]. The remaining kinetic energy is stored as elastic strain energy [40, 41]. After the particles come to a halt this energy is released allowing the particles to rebound. Elastic recovery of the granules occurs and there is no permanent plastic deformation. The liquid bridge is assumed to rupture at $2h_0$ as shown in Figure 1.15(d). Below the equations for these various stages are studied. In the discussion the h -axis is referenced such that $h = 0$ corresponds to the mid-point between the particles.



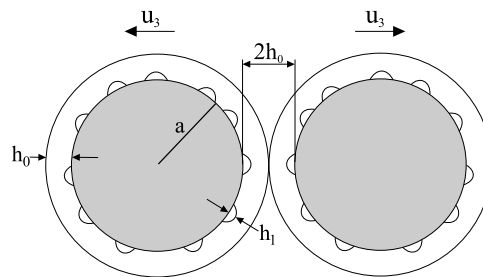
(a) Initially the particles are travelling at speed u_0 . The fluid layers contact at a separation distance of $2h_0$ as shown.



(b) Viscous dissipation reduces the speed of the particles to u_1 at a separation distance of $2h_1$. The remaining kinetic energy is stored as elastic strain energy.



(c) The stored elastic energy is released and the particles rebound with speed $u_2 = -eu_1$.



(d) The particles return to a separation distance of $2h_0$ at speed u_3 . The liquid bridge is assumed to rupture at this point as shown.

Figure 1.15: Figures for the Ennis *et al.* [4] coalescence model showing (a) the approach stage, (b) and (c) the viscous dissipation stage and (d) the rebound stage. This figure assumes that $u_3 > 0$ and that rebound occurs.

Assuming a small gap separation distance $2h_0 \ll a$, and quasi-steady conditions, lubrication theory may be applied [17] to obtain the viscous retarding force of a dynamic liquid bridge. Adams and Perchard [42] achieve this using an asymptotic solution where the motion of the approaching spheres is divided into inner and outer regions. Deformation occurs in the inner region but is negligible in the outer region. For a Newtonian fluid, the viscous retarding force of a dynamic liquid bridge is obtained as

$$F_{\text{vis}} = \frac{3\pi\mu a^2}{2h} \frac{dh}{dt} \quad (1.32)$$

where the fluid is assumed to be Newtonian and incompressible with viscosity μ .

Since the particles are identical a force balance on an individual granule is considered. This gives

$$\begin{aligned} m \frac{du_a}{dt} &= F_{\text{vis}} \\ &= \frac{3\pi\mu a^2}{2h} \frac{dh}{dt} \end{aligned} \quad (1.33)$$

where u_a denotes the approach velocity of the particles. Rearrangement of Equation (1.33) gives

$$\begin{aligned} \frac{du_a}{dh} &= \frac{3\pi\mu a^2}{2hm} \\ &= \frac{\kappa}{h} \end{aligned} \quad (1.34)$$

where $\kappa = \frac{3\pi\mu a^2}{2m}$ has been introduced. Integrating Equation (1.34) gives

$$u_a(h) = \kappa \ln(h) + C. \quad (1.35)$$

The initial condition $u(h_0) = u_0$, shown in Figure 1.15(a), is applied which gives $C = u_0 - \kappa \ln(h_0)$. Therefore

$$u_a(h) = u_0 - \kappa \ln\left(\frac{h_0}{h}\right). \quad (1.36)$$

As discussed above, the approach of the particles is damped by viscous dissipation. The particles touch at $h = h_1$ with speed $u = u_1$ as shown in Figure 1.15(b). From Equation (1.36), at $h = h_1$,

$$u_1 = u_0 - \kappa \ln\left(\frac{h_0}{h_1}\right). \quad (1.37)$$

If, during the approach stage, $u_1 = 0$ then the particles coalesce prior to the surfaces

touching. From Equation (1.37) this corresponds to

$$u_0 \leq \kappa \ln \left(\frac{h_0}{h_1} \right). \quad (1.38)$$

If $u_1 > 0$ then the remaining kinetic energy of the particles is stored as elastic strain energy [40]. Some elastic loss occurs because the particles deform; the rebound velocity following impact is [40]

$$u_2 = -eu_1 \quad (1.39)$$

where e denotes the coefficient of restitution of the particles. The viscous force of the liquid bridge again retards the motion of the particles. From Equation (1.34), and accounting for the change in direction,

$$\frac{du_r}{dh} = -\frac{\kappa}{h}, \quad (1.40)$$

where u_r denotes the rebound velocity. Using the initial condition $u = u_2$ at $h = h_1$, Equation (1.40) is solved to obtain

$$\begin{aligned} u_r(h) &= u_2 - \kappa \ln \left(\frac{h}{h_1} \right) \\ &= eu_1 - \kappa \ln \left(\frac{h}{h_1} \right). \end{aligned} \quad (1.41)$$

Combining Equation (1.41) and Equation (1.37) gives the rebound speed of the particles at $h = h_0$ as

$$\begin{aligned} u_3 &= u_r(h_0) \\ &= eu_1 - \kappa \ln \left(\frac{h_0}{h_1} \right) \\ &= e \left[u_0 - \kappa \ln \left(\frac{h_0}{h_1} \right) \right] - \kappa \ln \left(\frac{h_0}{h_1} \right) \\ &= eu_0 - (e + 1)\kappa \ln \left(\frac{h_0}{h_1} \right). \end{aligned} \quad (1.42)$$

The viscous Stokes number [40] compares the initial kinetic energy of the particles to the energy dissipated by the liquid bridge through the collision as given by

$$\begin{aligned} \text{St} &= \frac{\frac{1}{2}m(2u_0)^2}{2h F_{\text{vis}}} \\ &= \frac{2mu_0}{3\pi\mu a^2} \\ &= \frac{u_0}{\kappa}. \end{aligned} \quad (1.43)$$

Using Equation (1.43), Equation (1.42) may be rewritten as

$$u_3 = u_0 \left[e - \frac{1}{\text{St}}(1 + e) \ln \left(\frac{h_0}{h_1} \right) \right]. \quad (1.44)$$

Of interest for granulation is finding the critical Stokes number St^* as this corresponds to the particles coming to a halt, after rebound, at a separation distance of $2h_0$. Setting $u_3 = 0$ in Equation (1.44) and rearranging gives

$$\text{St}^* = \left(1 + \frac{1}{e} \right) \ln \left(\frac{h_0}{h_1} \right). \quad (1.45)$$

For $\text{St} \leq \text{St}^*$ collisions between particles result in coalescence. If $\text{St} > \text{St}^*$ the particles rebound [4].

For the case where the particles coalesce before their surfaces come into contact (during the approach stage shown in Figure 1.15(b)), Equation (1.38) may also be rewritten using the Stokes number from Equation (1.43) as

$$\text{St} \leq \ln \left(\frac{h_0}{h_1} \right). \quad (1.46)$$

For non-identical particles, Ennis *et al.* [4] provide results using the harmonic mean particle mass and radius as defined in Equations (1.8) and (1.9). If it is assumed that both particles are travelling at an initial relative speed of $2u_0$, the viscous Stokes number is given by

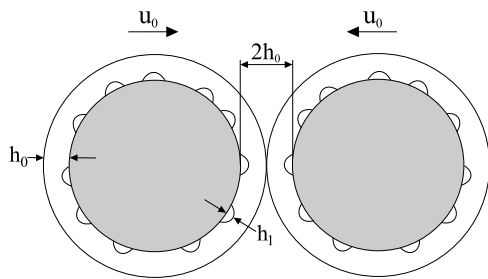
$$\text{St} = \frac{2\tilde{m}u_0}{3\pi\mu\tilde{a}^2}. \quad (1.47)$$

This expression reduces to the Stokes number from Equation (1.43) for identical particles.

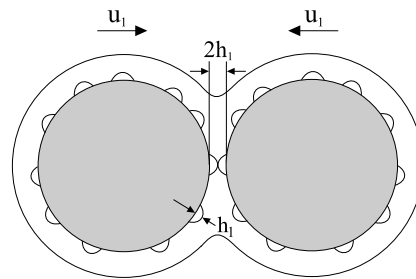
Liu *et al.* [26] extend the model of Ennis to account for the plastic deformation of the granule surfaces which becomes important in high-shear systems. The granules are assumed to be simple elastic-plastic solids with an elastic modulus E and a dynamic yield stress Y . Both properties are assumed to be independent of the stress-strain history as detailed by Johnson [41].

The model defines two types of coalescence: type I coalescence occurs if the kinetic energy is entirely dissipated by the liquid bridge during the approach stage and type II coalescence occurs if the particles coalesce following the rebound. If $u_1 > 0$ then the particles make contact. A portion of the incoming kinetic energy causes permanent plastic deformation while the remainder is stored as elastic strain energy.

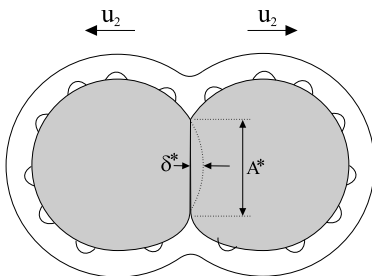
Figure 1.16(a) shows the approach stage which is the same initial arrangement considered



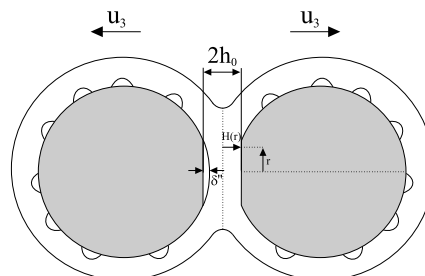
(a) Initially the particles are travelling at speed u_0 . The fluid layers contact at a separation distance of $2h_0$ as shown.



(b) Viscous dissipation reduces the speed of the particles to u_1 at a separation distance of $2h_1$. The remaining kinetic energy causes some plastic deformation and the remainder is stored as elastic strain energy.



(c) The stored elastic energy is released and the particles rebound with speed u_2 .



(d) The particles return to a separation distance of $2h_0$ at speed u_3 . The liquid bridge is assumed to rupture at this point.

Figure 1.16: Figures for the Liu *et al.* [26] coalescence model showing (a) the approach stage, (b) and (c) plastic deformation stage and (d) the rebound stage. This figure assumes that $u_3 > 0$ and that rebound occurs.

by Ennis *et al.* [4]. That is, two particles are involved in a head-on collision and their fluid layers come into initial contact at a separation distance of $2h_0$. Their motion is damped by the liquid bridge according to Equation (1.33). Equation (1.46) gives the condition for the particles to come to halt before the surfaces touch. Liu *et al.* [26] terms this as type I coalescence.

If $u_1 > 0$ the particles touch and the impact is assumed to be an elastic-plastic deformation, meaning that a portion of the incoming kinetic energy is dissipated during the plastic deformation while the remainder is stored as elastic strain energy. Johnson [41] shows that the total energy absorbed is given by

$$\begin{aligned} \frac{1}{2}\tilde{m}(2u_1)^2 &= E_p + E_e \\ &= \int_0^{\delta^*} p_m d\delta \end{aligned} \quad (1.48)$$

where E_e denotes the elastic strain energy, E_p the plastic energy of deformation, p_m is the mean contact pressure during the impact, δ is the mean compression distance into the particle and A is the area of contact between the flattened spheres. The values δ^* and A^* denote δ and A at the point of maximum deformation as shown in Figure 1.16(c). Johnson [41] applies the approximation $p_m \approx 3.0Y$, obtained from experiment, allowing the integral from Equation (1.48) to be evaluated as

$$E_p + E_e = \frac{1}{2}\tilde{m}(2u_1)^2 = \frac{3Y(A^*)^2}{4\pi\tilde{a}}. \quad (1.49)$$

For $\delta \ll \tilde{a}$, the area of contact in terms of δ is

$$A = 2\pi\tilde{a}\delta. \quad (1.50)$$

Substituting Equation (1.50) into Equation (1.48), integrating and rearranging gives the area of contact at the point of maximum deformation as

$$A^* = 2u_1 \left(\frac{2\pi\tilde{a}\tilde{m}}{3Y} \right)^{\frac{1}{2}}. \quad (1.51)$$

Substituting Equation (1.51) into Equation (1.50) gives the maximum penetration distance as

$$\delta^* = 2u_1 \left(\frac{\tilde{m}}{6\pi\tilde{a}Y} \right)^{\frac{1}{2}}. \quad (1.52)$$

The amount of energy from the elastic-plastic collision, given in Equation (1.49)), which

is stored as elastic strain energy is [41]

$$\begin{aligned} E_e &= \frac{2.7\sqrt{\pi}Y^2}{E^*}(A^*)^{\frac{3}{2}} \\ &= 5.4\sqrt{2}\frac{\pi^{\frac{5}{4}}Y^2}{E^*}\left(\frac{2\tilde{m}\tilde{a}}{3Y}\right)^{\frac{3}{4}}u_1^{\frac{3}{2}} \end{aligned} \quad (1.53)$$

where

$$E^* = \left(\frac{1-\nu_1^2}{E_1} + \frac{1-\nu_2^2}{E_2}\right)^{-1}$$

and E_1 and E_2 are the elastic moduli of the colliding particles and ν_1 and ν_2 are their Poisson ratios [41].

From Equation (1.49) and Equation (1.53) the amount of energy dissipated by the plastic deformation is

$$E_p = \frac{3Y(A^*)^2}{4\pi\tilde{a}} - \frac{2.7\sqrt{\pi}Y^2}{E^*}(A^*)^{\frac{3}{2}}. \quad (1.54)$$

The particles rebound due to the stored elastic energy. Therefore

$$E_e = \frac{1}{2}\tilde{m}(2u_2)^2 \quad (1.55)$$

where u_2 is the rebound speed as shown in Figure 1.16(c).

Substituting Equation (1.53) into Equation (1.55) and rearranging gives

$$u_2 = \frac{1}{\tilde{m}^{\frac{1}{8}}}\left(\frac{5.4Y^2\pi^{\frac{5}{4}}}{\sqrt{2}\tilde{m}E^*}\right)^{\frac{1}{2}}\left(\frac{2\tilde{a}}{3Y}\right)^{\frac{3}{8}}u_1^{\frac{3}{4}}. \quad (1.56)$$

After the particles separate some elastic recovery occurs. The extent of this recovery is [41]

$$\begin{aligned} \delta' &= \frac{9\sqrt{\pi}Y}{4E^*}(A^*)^{\frac{1}{2}} \\ &= \frac{9\sqrt{\pi}Y}{4E^*}(2u_1)^{\frac{1}{2}}\left(\frac{2\pi\tilde{m}\tilde{a}}{3Y}\right)^{\frac{1}{4}} \end{aligned} \quad (1.57)$$

where A^* from Equation (1.51) has been used.

The amount of permanent plastic deformation is therefore

$$\begin{aligned} \delta'' &= \delta^* - \delta' \\ &= 2u_1\left(\frac{\tilde{m}}{6\pi\tilde{a}Y}\right)^{\frac{1}{2}} - \frac{9\sqrt{\pi}Y}{4E^*}(2u_1)^{\frac{1}{2}}\left(\frac{2\pi\tilde{m}\tilde{a}}{3Y}\right)^{\frac{1}{4}}. \end{aligned} \quad (1.58)$$

For rebound, the viscous force of the liquid bridge retards the motion of the particles. The force exerted on the particles is dependent on the geometry of the flattened particles. For separation distances $h \ll \tilde{a}$, Liu *et al.* [26] determine that the separation distance between spheres is $H(r) = h$ for the flattened portion of the particles and $H(r) \approx h - \delta'' + \frac{r^2}{2R}$ for the remaining spherical regions (see Figure 1.16(d)).

From lubrication theory [17], the equation for the viscous force exerted by a Newtonian liquid on two axi-symmetric particles is [42]

$$\hat{F}_{\text{vis}} = \frac{3\pi\mu}{2} \frac{dh}{dt} \int_0^R \frac{r^3}{H(r)^3} dr \quad (1.59)$$

where \hat{F}_{vis} is the retarding force of the liquid bridge during rebound. Liu *et al.* [26] substitutes the values of $H(r)$ into Equation (1.59) and integrates to obtain

$$\hat{F}_{\text{vis}} = \frac{3\pi\mu\tilde{a}^2}{2} \left(\frac{(\delta'')^2}{h^3} + \frac{\delta''}{h^2} + \frac{1}{h} \right) \frac{dh}{dt}. \quad (1.60)$$

This equation reduces to the expression derived by Ennis *et al.* [4] in Equation (1.33) for the case of negligible deformation $\delta'' = 0$. During rebound the motion of the particles is retarded by the viscous force of the fluid according to

$$\tilde{m} \frac{du_r}{dt} = \hat{F}_{\text{vis}}. \quad (1.61)$$

Liu *et al.* [26] integrate this equation subject to the initial condition $u = u_2$ at $h = 0$. They subsequently find that the velocity u_3 at the separation distance $2h_0$ where liquid bridge rupture is

$$u_3 = u_2 - \frac{3\pi\mu\tilde{a}^2(\delta'')^2}{8\tilde{m}h_0^2} \left[\left(\frac{h_0^2}{h_1^2} - 1 \right) + \frac{2h_0}{\delta''} \left(\frac{h_0}{h_1} - 1 \right) + \frac{2h_0^2}{(\delta'')^2} \ln \left(\frac{h_0}{h_1} \right) \right]. \quad (1.62)$$

For $u_3 < 0$ type II coalescence is said to have occurred. Liu *et al.* [26] rewrite Equation (1.62) in terms of the Stokes deformation number and the viscous Stokes number. The following result is obtained:

$$\begin{aligned} \left(\frac{Y}{E^*} \right)^{\frac{1}{2}} \text{St}_{\text{def}}^{-\frac{9}{8}} &< \frac{0.172}{\text{St}} \left(\frac{2\tilde{a}}{h_0} \right)^2 \left[1 - \frac{1}{\text{St}} \ln \left(\frac{h_0}{h_1} \right) \right]^{\frac{5}{4}} \\ &\times \left[\left(\frac{h_0^2}{h_1^2} - 1 \right) + \frac{2h_0}{\delta''} \left(\frac{h_0}{h_1} - 1 \right) + \frac{2h_0^2}{(\delta'')^2} \ln \left(\frac{h_0}{h_1} \right) \right] \\ &\times \left(1 - 7.36 \left(\frac{Y}{E^*} \right) (\text{St}_{\text{def}})^{-\frac{1}{4}} \left[1 - \frac{1}{\text{St}} \ln \left(\frac{h_0}{h_1} \right)^{-\frac{1}{2}} \right] \right). \end{aligned} \quad (1.63)$$

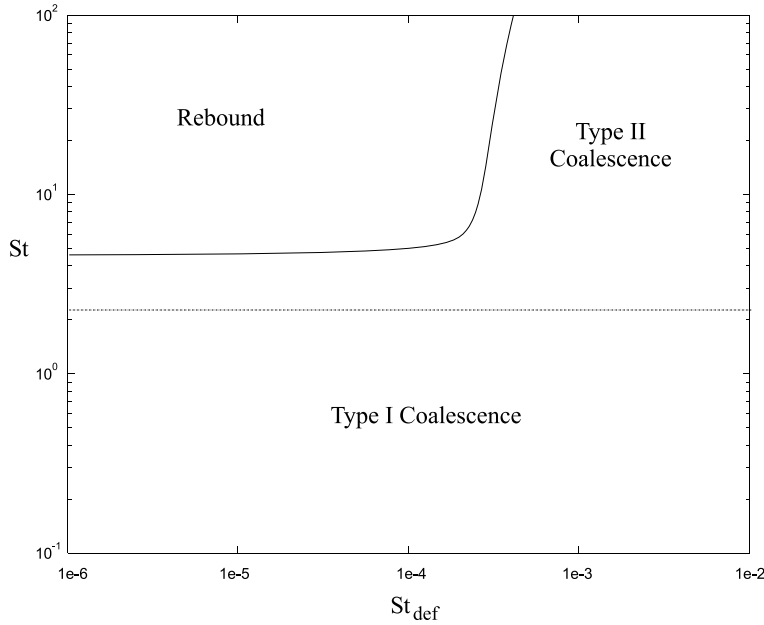


Figure 1.17: Predictions of the Liu *et al.* [26] coalescence model showing the boundaries for (i) type I coalescence (particle coalesce prior to contact), (ii) type II coalescence (particles coalesce after the particles touch) and (iii) the particles rebound. This figure is reproduced from [26] and was created used the parameters $\frac{Y}{E^*} = 0.01$, $\frac{h_0}{h_1} = 10$ and $\frac{2\bar{a}}{h_0} = 100$.

Three regions are defined: (i) type I coalescence, (ii) type II coalescence and (iii) particle rebound which correspond to $u_1 < 0$, $u_3 < 0$ and $u_3 \geq 0$ respectively. The results obtained by Liu *et al.* [26] are reproduced in Figure 1.17. The results reduce to those of Ennis *et al.* [4] for the case of negligible deformation which occurs for $St_{\text{def}} \ll 1$; the intercepts on the vertical axis of this figure correspond to predictions from the Ennis model.

The results show that type II coalescence can occur at high Stokes deformation and high viscous Stokes numbers. This occurs because more energy is dissipated in a plastic collision if the particles are more deformable which makes coalescence more likely.

Chapter 2 presents a solution for dynamic liquid bridges between two approaching, rigid spheres. The arrangement modelled is simpler than the cases investigated by Ennis *et al.* [4] and Liu *et al.* [26]. Lubrication theory is not applied and the particles do not rebound. Instead, the motion of the fluid is derived using the Navier-Stokes equations with the low Reynolds number approximation. The liquid bridge is approximated as a cylinder.

1.4 Granulation Simulations

Two main approaches are taken for macro-scale modelling of granulation. They are the population balance model and the distinct element method (DEM). The aim of both simulations is to model the mechanisms discussed in Section 1.2 and to predict the steady-state granule size distribution. Both models are now discussed.

Population balance models provide a statistical description of an ensemble of particles that are undergoing the mechanisms of coalescence and breakage*. They have numerous applications in the engineering sciences including granulation, the coagulation of aerosols and other fine particles (e.g. soot, ash and volcanic particles), polymerisation, and cell growth. When the balance is solved, statistical properties, such as the particle size distribution, are able to be obtained.

If coalescence is dependent only on particle size, where size is a continuous variable, the following one-dimensional population balance equation for coalescence is obtained [11]:

$$\frac{\partial n(x, t)}{\partial t} = \frac{1}{2} \int_0^x K(x-y, y)n(x-y, t)n(y, t) dy - \int_0^\infty K(x, y)n(x, t)n(y, t) dy. \quad (1.64)$$

Here x is a continuous variable that represents particle size and $n(x, t)$ denotes the number of particles in the size interval $[x, x+dx]$. $n(x, t)$ increases when two smaller particles of the appropriate size coalesce and decreases when coalescence occurs with any other particle. The coalescence kernel $K(x, y)$ gives the coalescence rate of $[x, x+dx]$ and $[y, y+dy]$ particles. Particle breakage may be included by introducing the function $f(x, y)$ which gives the rate of $[x, x+dx]$ and $[y, y+dy]$ daughter particle formation [43]. Including the effects of breakage, the population balance equations become:

$$\begin{aligned} \frac{\partial n(x, t)}{\partial t} = & \frac{1}{2} \int_0^x K(x-y, y)n(x-y, t)n(y, t) dy - \int_0^\infty K(x, y)n(x, t)n(y, t) dy \\ & - \frac{1}{2}n(x, t) \int_0^x f(y, x-y) dy - \int_x^\infty n(y, t)f(x, y-x)dy. \end{aligned} \quad (1.65)$$

Equation (1.64) and Equation (1.65) are integro-partial differential equations [43]. Analytic solutions can be found to these equations for simple $K(x, y)$ and $f(x, y)$ functions. However, these generally correspond to non-physical cases. Numerical approaches are required for more complex functions.

Numerical solutions to Equations (1.64) and (1.65) may be obtained by discretising the continuous equations. Upon doing this, for Equation (1.64), the following system of

*A source term for the particle addition and a sink term for particle removal may also be included [11]. In this work a closed system is considered where these terms are both equal to zero.

ordinary differential equations is obtained:

$$\frac{dn_i}{dt} = \frac{1}{2} \sum_{j=1}^{i-1} K_{j,i-j} n_j(t) n_{i-j}(t) - n_i(t) \sum_{j=1}^{\infty} K_{i,j} n_j(t). \quad (1.66)$$

In Equation (1.66) i is an integer that denotes particle size and $K_{i,j}$ is the discrete analogue of $K(x, y)$. The size divisions, as referenced by i , may be linear or geometric [44, 45]. Coarser grids are possible for geometric size divisions. Equation (1.66) may also be derived directly in a discrete setting, such as granulation, by counting collisions between particles. This is the approach taken in Chapter 5.

Multi-dimensional population balance models are used when the collision and/or coalescence rate depends on more than one particle property. In the continuous setting it is possible to write $n = n(x_1, x_2, \dots, t)$ where each x_i represents a dependent property. Granulation is dependent on numerous particle characteristics including shape, composition, porosity and pore saturation. Research has recently commenced into applying multi-dimensional population balance models to granulation [44]. Care must be taken, however, to model only the primary mechanisms. Otherwise the model may become overly complex and make inaccurate predictions. Conventional numerical techniques may be applied to multi-dimensional balances but Monte Carlo and finite element methods (FEM) are preferred because they are more computationally efficient [46]. In Chapter 5 of this thesis, a hybrid two-dimensional population balance is presented where collision is dependent only on particle size but coalescence is dependent on both particle size and surface wetness (or stickiness).

The distinct element method (DEM) was developed by Cundall and Strack [47]. The objective of the DEM model is to simulate the individual particle interactions by modelling the particle-particle contacts on a micro-scale. Newton's second law is applied to update the position, velocity and acceleration of the particles and determine the linear and angular velocities following a particle-particle collision. DEM models have some advantages over population balance models including the ability to define complex particle-particle interaction laws and to allow individual particles to have unique shapes. The location of the particles is also known throughout the simulation. However, the model is more computationally intensive than population balance models. DEM models use a small integration time-step so that particles only contact their nearest neighbours. Overlap between particles is assumed to be small in comparison with their size.

1.5 Thesis Preview

The topics studied in this thesis are (i) liquid bridges between two and three particles, (ii) a model for moderately large agglomerates, allowing the stickiness of moderately large agglomerates to be estimated, and (iii) an extended population balance model which allows simulations of wet granulation to be performed. Each of these studies are now summarised below.

Chapter 2 studies liquid bridges between two particles. The chapter is split into two independent studies; static liquid bridges are studied in Section 2.2 and dynamic liquid bridges are studied in Section 2.5. For the static case, the Young-Laplace equation is solved numerically in Section 2.3 and then analytically in Section 2.5. The numerical results obtained allow the liquid bridge volume to be related to liquid bridge properties including the inter-particle separation distance, liquid bridge surface area, inter-particle force and the Gibbs free surface energy. In Section 2.5 a new closed form analytical solution to the Young-Laplace equation is obtained allowing the true shape of the liquid bridge to be written in terms of known mathematical functions. Also in this section, the phase portrait of the Young-Laplace equation is obtained which relates the height and the slope of the fluid surface. The portrait is used to show that six distinct types of static liquid bridges exist. Section 2.6 investigates the dynamic motion of a liquid bridge between two approaching spheres where the bridge is approximated as a cylinder. The motion of the bridge is derived from first principles using mass conservation and the Navier-Stokes equations. The low Reynolds number approximation ($Re \ll 1$) is applied. As the spheres approach their motion is shown to be damped by the viscosity of the liquid bridge.

Chapter 3 studies static liquid bridges between three equally sized primary particles. The particles are equally separated and have their centres located on the vertices of an equilateral triangle. Because of symmetry, the fluid surface is able to be obtained by solving, and then appropriately reflecting, a small portion of the entire surface. As required by the Young-Laplace equation, the fluid surface must have constant mean curvature (CMC). The boundary conditions for the problem are (i) the contact angle of the fluid at the three-phase contact line and (ii) the surface and its derivatives must be continuous along the contour where the surface is reflected. The equations for the mean curvature and boundary conditions are derived and numerically solved on a discrete mesh. The liquid bridge surface area, volume and binding force is calculated for given values of the inter-particle separation distance and mean curvature. Agreement with an experimental point is provided.

In Chapter 4 a model to estimate the stickiness of moderately large agglomerates is proposed. The primary particles are added one at a time in a closely packed arrangement. The agglomerate model has two parameters which are (i) a minimum separation distance between spheres and (ii) a saturation parameter for the fluid. By varying these parameters, for a given number of particles, results are obtained, using computational geometry, which relate the fluid-to-solid volume ratio to the stickiness of the particles. The results of the model are presented in Sections 4.9 and 4.10. Results for the case of maximum consolidation are provided in Section 4.10. These results are used in the population balance modelling work of Chapter 5.

Chapter 5 presents a mathematical model for modelling coalescence in wet granulation systems. The equations were independently derived by Professor Robert McLachlan and myself in both continuous and discrete form. However, it was later revealed, by a literature search, that a simpler model was proposed by Smoluchowski [48] in 1917. In the text the agglomeration model is presented as an evolution of this earlier work by adding a system of differential equations to represent the transfer and drying of binder. The surface wetness results from Section 4.10 are used for modelling the rate of particle coalescence. The results obtained show the effect of the fluid-to-solid ratio and the rate of drying for several different collision rate functions.

The original work presented in this thesis is now summarised:

- **Section 2.3.** Numerical solution of static liquid bridges between two particles where the radii of the primary particles may be different. Results at the point of rupture are provided in terms of particle radii and the contact angle θ . This research extends the work of Lian [35] who investigated the case where the particles have the same radius.
- **Section 2.5.** Analytic solution and phase portrait of the Young-Laplace equation for liquid bridges between two rigid particles. This is the first time that an analytic solution has been obtained for this problem.
- **Section 2.6.** Viscous dissipation of a dynamic liquid bridge between two moving particles. This arrangement is obtained by solving the Navier-Stokes equations and assuming the low Reynolds number approximation. This differs to the approach taken by Ennis *et al.* [4] and Liu *et al.* [26] who apply lubrication theory to obtain a solution.
- **Chapter 3.** Numerical solution of static liquid bridges between three particles. This is the first time that the Young-Laplace equation has been solved for this arrangement.

-
- **Chapter 4.** Novel, simplified geometric model for the placement of particles and liquid bridges in moderately large agglomerates. The model enables crucial agglomerate properties, such as their surface area, wetness (the fractional wet surface area) and volume, to be estimated. No comparable work exists in the literature.
 - **Chapter 5.** Population balance model for wet granulation. This model is developed by extending the model of Smoluchowski [48] to incorporate the effects of binder fluid. Functions for the inter-particle collision rate and drying rate are proposed, including functions which are derived from the geometric model (described above) for the case of maximum particle consolidation. The model is solved numerically for a range of coalescence kernels. Results are presented which show the effect of binder volume and the drying rate. The extensions to the Smoluchowski model are new.

Liquid Bridges Between Two Particles

2.1 Introduction

Section 2.2 of this chapter studies static liquid bridges and Section 2.5 dynamic liquid bridges between two particles. For the static case, in Section 2.3, a numerical method to solve the Young-Laplace equation is presented where the radii of the primary particles may, in general, be different. The solution builds on the work of [31–35] as discussed in Section 1.3.2. In Section 2.5 an analytic solution to the Young-Laplace equation is obtained along with an associated phase portrait. Section 2.6 investigates the dynamic motion of a liquid bridge between two approaching spheres. The motion of the fluid is derived using the mass conservation and Navier-Stokes equations. The low Reynolds number approximation is applied and the bridge profile is approximated as a cylinder.

2.2 The Young-Laplace Equation

From Equation (1.13), the Young-Laplace equation, in the absence of gravitational forces, is

$$H_0 = \frac{\Delta p}{2\gamma_{lv}} \quad (2.1)$$

where H_0 is the mean curvature, γ_{lv} is the surface tension of the fluid and Δp is the pressure difference due to the presence of the fluid. (Δp is defined to be positive when the internal bridge pressure is higher than the external (or ambient) pressure.) Liquid bridges between two particles have rotational symmetry, as discussed in Section 1.3.2,

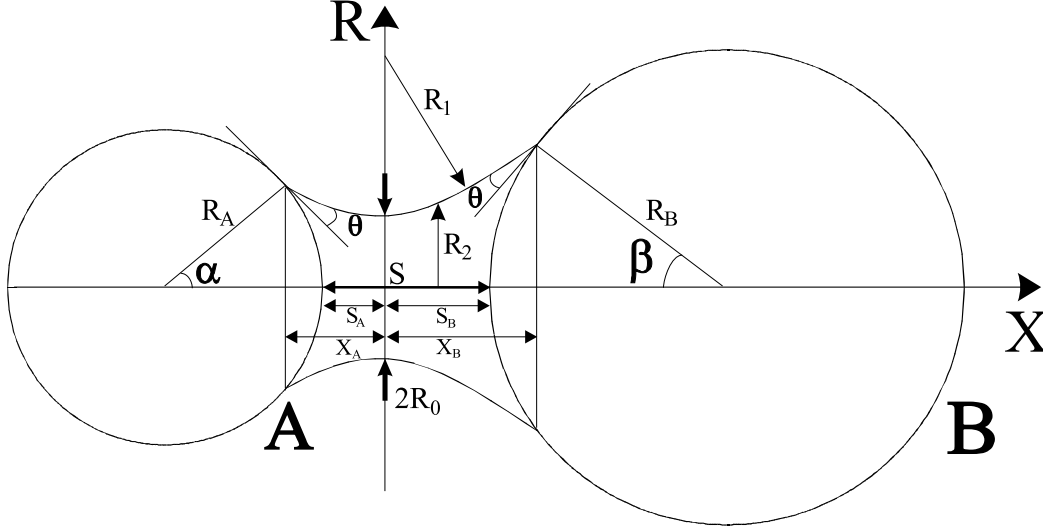


Figure 2.1: Static liquid bridge drawn in the $X - R$ plane between particles ‘A’ and ‘B’ with non-dimensional radii R_A and R_B . The fluid has contact angle θ . The principal dimensionless radii of curvature are denoted by R_1 and R_2 . The height of the bridge at $X = 0$ is R_0 . In this figure $R_B = 1.5 R_A$, the half-filling angles are α and β and the non-dimensional separation distance between the particles is S .

allowing Equation (2.1) to be written as

$$\gamma_{lv} \left(\frac{r''}{(1+r'^2)^{3/2}} - \frac{1}{r(1+r'^2)^{1/2}} \right) = \Delta p. \quad (2.2)$$

The properties of liquid bridges defined by Equation (2.2) can be studied using non-dimensional variables $X = \frac{x}{\sigma}$, $R = \frac{r}{\sigma}$ and $\Delta P = \frac{\Delta p \sigma}{\gamma_{lv}}$ where σ is a scaling variable with the dimensions of length. For an ensemble of particles, σ can be chosen as a characteristic primary particle radius such as the mean particle size. Taking derivatives of the non-dimensional variables gives $\frac{dr}{dx} = \frac{dR}{dX}$ and $\frac{d^2r}{dx^2} = \frac{d}{dx} \left(\frac{dr}{dx} \right) = \frac{1}{\sigma} \frac{d^2R}{dX^2}$ which allows Equation (2.2) to be written as

$$\frac{R''}{(1+R'^2)^{3/2}} - \frac{1}{R(1+R'^2)^{1/2}} = \Delta P \quad (2.3)$$

where $R = R(X)$, $R' = \frac{dR}{dX}$ and $R'' = \frac{d^2R}{dX^2}$ and ΔP is the non-dimensional pressure difference.

Figure 2.1 illustrates a pendular liquid bridge between particles ‘A’ and ‘B’ with respective non-dimensional radii R_A and R_B . The origin is defined as the point where the bridge has height R_0 and tangent $R'(0) = 0$. The angle $\psi = \text{atan } R'$ measures the angle of incline of the fluid surface with respect to the X axis (see Figure 2.2). The contact points of the fluid and the spheres are defined by X_A , X_B and the half-filling angles by α and β . The non-dimensional separation distance between the particles is $S = S_A + S_B$ where the

distances S_A and S_B are measured from the origin to the closest points of the spheres as shown in Figure 2.1.

Section 2.3.1 details the calculation of the following non-dimensional liquid bridge properties: surface area A , volume V , inter-particle binding force F and the Gibbs free surface energy E . The relationship between the dimensional and non-dimensional variables is given by $a = \sigma^2 A$, $v = \sigma^3 V$, $f = \gamma_{lv} \sigma F$ and $e = \gamma_{lv} \sigma^2 E$.

Extending Equation (1.18) for spheres of radius R_A and R_B and applying non-dimensional variables gives the boundary conditions for this problem as:

$$\begin{aligned} R'(X_A) &= \tan\left(\frac{\pi}{2} - (\alpha + \theta)\right) \\ &= \cot(\alpha + \theta) \end{aligned} \tag{2.4}$$

and

$$\begin{aligned} R'(X_B) &= \tan\left(\frac{\pi}{2} - (\beta + \theta)\right) \\ &= \cot(\beta + \theta). \end{aligned} \tag{2.5}$$

The numerical solution of Equation (2.3), subject to the boundary conditions given in Equations (2.4) and (2.5), is performed in the following section.

2.3 Numerical Solution

The numerical calculation of liquid bridges was performed using the Matlab `ode45` integrator. The vector supplied was of the form:

$$\begin{aligned} \vec{y}(X) &= (y_1, y_2, y_3, y_4) \\ &= (R, R', A, \hat{V}) \end{aligned} \tag{2.6}$$

where y_1 denotes the height of the liquid bridge R , y_2 the slope of the surface R' , y_3 the fluid surface area A and y_4 the volume of revolution \hat{V} of the curve $R(X)$. The volume \hat{V} includes the volume of the spheres between S_A and X_A for particle A and S_B and X_B for particle B. (The striped shaded region in Figure 2.2 illustrates the volume of particle B which is included in \hat{V} .) The liquid bridge volume V is calculated in Section 2.3.1 by subtracting the appropriate volumes of the spheres from \hat{V} .

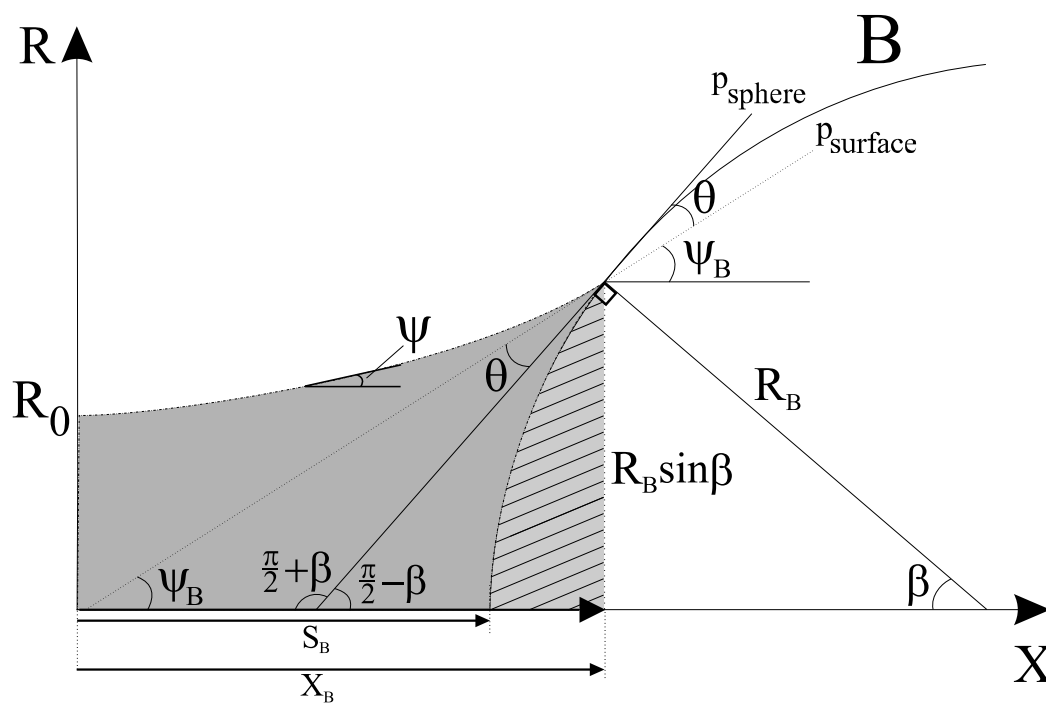


Figure 2.2: Enlarged view of the fluid contacting particle B at $X = X_B$. The portion of the fluid surface corresponding to $X \geq 0$ and $R \geq 0$ is shown. The tangent plane to the sphere is drawn as a solid line and the tangent plane to the fluid is drawn as a dotted line. The angle between the planes is equal to the contact angle θ . The fluid makes contact with particle 'B' at an angle ψ measured with respect to the (horizontal) X -axis.

The differential equations supplied to the solver are:

$$y'_1 = y_2 \quad (2.7a)$$

$$y'_2 = \Delta P(1 + y_2^2)^{\frac{3}{2}} + \frac{1 + y_2^2}{y_1} \quad (2.7b)$$

$$y'_3 = 2\pi y_1 \sqrt{1 + y_2^2} \quad (2.7c)$$

$$y'_4 = \pi y_1^2 \quad (2.7d)$$

where the primes denote differentiation with respect to X , i.e. $y'_1 = \frac{dy_1}{dX}$.

Equations (2.7a) and (2.7b) are the Young-Laplace equation from Equation (2.3) written as a first order system. Equations (2.7c) and (2.7d) are differential expressions for the surface area and volume of the surface of revolution for the curve $R(X)$ [49] (see Section 2.3.1).

Several approaches can be taken to solve Equation (2.2) subject to the boundary conditions. For instance, given ΔP , integration may begin on sphere A, the fluid surface generated, and, during integration, attempts made to fit sphere B such that a contact angle of θ occurs. For this approach the initial condition may be determined by specifying the half-filling angle α , as the starting height is then $R_A \sin \alpha$ and the starting slope $\cot(\alpha + \theta)$. If sphere B can be fitted then the values of X_B and β are determined. The integration span required for this approach is $X_A + X_B$.

The method used in this work is more efficient than the approach described above. Defining the particles such that $R_A \leq R_B$, Figure 2.3 illustrates how symmetry of the fluid surface may be used to reflect particle A about the R axis. Integration starts from the origin and attempts are made to fit both spheres during a single application of `ode45`. This approach requires a total integration span of X_B . The location of the boundary conditions X_A and X_B are numerically determined using the Matlab event handler.

The Matlab event handler uses zeros-crossing functions $D(\vec{y})$ to detect the X position of Matlab 'events' which correspond to $D(\vec{y}) = 0$. Integration may optionally terminate when an event occurs. To define the zeros-crossing function for particle B the boundary condition at $X = X_B$ is applied. From Figure 2.2, at $X = X_B$,

$$R = R_B \sin \beta. \quad (2.8)$$

Rearranging Equation (2.5) gives

$$\beta = \text{acot } R' - \theta. \quad (2.9)$$

Substituting Equation (2.9) into Equation (2.8) and rearranging gives

$$R_B \sin(\text{acot } R' - \theta) - R = 0. \quad (2.10)$$

The zeros-crossing function for particle B is therefore

$$D_B(\vec{y}) = R_B \sin(\text{acot } y_2 - \theta) - y_1. \quad (2.11)$$

Similarly, the zeros-crossing function for particle A at X_A is defined as

$$D_A(\vec{y}) = R_A \sin(\text{acot } y_2 - \theta) - y_1. \quad (2.12)$$

The zeros-crossing functions in Equations (2.11) and (2.12) are valid for both concave and convex liquid bridges. Since $R_A \leq R_B$ it follows, from Figure 2.3 and provided a solution exists, that $X_A \leq X_B$. If sphere A can be fitted then an event is recorded, which determines X_A , and integration continues. If sphere B can then be fitted then X_B is determined, also using an event, and integration terminates. If $R_A = R_B$ then $X_A = X_B$. If both boundary conditions can be met then the following integrals are evaluated using Matlab:

$$A_A = \int_0^{X_A} 2\pi y_1 \sqrt{1 + y_2^2} dX \quad A_B = \int_0^{X_B} 2\pi y_1 \sqrt{1 + y_2^2} dX \quad (2.13a)$$

$$\hat{V}_A = \int_0^{X_A} \pi y_1^2 dX \quad \hat{V}_B = \int_0^{X_B} \pi y_1^2 dX. \quad (2.13b)$$

These integrals are used to evaluate the liquid bridge properties which are discussed in Section 2.3.1.

The maximum integration span allowed for the solver was $X_{\max} = 2.5$. This was sufficient for the range of liquid bridge volumes explored in Section 2.4. If the boundary conditions are unable to be met prior to this limit it is assumed that no physical solution exists for the given combinations of R_0 , ΔP , R_A , R_B and θ .

For fixed θ , it was observed, numerically, that a unique fluid surface is generated for unique combinations of R_0 and ΔP . Thus, if a solution exists, a unique liquid bridge is obtained for unique combinations of R_0 , ΔP , R_A , R_B and θ . For fixed θ , R_A , R_B and R_0 , the free parameter corresponding to liquid bridges with different volumes V was found to be ΔP (or H_0).

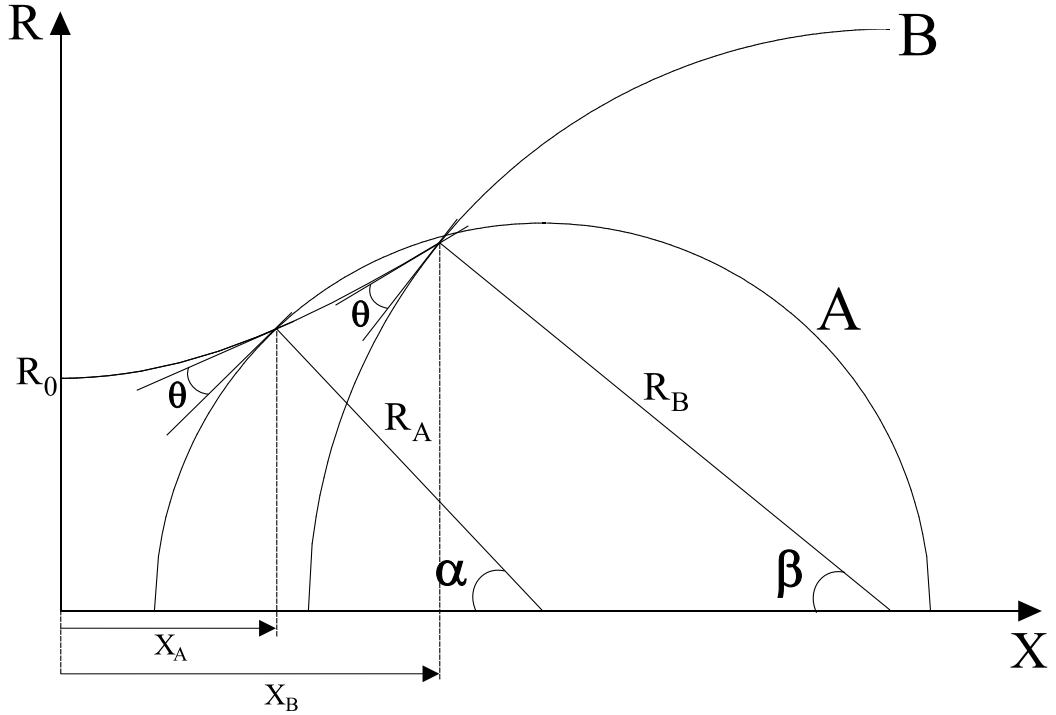


Figure 2.3: The approach taken to solve the Young-Laplace equation is to start at the origin and attempt to fit the spheres A and B where $R_A \leq R_B$. For this example $R_B = 1.5R_A$ and $\theta = 20^\circ$. The upper portion of particle A and the upper left quadrant of particle B is shown.

2.3.1 Liquid Bridge Properties

If the particles can be fitted to the fluid surface then X_A , X_B , α , β and the integrals in Equations (2.13a) and (2.13a) can be evaluated. Using these integrals, the following non-dimensional liquid bridge properties may be calculated: (i) inter-particle separation distance S , (ii) surface area A , (iii) volume V , (iv) inter-particle binding force F and (v) the Gibbs free surface energy E . The calculation of these quantities is now detailed.

(i) Separation distance

The inter-particle separation distance is given by

$$S = S_A + S_B. \quad (2.14)$$

From Figures 2.1 and 2.2, the distances S_A and S_B are given by

$$S_A = X_A - R_A(1 - \cos \alpha) \quad (2.15)$$

and

$$S_B = X_B - R_B(1 - \cos \beta). \quad (2.16)$$

(ii) Surface area

The liquid bridge $R(X)$ is a surface of revolution about the X axis with differential area element [49]

$$dS = 2\pi R \sqrt{1 + (R')^2} dX. \quad (2.17)$$

The surface area of the fluid is therefore

$$\begin{aligned} A &= 2\pi \left(\int_0^{X_A} R \sqrt{1 + (R')^2} dX + \int_0^{X_B} R \sqrt{1 + (R')^2} dX \right) \\ &= A_A + A_B. \end{aligned} \quad (2.18)$$

(iii) Volume

The volume of the liquid bridge is given by

$$V = \left(\pi \int_0^{X_A} R^2 dX - V_A \right) + \left(\pi \int_0^{X_B} R^2 dX - V_B \right) \quad (2.19)$$

where V_B is the volume of particle B included in the integral $\pi \int_0^{X_B} R^2 dX$ and V_A is the volume of particle A included in the integral $\pi \int_0^{X_A} R^2 dX$. (Figure 2.2 illustrates V_B as the striped shaded region.) Since particle B is centred at $(X_B + R_B \cos \beta, 0)$,

$$\begin{aligned} V_B &= \pi \int_{X_B - R_B(1 - \cos \beta)}^{X_B} \left[R_B^2 - (X - (X_B + R_B \cos \beta))^2 \right] dX \\ &= \pi R_B^3 \left(\frac{2}{3} - \cos \beta + \frac{1}{3} \cos^3 \beta \right). \end{aligned} \quad (2.20)$$

Similarly,

$$V_A = \pi R_A^3 \left(\frac{2}{3} - \cos \alpha + \frac{1}{3} \cos^3 \alpha \right). \quad (2.21)$$

Using the integrals evaluated in Equation (2.13b), the bridge volume is given by

$$V = \hat{V}_A - V_A + \hat{V}_B - V_B. \quad (2.22)$$

(iv) Inter-particle binding force

The inter-particle binding force is the sum of (i) the axial component of the surface tension force and (ii) the force resulting from the pressure difference due to the presence of the fluid. Since the arrangement is static the inter-particle force may be evaluated at any point X along the bridge. The expression for the force is

$$F(X) = 2\pi R(X) \cos \psi + \pi R(X)^2 \Delta P \quad (2.23)$$

where $R = R(X)$. Equation (2.23) may be written in terms of R' by substituting $\psi = \text{atan}(R')$ to give

$$\begin{aligned} F &= \frac{2\pi R}{\sqrt{1 + \tan^2 \psi}} + \pi R^2 \Delta P \\ &= \frac{2\pi R}{\sqrt{1 + (R')^2}} + \pi R^2 \Delta P. \end{aligned} \quad (2.24)$$

The analytic solution in Section 2.5 proves that the force F is constant along the length of the liquid bridge. Evaluating Equation (2.23) at $X = 0$ gives

$$F \Big|_{X=0} = 2\pi R_0 + \pi R_0^2 \Delta P \quad (2.25)$$

where $R_0 = R(0)$. Evaluating the force at X_B gives

$$F \Big|_{X=X_B} = 2\pi R(X_B) \sin(\beta + \theta) + \pi [R(X_B)]^2 \Delta P \quad (2.26)$$

and, at X_A ,

$$F \Big|_{X=X_A} = 2\pi R(X_A) \sin(\alpha + \theta) + \pi [R(X_A)]^2 \Delta P. \quad (2.27)$$

The expressions in Equations (2.23)-(2.27) have been numerically confirmed to give the same result. The numerical results in Section 2.4 use the expression given in Equation (2.25) to calculate the force.

(v) Gibbs free surface energy

The expression for the Gibbs free surface energy from Equation (1.27) is non-dimensionalised and extended to the case of $R_A \neq R_B$ to give

$$\begin{aligned} E &= 2\pi \left(\int_0^{X_A} R \sqrt{1 + (R')^2} dX - \cos \theta \int_{S_A}^{X_A} U_A \sqrt{1 + (U_A')^2} dX \right. \\ &\quad \left. + \int_0^{X_B} R \sqrt{1 + (R')^2} dX - \cos \theta \int_{S_B}^{X_B} U_B \sqrt{1 + (U_B')^2} dX \right) \end{aligned} \quad (2.28)$$

where U_A and U_B denote the non-dimensional profile of spheres A and B where

$$U_B(X) = \sqrt{R_B^2 - (X - (X_B + R_B \cos \beta))^2} \quad (2.29)$$

and

$$U_A(X) = \sqrt{R_A^2 - (X - (X_A + R_A \cos \alpha))^2}. \quad (2.30)$$

It can be shown that

$$U_A \sqrt{1 + (U_A')^2} = R_A.$$

Therefore, from Equation (2.28),

$$\begin{aligned} E &= 2\pi \left(\int_0^{X_A} R \sqrt{1 + (R')^2} dX - R_A \cos \theta (X_A - S_A) \right. \\ &\quad \left. + \int_0^{X_B} R \sqrt{1 + (R')^2} dX - R_B \cos \theta (X_B - S_B) \right) \\ &= A - 2\pi \cos \theta (R_A (X_A - S_A) + R_B (X_B - S_B)). \end{aligned} \quad (2.31)$$

2.3.2 Summary of the solution technique

For given R_0 and ΔP values the following steps are performed to generate a particular liquid bridge:

1. The spheres are defined so that $R_A \leq R_B$. Integration begins at the origin using the initial vector $\vec{y}_0 = (R_0, 0, 0, 0)$.
2. The Matlab event handler is used to determine the position of the spheres by locating the boundary conditions at X_A and X_B . The following zeros-crossing functions are supplied to the event handler:

For particle A, at $X = X_A$,

$$D_A(\vec{y}) = R_A \sin(\text{acot } y_2 - \theta) - y_1, \quad (2.32)$$

and, for particle B, at $X = X_B$,

$$D_B(\vec{y}) = R_B \sin(\text{acot } y_2 - \theta) - y_1. \quad (2.33)$$

3. If both spheres can be fitted then α , β , X_A and X_B are determined. The vector \vec{y} is then used to evaluate the integrals given in Equations (2.13a) and (2.13b). The liquid bridge properties are calculated as detailed in Section 2.3.1.

2.4 Numerical Results

Figures 2.4 - 2.6 show results of parametric solutions for concave pendular liquid bridges ($R_0 < 1$) obtained using the solution technique from Section 2.3. Figure 2.4 shows contours for $R_A = 1$, $R_B = 1$, $\theta = 0^\circ$ (perfect wetting), Figure 2.5 contours for $R_A = 1$, $R_B = 1.5$, $\theta = 0^\circ$ and Figure 2.6 contours for $R_A = 1$, $R_B = 1.5$, $\theta = 15^\circ$. The plots show the relationship between liquid bridge properties and the separation distance S . Individual contours represent a fixed volume of fluid V .

Two liquid bridge solutions are possible for certain combinations of S and V . In such cases, as discussed in Section 1.3.2, the arrangement with minimum Gibbs free surface energy E is the stable arrangement which occurs physically. Accordingly, the branches of the contour plots in Figures 2.4 - 2.6 are labelled stable and unstable. Figure 2.9 compares the profile of two stable and unstable liquid bridges. Figure 2.9(a) shows the stable arrangement corresponding to $R_A = 1$, $R_B = 1$, $\theta = 0^\circ$, $V = 0.5$ and $S = 0.8$ and Figure 2.9(b) the unstable equivalent. Figure 2.9(c) shows the stable arrangement for $R_A = 1$, $R_B = 1.5$, $\theta = 0^\circ$, $V = 0.7$ and $S = 0.7$ and Figure 2.9(d) the unstable equivalent. Compared to the stable configurations, the unstable arrangements have, in general, smaller R_0 values and at least one of the half-filling angles α and β larger. The unstable arrangements also have a higher surface area A , smaller inter-particle binding force F and are observed to occur for $\Delta P < 0$ (where the internal bridge pressure is lower than ambient pressure). The stable and unstable branches converge at a critical separation distance S_{rupture} which corresponds to rupture of the liquid bridge [33,35].

For the stable arrangements and fixed fluid volume V , the contour plots in Figures 2.4-2.6 show that decreasing the separation distance S increases R_0 . This is illustrated in Figure 2.8 where, for $R_A = 1$, $R_B = 1$ and $\theta = 0^\circ$, S is decreased from $S = 0.8$ to $S \approx 0$ such that a constant volume of fluid $V = 1$ is maintained. The half-filling angles α and β both increase as S decreases which corresponds to the fluid receding over the spheres. The inter-particle binding force F achieves a maximum at $S = 0$ since R_0 and the contact area at the interface boundary are both maximised at $S = 0$. (The contact area is maximised because α and β are both maximised at $S = 0$.)

Figure 2.10 provides plots of liquid bridge properties at the rupture condition. The cases provided are (i) $R_A = 1$, $R_B = 1$, $\theta = 0^\circ$, (ii) $R_A = 1$, $R_B = 1$, $\theta = 15^\circ$, (iii) $R_A = 1$, $R_B = 1.5$, $\theta = 0^\circ$ and (iv) $R_A = 1$, $R_B = 1.5$, $\theta = 15^\circ$. From the plots, increasing V_{rupture} increases R_0 , α , β and A and F . Increasing the contact angle θ is observed to increase the rupture separation distance S_{rupture} . The height R_0 also increases and F decreases.

The plots in Figure 2.10 were generated by locating the maximum distance S_{rupture} from

the contours in Figures 2.4 - 2.6 in terms of the fluid volume V . The Matlab `contour` and `gradient` commands were used to locate the turning point that separates the stable and unstable solutions as this corresponds to the rupture condition. The corresponding liquid bridge properties were then determined at S_{rupture} . Some ‘jitter’ and gaps occur in the plots; both effects are due to ΔP changing rapidly at the rupture point as shown in Figures 2.4(b)-2.6(b). The effect was able to be minimised by using high resolution meshes with step-sizes of 1×10^{-3} for R_0 and 1×10^{-4} for ΔP .

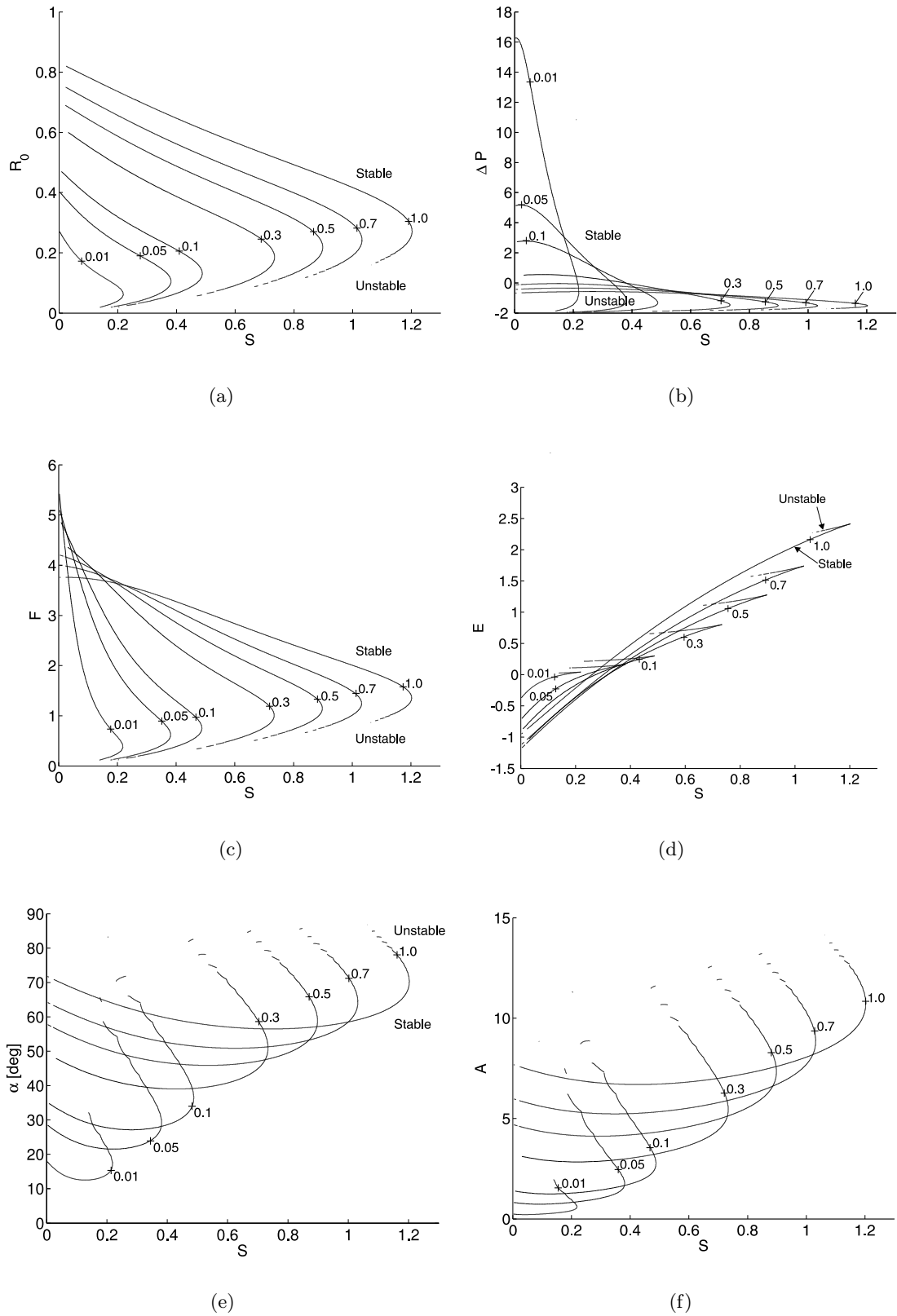


Figure 2.4: Contour plot for $R_A = 1$, $R_B = 1$ and $\theta = 0^\circ$. The contours represent a fixed fluid volume V and show the relationship between the liquid bridge properties and the separation distance S . The stable solutions have minimum Gibbs free surface energy. Rupture of the liquid bridges occur at the maximum separation distance for a given volume. (Note: $\alpha \equiv \beta$ since $R_A = R_B$.)

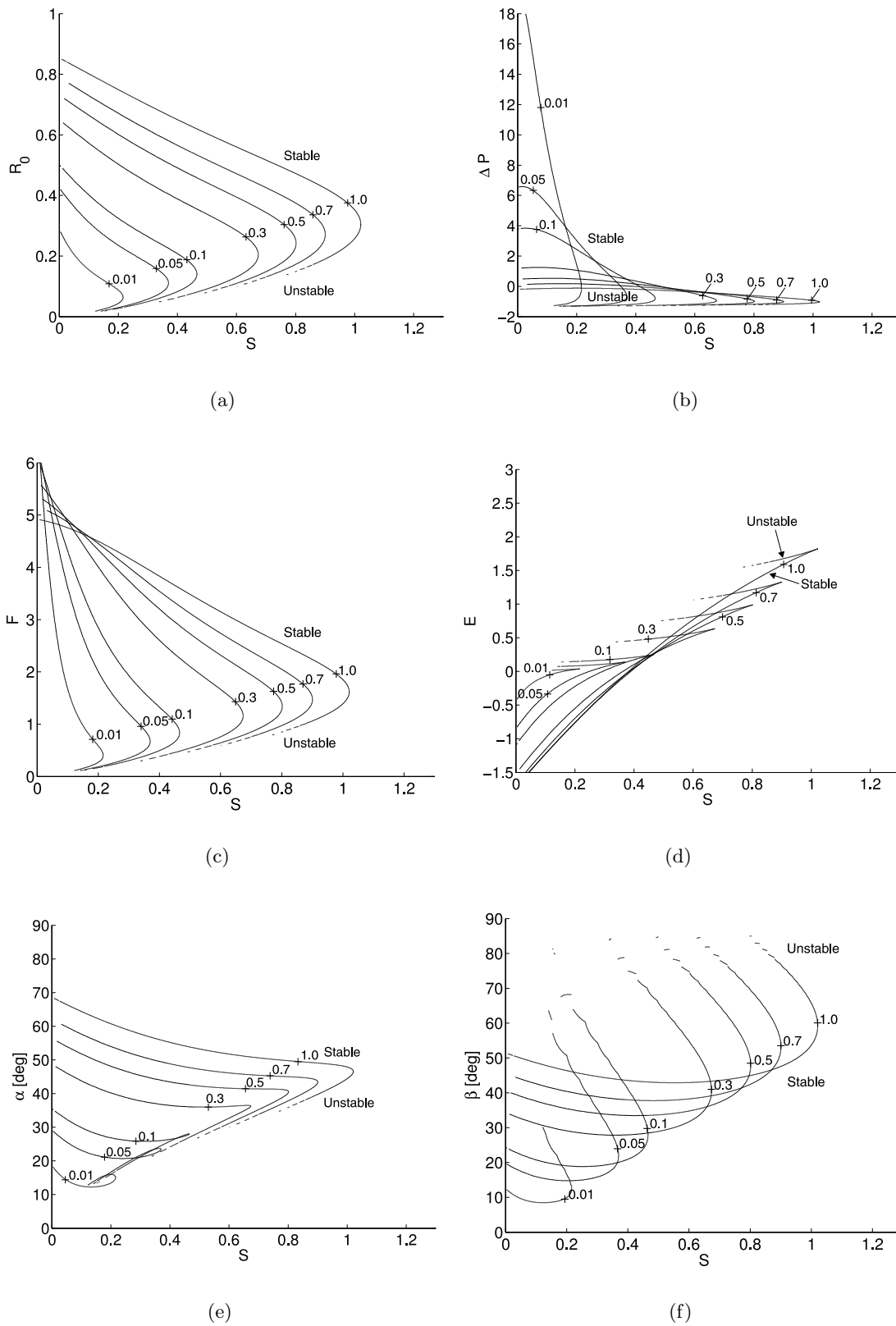
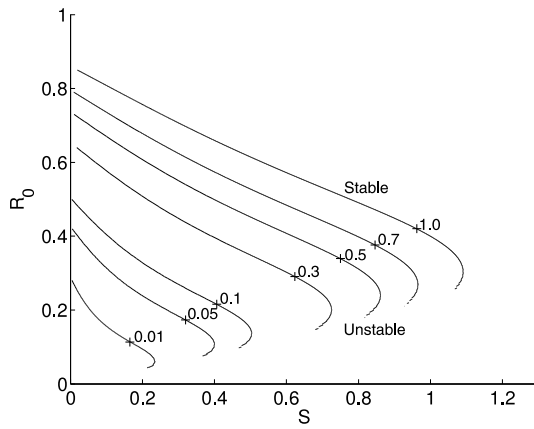
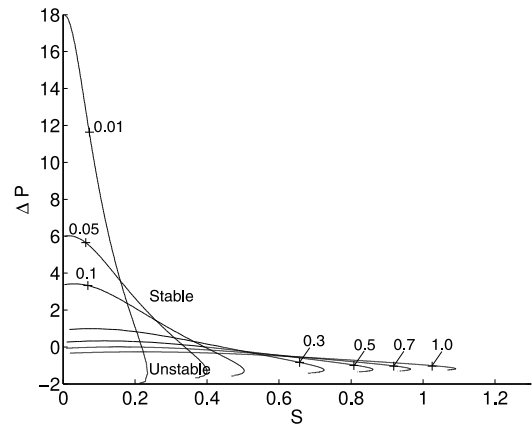


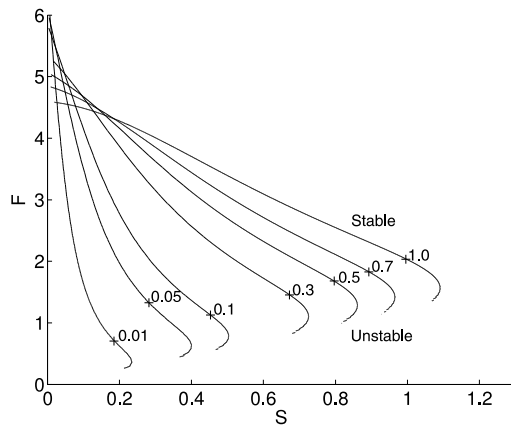
Figure 2.5: Contour plot for $R_A = 1$, $R_B = 1.5$ and $\theta = 0^\circ$. The contours represent a fixed fluid volume V and show the relationship between the liquid bridge properties and the separation distance S .



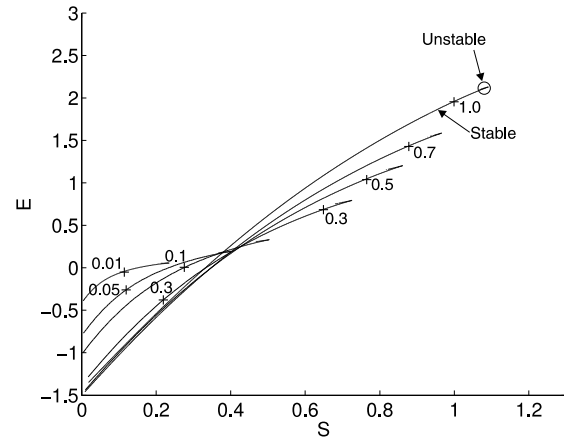
(a)



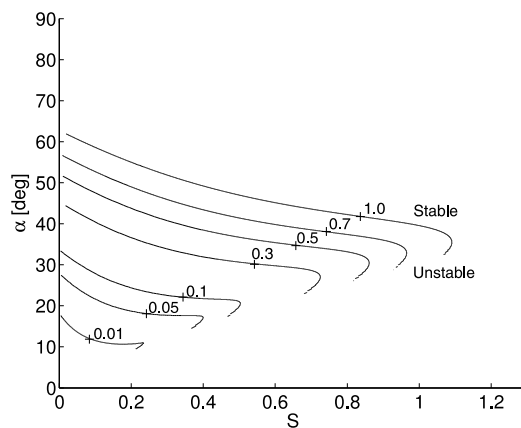
(b)



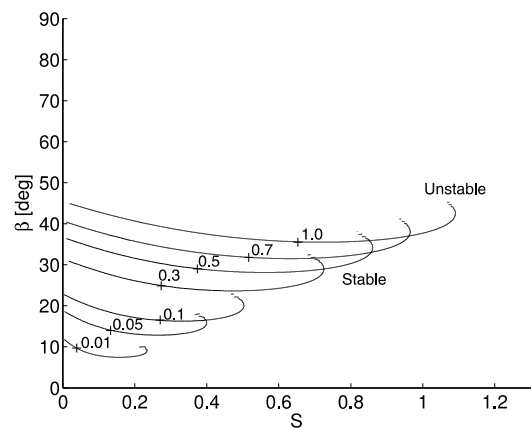
(c)



(d)

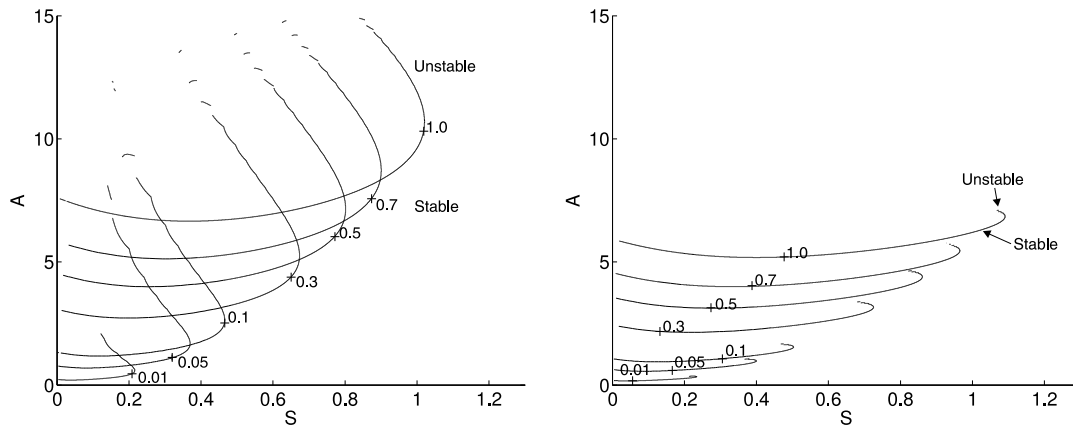


(e)



(f)

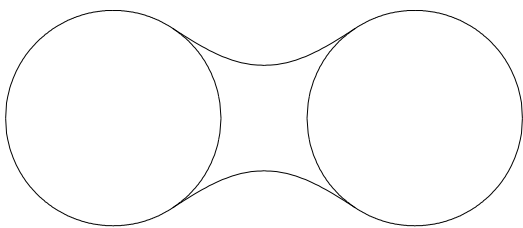
Figure 2.6: Contour plot for $R_A = 1$, $R_B = 1.5$ and $\theta = 15^\circ$. The contours represent a fixed fluid volume V and show the relationship between the liquid bridge properties and the separation distance S .



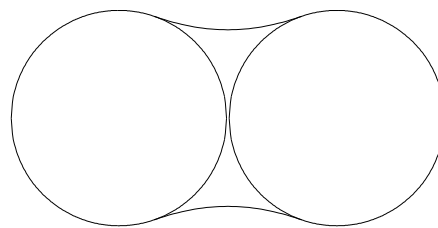
(a) Surface area A for $R_A = 1$, $R_B = 1.5$ and $\theta = 0^\circ$

(b) Surface area A for $R_A = 1$, $R_B = 1.5$ and $\theta = 15^\circ$

Figure 2.7: Contour plot showing liquid bridge surface area A for (a) $R_A = 1$, $R_B = 1.5$ and $\theta = 0^\circ$ and (b) $R_A = 1$, $R_B = 1.5$ and $\theta = 15^\circ$.

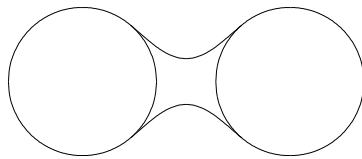


(a) $S = 0.8$ ($R_0 = 0.49$, $\Delta P = -0.90$)

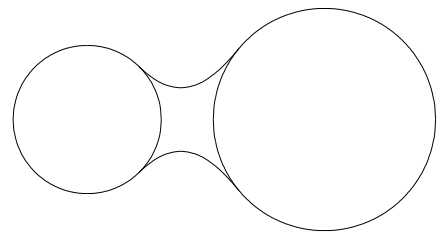


(b) $S \approx 0$ ($R_0 = 0.82$, $\Delta P = -0.66$)

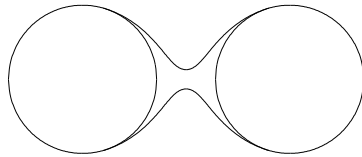
Figure 2.8: Liquid bridges with a fixed volume of $V = 1$ for $R_A = 1$, $R_B = 1$ and $\theta = 0^\circ$.



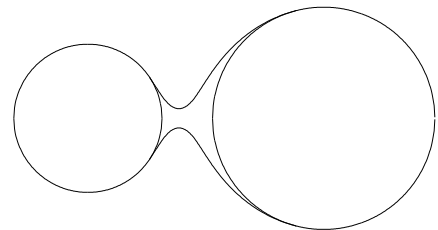
(a) Stable arrangement for $R_A = R_B = 1$, $\theta = 0^\circ$, $V = 0.5$ and $S = 0.8$. ($R_0 = 0.31$ and $\Delta P = -1.11$.)



(c) Stable arrangement for $R_A = 1$, $R_B = 1.5$, $\theta = 0^\circ$, $V = 0.7$ and $S = 0.7$. ($R_0 = 0.43$ and $\Delta P = -0.5023$.)



(b) Unstable arrangement for $R_A = R_B = 1$, $\theta = 0^\circ$, $V = 0.5$ and $S = 0.8$. ($R_0 = 0.13$ and $\Delta P = -1.75$.)



(d) Unstable arrangement for $R_A = 1$, $R_B = 1.5$, $\theta = 0^\circ$, $V = 0.7$ and $S = 0.7$. ($R_0 = 0.13$ and $\Delta P = -1.22$.)

Figure 2.9: Comparison of stable and unstable arrangements. Figures (a) and (b) show stable and unstable arrangements for $S = 0.8$ and $V = 0.5$. Figures (c) and (d) show the arrangements for $S = 0.7$ and $V = 0.7$. The stable arrangements occur physically.

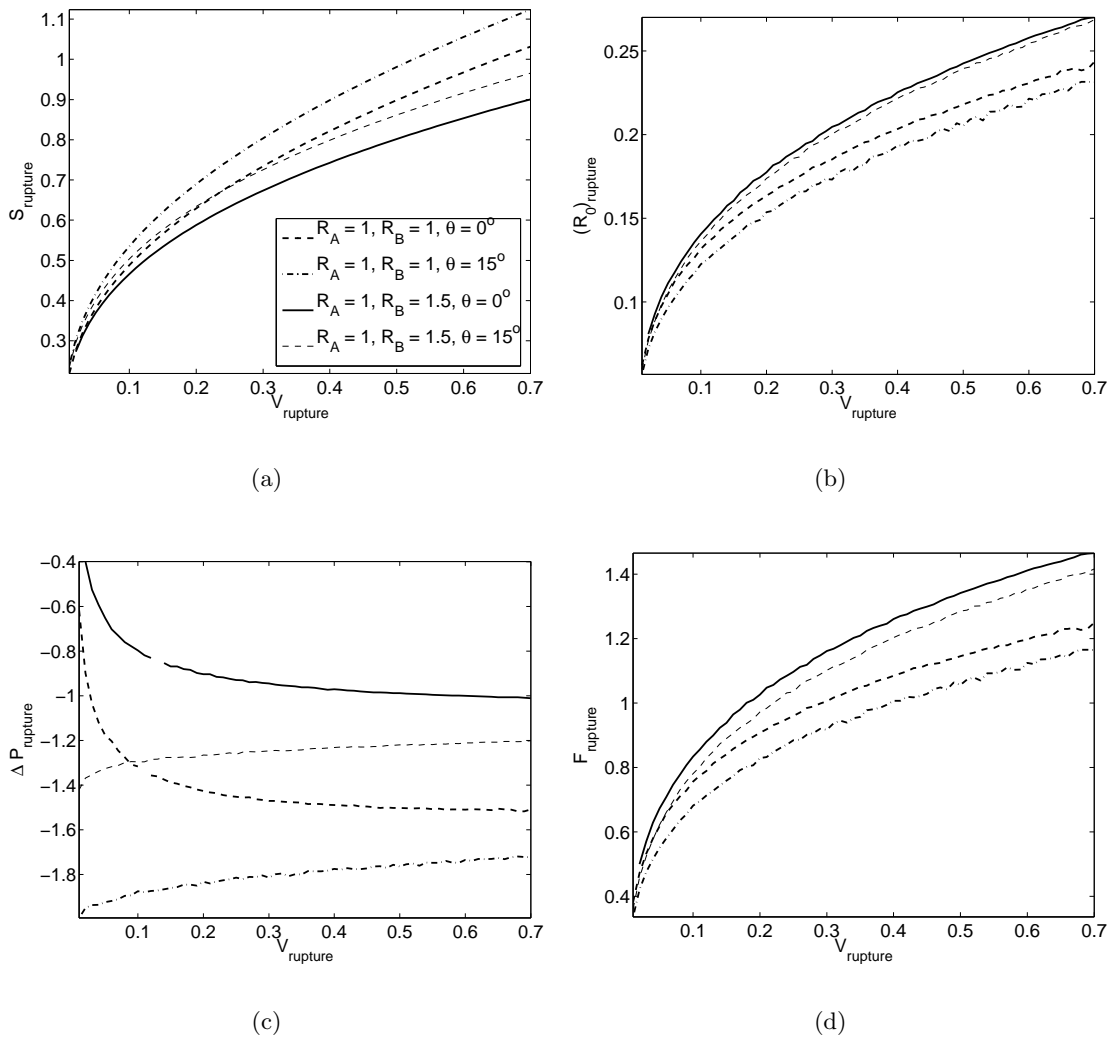
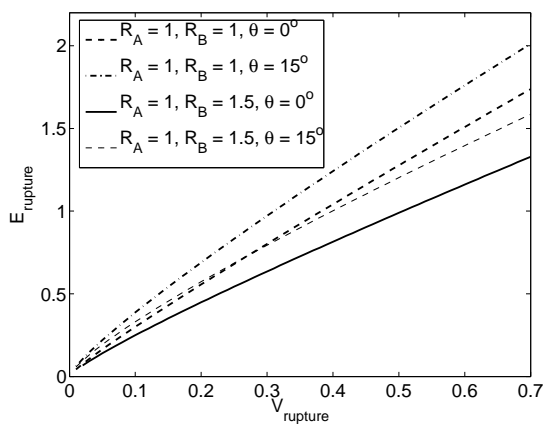
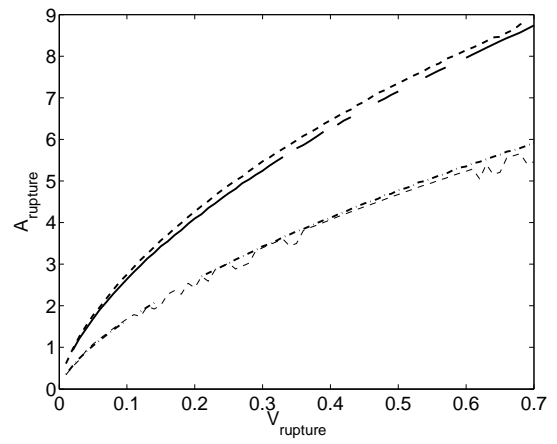


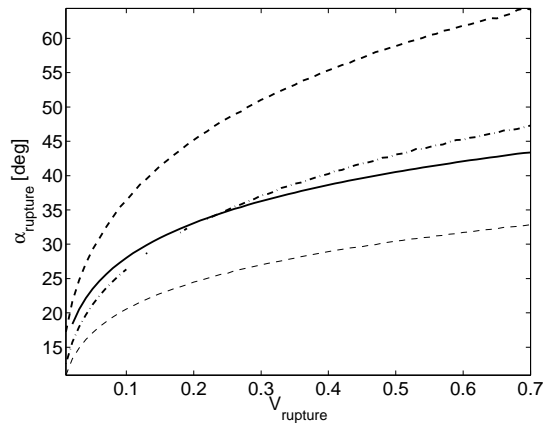
Figure 2.10: Liquid bridge properties at the point of rupture plotted with respect to the rupture volume V_{rupture} . The legend is provided in Figure (a).



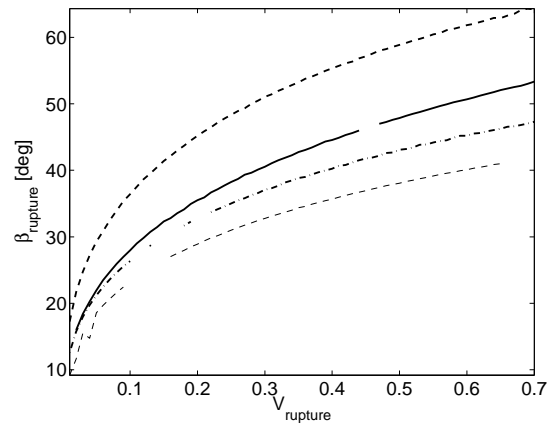
(c)



(d)



(e)



(f)

Figure 2.10: Liquid bridge properties at the point of rupture plotted with respect to the rupture volume V_{rupture} (continued). The legend is provided in Figure (a).

2.5 Analytic Solution

An analytic solution to Equation (2.3) is possible by making the substitution

$$U = (1 + R'^2)^{-\frac{1}{2}}. \quad (2.34)$$

Differentiating U with respect to X gives

$$\frac{dU}{dX} = -\frac{R'R''}{(1 + R'^2)^{\frac{3}{2}}}. \quad (2.35)$$

By applying the chain rule to Equation (2.35) we obtain

$$\frac{dU}{dR} = \frac{dU}{dX} \frac{dX}{dR} = -\frac{R''}{(1 + R'^2)^{\frac{3}{2}}}, \quad (2.36)$$

since $\frac{dX}{dR} = \frac{1}{R'}$.

The results in Equations (2.34) and (2.35) allow Equation (2.3) to be written as the following first order ordinary differential equation,

$$\frac{dU}{dR} + \frac{U}{R} = -\Delta P. \quad (2.37)$$

Integrating Equation (2.37) gives

$$U = \frac{C}{R} - \frac{R\Delta P}{2} \quad (2.38)$$

where C is a constant of integration. Rearranging Equation (2.38) in terms of C and substituting Equation (2.34) gives

$$C = R \left(\frac{1}{\sqrt{1 + R'^2}} + \frac{R\Delta P}{2} \right). \quad (2.39)$$

By comparing Equation (2.39) with Equation (2.24) it is found that $F = 2\pi C$ which proves that the inter-particle force is constant along the length of the bridge.

Combining Equations (2.34) and (2.38) and rearranging gives

$$\frac{dR}{dX} = \pm \frac{\sqrt{R^2 - (C - \frac{R^2\Delta P}{2})^2}}{C - \frac{R^2\Delta P}{2}}. \quad (2.40)$$

If $\Delta P = 0$ (and $C \neq 0$) then, from Equation (2.40), for a bridge where $R(X_0) = R_0$,

$$\int_{R_0}^R \frac{dR}{\sqrt{R^2 - C^2}} = \int_{X_0}^X \frac{dX}{C}. \quad (2.41)$$

To evaluate Equation (2.41), the integral

$$\int_{R_0}^{R_1} \frac{dR}{\sqrt{R^2 - C^2}} = \operatorname{acosh} \frac{R}{C} \Big|_{R_0}^{R_1} \quad (2.42)$$

is used [49]. It follows, from Equation (2.41), that

$$R(X) = C \cosh \left[\frac{X - X_0}{C} + \operatorname{acosh} \frac{R_0}{C} \right]. \quad (2.43)$$

It was confirmed that Equation (2.43) is correct by checking it with the numerical solution obtained in Section 2.3.

If $C = 0$ ($\Delta P \neq 0$) then Equation (2.40) can be solved to give

$$X^2 + R^2 = \left(\frac{2}{\Delta P} \right)^2 \quad (2.44)$$

showing that, for this case, the bridge is a sphere.

For $\Delta P \neq 0$, after rearranging Equation (2.40), the following integral is obtained which gives a parametric solution of the liquid bridge position X in terms of the height R ,

$$X(R) = \mp \int_{R_0}^{R_1} \frac{C - \frac{R^2 \Delta P}{2}}{\sqrt{R^2 - \left(C - \frac{R^2 \Delta P}{2}\right)^2}} dR. \quad (2.45)$$

The integral in Equation (2.45) is now written in standard form so that it can be evaluated using tables. The denominator is considered first. Now,

$$R^2 - \left(C - \frac{R^2 \Delta P}{2}\right)^2 = -\frac{\Delta P^2}{4} R^4 + (1 + C \Delta P) R^2 - C^2 \quad (2.46)$$

which is a quadratic in R^2 . The discriminant of Equation (2.46) is $\delta = 1 + 2C \Delta P$. Since it is required that $\delta > 0$ it follows that $C \Delta P > -\frac{1}{2}$. This gives a condition on the liquid bridge force in terms of the pressure difference ΔP .

The roots of Equation (2.46) are

$$\alpha^2, \beta^2 = \frac{2}{\Delta P^2} \left[1 + C \Delta P \mp \sqrt{1 + 2C \Delta P} \right]. \quad (2.47)$$

Let

$$\alpha = \sqrt{\frac{2}{\Delta P^2} \left[1 + C \Delta P + \sqrt{1 + 2C \Delta P} \right]} \quad (2.48)$$

and

$$\beta = \sqrt{\frac{2}{\Delta P^2} \left[1 + C \Delta P - \sqrt{1 + 2C \Delta P} \right]}. \quad (2.49)$$

Evidently, $\beta < \alpha$. Let R be such that

$$\beta < R \leq \alpha.$$

Writing Equation (2.46) in standard form, using the roots from Equation (2.47), gives

$$R^2 - \left(C - \frac{R^2 \Delta P}{2} \right)^2 = \frac{\Delta P^2}{4} (\alpha^2 - R^2)(R^2 - \beta^2). \quad (2.50)$$

It follows that the denominator of Equation (2.45) may be written as

$$\sqrt{R^2 - \left(C - \frac{R^2 \Delta P}{2} \right)^2} = \frac{|\Delta P|}{2} \sqrt{(\alpha^2 - R^2)(R^2 - \beta^2)}.$$

Therefore, from Equation (2.45),

$$\begin{aligned} X(R) &= \mp \frac{2}{|\Delta P|} \int_{R_0}^{R_1} \frac{C - \frac{R^2 \Delta P}{2}}{\sqrt{(\alpha^2 - R^2)(R^2 - \beta^2)}} dR \\ &= \mp \left[\frac{2C}{\Delta P} \int_{R_0}^{R_1} \frac{dR}{\sqrt{(\alpha^2 - R^2)(R^2 - \beta^2)}} - \int_{R_0}^{R_1} \frac{R^2 dR}{\sqrt{(\alpha^2 - R^2)(R^2 - \beta^2)}} \right]. \end{aligned} \quad (2.51)$$

To evaluate the integrals in Equation (2.51) the following integrals from Gradshteyn and Ryzhik [50] were used:

$$\int_{R_0}^{R_1} \frac{dR}{\sqrt{(\alpha^2 - R^2)(R^2 - \beta^2)}} = \frac{1}{\alpha} \left[\mathbf{F}(\chi_1, q) - \mathbf{F}(\chi_0, q) \right] \quad (2.52)$$

$$\begin{aligned} \int_{R_0}^{R_1} \frac{R^2 dR}{\sqrt{(\alpha^2 - R^2)(R^2 - \beta^2)}} &= \alpha \left[\mathbf{E}(\chi_1, q) - \mathbf{E}(\chi_0, q) \right] \\ &\quad - \frac{\sqrt{(\alpha^2 - R_1^2)(R_1^2 - \beta^2)}}{R_1} + \frac{\sqrt{(\alpha^2 - R_0^2)(R_0^2 - \beta^2)}}{R_0} \end{aligned} \quad (2.53)$$

where \mathbf{E} and \mathbf{F} respectively denote the Legendre-Jacobi incomplete elliptic integrals of

the first and second kind,

$$\chi_1 = \operatorname{asin} \left(\frac{\alpha \sqrt{R_1^2 - \beta^2}}{R_1 k} \right), \chi_0 = \operatorname{asin} \left(\frac{\alpha \sqrt{R_0^2 - \beta^2}}{R_0 k} \right)$$

and

$$q = \frac{k}{\alpha}, k = \sqrt{\alpha^2 - \beta^2}.$$

Both integrals are valid because $\beta < R \leq \alpha$.

Therefore, from Equation (2.51),

$$\begin{aligned} X(R) &= \int_{R_0}^{R_1} \frac{C - \frac{R^2 \Delta P}{2}}{\sqrt{R^2 - (C - \frac{R^2 \Delta P}{2})^2}} dR \\ &= \frac{2C}{\Delta P} \int_{R_0}^{R_1} \frac{dR}{\sqrt{(\alpha^2 - R^2)(R^2 - \beta^2)}} - \int_{R_0}^{R_1} \frac{R^2 dR}{\sqrt{(\alpha^2 - R^2)(R^2 - \beta^2)}} \\ &= \frac{2C}{\Delta P \alpha} \left[\mathbf{F}(\chi_1, q) - \mathbf{F}(\chi_0, q) \right] - \alpha \left[\mathbf{E}(\chi_1, q) - \mathbf{E}(\chi_0, q) \right. \\ &\quad \left. - \frac{\sqrt{(\alpha^2 - R_1^2)(R_1^2 - \beta^2)}}{R_1} + \frac{\sqrt{(\alpha^2 - R_0^2)(R_0^2 - \beta^2)}}{R_0} \right]. \end{aligned} \quad (2.54)$$

Equation (2.54) is a parametric solution of the liquid bridge surface. It was confirmed that this formula was correct by numerically evaluating Equation (2.54) and comparing it with the numerical solution obtained in Section 2.3. Agreement was confirmed by selecting a particular contour from the analytic solution, determining X for the integral, and numerically integrating to obtain the corresponding liquid bridge.

2.5.1 Phase Portrait

The normalised force C is related to the height and slope of the bridge surface (R , R') by Equation (2.39). Boundary conditions on R and R' , along with the pressure difference ΔP , determine the contour for a particular liquid bridge. Generic contours, characterising all possible liquid bridge configurations, can be obtained from Equation (2.39) by scaling. After substituting $\tilde{R} = R |\Delta P|$ and $\tilde{X} = X |\Delta P|$ into Equation (2.39) it follows that

$$C |\Delta P| = \tilde{R} \left(\frac{1}{\sqrt{1 + \tilde{R}'^2}} + \frac{\tilde{R}}{2} \right). \quad (2.55)$$

The angle ϕ is introduced where $R' = \tan \phi$ and therefore $\sqrt{1 + R'^2} = \sec \phi$. In terms of

ϕ , Equation (2.55) becomes

$$C |\Delta P| = \tilde{R} \left(\cos \phi + \frac{\tilde{R}}{2} \right) \quad \text{for } \Delta P > 0 \quad (2.56a)$$

$$C |\Delta P| = \tilde{R} \left(\cos \phi - \frac{\tilde{R}}{2} \right) \quad \text{for } \Delta P < 0. \quad (2.56b)$$

For $\Delta P = 0$, from Equation (2.39),

$$C = R \cos \phi \quad \text{for } \Delta P = 0. \quad (2.56c)$$

The phase portraits for Equations (2.56a)-(2.56c) are shown in Figures 2.11(a), 2.11(b) and 2.12. These figures theoretically predict six distinct types of static liquid bridges:

1. ‘Wavy’ Cylinder

$\Delta P > 0$ and $0 < C |\Delta P| < 0.5$ (Figure 2.11(a)).

With reference to Figure 2.11(a), for $0 < C |\Delta P| < 0.5$, periodic solutions exist for $|\phi| < 90^\circ$. The shape of the liquid surface is that of a ‘wavy’ cylinder.

2. Cylinder

$\Delta P > 0$ and $C |\Delta P| = 0.5$ (Figure 2.11(a)).

The point $C |\Delta P| = 0.5$, $\phi \equiv 0^\circ$ corresponds to a cylinder solution.

3. Sphere

$\Delta P > 0$ and $C |\Delta P| = 0$ (Figure 2.11(a)).

The critical contour at $\phi = 90^\circ$ ($C |\Delta P| = 0$) is the sphere described by Equation (2.44) which separates the cylinder and upwardly curved solutions.

4. Convex Liquid Bridge

$\Delta P > 0$ and $C |\Delta P| < 0$ (Figure 2.11(a)). For this case $C = \frac{F}{2\pi} < 0$ and the force between the particles is repelling.

5. Concave Liquid Bridge

(a) $\Delta P < 0$ and $C |\Delta P| > 0$ (Figure 2.11(b)).

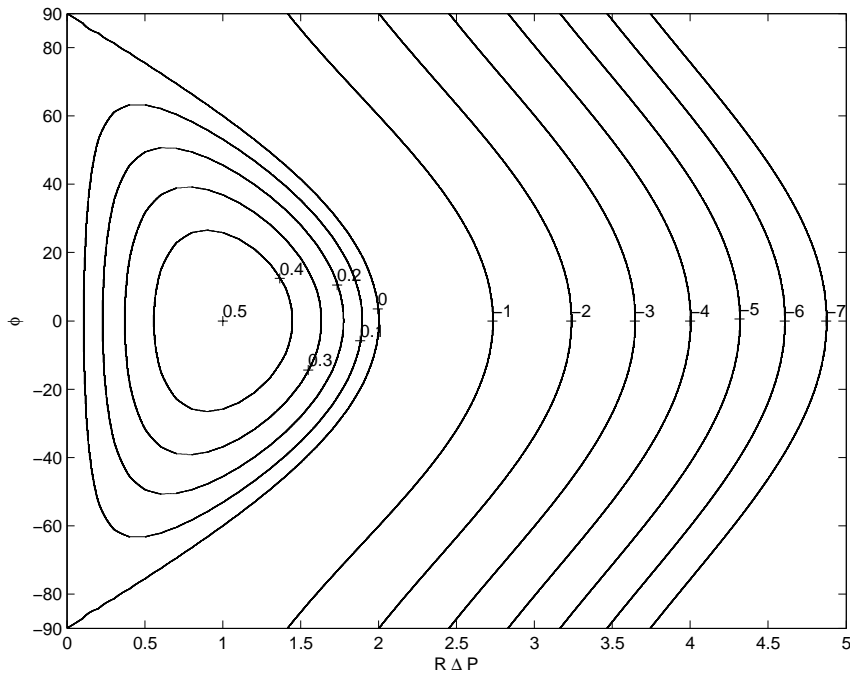
(b) $\Delta P = 0$ and $C > 0$ (Figure 2.12).

The liquid surface begins with initial height R_0 and curves upwards reaching a maximum height $R_{\max} > R_0$.

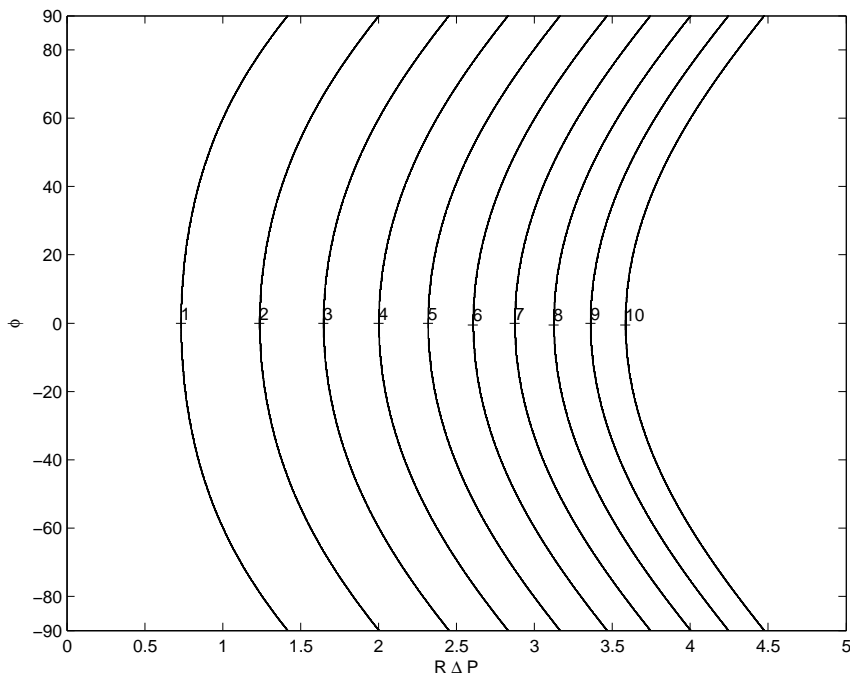
6. Vertical Planes

$\Delta P = 0$ and $C = 0$ (Figure 2.12).

For $\phi = 90^\circ$ the solution corresponds to two vertical planes separated by fluid.



(a) Phase portrait for $\Delta P > 0$ where $\phi = \arctan R'$. Contour labels are values of $C|\Delta P|$.



(b) Phase portrait for $\Delta P < 0$ where $\phi = \arctan R'$ is plotted against \tilde{R} . Contour labels are values of $C|\Delta P|$.

Figure 2.11: Phase portraits for liquid bridges with rotational symmetry.

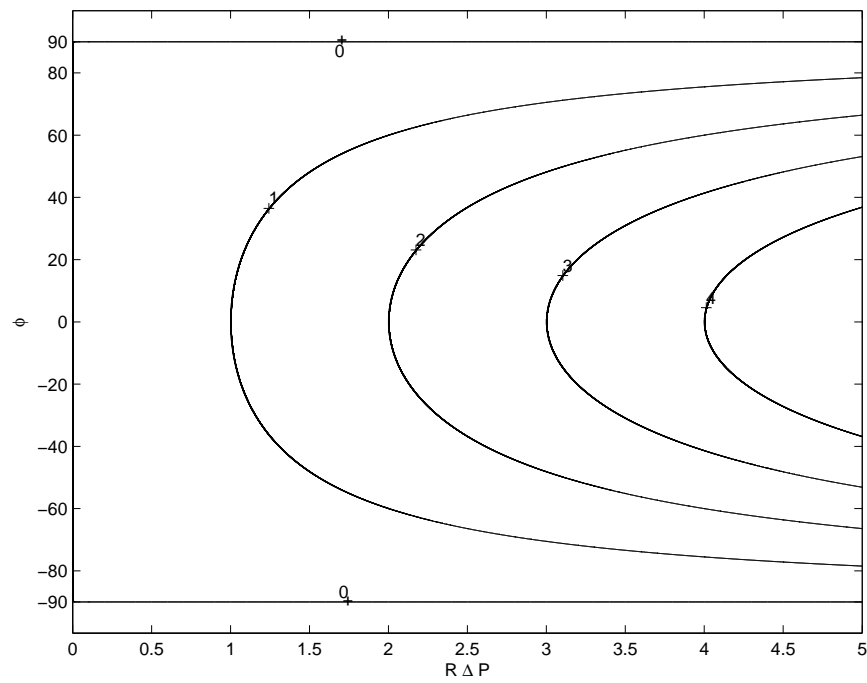


Figure 2.12: Phase portrait of liquid bridges with rotational symmetry for $\Delta P = 0$.

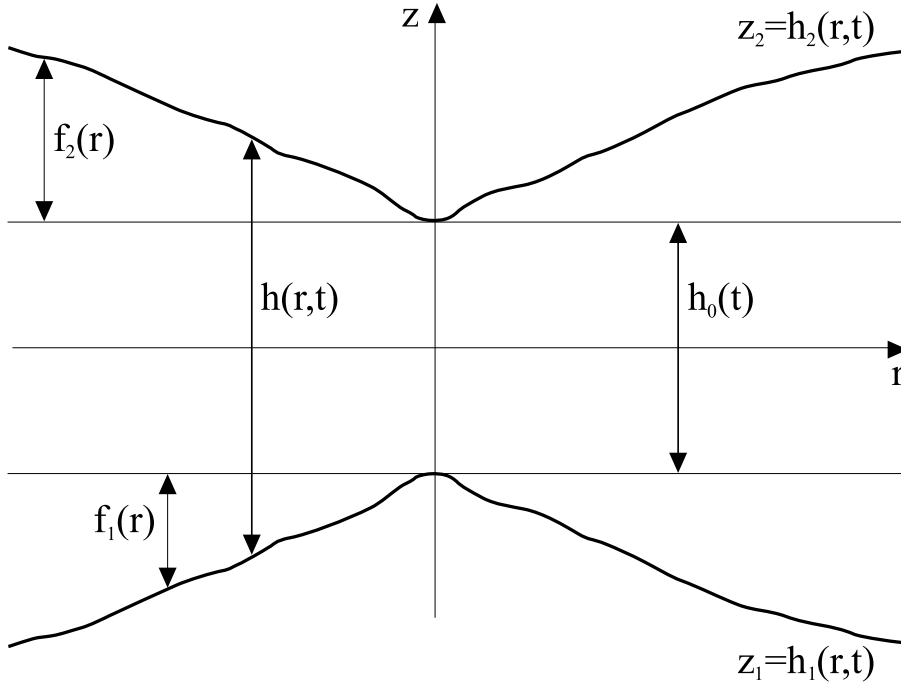


Figure 2.13: Figure showing two general surfaces that are approaching each other, described by $z_1 = h_1(r, t)$ and $z_2 = h_2(r, t)$. The separation distances between the surfaces is $h(r, t)$.

2.6 Dynamic Liquid Bridges

Dynamic liquid bridges have previously been studied by Ennis *et al.* [4] and Liu *et al.* [26] as detailed in Section 1.3.3. These models apply the full asymptotic solution for the liquid bridge viscous force from Equation (1.32) which was derived using lubrication theory. In this section a simplified arrangement is considered. The spheres are assumed to be rigid and the effect of rebound is not considered. The problem is solved by direct application of the Navier-Stokes equations using the low Reynolds number approximation.

Theory is presented for two general surfaces $z_1(r, t)$ and $z_2(r, t)$ with rotational symmetry about the z axis, as shown in Figure 2.13, and separated by a gap distance $h(r, t)$. $h_0(t)$ is the closest approach distance between the surfaces and $f_1(r)$ and $f_2(r)$ describe the shape of each surface relative to a radial datum line occurring at $z = -\frac{h_0(t)}{2}$ and $z = \frac{h_0(t)}{2}$. $z = 0$ is defined to be midway between the closest approach points of the two surfaces. The particular case for two approaching spheres, with a constant bridge volume V_0 , as illustrated in Figure 2.14, is examined.

To study the dynamics, a simplifying approximation is made that the shape of the bridge is a cylinder. The fluid velocity \vec{v} is assumed to be steady and at low Reynolds number

($\text{Re} \ll 1$) implying that the inertial force is negligible in comparison with the viscous force of the bridge. The fluid is assumed to be incompressible with constant viscosity μ and have uniform density ρ . Only viscous forces are studied. No other particle interactions, such as van der Waals, surface tension, electrostatics, or the body force effect of gravity are considered.

2.6.1 Balance Equations

Cylindrical coordinates (r, θ, z) are used and the velocity vector is $\vec{v} = (v_r, v_\theta, v_z)$ where v_r is the radial fluid velocity, v_θ the fluid velocity about the r - z axis and v_z the fluid velocity in the z direction. For this system, the mass conservation equation from Hughes and Gaylord [51] is used,

$$\frac{1}{r} \frac{\partial}{\partial r} (r v_r) + \frac{\partial v_z}{\partial z} = 0 \quad (2.57)$$

where, by symmetry, there is no rotational flow about the z or r axes and therefore $v_\theta = 0$.

Neglecting inertial terms, that is assuming $\text{Re} \ll 1$, the momentum equations from [51] reduce to:

$$0 = -\frac{\partial P}{\partial r} + \mu \left[\frac{\partial^2 v_r}{\partial r^2} + \frac{1}{r} \frac{\partial v_r}{\partial r} + \frac{\partial^2 v_r}{\partial z^2} - \frac{v_r}{r^2} \right] \quad (2.58)$$

$$0 = -\frac{\partial P}{\partial z} - \rho g + \mu \left[\frac{\partial^2 v_z}{\partial r^2} + \frac{1}{r} \frac{\partial v_z}{\partial r} + \frac{\partial^2 v_z}{\partial z^2} \right] \quad (2.59)$$

where $P = P(r, z)$ is the pressure within the liquid bridge. The approximation $v_z \ll v_r$ is applied which physically means that the bridges must have a small volume and that a small gap distance h must separate the particles (i.e. $h \ll R$). Since $v_z \ll v_r$, and because gravity is not considered in this approximation, a solution needs to only satisfy Equation (2.58).

2.6.2 Velocity Profile

Consider the volume flow rate Q of fluid displaced when surfaces z_1 and z_2 move toward each other. Since the surfaces have rotational symmetry,

$$Q = \int_{h_1(r,t)}^{h_2(r,t)} 2\pi r v_r dz. \quad (2.60)$$

To determine Q , we manipulate Equation (2.60) by taking the partial derivative of Q

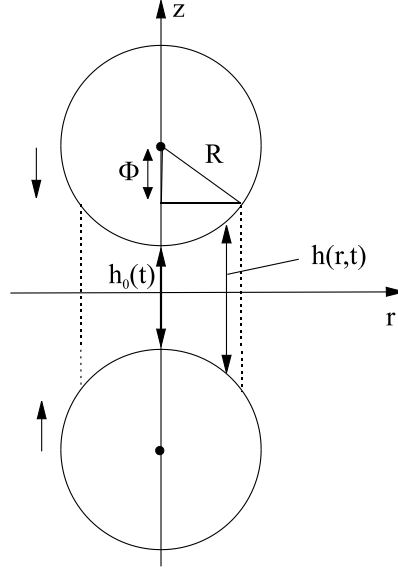


Figure 2.14: The scenario in which two approaching spheres of radius \mathbf{R} are connected together via a dynamic liquid bridge shown by the dotted lines.

with respect to r , and dividing through by r . Upon completing this, we obtain

$$\begin{aligned} \frac{1}{r} \frac{\partial}{\partial r} \left(\int_{h_1(r,t)}^{h_2(r,t)} 2\pi r v_r dz \right) &= \frac{2\pi}{r} \int_{h_1(r,t)}^{h_2(r,t)} \frac{\partial}{\partial r} (r v_r) dz \\ &+ \frac{2\pi}{r} \left(\frac{\partial h_2}{\partial r} v_r(r, h_2(r, t), t) - \frac{\partial h_1}{\partial r} v_r(r, h_1(r, t), t) \right) \end{aligned} \quad (2.61)$$

where the second term in Equation (2.61) arises upon application of the fundamental theorem of calculus and the chain rule. Now, since the fluid is unable to move through the surfaces,

$$v_r(r, h_1(r, t), t) = v_r(r, h_2(r, t), t) = 0.$$

This reduces Equation (2.61) to

$$\frac{1}{r} \frac{\partial Q}{\partial r} = \frac{2\pi}{r} \int_{h_1(r,t)}^{h_2(r,t)} \frac{\partial}{\partial r} (r v_r) dz. \quad (2.62)$$

Substituting Equation (2.57) into Equation (2.62) yields

$$\begin{aligned} \frac{1}{r} \frac{\partial Q}{\partial r} &= -2\pi \int_{h_1(r,t)}^{h_2(r,t)} \frac{\partial v_z}{\partial z} dz \\ &= -2\pi \left(v_z(r, h_2(r, t), t) - v_z(r, h_1(r, t), t) \right) \end{aligned} \quad (2.63)$$

Assuming that the separation functions $h_1(r, t)$ and $h_2(r, t)$ may be written as the sum

of a time dependent function $h_0(t)$ and radial functions $f_1(r)$ and $f_2(r)$, as illustrated in Figure 2.13, it is possible to write $h_1(r, t) = -\frac{1}{2}h_0(t) + f_1(r)$ and $h_2(r, t) = \frac{1}{2}h_0(t) + f_2(r)$. Now

$$\begin{aligned} v_z(r, h_1(r, t), t) &= \frac{\partial h_1}{\partial t}(r = 0, t) = -\frac{1}{2} \frac{dh_0}{dt} \\ v_z(r, h_2(r, t), t) &= \frac{\partial h_2}{\partial t}(r = 0, t) = \frac{1}{2} \frac{dh_0}{dt}. \end{aligned}$$

Therefore Equation (2.63) is equivalent to

$$\frac{1}{r} \frac{\partial Q}{\partial r} = -2\pi \left(\frac{1}{2} \frac{dh_0}{dt} - \frac{-1}{2} \frac{dh_0}{dt} \right) = -2\pi \frac{dh_0}{dt}. \quad (2.64)$$

Integrating Equation (2.64) gives

$$Q(r, t) = -2\pi \int_0^r r \frac{dh_0}{dt} dr = -\pi r^2 \frac{dh_0}{dt}. \quad (2.65)$$

For laminar flow, a parabolic radial velocity profile can be assumed,

$$v_r(r, z, t) = A(r, t) [z - h_1(r, t)] [h_2(r, t) - z] \quad (2.66)$$

where $A(r, t)$ is a function determined below and $h_1(r, t) \leq z \leq h_2(r, t)$. Substituting Equation (2.66) into Equation (2.60) gives

$$\begin{aligned} Q &= \int_{h_1(r, t)}^{h_2(r, t)} 2\pi r v_r dz \\ &= \int_{h_1(r, t)}^{h_2(r, t)} 2\pi r A(r, t) [z - h_1] [h_2 - z] dz \\ &= \frac{\pi r}{3} A(r, t) (h_2(r, t) - h_1(r, t))^3. \end{aligned} \quad (2.67)$$

Equating Equation (2.67) with Equation (2.65) gives $A(r, t) = \frac{-3r \frac{dh_0}{dt}}{h_2 - h_1}$. The radial velocity profile is therefore

$$v_r(r, z, t) = \frac{-3r [z - h_1(r, t)] [h_2(r, t) - z]}{[h_2(r, t) - h_1(r, t)]^3} \frac{dh_0}{dt} \quad (2.68)$$

Equation (2.68) is used to find the pressure profile P in the liquid bridge.

2.6.3 Determining the pressure

Rearranging Equation (2.58) gives

$$\frac{1}{\mu} \frac{\partial P}{\partial r} = \frac{1}{r} \frac{\partial}{\partial r} \left(r \frac{\partial v_r}{\partial r} \right) + \frac{\partial^2 v_r}{\partial z^2} - \frac{v_r}{r^2}. \quad (2.69)$$

After differentiating Equation (2.68), to find $\frac{\partial v_r}{\partial r}$ and $\frac{\partial^2 v_r}{\partial z^2}$, and substituting these results into Equation (2.69), we obtain, after tedious algebra,

$$\begin{aligned} \frac{1}{\mu} \frac{\partial P}{\partial r} = & \left[-\frac{27}{h^4} \frac{\partial h}{\partial r} + \frac{36r}{h^5} \left(\frac{\partial h}{\partial r} \right)^2 - \frac{9r}{h^4} \frac{\partial^2 h}{\partial r^2} \right] z^2 \frac{dh_0}{dt} \\ & + \left[\frac{18}{h^3} \frac{\partial h}{\partial r} - \frac{18r}{h^4} \left(\frac{\partial h}{\partial r} \right)^2 + \frac{6r}{h^3} \frac{\partial^2 h}{\partial r^2} \right] z \frac{dh_0}{dt} \\ & + \frac{6r}{h^3} \frac{dh_0}{dt} \end{aligned} \quad (2.70)$$

which is valid for arbitrary surfaces f_1 and f_2 described by a separation function h . The radial pressure profile $\frac{\partial P}{\partial r}$ for the case of equi-sized spheres of radius \mathbf{R} is obtained by calculating the separation distance function $h(r, t)$ as illustrated in Figure 2.14. For spheres,

$$h(r, t) = h_0(t) + 2(\mathbf{R} - \Phi)$$

where $\Phi = \sqrt{\mathbf{R}^2 - r^2}$.

Therefore

$$h(r, t) = h_0(t) + 2 \left(\mathbf{R} - \sqrt{\mathbf{R}^2 - r^2} \right). \quad (2.71)$$

Differentiating Equation (2.71) gives $\frac{\partial h}{\partial r} = \frac{2r}{\sqrt{\mathbf{R}^2 - r^2}}$ and $\frac{\partial^2 h}{\partial r^2} = \frac{2\mathbf{R}^2}{(\mathbf{R}^2 - r^2)^{\frac{3}{2}}}$. Substituting these into Equation (2.70) gives

$$\begin{aligned} \frac{1}{\mu} \frac{\partial P}{\partial r} = & \frac{\frac{dh_0}{dt}}{(\mathbf{R}^2 - r^2)^{\frac{3}{2}} h^3} \left[\frac{54r^3 - 72r\mathbf{R}^2}{h} z^2 + (28r\mathbf{R}^2 - 36r^3) z \right] \\ & + \frac{r^3}{(\mathbf{R}^2 - r^2)h^4} \left[144 \frac{dh_0}{dt} z^2 - 72z \frac{dh_0}{dt} \right] + \frac{6r}{h^3} \frac{dh_0}{dt} \end{aligned} \quad (2.72)$$

Equation (2.72) includes z terms which makes integration to find the pressure P difficult. However, since the fluid layer is small in comparison to \mathbf{R} , the vertically averaged pressure

\bar{P} provides an accurate approximation. Vertical averaging, given by

$$\frac{\partial \bar{P}}{\partial r} = \frac{1}{h} \int_0^{h(r,t)} \frac{\partial P}{\partial r} dz, \quad (2.73)$$

removes the explicit z dependence and integration is then straightforward. Substitution of Equation (2.72) into Equation (2.73) and integrating gives

$$\frac{\partial \bar{P}}{\partial r} = \frac{6r\mu(\mathbf{R}^2 + r^2)}{h^3(\mathbf{R}^2 - r^2)} \frac{dh_0}{dt}. \quad (2.74)$$

If the pressure of the liquid bridge at some $r = r_0$ is at ambient pressure P_{amb} , and the bridge expands to $r > r_0$ then the vertically averaged pressure is

$$\begin{aligned} \bar{P}(r, t) &= P_{\text{amb}} + \int_{r_0}^r \frac{\partial \bar{P}}{\partial r} dr \\ &= P_{\text{amb}} + 6\mu \frac{dh_0}{dt} \int_{r_0}^r \frac{r(\mathbf{R}^2 + r^2)}{h^3(\mathbf{R}^2 - r^2)} dr. \end{aligned}$$

The pressure difference is therefore

$$\bar{P}(r, t) - P_{\text{amb}} = 6\mu \frac{dh_0}{dt} \int_{r_0}^r \frac{r(\mathbf{R}^2 + r^2)}{h^3(\mathbf{R}^2 - r^2)} dr. \quad (2.75)$$

2.6.4 Force

The pressure difference between the internal and external regions of the liquid bridge, $\bar{P}(r, t) - P_{\text{amb}}$, provides the force which retards the motion of the particles.

The force F_{bridge} is given by integrating the pressure difference over the cross-sectional area of the liquid bridge. Using Equation (2.75), the force is

$$\begin{aligned} F_{\text{bridge}} &= m \frac{d^2 h_0}{dt^2} \\ &= \int_0^{r_0} (\bar{P}(r, t) - P_{\text{amb}}) dA \\ &= \int_0^{r_0} \left[2\pi \hat{r} \left(6\mu \frac{dh_0}{dt} \int_{r_0}^r \frac{\hat{r}(\mathbf{R}^2 + \hat{r}^2)}{h^3(\mathbf{R}^2 - \hat{r}^2)} dr \right) r \right] d\hat{r} dr \\ &= 6\pi\mu \frac{dh_0}{dt} \left[\int_0^{r_0} \int_0^r \frac{2\hat{r}(\mathbf{R}^2 + \hat{r}^2)}{h^3(\mathbf{R}^2 - \hat{r}^2)} r d\hat{r} dr \right. \\ &\quad \left. - \int_0^{r_0} r dr \int_0^{r_0} \frac{2\hat{r}(\mathbf{R}^2 + \hat{r}^2)}{h^3(\mathbf{R}^2 - \hat{r}^2)} d\hat{r} \right] \end{aligned} \quad (2.76)$$

or, equivalently,

$$\frac{d^2 h_0}{dt^2} = \frac{6\pi\mu}{m} \frac{dh_0}{dt} \left\{ G(r_0, h_0) - \frac{1}{2} r_0^2 H(r_0, h_0) \right\} \quad (2.77)$$

where the functions

$$\begin{aligned} G(r_0, h_0) &= \int_0^{r_0} \int_0^r \frac{2\hat{r}(\mathbf{R}^2 + \hat{r}^2)}{h^3(\mathbf{R}^2 - \hat{r}^2)} r \, d\hat{r} \, dr \\ H(r_0, h_0) &= \int_0^{r_0} \frac{2r(\mathbf{R}^2 + r^2)}{h^3(\mathbf{R}^2 - r^2)} \, dr \end{aligned} \quad (2.78)$$

are evaluated for current radius r_0 and separation h_0 . Fourth order Runge-Kutta integration, using the matlab `ode45` subroutine, is used to evaluate the integrals on the right hand side of Equation (2.78). (Note that the function h appearing in (2.78) is the separation function from Equation (2.71)). Once G and H are evaluated the bridge acceleration is determined using Equation (2.77).

2.6.5 Numerical Solution

To maintain a constant liquid bridge volume of V_0 , the radius r_f , corresponding to $h_0 = 0$ (where the spheres are touching), is specified. The volume to be maintained is then

$$\begin{aligned} V_0 &= \int_0^{r_f} 2\pi r \left(\mathbf{R} - \sqrt{\mathbf{R}^2 - r^2} \right) \, dr \\ &= \int_{\sqrt{\mathbf{R}^2 - r_f^2}}^{\mathbf{R}} 2\pi\Phi \left(\mathbf{R} - \Phi \right) \, d\Phi \end{aligned}$$

where the substitution $\Phi = \sqrt{\mathbf{R}^2 - r^2}$ has been used. It follows that

$$V_0 = 2\pi \left[\frac{1}{3}(\mathbf{R}^2 - r_f^2)^{\frac{3}{2}} + \frac{1}{2}\mathbf{R}r_f^2 - \frac{1}{3}\mathbf{R}^3 \right] \quad (2.79)$$

where V_0 is the bridge volume.

The problem begins with the initial separation $h_0(0)$ specified. As the separation distance changes, the current bridge radius r_0 changes in order to maintain the constant volume V_0 . If r_0 and h_0 are the bridge radius and separation distance at time t , we are required to solve

$$V_0 = 2\pi \left[\frac{(\mathbf{R}^2 - r_0^2)^{\frac{3}{2}}}{3} + \frac{\mathbf{R}r_0^2}{2} - \frac{\mathbf{R}}{3} \right] + \pi r_0^2 h_0. \quad (2.80)$$

For given V_0 and h_0 there is a unique solution for r_0 which is determined numerically.

Equations (2.77) and (2.80) define a second order differential algebraic equation (DAE) subject to one constraint. Integration of Equation (2.77) to obtain the bridge velocity and separation distance is achieved using a fourth order Runge Kutta integrator.

Depending on the initial values of h_0 and $\frac{dh_0}{dt}$, the liquid bridge exhibits four types of behaviour. Two cases occur for $\frac{dh_0}{dt} < 0$. If a small initial gap distance separates the particles, and, provided the magnitude of the initial velocity $\frac{dh_0}{dt}(0)$ is sufficiently large, the particles will collide. However, since the fluid has no inertia, energy is not stored in the liquid bridge and the particles do not rebound. If the initial gap separation is too large, or the initial velocity insufficient, the bridge motion is damped by the fluid viscosity and the particles slow but do not touch. This is due to the internal pressure of the bridge equalising to that of external (ambient) pressure. Since no pressure difference exists across the liquid bridge, the bridge force $F_{\text{bridge}} = 0$ (cf. Equation (2.77)) and no further particle movement occurs. Critical values for the initial separation and velocity are a function of the parameters for the problem (such as R , m and μ). Two cases occur when the particles are initially moving away, i.e. $\frac{dh_0}{dt} > 0$. Given this initial condition, an escape velocity $\frac{dh}{dt}^*$ exists such that, if $\frac{dh_0}{dt}(0) < \frac{dh}{dt}^*$, the liquid bridge is able to retard the motion and the particles will then come to a stop. If $\frac{dh_0}{dt}(0) \geq \frac{dh}{dt}^*$ the particles continue to move apart.

2.6.6 Example

In Figure 2.15 two examples are shown. The dashed line plot shows two spheres approaching, slowing and colliding. The initial conditions used are $h_0(0) = 0.04 \text{ mm}$ and $\frac{dh_0}{dt}(0) = -2.2 \text{ mm s}^{-1}$. The solid line case shows approaching spheres which do not collide, using the initial conditions of $h_0(0) = 0.04 \text{ mm}$ and $\frac{dh_0}{dt}(0) = -0.2 \text{ mm s}^{-1}$. For both examples, the values of the parameters used are $\mathbf{R} = 1 \text{ mm}$, $r_0 = 0.7 \text{ mm}$, $\mu = 10^{-3} \text{ g mm}^{-1}$, and particle mass $m = 0.1 \text{ g}$.

The equations for the motion of the fluid were obtained using the Navier-Stokes equations with the low Reynolds number approximation. The solution obtained may be applied to granulation systems provided that the assumptions of the model are met. It is acknowledged that the models of Ennis *et al.* [4] and Liu *et al.* [26] are more suited to modelling granulation because they include the effects of particle deformation and rebound. The results of this model have also not been compared with the aforementioned workers.

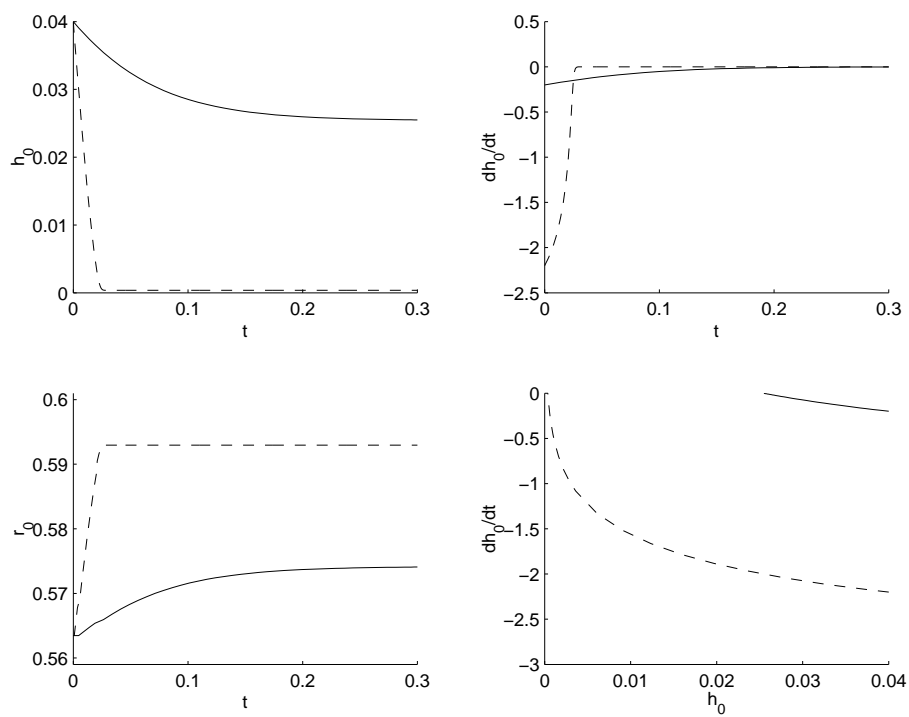


Figure 2.15: Two solutions from Equations (2.77)-(2.80) are plotted for an initial separation of $h_0(0) = 0.04$ mm. The solid line case has initial particle velocity $\frac{dh_0}{dt}(0) = -0.2$ mm s⁻¹ and the dashed line case $\frac{dh_0}{dt}(0) = -2.2$ mm s⁻¹.

Static Liquid Bridges Between Three Particles

3.1 Introduction

In this chapter the configuration of three equally sized (spherical) primary particles held together by a capillary state static liquid bridge is investigated. The particles are equally spaced with sphere centres arranged on the vertices of an equilateral triangle. The arrangement is illustrated in Figure 3.1. For an interface at thermodynamic equilibrium the fluid surface is required to have constant mean curvature H_0 as the Young-Laplace equation must be satisfied. In the absence of gravity this equation is

$$H_0 = \frac{\Delta p}{2\gamma_{lv}} \quad (3.1)$$

where Δp is the pressure jump when passing from external (ambient) pressure towards the centre of the liquid surface and γ_{lv} is the surface tension. The analogous configuration of two particles, discussed in Chapter 2, has rotational symmetry. This allows the second order ordinary differential equation from Equation (1.16) to be derived [31]. This symmetry does not exist in the three particle case and a different approach is needed. There is no prior work on this arrangement in the literature.

To investigate the three particle problem the surface is parameterised using cylindrical coordinates r and θ where the height of the surface is given by $z = z(r, \theta)$. The transformation between cylindrical and Cartesian coordinates (X, Y, Z) is defined by

$$\mathbf{Z}(r, \theta) = (X, Y, Z) = (r, z \cos \theta, z \sin \theta) \quad (3.2)$$

where \mathbf{Z} denotes the surface in Cartesian coordinates. The Jacobian of the transformation

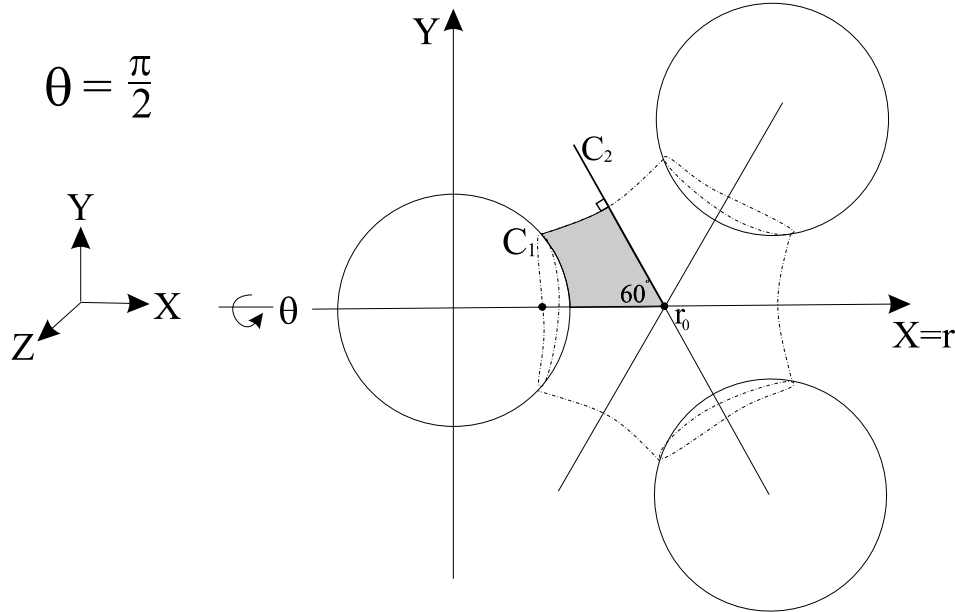


Figure 3.1: Cross-section of a liquid bridge between three particles. The dotted outline shows the boundary of the fluid surface z with constant mean curvature H_0 . Along contour C_1 , the three-phase contact line, the angle between the sphere and the fluid is equal to the fluid contact angle α . The fluid surface is reflected and is continuous and smooth about contour C_2 . The view shown is a cross-section for $\theta = \frac{\pi}{2}$ where the angle between C_2 and the r -axis is 60° . When $\theta = 0^\circ$, perpendicular to the view shown in this figure, the angle between contour C_2 and the r -axis is 90° .

is given by

$$J(r, \theta) = z. \quad (3.3)$$

The problem is arranged using an r -axis aligned from the centre point of one of the primary particles at $r = 0$ to the central point of the liquid bridge at $r = r_0$. Due to symmetry, it is sufficient to solve the problem for only $1/12$ of the complete fluid surface (the shaded region in Figure 3.1). This is because the surface is reflected (vertically) about the Z axis and because it may be divided into the six reflected regions shown in Figure 3.1 which are $\frac{\pi}{2}$ -periodic with respect to θ . The contour C_2 , which is called the symmetry contour, bisects the liquid bridge between adjacent particles. Along C_2 , the fluid surface z and its partial derivatives are required to be continuous. Contour C_1 represents the three-phase contact line.

Figure 3.1 shows a plan view corresponding to $\theta = \frac{\pi}{2}$; in this view the angle ϕ between the r -axis and the symmetry contour is 60° . When $\theta = 0^\circ$, corresponding to an elevation (side-on) view, the angle between the r -axis and contour C_2 is 90° . For intermediate values of θ , the angle between the r -axis and the symmetry contour C_2 varies smoothly between 60° and 90° .

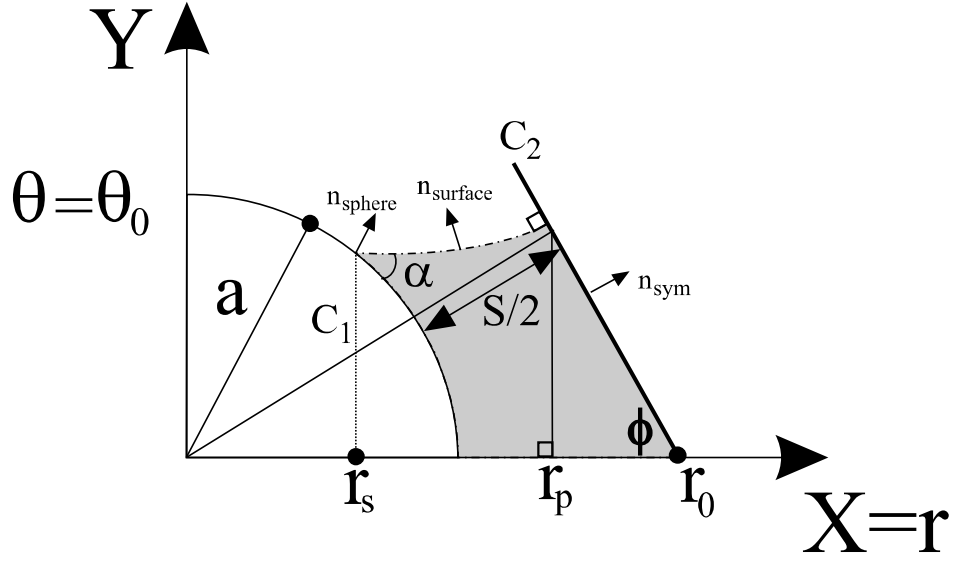


Figure 3.2: Enlarged view of Figure 3.1. The liquid bridge profile is obtained by solving for the shaded region. This figure is for a given $\theta = \theta_0$. r_s is the location of the intersection between the fluid and the sphere of radius a . r_p is the intersection between the fluid and the symmetry plane contour. S is the separation distance between spheres.

Equation (3.1) is enforced by expressing the mean curvature H_0 in terms of z and the partial derivatives of z . This leads to a second-order elliptic partial differential equation which is required to be satisfied at all points on the fluid surface. Similarly, the boundary conditions along C_1 and C_2 are written in terms of z and its partial derivatives. The coupled non-linear system of equations are formidable to solve because of (i) full non-linearity (ii) non-linear boundary conditions and (iii) boundary conditions which are imposed at an unknown location. This chapter explains how to derive this system and how to obtain a solution using a non-linear equation solver.

Figure 3.2 shows an enlarged view of the solution region. For a given $\theta \equiv \theta_0$, the three phase contact line contour C_1 occurs at $r = r_s$ where the fluid intersects the sphere. The fluid surface intersects the symmetry contour C_2 at $r = r_p$. The relationship between r_0 and the inter-particle separation distance S is

$$r_0 = r_p + (r_0 - r_p) = \left(\frac{\sqrt{3}}{2} + \frac{1}{2\sqrt{3}} \right) \left(a + \frac{S}{2} \right) = \frac{2}{\sqrt{3}} \left(a + \frac{S}{2} \right) \quad (3.4)$$

or

$$S = \sqrt{3}r_0 - 2a \quad (3.5)$$

where the sphere has radius a .

3.2 Derivation of the Equations

The equations for the constant mean curvature (CMC) of the fluid surface and the boundary conditions are now derived.

3.2.1 Mean Curvature

In differential geometry, surfaces may be described by two quadratic differential forms known as the first and second fundamental forms [52]. By expressing the surface $z(r, \theta)$ in terms of these functions a differential equation for the mean curvature may be derived.

The first fundamental form, denoted by I, represents the arc-length s on a surface and is given by

$$I = ds^2 = E dr^2 + 2F dr d\theta + G d\theta^2 \quad (3.6)$$

with coefficients in Cartesian coordinates given by

$$E = \mathbf{Z}_r \cdot \mathbf{Z}_r, F = \mathbf{Z}_r \cdot \mathbf{Z}_\theta, G = \mathbf{Z}_\theta \cdot \mathbf{Z}_\theta. \quad (3.7)$$

Standard notation has been used for the partial derivatives, for example $\mathbf{Z}_r = \frac{\partial \mathbf{Z}}{\partial r}$ and $\mathbf{Z}_\theta = \frac{\partial \mathbf{Z}}{\partial \theta}$.

The second fundamental form, denoted by II, is derived from the curvature of the surface and is equal to

$$II = e dr^2 + 2f dr d\theta + g d\theta^2$$

where the coefficients are given by

$$e = \mathbf{Z}_{rr} \cdot \mathbf{Z}_r \times \mathbf{Z}_\theta, f = \mathbf{Z}_{r\theta} \cdot \mathbf{Z}_r \times \mathbf{Z}_\theta \text{ and } g = \mathbf{Z}_{\theta\theta} \cdot \mathbf{Z}_r \times \mathbf{Z}_\theta. \quad (3.8)$$

In terms of the above coefficients the mean curvature H is given by

$$H = \frac{Eg - 2fF + eG}{2(EG - F^2)^{\frac{3}{2}}}. \quad (3.9)$$

To evaluate Equation (3.9), in the cylindrical coordinates of Equation (3.2), the following partial derivatives are required:

$$\begin{aligned}
\mathbf{Z}_r &= \frac{\partial \mathbf{Z}}{\partial r} = (1, z_r \cos \theta, z_r \sin \theta) \\
\mathbf{Z}_\theta &= \frac{\partial \mathbf{Z}}{\partial \theta} = (0, z_\theta \cos \theta - z \sin \theta, z_\theta \sin \theta + z \cos \theta) \\
\mathbf{Z}_{rr} &= \frac{\partial^2 \mathbf{Z}}{\partial r^2} = (0, z_{rr} \cos \theta, z_{rr} \sin \theta) \\
\mathbf{Z}_{r\theta} &= \frac{\partial^2 \mathbf{Z}}{\partial \theta \partial r} = (0, z_{r\theta} \cos \theta - z_r \sin \theta, z_{r\theta} \sin \theta + z_r \cos \theta) \\
\mathbf{Z}_{\theta\theta} &= \frac{\partial^2 \mathbf{Z}}{\partial \theta^2} = (0, z_{\theta\theta} \cos \theta - 2z_\theta \sin \theta - z \cos \theta, z_{\theta\theta} \sin \theta + 2z_\theta \cos \theta - z \sin \theta).
\end{aligned} \tag{3.10}$$

Substituting the above partial derivatives into Equations (3.7) and (3.8) and simplifying gives

$$e = -z - z_{rr}, f = z_r z_\theta - z z_{r\theta}, g = z^2 - z z_{\theta\theta} + 2z_\theta^2 \tag{3.11}$$

and

$$E = 1 + z_r, F = z_r z_\theta, G = z^2 + z_\theta^2. \tag{3.12}$$

Substituting Equations (3.11) and (3.12) into Equation (3.9) gives, after simplification, the following second order non-linear elliptic partial differential equation expression,

$$H = \frac{z^2 - z z_{\theta\theta} + 2z_\theta^2 + z_r^2 z^2 - z z_{\theta\theta} z_r^2 + 2z z_r z_\theta z_{r\theta} - z_{rr} z^3 - z z_{rr} z_\theta^2}{2(z_\theta^2 + z^2(1 + z_r^2))^{\frac{3}{2}}} =: \frac{P}{Q} \tag{3.13}$$

where P and Q denote the numerator and denominator of H . In order for the surface $z(r, \theta)$ to have constant mean curvature H_0 , thus satisfying Equation (3.1), Equation (3.13) must be satisfied at all points on the fluid surface.

3.2.2 Boundary conditions

(i) Fluid contact angle

The contact angle α is a physical property of the fluid which is satisfied along contour C_1 and is equal to

$$\alpha = \text{acos}(n_{\text{surface}} \cdot n_{\text{sphere}}) \tag{3.14}$$

where n_{surface} is the unit outward pointing fluid surface normal and n_{sphere} is the unit normal vector for the sphere as shown in Figure 3.2.

Expressions are now derived for n_{surface} and n_{sphere} to allow Equation (3.14) to be written in terms of z . Using the results from Equation (3.10) the outward pointing unit normal

vector for the surface is given by

$$n_{\text{surface}} = \frac{\mathbf{Z}_r \times \mathbf{Z}_\theta}{|\mathbf{Z}_r \times \mathbf{Z}_\theta|} = \frac{1}{\sqrt{z^2 z_r^2 + z_\theta^2 + z^2}} (z z_r, -z_\theta \sin \theta - z \cos \theta, z_\theta \cos \theta - z \sin \theta). \quad (3.15)$$

The boundary condition for the three-phase contact line occurs at the intersection between the fluid and the sphere. In Cartesian coordinates a sphere of radius a has equation

$$\begin{aligned} \mathbf{Z}_{\text{sphere}}(r, \theta) &= (r, z_{\text{sphere}} \cos \theta, z_{\text{sphere}} \sin \theta) \\ &= \left(r, \sqrt{a^2 - r^2} \cos \theta, \sqrt{a^2 - r^2} \sin \theta \right) \end{aligned} \quad (3.16)$$

where the sphere in the cylindrical coordinates of Equation (3.2) is

$$z_{\text{sphere}}(r, \theta) = \sqrt{a^2 - r^2}. \quad (3.17)$$

From Equation (3.16) the normal vector to the sphere is

$$n_{\text{sphere}} = \frac{1}{a} \left(r, \sqrt{a^2 - r^2} \cos \theta, \sqrt{a^2 - r^2} \sin \theta \right). \quad (3.18)$$

Substituting Equations (3.18) and (3.15) into Equation (3.14) gives an expression for the contact angle α as

$$\begin{aligned} \alpha &= \text{acos} (n_{\text{surface}} \cdot n_{\text{sphere}}) \\ &= \text{acos} \left(\frac{z}{a \sqrt{z^2 z_r^2 + z_\theta^2 + z^2}} \left(r z_r - \sqrt{a^2 - r^2} \right) \right). \end{aligned} \quad (3.19)$$

Equation (3.19) is required to be satisfied along contour C_1 .

(ii) Symmetry Plane

The fluid surface intersects the symmetry plane along contour C_2 . It is necessary for n_{sym} and n_{surface} to be orthogonal along C_2 , as shown in Figure 3.2, as this condition allows the continuity of z along with its partial derivatives. In Cartesian coordinates the unit outward pointing symmetry contour normal is $n_{\text{sym}} = \frac{1}{2}(\sqrt{3}, 1, 0)$. Therefore the angle

between the fluid surface and the symmetry contour is

$$\begin{aligned}\beta &= \text{acos} (n_{\text{surface}} \cdot n_{\text{sym}}) \\ &= \text{acos} \left(\frac{1}{2\sqrt{z^2 z_r^2 + z_\theta^2 + z^2}} z_\theta \sin \theta + z \cos \theta - \sqrt{3} z z_r \right) \equiv 90^\circ.\end{aligned}\quad (3.20)$$

Equations (3.13), (3.19) and (3.20) provide the necessary equations to determine the profile of the liquid bridge surface.

3.3 Numerical Solution

The problem is solved on an $n \times m$ mesh. The discrete approximation to $z(r, \theta)$ is denoted by $\hat{z}_{(i,j)}$ where i and j denote mesh points that correspond to r and θ values. To approximate the derivatives for the mean curvature and the boundary conditions the following second order central difference formulae are applied:

$$\hat{z}_r(i, j) = \frac{\hat{z}_{(i+1,j)} - \hat{z}_{(i-1,j)}}{2\Delta r}, \quad \hat{z}_\theta(i, j) = \frac{\hat{z}_{(i,j+1)} - \hat{z}_{(i,j-1)}}{2\Delta \theta}, \quad (3.21a)$$

$$\hat{z}_{rr}(i, j) = \frac{\hat{z}_{(i+1,j)} - 2\hat{z}_{(i,j)} + \hat{z}_{(i-1,j)}}{\Delta r^2}, \quad \hat{z}_{\theta\theta}(i, j) = \frac{\hat{z}_{(i,j+1)} - 2\hat{z}_{(i,j)} + \hat{z}_{(i,j-1)}}{\Delta \theta^2} \quad (3.21b)$$

$$\hat{z}_{r\theta}(i, j) = \frac{\hat{z}_{(i+1,j+1)} - \hat{z}_{(i+1,j-1)} - \hat{z}_{(i-1,j+1)} + \hat{z}_{(i-1,j-1)}}{4\Delta r\Delta \theta} \quad (3.21c)$$

where Δr and $\Delta \theta$ denote the step sizes of r and θ . The derivatives \hat{z}_{rr} and $\hat{z}_{\theta\theta}$ require 5 point numerical stencils and the derivative $\hat{z}_{r\theta}$ requires a 9 point numerical stencil. Therefore, to enforce the constant mean curvature requirement, from the Young-Laplace equation, mesh points are required on either side of the boundary contours at C_1 and C_2 . (Contour C_1 represents the three-phase contact line and Contour C_2 is the symmetry contour which bisects the liquid bridge between adjacent particles as discussed in Section 3.1.) The solid points in Figure 3.3 represent points where constant mean curvature is imposed and the open circles represent points where the boundary conditions are imposed.

For the j values, since $0 \leq \theta \leq \frac{\pi}{2}$, we set $j = 0 : \frac{\pi}{2m} : \frac{\pi}{2}$. The initial attempt at solving this problem defined the r mesh for $0 \leq r \leq r_0$ using $i = 0 : \frac{r_0}{n} : r_0$. By experiment, however, it was found that the solver would converge only if the value of r_s (the fluid sphere/intersection point) was close to $r = 0$. When r_s was close to a , the solver encountered difficulty attempting to extend the fluid surface to the left of the fluid/sphere boundary because these mesh points are outside the physical domain. To solve this problem, an initial solution was obtained on a rough 5×5 mesh using

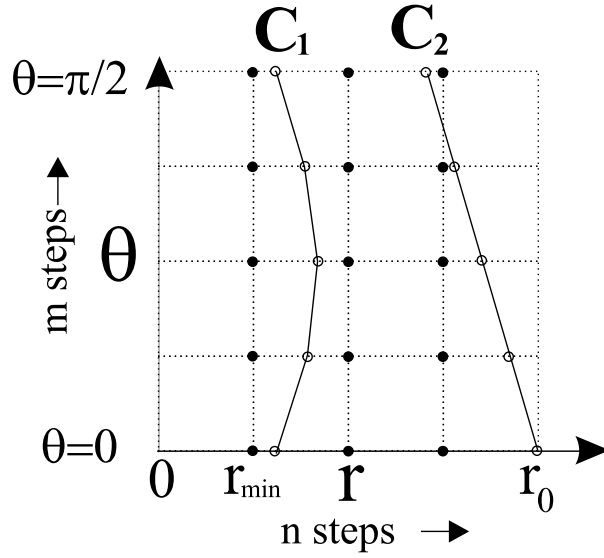


Figure 3.3: Illustration of the numerical solution on the initial 5×5 mesh. In this case the r mesh ranges from 0 to r_0 . The mean curvature requirement is solved on internal points (solid circles) corresponding to $r \neq 0$ and $r \neq r_0$. Boundary conditions are imposed at the open circles. The value r_{\min} defines the starting r value for higher resolution (10×10 and 15×15) meshes. On these meshes the constant mean curvature requirement is solved on mesh points such that $r \neq r_{\min}$ and $r \neq r_0$.

$i = 0 : \frac{r_0}{n} : r_0$. If a solution exists this case would converge since there are only a small number of mesh points to the left of r_s . The solution $\hat{z}_{(i,j)}$ obtained allowed the value of r_s to be estimated using the function \hat{z}_2 (detailed in Section 3.3.2) and the minimum value of r_s on the 5×5 mesh was calculated as r_{\min} . Solutions obtained on higher resolution meshes used r values defined at $i = r_{\min} : \frac{r_{\min}}{n} : r_0$.

The constant mean curvature requirement is solved at mesh points corresponding $r \neq r_{\min}$ and $r \neq r_0$ (or $r \neq 0$ and $r \neq r_0$ on the initial 5×5 mesh) which provides $(n - 2)m$ equations. The boundary conditions each provide m equations. Together these equations uniquely determine the problem as there are mn mesh points. The following section details how the mean curvature and boundary conditions are imposed on the rectangular mesh.

3.3.1 Constant Mean Curvature (CMC)

The constant mean curvature requirement is enforced by solving Equation (3.13) using the approximations for the derivatives of z from Equations (3.21a)-(3.21c). This is given by the condition

$$\hat{P}_{(i,j)} - \hat{Q}_{(i,j)}H_0 = 0 \quad (3.22)$$

where $\hat{P}_{(i,j)}$ and $\hat{Q}_{(i,j)}$ are the numerator and the denominator of Equation (3.13) evaluated at mesh point (i, j) . When derivatives of \hat{z} with respect to θ are evaluated on a $\theta = 0$ or $\theta = \frac{\pi}{2}$ boundary the data is recycled since the surface is $\frac{\pi}{2}$ periodic with respect to θ .

3.3.2 Boundary conditions

(i) Fluid/sphere intersection

To detect contour C_1 the difference in height between the fluid surface \hat{z} and the sphere z_{sphere} is considered using

$$\hat{z}_2 = \hat{z} - z_{\text{sphere}} \quad (3.23)$$

where z_{sphere} is given by Equation (3.17). For each value of $\theta \equiv \theta_0$, corresponding to a particular $j = j_0$, the position where the fluid and sphere intersect at $r = r_s$ needs to be determined. For a given j_0 this point is determined by finding the point $i = i_s$ such that $\hat{z}_2(i_s, j_0) < 0$ and $\hat{z}_2(i_s + 1, j_0) > 0$ as these mesh points are on either side of r_s . To obtain the contact angle at $r = r_s$, Equation (3.19) is used to evaluate $\hat{\alpha}(i_s, j_0)$ and $\hat{\alpha}(i_s + 1, j_0)$ at $\hat{z}(i_s, j_0)$ and $\hat{z}(i_s + 1, j_0)$. The contact angle α^* at $r = r_s$ is obtained using linear interpolation by

$$\alpha_{j_0}^* = t\hat{\alpha}(i_s, j_0) + (1 - t)\hat{\alpha}(i_s + 1, j_0) \quad (3.24)$$

where

$$t = \frac{\hat{z}_2(i_s + 1, j_0)}{\hat{z}_2(i_s + 1, j_0) - \hat{z}_2(i_s, j_0)}. \quad (3.25)$$

(ii) Symmetry plane

For a particular $\theta \equiv \theta_0$ interpolation is also used to determine the angle β at the symmetry contour as $\beta \equiv \frac{\pi}{2}$ when a solution is obtained. The symmetry contour has equation

$$z_{\text{sym}} = \frac{\sqrt{3}(r_0 - r)}{\cos \theta}. \quad (3.26)$$

Therefore to detect the position of C_2 , the function

$$\begin{aligned} \hat{z}_3 &= \hat{z} \cos \theta - z_{\text{sym}} \cos \theta \\ &= \hat{z} \cos \theta - \sqrt{3}(r_0 - r) \end{aligned}$$

is calculated and interpolation is used to obtain β^* as

$$\beta_{j_0}^* = t\hat{\beta}(i_s, j_0) + (1 - t)\hat{\beta}(i_s + 1, j_0) \quad (3.27)$$

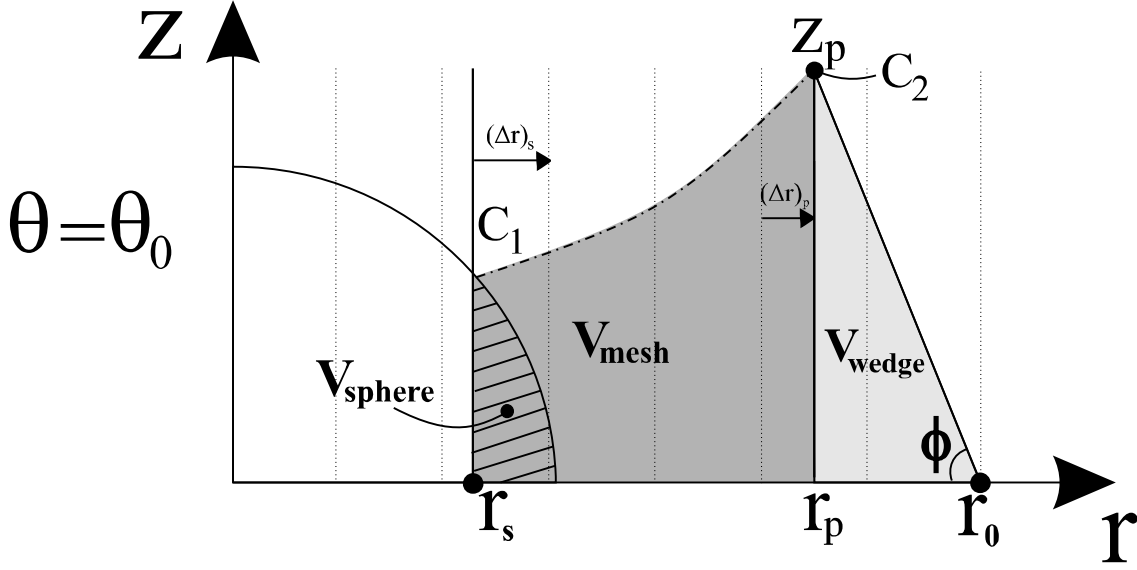


Figure 3.4: Regions V_{sphere} , V_{mesh} and V_{wedge} defined to calculate the bridge volume V . This figure is for a particular $\theta = \theta_0$. The shaded regions are V_{sphere} (striped grey), V_{mesh} (grey) and V_{wedge} (light grey). The angle between the symmetry plane and the r axis is $\phi = \text{atan}\left(\frac{z_p}{r_0 - r_p}\right)$. The dotted vertical lines are representative of the numerical mesh in the r direction.

where $\hat{z}_3(i_p, j_0) < 0$ and $\hat{z}_3(i_{p+1}, j_0) > 0$ and $\hat{\beta}_{(i_p, j_0)}$ and $\beta_{(i_{p+1}, j_0)}$ are solved using Equation (3.20) and

$$t = \frac{\hat{z}_3(i+1, j_0)}{\hat{z}_3(i+1, j_0) - \hat{z}_3(i, j_0)}. \quad (3.28)$$

For the point on the symmetry plane at $r = r_0$ and $\theta = \frac{\pi}{2}$ the one sided difference

$$\hat{z}_{r(n, m)} \approx \frac{3\hat{z}_{(n, m)} - 4\hat{z}_{(n-1, m)} + \hat{z}_{(n-2, m)}}{2\Delta r} \quad (3.29)$$

is used which is $O(\Delta r^2)$ and is consistent with Equations (3.21a)-(3.21c).

3.3.3 Complete System of Equations

To summarise the discussion of Sections 3.3.1 and 3.3.2 the system of equations are:

$$\mathbf{F}(\hat{z}_{(i,j)}) = \begin{bmatrix} \alpha_1^* - \alpha \\ \vdots \\ \alpha_n^* - \alpha \\ \hat{P}_{(2,1)} - \hat{Q}_{(2,1)}H_0 \\ \vdots \\ \hat{P}_{(m-1,n)} - \hat{Q}_{(m-1,n)}H_0 \\ \beta_1^* - \frac{\pi}{2} \\ \vdots \\ \beta_n^* - \frac{\pi}{2} \end{bmatrix} \quad (3.30)$$

where \mathbf{F} is the function involving constant mean curvature and boundary condition terms. Convergence is obtained when

$$|\mathbf{F}(\hat{z}_{(i,j)})| \leq \epsilon$$

for a specified tolerance ϵ . The vector in Equation (3.30) has length nm : the first m rows account for the fluid/sphere intersection, the following $(n-2)m$ rows for the constant mean curvature requirement and the remaining m rows for the symmetry plane boundary.

In Section 3.3.5 it is confirmed numerically that second order convergence is obtained for $\hat{z}_{(i,j)}$.

3.3.4 Liquid Bridge Properties

Given that a solution is obtained, this section discusses the numerical calculation of the liquid bridge volume, surface area and inter-particle binding force.

(i) Volume

Numerical integration is used to calculate the volumes V_{mesh} , V_{sphere} and V_{wedge} . These regions are illustrated in Figure 3.4 for a constant $\theta \equiv \theta_0$ slice. Since these volumes are portions of the solution region from Figure 3.2, the total bridge volume is given by

$$V = 12(V_{\text{mesh}} - V_{\text{sphere}} + V_{\text{wedge}}). \quad (3.31)$$

As integrals, the volumes in Equation (3.31) are given by

$$V_{\text{mesh}} = \int_0^{\frac{\pi}{2}} \int_{r_s}^{r_p} \int_0^z z \, dz \, dr \, d\theta \quad (3.32a)$$

$$V_{\text{wedge}} = \int_0^{\frac{\pi}{2}} \int_{r_p}^{r_0} \int_0^z z_{\text{wedge}} \, dz \, dr \, d\theta \quad (3.32b)$$

$$V_{\text{sphere}} = \int_0^{\frac{\pi}{2}} \int_{r_s}^a \int_0^z z_{\text{sphere}} dz dr d\theta \quad (3.32c)$$

as the Jacobian in cylindrical coordinates is $|J| = z$. The terms z , z_{sphere} and z_{wedge} denote the respective heights of the fluid surface, the sphere and the wedge shaped portion of the bridge.

The height of z_{wedge} is given by

$$z_{\text{wedge}} = \frac{z_p(r_0 - r)}{r_0 - r_p} \quad (3.33)$$

since z_{wedge} is a straight line segment between (r_p, z_p) and $(r_0, 0)$.

To numerically evaluate Equation (3.32a) the function $v = \frac{1}{2}\hat{z}^2$ is introduced. Then

$$\begin{aligned} V_{\text{mesh}} &= \int_0^{\frac{\pi}{2}} \int_{r_s}^{r_p} \int_0^z z dz dr d\theta \\ &= \int_0^{\frac{\pi}{2}} \int_{r_s}^{r_p} \left[\frac{1}{2} z(r, \theta)^2 \right]_0^z dr d\theta \\ &\approx \int_0^{\frac{\pi}{2}} \int_{r_s}^{r_p} v dr d\theta. \end{aligned} \quad (3.34)$$

In the following equation, $v_{(s,\theta)}$ and $v_{(p,\theta)}$ are obtained by interpolation because, in general, r_s and r_p do not occur on the mesh. The step sizes Δr_s and Δr_p refer to the distance between the interpolated point and the following mesh point as shown in Figure 3.4. From Equation (3.34),

$$\begin{aligned} V_{\text{mesh}} &\approx \frac{1}{2} \int_0^{\frac{\pi}{2}} \left[v_{(s,\theta)} \Delta r_s + 2 \sum_{i=s+1}^{p-1} v_{(i,\theta)} \Delta r + v_{(p,\theta)} \Delta r_p \right] d\theta \\ &\approx \frac{\Delta \theta}{2} \times \frac{1}{2} \left[v_{(s,1)} \Delta r_s + 2 \sum_{i=s+1}^{p-1} v_{(i,1)} \Delta r + v_{(p,1)} \Delta r_p \right. \\ &\quad \left. + 2 \sum_{j=2}^{m-1} \left(v_{(s,j)} \Delta r_1 + 2 \sum_{i=s+1}^{p-1} v_{(i,j)} \Delta r + v_{(p,j)} \Delta r_p \right) \right. \\ &\quad \left. + v_{(s,m)} \Delta r_1 + 2 \sum_{i=s+1}^{p-1} v_{(i,m)} \Delta r + v_{(p,m)} \Delta r_p \right]. \end{aligned} \quad (3.35)$$

From Equation (3.32b), the volume of the wedge is

$$\begin{aligned}
 V_{\text{wedge}} &= \int_0^{\frac{\pi}{2}} \int_{r_p}^{r_0} \int_0^z z_{\text{wedge}} dz dr d\theta \\
 &= \int_0^{\frac{\pi}{2}} \int_{r_p}^{r_0} \frac{1}{2} z_{\text{wedge}}^2 dr d\theta \\
 &= \int_0^{\frac{\pi}{2}} \int_{r_p}^{r_0} \frac{1}{2} \left(\frac{z_p(r_0 - r)}{r_0 - r_p} \right)^2 dr d\theta \\
 &= \int_0^{\frac{\pi}{2}} \frac{1}{6} z_p^2 (r_0 - r_p) d\theta
 \end{aligned} \tag{3.36}$$

and that of the sphere, from Equation (3.32c),

$$\begin{aligned}
 V_{\text{sphere}} &= \int_0^{\frac{\pi}{2}} \int_{r_s}^a \int_0^z z_{\text{sphere}} dz dr d\theta \\
 &= \int_0^{\frac{\pi}{2}} \int_{r_s}^a \frac{1}{2} z_{\text{sphere}}^2 dr d\theta \\
 &= \int_0^{\frac{\pi}{2}} \left(\frac{a^3}{3} - \frac{a^2 r_s}{2} + \frac{r_s^3}{6} \right) d\theta.
 \end{aligned} \tag{3.37}$$

Since the values of r_s , r_p and z_p change with respect to θ the trapezium rule is used to numerically integrate the expressions for the above volumes. Combining them allows the volume V from Equation (3.31) to be calculated.

(ii) Surface Area

The surface area of the liquid bridge is given by

$$\begin{aligned}
 S &= 12 \int_0^{\frac{\pi}{2}} \int_{r_s}^{r_p} dS \\
 &= 12 \int_0^{\frac{\pi}{2}} \int_{r_s}^{r_p} |\mathbf{Z}_r \times \mathbf{Z}_\theta| dr d\theta \\
 &= 12 \int_0^{\frac{\pi}{2}} \int_{r_s}^{r_p} \sqrt{z^2(1 + z_r^2) + z_\theta^2} dr d\theta.
 \end{aligned} \tag{3.38}$$

To evaluate Equation (3.38), $u = \sqrt{\hat{z}^2(1 + \hat{z}_r^2) + \hat{z}_\theta^2}$ is introduced. Then

$$S \approx 12 \int_0^{\frac{\pi}{2}} \int_{r_s}^{r_p} u dr d\theta. \tag{3.39}$$

Using the trapezium rule to calculate Equation (3.39) gives

$$\begin{aligned}
S &\approx 12 \times \frac{1}{2} \int_0^{\frac{\pi}{2}} \left[u_{(s,\theta)} \Delta r_1 + 2 \sum_{i=s+1}^{p-1} u_{(i,\theta)} \Delta r + u_{(p,\theta)} \Delta r_p \right] d\theta \\
&\approx 12 \times \frac{\Delta\theta}{2} \times \frac{1}{2} \left[u_{(s,1)} \Delta r_1 + 2 \sum_{i=s+1}^{p-1} u_{(i,1)} \Delta r + u_{(p,1)} \Delta r_p \right. \\
&\quad \left. + 2 \sum_{j=2}^{m-1} \left(u_{(s,j)} \Delta r_1 + 2 \sum_{i=s+1}^{p-1} u_{(i,j)} \Delta r + u_{(p,j)} \Delta r_p \right) \right. \\
&\quad \left. + u_{(s,m)} \Delta r_1 + 2 \sum_{i=s+1}^{p-1} u_{(i,m)} \Delta r + u_{(p,m)} \Delta r_p \right]. \tag{3.40}
\end{aligned}$$

(iii) Inter-particle binding force

The inter-particle force between the particles is resolved at the three phase contact line, similar to the approach of De Bishop and Rigole [31], for the two particle case, to give,

$$\begin{aligned}
F &= 4\gamma_{lv} \int_0^{\frac{\pi}{2}} z(r_s, \theta) \sin(\delta + \alpha) d\theta + \Delta p \int_0^{\frac{\pi}{2}} \int_0^z z dz d\theta \\
&= 4\gamma_{lv} \int_0^{\frac{\pi}{2}} z(r_s, \theta) \sin(\delta + \alpha) d\theta + \Delta p \int_0^{\frac{\pi}{2}} \frac{z^2}{2} d\theta \\
&= \gamma_{lv} \int_0^{\frac{\pi}{2}} \left(4 z(r_s, \theta) \sin(\delta + \alpha) + H_0 z^2 \right) d\theta. \tag{3.41}
\end{aligned}$$

In Equation (3.41), the first term is the surface tension force resolved in the r -axis direction and the factor of 4 occurs because $0 \leq \theta \leq \frac{\pi}{2}$. The second term is the force due to the capillary pressure. The half-filling angle between the r -axis and the point of contact between the fluid and the sphere is $\delta = \arccos\left(\frac{r_s}{a}\right)$.

3.3.5 Solving the System using Matlab

The non-linear system of equations given in Equation (3.30) were solved using the Matlab `fsolve` command. The model parameters α , a , r_0 and $H_0 = \frac{\Delta p}{2\gamma_{lv}}$ define a particular liquid bridge. If a solution exists, for specified parameter values, the steps below were followed to produce a solution:

1. A 5×5 mesh is formed as detailed in Section 3.2.2 where the meshes start at $r = 0$ and $\theta = 0$.
2. The solver is provided an initial guess of a cylinder where $\hat{z}_{(i,j)} \equiv \text{constant}$.

3. The function \mathbf{F} from Equation (3.30) and $\hat{z}_{(i,j)}$ is supplied to `fsolve` which attempts to find a solution such that

$$|\mathbf{F}(\hat{z}_{(i,j)})| \leq \epsilon \quad (3.42)$$

where $\epsilon = 1 \times 10^{-15}$. The value of r_{\min} is determined by finding the smallest r value for the fluid/sphere intersection with respect to θ .

4. The original $\hat{z}_{(i,j)}$ solution is interpolated onto a 10×10 mesh. Subsequent $\hat{z}_{(i,j)}$ solutions are attempted on 10×10 and 15×15 meshes where the r mesh starts at r_{\min} at the θ mesh at 0.
5. If a solution $\hat{z}_{(i,j)}$ is obtained on the 15×15 mesh then the properties detailed in Section 3.3.4 are calculated.

The algorithm used by `fsolve` to solve Equation (3.42) was the default option which was ‘Trust-Region Dogleg’.

(i) Convergence and Solution Checks

The following checks were made to confirm that a valid solution was obtained:

1. Second order convergence was confirmed for the solution $\hat{z}_{(i,j)}$ as the mesh step-size was reduced. This behaviour is expected because second order expressions have been used for the \hat{z} derivatives.
2. The methods used in this work were tested by solving the two particle liquid bridge problem. This was achieved by modifying the boundary condition at C_2 from a symmetry contour to a second sphere of radius a . Figure 3.5 illustrates the arrangement. The full expression for the constant mean curvature was used from Equation (3.9). r_{\min} was calculated in a similar fashion to the method described in Section 3.3.

For the two particle case, the following expressions replace those of Equations (3.31), (3.38) and (3.41) for the volume and surface area:

$$V = 4(V_{\text{mesh}} - 2V_{\text{sphere}}), \quad (3.43)$$

where

$$V_{\text{mesh}} = \int_0^{\frac{\pi}{2}} \int_{r_{s_1}}^{r_{s_2}} \int_0^z z \, dz \, dr \, d\theta \quad (3.44a)$$

$$V_{\text{sphere}} = \int_0^{\frac{\pi}{2}} \int_{r_{s_1}}^a \int_0^z z_{\text{sphere}} \, dz \, dr \, d\theta \quad (3.44b)$$

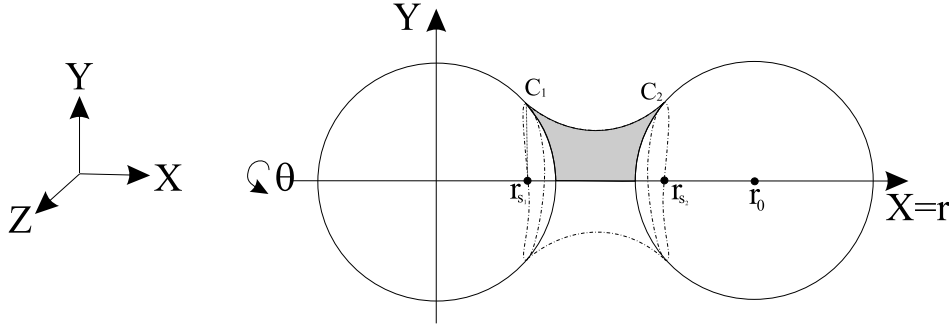


Figure 3.5: Testing the solver using the known solution to the Young-Laplace equation. Boundary conditions occur along the contours C_1 and C_2 where the contact angle is α .

and the surface area is given by

$$\begin{aligned}
 S &= 4 \int_0^{\frac{\pi}{2}} \int_{r_{s_1}}^{r_{s_2}} dS \\
 &= 4 \int_0^{\frac{\pi}{2}} \int_{r_{s_1}}^{r_{s_2}} |\mathbf{Z}_r \times \mathbf{Z}_\theta| dr d\theta \\
 &= 4 \int_0^{\frac{\pi}{2}} \int_{r_{s_1}}^{r_{s_2}} \sqrt{z^2(1 + z_r^2) + z_\theta^2} dr d\theta.
 \end{aligned} \tag{3.45}$$

The expression for the inter-particle binding force is the same as Equation (3.41). Analogous to the approach taken in Section 3.3.4, the integrals from Equation (3.45), (3.44a) and (3.44b) are evaluated using the trapezium rule. Agreement was obtained between `fsolve` and the solution of `ode45` from Chapter 2.

- Equation (3.13) and the subroutines used to calculate the mean curvature of a surface $\hat{z}_{(i,j)}(r, \theta)$ were verified by using a sphere as a test case. Analytically it may be shown that a sphere of radius a has constant mean curvature $H_0 = \frac{1}{a}$. The sphere was centred at $(X, Y, Z) = (0, 0, 1)$ and had equation

$$z_{\text{sphere}}(r, \theta) = \sin \theta \pm \sqrt{a^2 - r^2 - \cos^2 \theta}. \tag{3.46}$$

(The sphere was displaced from the origin because a sphere at the origin has all partial derivatives of z with respect to θ equal to zero. This is a trivial case for Equation (3.13)). Agreement was obtained.

- The surfaces obtained from the solver were independently checked for constant mean curvature. This was achieved by using the file `mcurvature` which was written by Ahmed Elnaggar and downloaded from the Matlab Central File exchange (www.mathworks.com/matlabcentral/fileexchange). Agreement was obtained with

the code used in this work.

5. Checks regarding the scaling were made. By scaling the inter-particle separation distance as $\hat{S} = \rho S$, particle radii as $\hat{R} = \rho R$, and the mean curvature as $\hat{H}_0 = \frac{H_0}{\alpha}$, it was found that $\hat{A} = \rho^2 A$ and $\hat{V} = \rho^3 V$. This indicates that the formulations for the surface area and volume from Equations (3.31) and (3.38) are scaling correctly.

3.4 Results

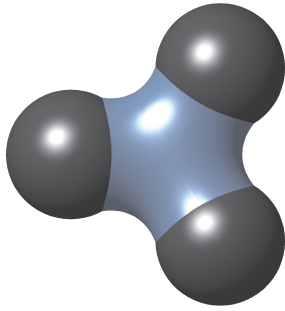
Figure 3.6 shows solutions of static liquid bridges between three particles. The parameters used and liquid bridge properties obtained for each of the examples are listed in the captions of the figures. The surface tension used to calculate the force F was $\gamma_{lv} = 63.1 \text{ mNm}^{-1}$. Due to individual solutions being time consuming, a full parameter space solution was unable to be obtained for the three particle problem. However, the inter-particle binding force F is observed to increase when the separation distance decreases. Figure 3.6(e) shows that the force is strongest for $s \approx 0$. This prediction agrees with the parameter space solutions obtained in Chapter 2 for static liquid bridges between two particles.

Experimentally, for fixed a , s (or r_0) and α , it was found that the free parameter corresponding to liquid bridges with different volumes V is H_0 .

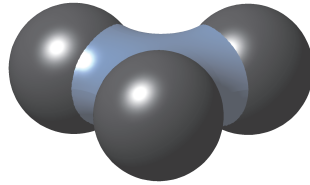
3.4.1 Agreement with Experiment

The modelling work presented in this chapter is supported by experimental work performed by Damiano Rossetti and Stefaan Simons of the Department of Chemical Engineering, University College, London (UCL). Figure 3.7(a) shows three glass ballotini particles, ‘A’, ‘B’, and ‘C’, of radii $R_A = 35.4 \mu\text{m}$, $R_B = 40.8 \mu\text{m}$ and $R_C = 40.8 \mu\text{m}$ with a glycerol droplet attached to particle B. The fluid has a surface tension of $\gamma_{lv} = 63.1 \text{ mNm}^{-1}$ and a contact angle of 50° (measured geometrically using Figure 3.7(a)). The volume of the droplet was calculated to be $V = 65,596 \mu\text{m}^3$. Figure 3.7(b) shows the formation of a liquid bridge after the primary particles were then moved closer. The volume of the bridge volume is equal to that of the droplet.

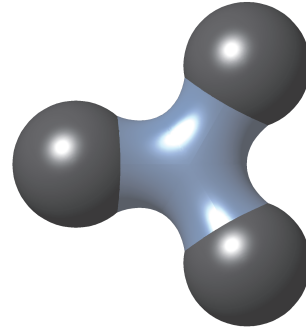
The outline of the primary particles from Figure 3.7(b) is plotted along with X – Y coordinates in Figure 3.8(a). Particle C is located at the origin, particle A at $(47.38, 64.61) \mu\text{m}$ and particle B at $(86.15, -10.16) \mu\text{m}$. The central point ‘O’ is $48.40 \mu\text{m}$ from the centre of the primary particles and is located at $(45.59, 16.25) \mu\text{m}$. Measured from the



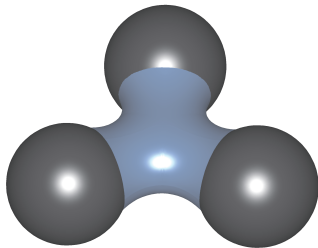
(a) $a = 39 \mu m$, $r_0 = 60 \mu m$,
 $s \approx 26 \mu m$, $\alpha = 20^\circ$, $H_0 =$
 0.004 , $V = 184,161 \mu m^3$,
 $A = 15,491 \mu m^2$, $F =$
 $12.84 \mu N$.



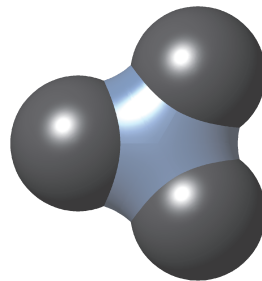
(b) Figure (a) rotated.



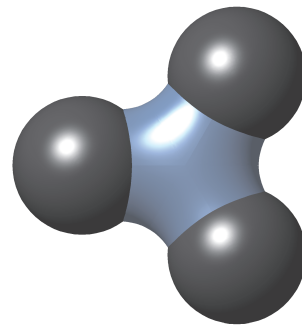
(c) $a = 39 \mu m$, $r_0 = 70 \mu m$,
 $s \approx 43 \mu m$, $\alpha = 20^\circ$, $H_0 =$
 0.0078 , $V = 178,172 \mu m^3$,
 $A = 16,638 \mu m^2$, $F =$
 $11.15 \mu N$.



(d) Figure (c) rotated.



(e) $a = 39 \mu m$, $r_0 =$
 $46 \mu m$, $s \approx 0 \mu m$, $\alpha =$
 40° , $H_0 = 0.072$, $V \approx$
 $80,000 \mu m^3$, $F = 13.80 \mu N$,
 $(\gamma_{lv} = 63.1 mNm^{-1})$.



(f) $a = 39 \mu m$, $r_0 = 58 \mu m$,
 $s \approx 24 \mu m$, $\alpha = 40^\circ$, $H_0 =$
 0.0071 , $V \approx 150,000 \mu m^3$,
 $F = 12.21 \mu N$, $(\gamma_{lv} =$
 $63.1 mNm^{-1})$.

Figure 3.6: Images of liquid bridges between three particles for a range of different parameters.

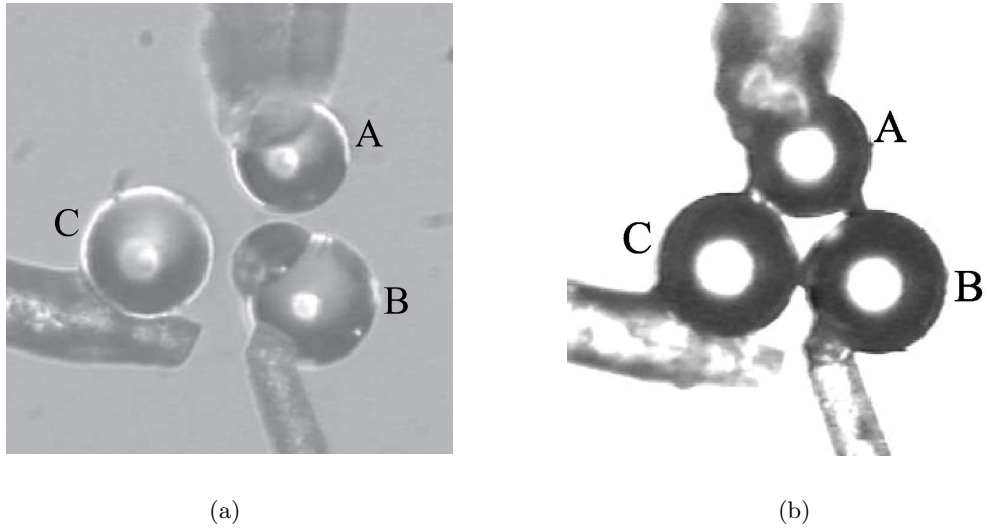
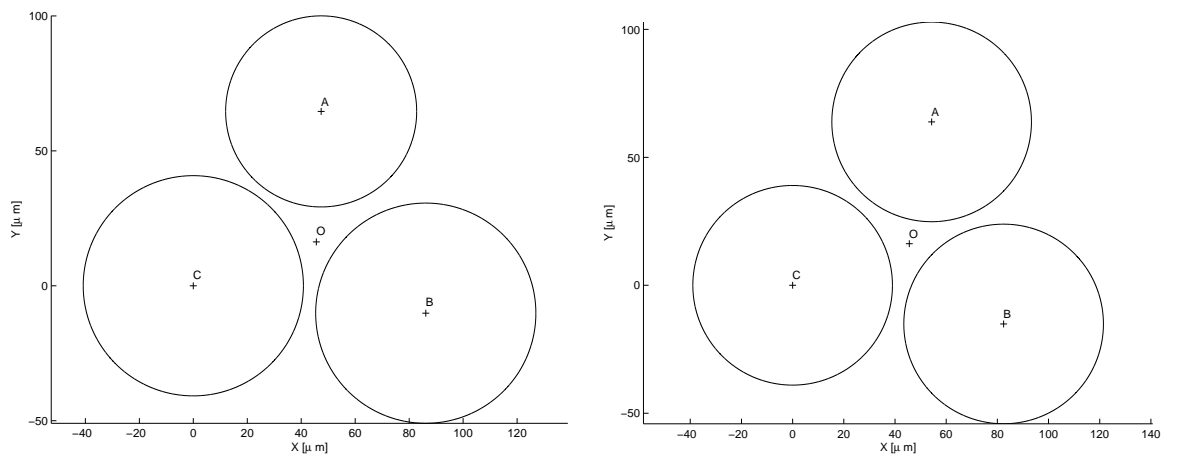


Figure 3.7: Images from the experiment to verify the model. Glass ballotini are used for the primary particles. Figure (a) shows a glycerol droplet placed onto primary particle B. In figure (b) the particles are moved closer together to form a liquid bridge.



(a) The location/size of primary particles from Figure 3.7(b) with $X - Y$ coordinates attached.

(b) The configuration used to obtain a solution from the model. This is based on figure (a), but has spheres of equal size ($a = \bar{R} = 39\mu m$) and $\angle AOB = \angle COB = \angle COA = 120^\circ$.

Figure 3.8: Figure (a) shows the outline of the primary particles from the experiment. Figure (b) shows the problem that was solved using the model. The liquid bridge is not shown in this figure.

point O, the angles between the particles are $\angle AOB = 120.94^\circ$, $\angle COB = 127.32^\circ$ and $\angle COA = 111.74^\circ$.

The profile of the fluid obtained by experiment is now compared with that predicted by the model. The experimental arrangement approximates the symmetry of the model. However, since the symmetry is not exact, the size and location of the primary particles are modified slightly to obtain the appropriate parameters for the model. The average radius of the particles is $\bar{R} = \frac{R_A + R_B + R_C}{3} = 39\mu m$ and this is taken for the primary particle radius a . The position of the spheres was adjusted to obtain $\angle AOB = \angle COB = \angle COA = 120^\circ$ while the coordinates of the points C and O and the distance $r_0 = 48.40\mu m$ were fixed. Following the adjustment particle A is located at $(54.32, 63.85)\mu m$ and particle B at $(82.45, -15.11)\mu m$. Figure 3.8(b) shows the outline primary particles after the adjustment.

Figure 3.9 compares the experimental result with the result from the model. The solution was generated using the parameters $H_0 = 0.0072$ (4 d.p.), $r_0 = 48.40\mu m$, $\alpha = 50^\circ$ and $a = 39\mu m$. The liquid bridge surface area and volume were calculated to be $A = 6,172\mu m^2$ and $V = 65,596\mu m^3$. The shape of the liquid bridge appears similar between model and experiment. The inter-particle binding force is predicted by the model, using Equation (3.41), to be $F = 11.92\mu N$. This is stronger than that found experimentally for two similar sized silanised glass ballotini particles which ranges between 1 and $8\mu N$ depending on the separation distance [53]. It is believed that the additional strength is due to the greater perimeter of contact at the interface boundary. However, measurements of the inter-particle binding force were not taken experimentally, and it is noted that measurements these will need to be obtained, as the result of future work, to further validate the predictions of the model.

Extension to larger arrangements

The model provided in this chapter can be extended to static liquid bridges between four particles by introducing an additional symmetry contour C_3 . The treatment of this contour would be similar to that used for C_2 . Figure 3.1 shows that contour C_2 makes an angle of 60° between the X and Y axis and contour C_3 would make an angle of 60° between the X and Z axis. Symmetry of the four particle case could also be used to obtain results for five particle agglomerates where the fifth particle is the mirror image of the fourth particle about the $X - Y$ axis.

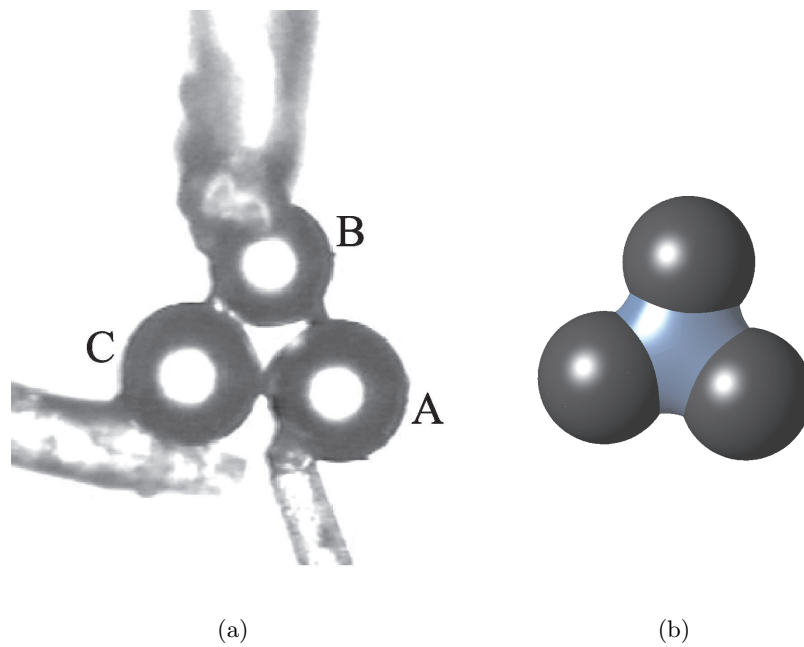


Figure 3.9: The experimental arrangement (a) and the result from the model (b). The volume of the liquid bridge is $V = 65,596 \mu\text{m}^3$.

Modelling the Agglomeration Process

4.1 Introduction

Despite the success of the direct solution to liquid bridges between three particles in the previous chapter, a full solution to agglomerates containing an arbitrary number of liquid bridges, by solving the Young-Laplace equation, is prohibitively expensive [32]. This chapter proposes and develops a novel, simplified geometric model for the placement of particles and liquid bridges in moderately large agglomerates. The liquid bridges do not have constant mean curvature. Instead, an approximate surface is used for the fluid surface. The model enables crucial agglomerate properties, such as their surface area, wetness and volume, to be estimated. The results of this work are presented in Section 4.9 and they allow the agglomerate size and the volume of binder fluid to be related, for a particular inter-particle separation distance, to the particle stickiness (or surface wetness). The results are used later in the population balance model of Chapter 5 to estimate the rates of particle coalescence.

The model represents agglomerates as a collection of equally-sized spherical primary particles of radius R and an approximate binder surface which is formed from a union of fluid segments. Each of the fluid segments are individually convex and are based on a tetrahedron. The fluid is assumed to be in the capillary saturation state and thus uniformly fill the agglomerate voids. The model adds primary particles to an existing agglomerate one at a time to simulate the layering mechanism discussed in Section 1.2.2. The primary particles are bound together using tetrahedra which are added concurrently with additional particles. The edges of the tetrahedra represent liquid bridges. The starting arrangement is the four particle agglomerate which is illustrated schematically in Figure 4.1(a).

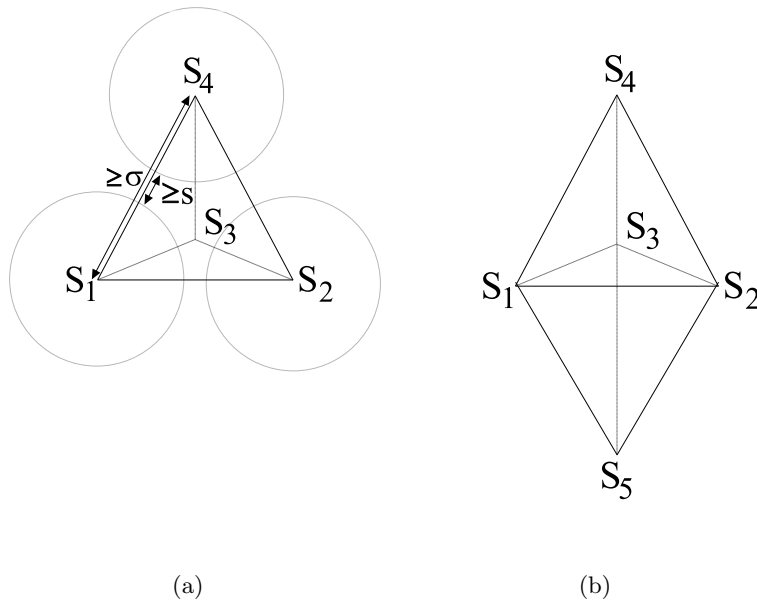


Figure 4.1: The tetrahedron on the left defines placement of the spheres for primary particles 1-4. When a fifth particle is added the arrangement is given by the two tetrahedra as shown on the right. The primary particles at the points S_1 , S_2 and S_4 are illustrated as circles in Figure 4.1(a).

The model has two parameters. The first is the minimum separation distance between the sphere centres σ . This parameter represents the consolidation state of the particle and it is defined by $\sigma = 2R + s$ where s is the minimum separation distance between the closest points on the spheres as shown in Figure 4.1(a). The edges of the tetrahedra are required to have a minimum length of σ . Therefore $|S_i - S_j| \geq \sigma$ for all $i \neq j$. The inequality occurs because it is not possible to continually pack particles in \mathbb{R}^3 such that neighbouring spheres are either touching or are separated by a fixed distance s [54]. When adding a particle, the total bond length of the tetrahedra edges is minimised to minimise the overall surface area of the liquid bridges. The second parameter relates to the saturation state of the fluid and it is denoted by δ . In Section 4.4 we explain how the tetrahedra are ‘expanded’ to allow a variable volume of binder to exist in the particle. The position of the spheres are independent of δ .

The placement of the particles and liquid bridges are defined in Matlab using a series of matrices which are updated as particles are added. The coordinates of the primary particles are stored in a matrix S as row vectors and indices of the tetrahedra vertices are stored in a matrix T . Since the tetrahedra are based on the position of the primary particles, each row entry t in T , defining a particular tetrahedron, references coordinates in S . Additional tetrahedra bond to the faces of existing tetrahedra. Therefore a face matrix F is maintained where each row f defines a face and indices are used to reference

the vertices in S . The calculations for adding particles use the faces and therefore, for each face $f \in F$, relevant information is stored including the unit outward pointing normal vector \vec{n} , an estimate point \vec{e} (used if the face is subsequently selected to bond to a new particle) and a flag as to whether the face is internal (1) or external (0). Faces become internal if they bond to a particle. The estimate point for a face f is the point a distance σ from the geometric mid-point of the face in the direction of \vec{n} .

An edge matrix E is also maintained. However this matrix is used for drawing the agglomerate only and is not involved in the calculations for adding particles.

Example

The matrices for the four particle agglomerate shown in Figure 4.1(a) are defined as

$$S = \sigma \begin{bmatrix} 0 & 0 & \frac{1}{2}\sqrt{\frac{3}{2}} \\ \frac{1}{\sqrt{3}} & 0 & -\frac{1}{2\sqrt{6}} \\ -\frac{1}{2\sqrt{3}} & \frac{1}{2} & -\frac{1}{2\sqrt{6}} \\ -\frac{1}{2\sqrt{3}} & -\frac{1}{2} & -\frac{1}{2\sqrt{6}} \end{bmatrix},$$

$$T = \begin{bmatrix} 1 & 2 & 3 & 4 \end{bmatrix}, \quad F = \begin{bmatrix} 1 & 2 & 3 & \vec{n}_1 & \vec{e}_1 & 1 \\ 1 & 3 & 4 & \vec{n}_2 & \vec{e}_2 & 1 \\ 1 & 2 & 4 & \vec{n}_3 & \vec{e}_3 & 1 \\ 2 & 3 & 4 & \vec{n}_4 & \vec{e}_4 & 1 \end{bmatrix}, \quad E = \begin{bmatrix} 1 & 2 \\ 1 & 3 \\ 1 & 4 \\ 2 & 3 \\ 2 & 4 \\ 3 & 4 \end{bmatrix}.$$

The final column of F indicates that all the faces are external for the initial arrangement.

The steps detailed in Section 4.2 are followed when adding a particle. The results for adding a fifth particle are stated here to illustrate how the matrices are updated. The new particle bonds to face [1 2 3]. By solving an optimisation problem the coordinates of the new particle are $S_5 = \left(\frac{5\sigma}{6\sqrt{3}}, \frac{5\sigma}{6}, \frac{5\sigma}{6\sqrt{6}}\right)$. A single tetrahedron is formed which has vertices [1 2 3 5]. (More complex situations require multiple tetrahedra.) The faces formed due to this tetrahedron are [5 1 2], [5 1 3] and [5 2 3]. The face [1 2 3] is the bonding face so its flag is changed from external to internal. These steps update the matrices to the following:

$$S = \sigma \begin{bmatrix} 0 & 0 & \frac{1}{2}\sqrt{\frac{3}{2}} \\ \frac{1}{\sqrt{3}} & 0 & -\frac{1}{2\sqrt{6}} \\ -\frac{1}{2\sqrt{3}} & \frac{1}{2} & -\frac{1}{2\sqrt{6}} \\ -\frac{1}{2\sqrt{3}} & -\frac{1}{2} & -\frac{1}{2\sqrt{6}} \\ \frac{5}{6\sqrt{3}} & \frac{5}{6} & \frac{5}{6\sqrt{6}} \end{bmatrix},$$

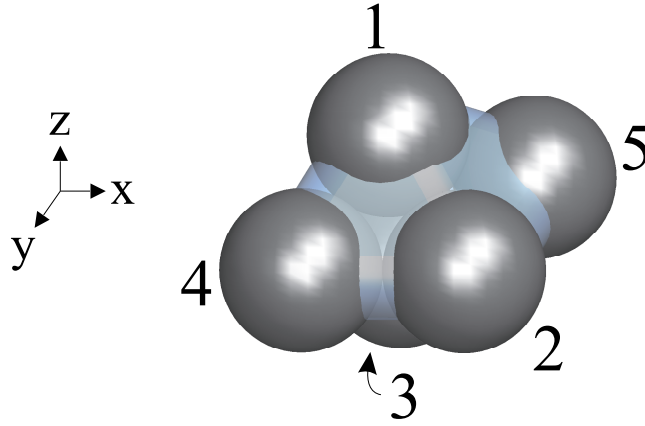


Figure 4.2: A five particle agglomerate formed by the model for $s = 0$ and $\delta = 0.6$.

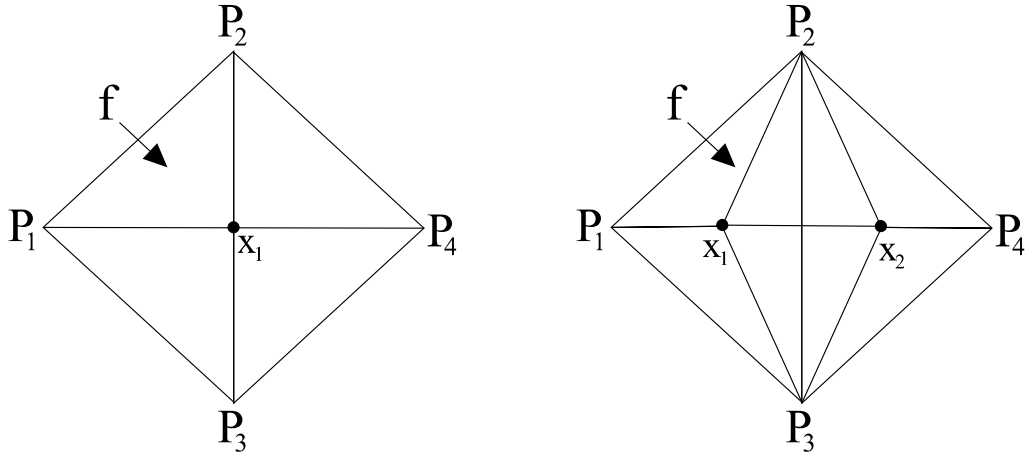
$$T = \begin{bmatrix} 1 & 2 & 3 & 4 \\ 1 & 2 & 3 & 5 \end{bmatrix}, \quad F = \begin{bmatrix} 1 & 2 & 3 & \vec{n}_1 & \vec{e}_1 & 0 \\ 1 & 3 & 4 & \vec{n}_2 & \vec{e}_2 & 1 \\ 1 & 2 & 4 & \vec{n}_3 & \vec{e}_3 & 1 \\ 2 & 3 & 4 & \vec{n}_4 & \vec{e}_4 & 1 \\ 5 & 1 & 2 & \vec{n}_5 & \vec{e}_5 & 1 \\ 5 & 1 & 3 & \vec{n}_6 & \vec{e}_6 & 1 \\ 5 & 2 & 3 & \vec{n}_7 & \vec{e}_7 & 1 \end{bmatrix}, \quad E = \begin{bmatrix} 1 & 2 \\ 1 & 3 \\ 1 & 4 \\ 3 & 4 \\ 2 & 3 \\ 2 & 4 \\ 1 & 5 \\ 2 & 5 \\ 3 & 5 \end{bmatrix}.$$

The five particle agglomerate is illustrated in Figure 4.2 for $\sigma = 2R$ ($s = 0$). The fluid surface, discussed in Section 4.4, is also shown in this figure for a saturation state of $\delta = 0.6$.

4.2 Adding Particles

Agglomerates are modelled on the approximately spherical particles formed in high-shear systems. The matrices S , T , F and E are maintained in order because additional objects are appended to them. Therefore spherical agglomerates are formed by requiring the incoming particle to bond with the first external face in F .

The set of faces that a particle bonds with are called the *contact faces*. These are determined by performing tests between the initial contact face f and its neighbours. The test consists of two scenarios which compares the shapes of the proposed tetrahedra. A quantity called the *skewness number* (defined below) is introduced to measure how much



(a) Determining the point to place particle x_1 in the one particle case.

(b) Determining the point to place particles x_1 and x_2 in the two particle case.

Figure 4.3: Adding a single particle (a), or two particles (b) between face f , with vertices P_1, P_2, P_3 , and a neighbouring face m with vertices P_2, P_3, P_4 .

a proposed tetrahedron deviates from a regular (or ideal) tetrahedron of the same volume. The skewness number of a regular tetrahedron is zero. The test resulting in the lowest average skewness number is considered to be more optimal. Although the tests do not formally minimise the surface free energy this criteria does prevent ‘skewed’ tetrahedra from being formed which were found to have a higher overall surface area in test cases.

The skewness number compares the volume of a tetrahedron t_i , as given by

$$V = \frac{1}{6} |\vec{a} \cdot \vec{b} \times \vec{c}| \quad (4.1)$$

where \vec{a} , \vec{b} , \vec{c} are vectors from one vertex of the tetrahedron to the other vertices, to that of a regular (ideal) tetrahedron containing the same volume V . The edge length of a regular tetrahedron with volume V is

$$L_{\text{ideal}} = \left(\frac{12}{\sqrt{2}} V \right)^{\frac{1}{3}}. \quad (4.2)$$

The non-dimensional skewness number κ measures the deviation in length of the six edges from L_{ideal} as given by

$$\kappa = \frac{\sum_{i=1}^6 |L_i - L_{\text{ideal}}|}{L_{\text{ideal}}}. \quad (4.3)$$

The model permits only one particle to be added at a time. The test therefore considers whether it is more optimal to add one particle between f and its neighbour or two. If it is more optimal to add two then the neighbour cannot be a contact face. Conversely, if it

is more optimal to add one then the neighbour becomes a contact face. All contact faces test their neighbours pairwise, excluding the parent, using the skewness criteria. This may result in additional contact faces. Both tests are now defined in more detail.

The first scenario places one particle between the face f with vertices $[P_1 P_2 P_3]$ and a neighbouring face with vertices $[P_2 P_3 P_4]$ as shown in Figure 4.3(a). Two tetrahedra are required with vertices at $t_1 = [x_1 P_1 P_2 P_3]$ and $t_2 = [x_1 P_2 P_3 P_4]$. (Note: The P vertices exist in S . They are used here as a generic reference to vertices on the tetrahedra.) The placement of the new particle at x_1 is determined by minimising the total bond length shown in Figure 4.3(a) which is

$$\Xi_1 = \sum_{i=1}^4 |x_1 - P_i| \quad (4.4)$$

with constraints on the bond length

$$|x_1 - P_j| \geq \sigma \quad (4.5)$$

for $j = 1, 2, 3, 4$. The above problem was solved using the `fmincon` command of the Matlab optimisation toolbox where the objective function was given by Equation (4.4) and the non-linear inequality constraints were given by Equation (4.5). The starting x_1 value provided was \vec{e} from face f . The volume of t_1 and t_2 are calculated using Equation (4.1) as V_1 and V_2 . (The vectors \vec{a} , \vec{b} and \vec{c} for f may be given as $\vec{a} = P_2 - P_1$, $\vec{b} = P_3 - P_1$ and $\vec{c} = x_1 - P_1$ and as $\vec{a} = P_2 - P_4$, $\vec{b} = P_3 - P_4$ and $\vec{c} = x_1 - P_4$ for the neighbour.) Corresponding to V_1 and V_2 the skewness numbers κ_1 and κ_2 are calculated using Equation (4.3) and their average is taken as $\hat{\kappa}_1$.

The second scenario positions two particles between f and the neighbour as shown in Figure 4.3(b). The three tetrahedra required have their vertices located at $t_1 = [x_1 P_1 P_2 P_3]$, $t_2 = [x_1 P_2 P_3 x_2]$ and $t_3 = [x_2 P_2 P_3 P_4]$. The placement of the particles at x_1 and x_2 is determined by minimising the total bond length shown in Figure 4.3(b) which is

$$\Xi_2 = \sum_{i=1}^3 |x_1 - P_i| + \sum_{j=2}^4 |x_2 - P_j| + |x_1 - x_2| \quad (4.6)$$

with constraints on the bond length given by

$$|x_1 - P_j| \geq \sigma, |x_2 - P_j| \geq \sigma \text{ and } |x_1 - x_2| \geq \sigma. \quad (4.7)$$

The starting value for x_1 used \vec{e} from f and the starting value for x_2 used \vec{e} from the neighbouring face. The skewness of the three tetrahedra is calculated and their average

is taken as $\hat{\kappa}_2$.

If $\hat{\kappa}_1 < \hat{\kappa}_2$ then the neighbour becomes a contact face. After determining the set of contact faces the placement of the particle is obtained by minimising the objective function

$$\Xi_3 = \sum_{i=1}^3 |x_1 - P_i| + \sum_{j=1}^{n_F-1} |x_1 - P_{k(j)}| \quad (4.8)$$

where n_F denotes the number of contact faces and the function $k(j)$ returns the index of the vertex on contact face j which is not common to the vertices on the existing contact faces. The constraints on the bond lengths are

$$|x_1 - P_i| \geq \sigma \text{ and } |x_1 - P_{k(j)}| \geq \sigma \quad (4.9)$$

where $i = 1, 2, 3$ and $j = 1, 2, \dots, n_F - 1$. The starting value for x_1 used \vec{e} from face f . Equation (4.8) and Equation (4.9) minimise the total bond length such that the particle bonds with all contact faces.

After the placement of the particle is calculated the contact faces have their flags changed from external to internal, the new tetrahedra and faces are added to T and F and the position of the sphere to be added is appended to S .

4.3 Examples of Particle Placement

Figure 4.4 illustrates the algorithm discussed in the previous section when adding a primary particle to a five particle agglomerate. The original primary particles are labelled ‘1’-‘5’ in Figures 4.4(a)-(c) and the initial contact face is $f = [1\ 3\ 4]$. Figures 4.4(a) and 4.4(b) consider a contact face comparison between f and a neighbouring face $[1\ 2\ 4]$. The sphere labelled ‘A’ in Figure 4.4(a) is the position, as determined by optimisation, when adding one particle between the faces. In Figure 4.4(b) spheres ‘B’ and ‘C’ are the optimal placement when adding two spheres between the faces. For the one particle case the tetrahedra required are $[1\ 3\ 4\ A]$ and $[1\ 2\ 4\ A]$. By calculation these tetrahedra have an average skewness of $\hat{\kappa}_1 = 1.83$ (to 2 d.p.). For the two particle case three tetrahedra are required: $[1\ 3\ 4\ B]$, $[1\ 4\ B\ C]$ and $[1\ 4\ C\ 2]$. By calculation the average skewness of these tetrahedra is $\hat{\kappa}_2 = 0.36$. Since $\hat{\kappa}_2 < \hat{\kappa}_1$ it is more optimal for two particles to be added between the faces; hence face $[1\ 2\ 4]$ is not a contact face. Similarly the other neighbours to the face $[1\ 3\ 4]$, which are $[2\ 3\ 4]$ and $[5\ 1\ 3]$, also yield $\hat{\kappa}_2 < \hat{\kappa}_1$. Hence the only contact face is f . Figure 4.4(d) shows the actual placement for the sixth particle by solving Equation (4.8). Hence one new entry is added to T ($[1\ 3\ 4\ 6]$) and the face and

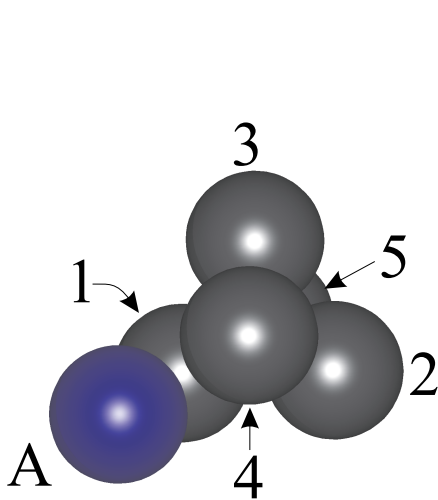
edge entries in F and E are updated accordingly.

The first time more than one tetrahedra is required, when adding a particle, is when an eight particle agglomerate is formed. For this case the initial contact face is $f = [1\ 5\ 2]$. The neighbouring faces to f are $[1\ 3\ 5]$, $[5\ 2\ 3]$ and $[7\ 1\ 2]$. Faces $[1\ 3\ 5]$ and $[5\ 2\ 3]$ return $\hat{\kappa}_2 < \hat{\kappa}_1$ but the comparison between $[7\ 1\ 2]$ and f gives $\hat{\kappa}_2 > \hat{\kappa}_1$. (The results of these tests are shown as crosses and ticks in Figure 4.5(b).) Therefore $[7\ 1\ 2]$ is a contact face. This face tests its neighbouring faces, less the parent $[1\ 2\ 5]$, which are $[7\ 1\ 4]$ and $[7\ 2\ 4]$ but these tests result in $\hat{\kappa}_2 < \hat{\kappa}_1$. Therefore the contact faces are $[1\ 2\ 5]$ and $[7\ 1\ 2]$. The placement of the new particle is determined by solving Equation (4.8). The new tetrahedra added are $[1\ 2\ 5\ 8]$ and $[7\ 1\ 2\ 8]$ and the contact faces $[1\ 2\ 5]$ and $[7\ 1\ 2]$ have their flag changed to internal.

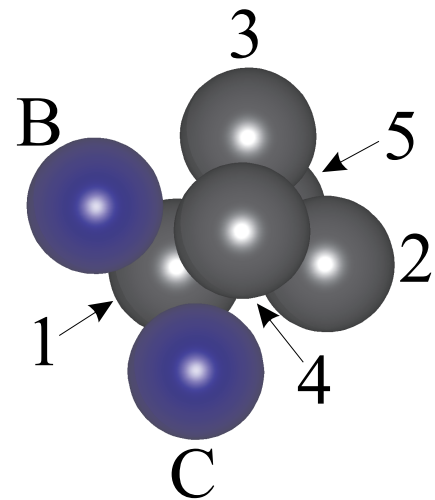
4.4 Defining the Fluid Surface

The fluid surface is based on the position of the tetrahedra as defined in T . The saturation parameter δ adjusts the position of the tetrahedra faces to allow a varied volume of fluid to exist in the agglomerate. The state $\delta = 0$ corresponds to a minimum state where the fluid segments are connected to the centre of the primary particles. For $\delta > 0$ the external faces are moved in the direction of their outward pointing normal vectors up to a maximum value of $\delta = 1$. For $\delta = 1$ the faces are displaced a distance R to match the radius of the spheres. The position of the spheres remain fixed as δ is varied.

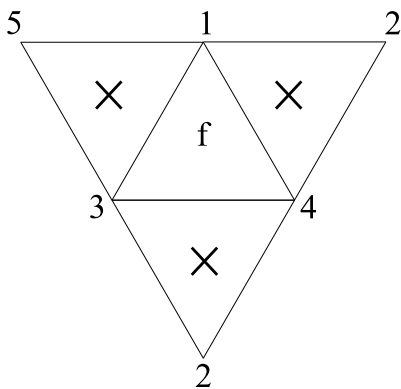
Figure 4.6 shows a fluid segment formed for a particular $t \in T$ with vertices $[P_1\ P_2\ P_3\ P_4]$. To illustrate the expansion of the faces, \vec{n}_1 is used to denote the outward pointing normal vector of face f_1 with vertices $[P_1\ P_2\ P_3]$. The expanded vertices due to this face are shown in Figure 4.6(b) as $u_1 = P_1 + \delta\vec{n}_1$, $u_2 = P_2 + \delta\vec{n}_1$ and $u_3 = P_3 + \delta\vec{n}_1$. For $\delta \neq 0$, cylinders of radius δ connect adjacent faces together along their edges as shown in Figure 4.6(c). In Section 4.5 a computational geometry toolbox is used to calculate properties of the agglomerates. The toolbox requires the fluid segments (and spheres) to be convex and bounded. The objects formed in Figure 4.6(c) are convex. They may be bounded by using a routine from the toolbox to intersect the fluid segments with half-spaces which pass through the u_i vertices (Section 4.5 discusses half-spaces). To illustrate, Figure 4.6(c) shows the vertices u_6 , u_9 and u_{10} that the half-space passes through due to the tetrahedron vertex P_4 . The inequality of the half-space is determined by including the mean point of the fluid segment following the intersection. The completed fluid segment is shown in Figure 4.6(d). The fluid segments are required to be in the same saturation state δ for a given agglomerate. The fluid segment corresponding to tetrahedron t_j is



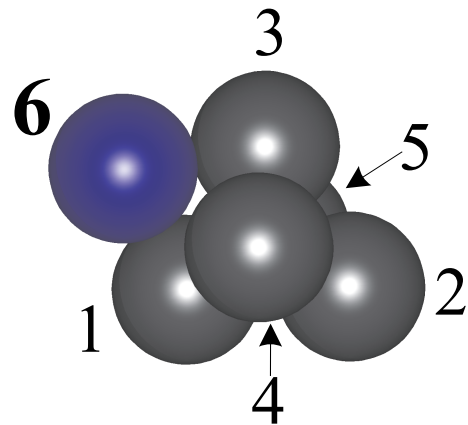
(a) Sphere A is the position for placing one particle between faces $[1\ 3\ 4]$ and $[1\ 2\ 4]$. In this case two tetrahedra are required: tetrahedra (with vertices) $[1\ 3\ 4\ A]$ and $[1\ 2\ 4\ A]$.



(b) Spheres B and C are the placement (as determined by optimisation), for placing two particles between faces $[1\ 3\ 4]$ and $[1\ 2\ 4]$. In this case, three tetrahedra are required: $[1\ 3\ 4\ B]$, $[1\ 4\ B\ C]$, and $[1\ 4\ C\ 2]$.

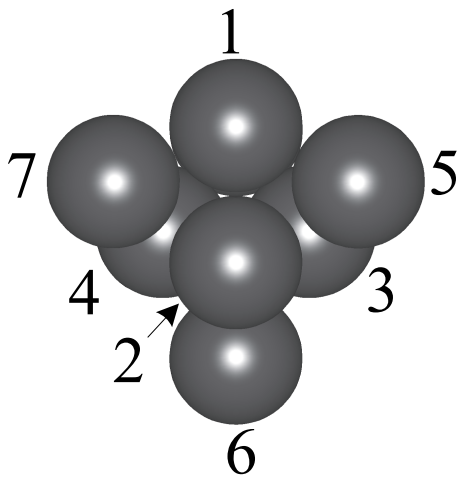


(c) Diagram of the contact faces.

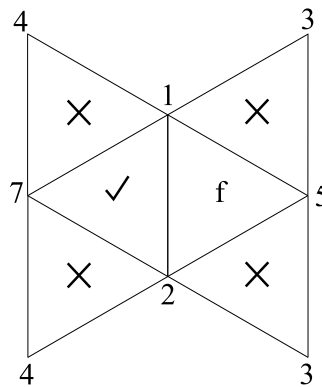


(d) The actual position for the 6th sphere, as determined by optimisation.

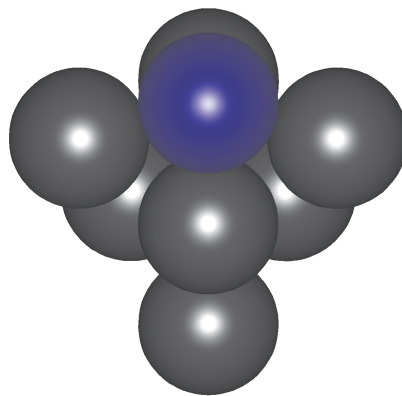
Figure 4.4: Adding a particle to a five particle agglomerate. A contact face comparison between faces $[1\ 3\ 4]$ and $[1\ 2\ 4]$ is shown in figures (a) and (b). A single contact face exists for this case ($[1\ 3\ 4]$), with contact spheres 1, 3 and 4. Figure (c) illustrates the placement of the new particle.



(a) Adding a particle to an 8 particle agglomerate. The initial contact face f is $[1\ 5\ 2]$.



(b) The result after adding particle to the contact faces $[1\ 5\ 2]$ and $[7\ 1\ 2]$



(c) The result after adding particle to the contact faces $[5\ 1\ 2]$ and $[7\ 1\ 2]$

Figure 4.5: Adding a new particle to a 8 particle agglomerate. In this case, there are 2 contact faces, and 2 tetrahedra are therefore added: $[5\ 1\ 2\ 9]$ and $[7\ 1\ 2\ 9]$. (The 8th particle, attached to spheres 2, 3 and 4, is not visible in this view).

denoted by \mathbf{T}_j .

Originally a convex hull routine from the toolbox was used to form the half-spaces for the spheres and fluid segments. Since the objects were already convex, however, it is more efficient to form the objects in face-vertex format. In this format the half-spaces may be readily obtained. We show how this was completed for the fluid segments. Faces are defined on the segments due to the four expanded faces, shown in Figure 4.6(b), and, by defining vertices on the cylinders, faces for the cylinders are defined by using triangular mapping. Vertices are defined on the cylinders along circular arcs between adjacent u_i points as shown in Figure 4.7(b). We show how vertices are defined for one of the arcs. Figure 4.7(a) shows a view from the point P_4 to the points P_1 , P_2 and P_3 which lie in the same plane. The arc γ_1 centred at P_2 exists between the points $u_5 = P_2 + \delta\vec{n}_2$ and $u_{11} = P_2 + \delta\vec{n}_3$ and has the equation $|x - P_2| = \delta$ where $x \in \gamma_1$. The angle between the faces f_2 and f_3 is calculated as $\theta = \arccos\left(\frac{\vec{n}_2 \cdot \vec{n}_3}{|\vec{n}_2||\vec{n}_3|}\right)$ and an incremental angle $\Delta\theta = \frac{\theta}{k}$ is defined where k is the number of vertices along the arcs. The vector \vec{n}_* is introduced which is orthogonal to \vec{n}_2 as shown in Figure 4.7(a). The points along γ_1 are given by

$$v_i = P_2 + \delta [\cos(i\Delta\theta)\vec{n}_2 + \sin(i\Delta\theta)\vec{n}_*] \quad (4.10)$$

where $i = 1, 2, \dots, k$. But now

$$\vec{n}_3 = \cos\theta\vec{n}_2 + \sin\theta\vec{n}_*. \quad (4.11)$$

Therefore

$$\begin{aligned} v_i &= P_2 + \delta [\cos(i\Delta\theta)\vec{n}_2 + \sin(i\Delta\theta)(\csc\theta\vec{n}_3 - \cot\theta\vec{n}_2)] \\ &= P_2 + \delta [(\cos(i\Delta\theta) - \sin(i\Delta\theta)\cot\theta)\vec{n}_2 + \sin(i\Delta\theta)\csc\theta\vec{n}_3]. \end{aligned} \quad (4.12)$$

The arc at the opposite end of the cylinder is denoted by γ_2 . Points on this arc are also denoted by v_i but for $i = k + 1, \dots, 2k$. The steps above are repeated for the remaining cylinders and superscripts are introduced for v_i to label the corresponding edges with the above case being denoted by $^{(2,4)}v_i$.

The face-vertex matrix for the fluid segments is defined by

$$\begin{bmatrix} u_1 & u_4 & u_7 & u_{10} & ^{(1,2)}v_1 & ^{(1,2)}v_1 & \dots & ^{(1,2)}v_{k-1} & \dots & \boxed{^{(2,4)}v_1} & ^{(2,4)}v_1 & \dots \\ u_2 & u_5 & u_8 & u_{11} & ^{(1,2)}v_{k+2} & ^{(1,2)}v_2 & \dots & ^{(1,2)}v_k & \dots & ^{(2,4)}v_{k+2} & ^{(2,4)}v_2 & \dots \\ u_3 & u_6 & u_9 & u_{12} & ^{(1,2)}v_{k+1} & ^{(1,2)}v_{k+2} & \dots & ^{(1,2)}v_{2k} & \dots & ^{(2,4)}v_{k+1} & ^{(2,4)}v_{k+2} & \dots \end{bmatrix}^t.$$

The box in the above matrix represents the shaded face shown in Figure 4.7(b). After the objects are formed they are bounded by intersecting them with half-spaces as described

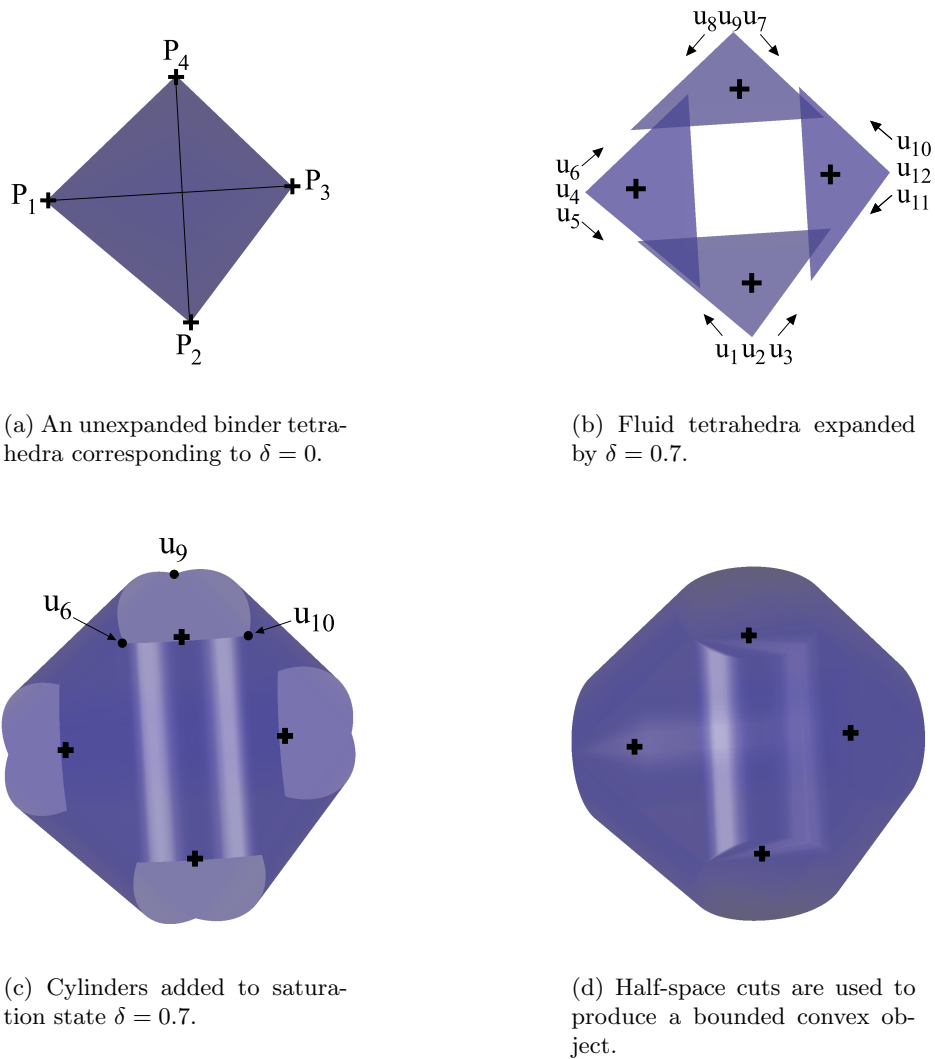


Figure 4.6: Creation of a binder fluid segment

earlier.

4.5 Agglomerate Properties

An agglomerate is the union of n_S primary particles with n_T tetrahedra as given by

$$\left(\bigcup_{i=1}^{n_S} \mathbf{S}_i \right) \cup \left(\bigcup_{i=1}^{n_T} \mathbf{T}_i \right) \quad (4.13)$$

where \mathbf{S}_i denotes a sphere of radius R centred at S_i and \mathbf{T}_i denotes the expanded tetrahedron based on the vertices referenced by t_i . The objective is to calculate properties of this union.

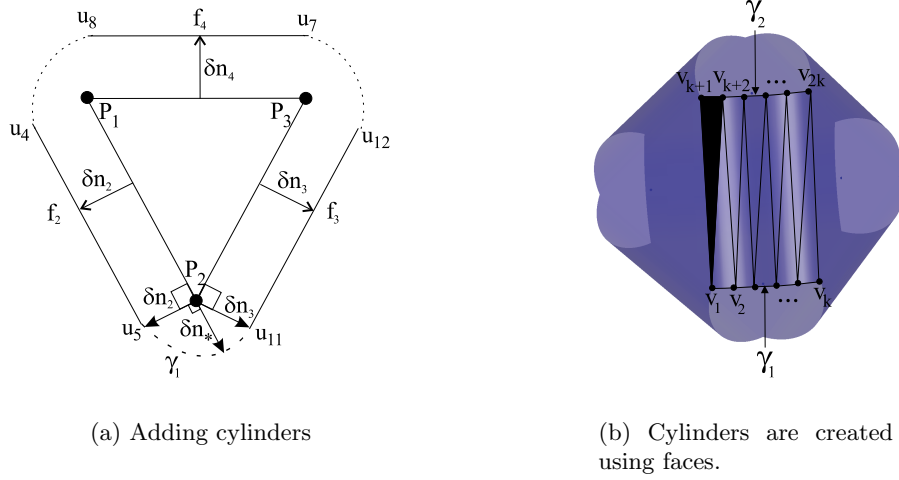


Figure 4.7: Adding cylinders, and the faces which make up the object.

The union in Equation (4.13) will, in general, be non-convex. However, since the individual \mathbf{S}_i and \mathbf{T}_i components are convex, the formula for a union of convex components \mathbf{A}_i may be applied. This is given by [55]

$$\bigcup_i \mathbf{A}_i = \sum_i \mathbf{A}_i - \sum_{i \neq j} \mathbf{A}_i \cap \mathbf{A}_j + \sum_{i \neq j \neq k} \mathbf{A}_i \cap \mathbf{A}_j \cap \mathbf{A}_k - \dots \pm \bigcap_i \mathbf{A}_i. \quad (4.14)$$

(Note: In general the union of non-convex objects can only be evaluated by first dividing the object into convex regions and then summing properties of the convex portions piecewise [55]. However, this requirement has been achieved in this case because the spheres and the fluid segments are already convex.).

The intersections on the right hand side of Equation (4.14) are now considered with the objective of evaluating Equation (4.13). It is clear that $\mathbf{S}_i \cap \mathbf{S}_j = \emptyset$ for $i \neq j$ since $\sigma \geq 2R$. For the \mathbf{T}_i set, however, neighbouring tetrahedra overlap for $\delta > 0$. As an example, Figure 4.8(a) illustrates overlapping binder fluid segments for the five particle case where $\delta = 0.7$. To minimise the number of intersections required, the tetrahedra may first be intersected with appropriate half-spaces, “cutting” them so that neighbouring tetrahedra intersect only along the cut faces and $\mathbf{T}_i \cap \mathbf{T}_j = \emptyset$ for all $i \neq j$. If cuts are not introduced then the number of intersections that occur for n overlapping objects is

$$\sum_{k=2}^n \binom{n}{k} = 2^n - n - 1.$$

The worst case scenario for this problem occurs when one of the central spheres, corresponding to the original four particle agglomerate, is surrounded by 12 neighbours. This

is a packing arrangement known as the kissing sphere problem in \mathbb{R}^3 [54]. This configuration results in $n = 20$ overlapping tetrahedra which meet at the central sphere vertex and 1,048,555 intersections. The implementation of the cuts are discussed in Section 4.6. The binder is equivalent after the intersections are completed because the fluid continues to uniformly fill the internal voids of the agglomerate. The cuts reduce Equation (4.14) to

$$\left(\bigcup_{i=1}^{n_S} \mathbf{S}_i \right) \cup \left(\bigcup_{i=1}^{n_T} \mathbf{T}_i \right) = \sum_i \mathbf{S}_i + \sum_i \mathbf{T}_i - \sum_{i \neq j} \mathbf{S}_i \cap \mathbf{T}_j. \quad (4.15)$$

The geometric bounding toolbox (GBT) version 7 for Matlab [56] was purchased with the intention of evaluating the union in Equation (4.15). The toolbox represents objects as polyhedra which are bounded convex sets formed by the intersection of a finite number of half-spaces [56]. A half-space is defined by

$$\vec{n} \cdot (\vec{x} - \vec{x}_0) = 0 \quad (4.16)$$

where $\vec{n} \neq \vec{0}$ is an outward pointing normal vector, \vec{x}_0 is a point on the plane and $\vec{x} \in \mathbb{R}^n$. The polyhedron is the bounded region in \mathbb{R}^3 given by the set of the half-space inequalities

$$\vec{n} \cdot (\vec{x} - \vec{x}_0) \leq 0. \quad (4.17)$$

It is common to define $d = \vec{n} \cdot \vec{x}_0$ which allows Equation (4.17) to be written

$$\vec{n} \cdot \vec{x} \leq d. \quad (4.18)$$

The toolbox internally stores the half-spaces in an matrix H where each row, defining a half-space, is given by $h = [\vec{n} \ d]$.

The first attempt to evaluate Equation (4.15) used the convex hull algorithm of GBT to form polyhedra given the vertices of the spheres \mathbf{S}_i (obtained using the Matlab `sphere` command) and the vertices of the tetrahedra \mathbf{T}_i by determining the u_i and v_i points as in Section 4.4. The resolution of the objects is given by k : k vertices exist on the cylinder arcs and k^2 vertices exist on the spheres. The following GBT functions [56] were used to evaluate the union given by Equation (4.15):

1. The intersection of two convex polyhedra. This function was used to calculate the intersections between the spheres and fluid segments given in Equation (4.15). (Note: The intersection of two convex polyhedra is convex.)
2. The intersection of a half-space with a polyhedron. This function was used to cut the tetrahedra so that $\mathbf{T}_i \cap \mathbf{T}_j = \emptyset$ for $i \neq j$. (This function is also used internally

by the toolbox for Item 1 as two polyhedra are intersected by intersecting one of the polyhedra with the half-spaces of the other.)

3. The surface area and volume of a polyhedron. These functions were used to calculate the agglomerate properties required in Section 4.7.

Using GBT to solve Equation (4.15) was found to be very slow especially for high k values*. The efficiency problems were due to a combination of the following:

1. The convex hull algorithm was being applied even though the objects were known to be convex. This was computationally costly because the routine requires the smallest convex set to be obtained upon the addition of each new vertex.
2. The complete GBT code was implemented using Matlab script files (or m-files). This had a significant impact on performance because Matlab is an interpreter and the major routines contained nested `for` loops. An attempt was made to convert the m-files into C code using the Matlab compiler, with the objective of compiling the code into `MeX`, but this was not successful.
3. The calculation of the surface area and volume required faces and vertex but GBT did not retain the face-vertex structure of the polyhedra after the objects were initially formed. Instead this was calculated on demand but this was time consuming. This was a problem in this application because the surface area and volume of the objects needs to be calculated repeatedly as discussed in Section 4.7.
4. The GBT routines supported arbitrary dimensions but they were not optimised for calculations in \mathbb{R}^3 .

Item 1 was addressed by forming the half-space matrix H manually using the face-vertex format discussed in Section 4.4. However the performance of GBT was still very poor. Jonathan Marshall[†] helped with problems 2-4 by writing a custom built toolbox for this application. It provided similar functionality to GBT but it was considerably more efficient and supported partial wet and dry surface area calculations for polyhedra. The toolbox was written in C++ and it is referred to now as the ‘C++ toolbox’. It was used as a replacement for GBT.

The differences between GBT and the C++ toolbox when using them externally are:

*In a trial run the time required to intersect two spheres with 1,000 vertices on each sphere took approximately 4 hours on a Pentium III 1 GHz processor using GBT.

[†]formally of the Institute of Fundamental Sciences, Massey University, New Zealand.

1. The C++ toolbox does not include a convex hull algorithm. Instead convex objects are defined by using the face-vertex format as described in Section 4.4.
2. The C++ toolbox retains the face and vertices in addition to the set of half-spaces. These are updated following half-space intersections allowing the surface area and volume to be efficiently calculated.
3. To support partial wet and dry surface area the C++ toolbox introduced flags to define each face on the polyhedra as of type **wet**, **dry** or **cut**. **Wet** faces contribute to the wet surface area and **dry** faces to the dry surface area. Faces of type **cut** occur when half-space cuts are introduced to avoid overlap between the tetrahedra. These faces do not contribute to the surface area calculations. Faces on the spheres \mathbf{S}_i are initialised to type **dry** and the faces on the tetrahedra \mathbf{T}_j to type **wet**. When a face is formed on a polyhedra, due to an intersection with a half-space, the new face inherits the flag of the half-space. If polytope P_1 is dry and polytope P_2 is wet then $A_{\text{dry}}(P_1 \cap P_2)$ returns the area of $P_1 \cap P_2$ which is common to P_1 (the **dry** area) and $A_{\text{wet}}(P_1 \cap P_2)$ returns the area which is common to P_2 (the **wet** area).

The dry surface area of the polyhedron P is denoted by $A_{\text{dry}}(P)$ and the wet surface area by $A_{\text{wet}}(P)$. The total surface area is denoted $A(P)$ and the polyhedron volume by $V(P)$.

4.6 Half-space Intersections with the Tetrahedra

This section discusses how the fluid segments are intersected with half-spaces so that $\mathbf{T}_i \cap \mathbf{T}_j = \emptyset$ for $i \neq j$.

Consider a fluid segment to be added which is based on vertices referenced by t . The k neighbouring fluid segments are based on the vertices as given by $t_k \in T$. For each neighbour, corresponding to a particular k , the common vertices between t and t_k are determined. If t and t_k share three common vertices then both fluid segments are cut along the corresponding face. If two vertices are common then the segments are cut along an edge. If one vertex is common then both segments are cut at a point.

Figure 4.8 shows a fluid segment due to tetrahedron t_2 which has been added that overlaps with a segment formed from t_1 . The common face shared between t_1 and t_2 is denoted by f and has normal vector \vec{n} . The half-space used to cut the segments lies in the plane of f and passes through the centre of the three common primary particles. The sign of the half-space for t_2 is determined by including the mean-point of the segment following the cut. The sign is reversed when cutting the fluid segment for t_1 . The completed fluid segments are shown in Figure 4.8(b).

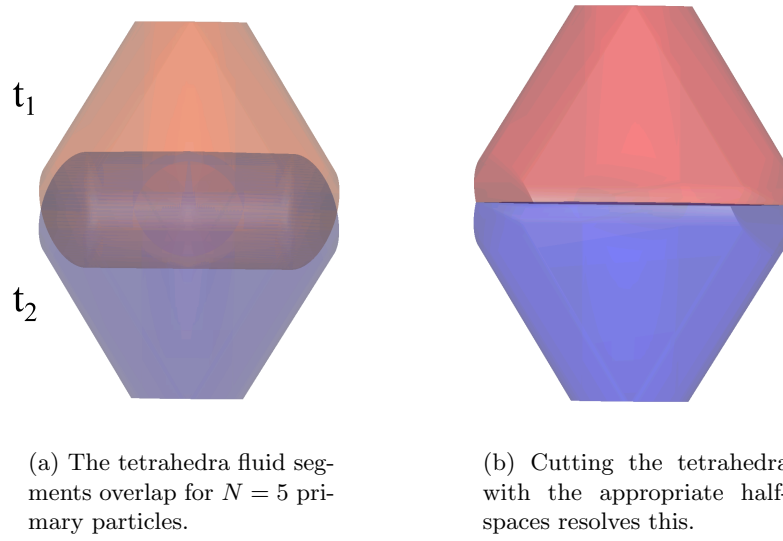


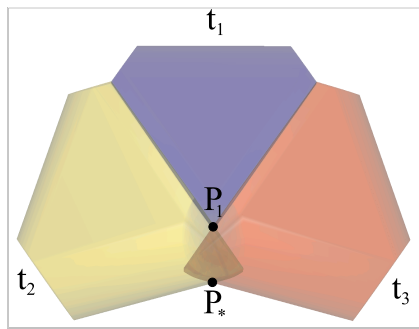
Figure 4.8: Overlap at a face for two adjacent tetrahedra. First required for $N = 5$ (2 tetrahedra). (These drawings were created for a binder tetrahedron that has $\delta = 0.7$, and a separation between spheres of $\sigma = 0.5$). Primary particles are not drawn in this figure.

Figure 4.9 illustrates two fluid segments based on tetrahedra t_2 and t_3 which meet along an edge. The t_3 fluid segment has been added and, in Figure 4.9(a), the face shared between t_3 and t_1 has been cut. The edge is viewed side on in Figure 4.10 as a schematic diagram. In this figure the vertices of the tetrahedra are labelled by $t_1 = [P_1 P_2 P_3 P_4]$, $t_2 = [P_1 P_2 P_3 P_5]$ and $t_3 = [P_1 P_3 P_4 P_6]$. The faces from the edge are $f_2 = [P_1 P_3 P_5]$ and $f_3 = [P_1 P_3 P_6]$ and they have respective outward pointing normal vectors \vec{n}_2 and \vec{n}_3 . The point $P_* = P_1 + \frac{1}{2}(\vec{n}_2 + \vec{n}_3)$ shown in Figure 4.9(a) is calculated. The points P_1 , P_3 and P_* lie in the plane of the half-space that is used to cut the segments. The half-space normal vector is given by

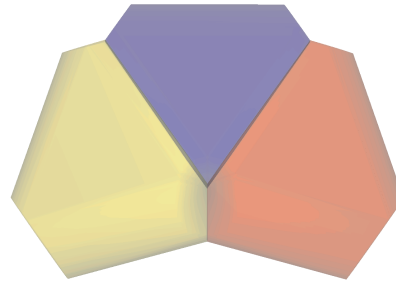
$$\vec{n}_* = \frac{(P_1 - P_3) \times (P_* - P_3)}{|(P_1 - P_3) \times (P_* - P_3)|}.$$

When cutting the segment due to t_3 the mean point of the tetrahedra is included following the half-space cut. The sign is reversed when cutting the segment due to t_2 .

The point cut is shown in Figure 4.11. The box shows the region where cuts have been completed to avoid overlap. Consider two of the segments that meet at a point which are based on $t_1 = [P_1 P_2 P_3 P_4]$ and $t_2 = [P_1 P_5 P_6 P_7]$. The mid-point of the faces opposite point P_1 were calculated. The mid-point of the face $[P_2 P_3 P_4]$ on tetrahedron t_1 is denoted by P_* and the mid-point of the face $[P_5 P_6 P_7]$ on t_2 is denoted by \hat{P} . The normal vector of the half-space is given by $\vec{n}_* = \frac{P_* - \hat{P}}{|P_* - \hat{P}|}$ and a point on the half-space by P_1 .



(a) The tetrahedra fluid segments overlap for $N = 7$ primary particles.



(b) Cutting the tetrahedra with the appropriate half-spaces resolves this.

Figure 4.9: An edge cut. First required for $N = 6$ (3 tetrahedra).

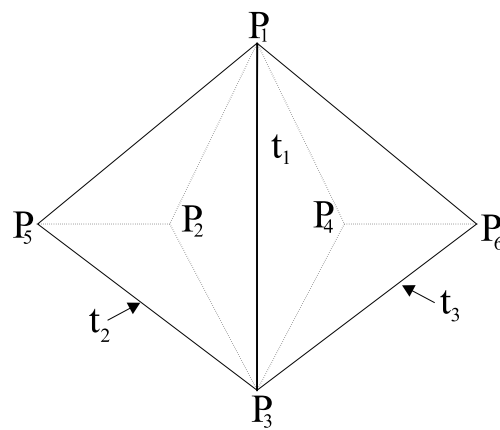
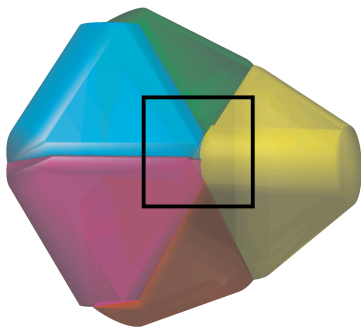
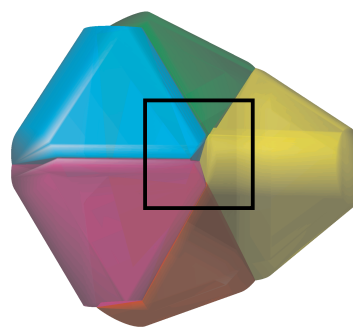


Figure 4.10: Schematic diagram showing the vertices for an edge cut. In this figure tetrahedron t_1 is behind t_2 and t_3 .



(a) Tetrahedra meeting at a vertex.



(b) Cutting the tetrahedra avoids overlap.

Figure 4.11: Point cut. First required for $N = 9$ (7 tetrahedra).

4.7 Calculating Agglomerate Properties

Figure 4.12 shows images of agglomerates formed by this model. For each agglomerate the objective is to calculate properties including the volume of binder fluid and the surface area of the particle that is binder and dry particle.

The volume of binder is equal to the volume of the fluid segments less the volumes of the intersected portions. For n_T tetrahedra

$$V_{\text{binder}} = \sum_{j=1}^{n_T} \left[V(\mathbf{T}_j) - \sum_{i=1}^4 V(\mathbf{S}_{\xi(\mathbf{i},j)} \cap \mathbf{T}_j) \right] \quad (4.19)$$

where the function $\xi(\mathbf{i}, \mathbf{j})$ gives the index of the spheres in S which intersect with the fluid segment \mathbf{T}_j . The surface area of the binder on the particle is given by

$$A_{\text{binder}} = \sum_{j=1}^{n_T} \left[A(\mathbf{T}_j) - \sum_{i=1}^4 A_{\text{wet}}(\mathbf{S}_{\xi(\mathbf{i},j)} \cap \mathbf{T}_j) \right] \quad (4.20)$$

and the surface area that is dry particle by

$$A_{\text{particle}} = N A_{\text{sphere}} - \sum_{j=1}^{n_T} \sum_{i=1}^4 A_{\text{dry}}(\mathbf{S}_{\xi(\mathbf{i},j)} \cap \mathbf{T}_j) \quad (4.21)$$

where $A(\mathbf{S}_{\xi(\mathbf{i},j)})$ denotes the total surface area of the sphere $\mathbf{S}_{\xi(\mathbf{i},j)}$. Since the spheres have the same radius this area is calculated as $A_{\text{sphere}} \equiv A(\mathbf{S}_{\xi(\mathbf{i},j)})$ for a given resolution k .

The stickiness (or wetness) is defined as the wet fraction of the total surface area as given by

$$W = \frac{A_{\text{binder}}}{A_{\text{binder}} + A_{\text{particle}}} \quad (4.22)$$

where A_{binder} is the wet surface area and A_{particle} is the dry surface area of the agglomerate.

Example

The formulae from Equations (4.19)-(4.21) are now illustrated for the four particle agglomerate shown in Figure 4.13(a). Figure 4.13(b) shows the intersected portions between the spheres and fluid segments along with the **wet** and **dry** faces of the portion $\mathbf{S}_4 \cap \mathbf{T}_1$. Now $t_1 = [1 \ 2 \ 3 \ 4]$ and therefore $\xi(1, 1) = 1$, $\xi(2, 1) = 2$, $\xi(3, 1) = 3$ and $\xi(4, 1) = 4$. From Equation (4.19), for $n_T = 1$,

$$V_{\text{binder}} = V(\mathbf{T}_1) - \sum_{i=1}^4 V(\mathbf{S}_{\xi(\mathbf{i},1)} \cap \mathbf{T}_1). \quad (4.23)$$

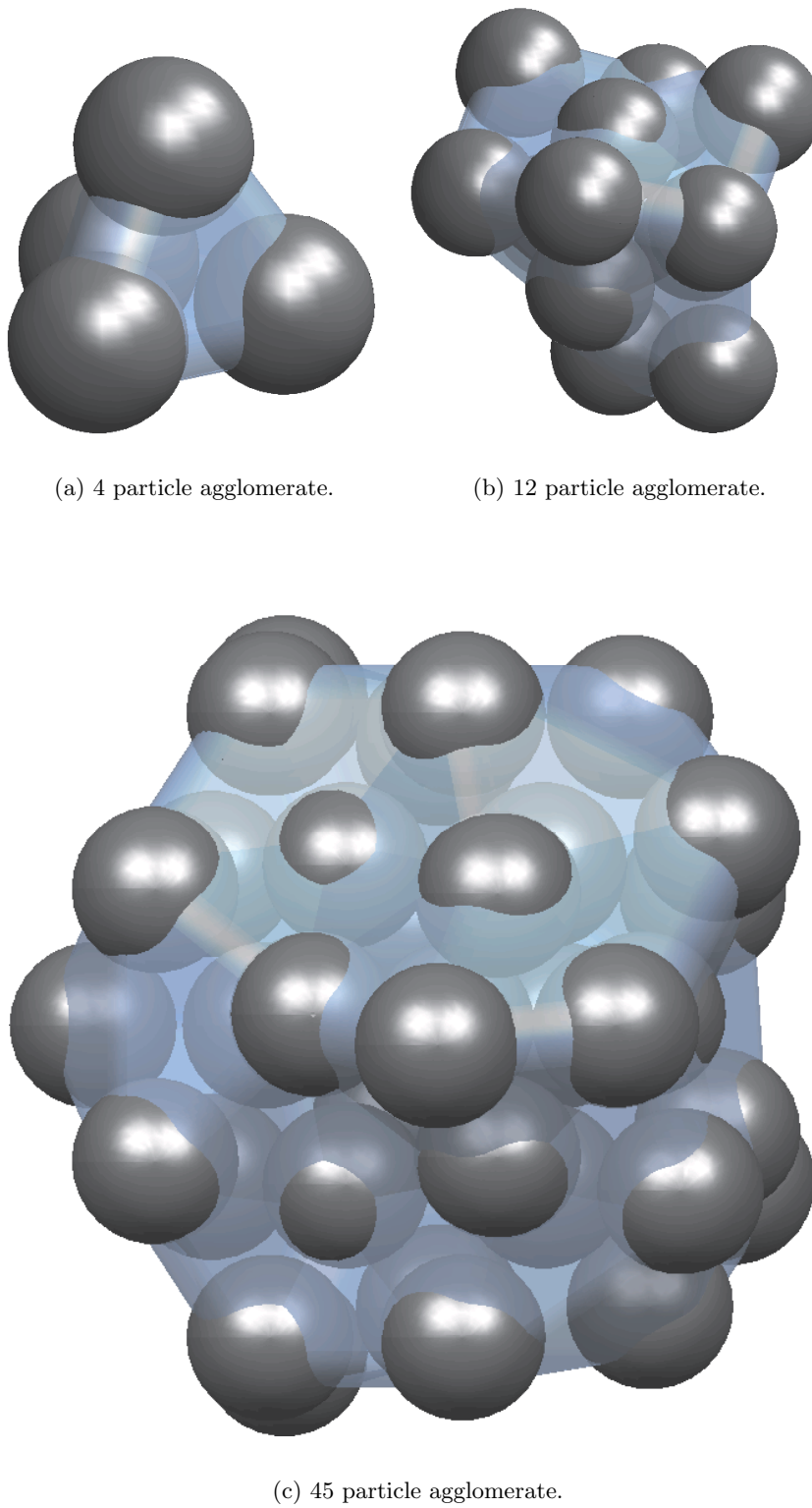
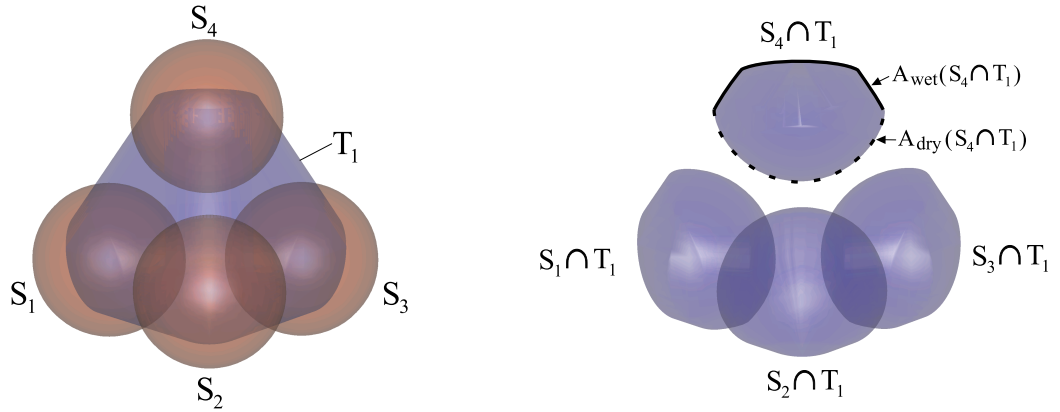


Figure 4.12: Agglomerates created by the model detailed in Chapter 4.



(a) A four particle agglomerate, showing placement of primary particles and binder fluid.

(b) Polyhedra resulting from the intersection between primary particles and binder fluid.

Figure 4.13: In Figure 4.13(a), primary particles and the binder tetrahedra is drawn. Figure (b) shows the intersected portions, obtained by intersecting the spheres with the binder fluid. For this figure $\delta = 0.7$ and $s = 0.5$.

The surface area of the agglomerate that is binder (**wet**) is

$$A_{\text{binder}} = A(\mathbf{T}_1) - \sum_{i=1}^4 A_{\text{wet}}(\mathbf{S}_{\xi(i,1)} \cap \mathbf{T}_1) \quad (4.24)$$

and the area of the agglomerate that is particle (**dry**) is

$$A_{\text{particle}} = 4A_{\text{sphere}} - \sum_{i=1}^4 A_{\text{dry}}(\mathbf{S}_{\xi(i,1)} \cap \mathbf{T}_1). \quad (4.25)$$

The total agglomerate surface area is given by

$$A_{\text{total}} = A_{\text{binder}} + A_{\text{particle}}. \quad (4.26)$$

4.8 Solving the Model

This section details the steps taken to solve the model. This model has three parameters: the agglomerate size N , the minimum separation distance between sphere centres σ and the fluid saturation state δ . For each σ the computationally intensive part of this problem is evaluating the intersected portions for the N and δ parameter space. Since σ and δ are independent the placement of the spheres and tetrahedra are calculated in Matlab for N

primary particles. Then each node on a parallel computer[‡] solves a particular σ value for N primary particles where δ is a parameter. The steps taken are as follows:

1. For each value of σ the placement of the spheres and tetrahedra were generated in Matlab using the steps detailed in Section 4.2. After a new particle is added the S , T and F matrices are updated along with a script file which is used to recreate the placement of the spheres and tetrahedra. The script file provides a list of the fluid segments to be formed, the type of cuts required and the half-spaces required for the cuts. For each σ value the script file and the matrices are saved to disk after an N particle is generated in Matlab.
2. The dataset for a σ value is loaded by a C++ program which uses functions from the C++ toolbox. Using the script file each instance of the C++ program creates the spheres and fluid segments, intersects them as appropriate and calculates the agglomerate properties. The C++ program is run in parallel where each node solves a particular σ value for the two-dimensional N and δ parameter space. The N loop is completed first (i.e. for a fixed δ value) since all the fluid segments must be in the same saturation state δ .
3. After evaluation of a σ datafile is complete the node writes the calculated properties to disk. Once all of the nodes are complete the data is combined for analysis in Matlab which is the subject of the following section.

4.9 Results of the Model

In this section results are presented for the wetness of agglomerates as a function of the number of particles N , the minimum separation distance s between particles and the quantity of binder δ . The agglomerate model was solved using the parameters $N = 50$ (i.e. agglomerates between 4 and 50 primary particles) where $0 \leq s \leq R$ (or $2R \leq \sigma \leq 3R$) and $0 \leq \delta \leq 1$. The number of steps used for the s and δ variables was 100 so that $\Delta s = 0.01R$ and $\Delta \delta = 0.01$. The resolution used for the polyhedra objects was $k = 30$.

The results below are presented in terms of a volume ratio between the binder fluid and the primary particles. For an N particle agglomerate, the fluid-to-solid volume ratio is defined as

$$V^* = \frac{V_{\text{binder}}}{NV_{\text{solid}}} \quad (4.27)$$

[‡]The parallel computer used was the Massey University **sisters** Beowulf cluster which has 16 PIII processors @ 867 MHz.

where V_{binder} is the binder volume and the volume of a primary particle is $V_{\text{solid}} = \frac{4}{3}\pi R^3$. The surface areas A_{binder} , A_{particle} and A_{total} are also normalised as

$$A_{\text{binder}}^* = \frac{A_{\text{binder}}}{NA_{\text{solid}}}, \quad (4.28)$$

$$A_{\text{particle}}^* = \frac{A_{\text{particle}}}{NA_{\text{solid}}} \quad (4.29)$$

and

$$A_{\text{total}}^* = \frac{A_{\text{total}}}{NA_{\text{solid}}} \quad (4.30)$$

where $A_{\text{solid}} = 4\pi R^2$. From Equation (4.26), $A_{\text{total}}^* = A_{\text{binder}}^* + A_{\text{particle}}^*$.

The dependent variables are W , A_{binder}^* and A_{total}^* and the parameters are s , δ , N and V^* . The graphs in Figures 4.14 - 4.18 show the response of the dependent variables to the parameters. Results for the complete parameter space may be viewed because the parameter along the contours is δ and subplots are used to show results for fixed values of one of the parameters.

The figures that are presented are as follows:

1. Figure 4.14 shows the relationship between W and s . The subplots are for fixed values of V^* and the curves represent agglomerates of a fixed size. The parameter along the curves is δ as indicated.
2. Figure 4.15 shows the relationship between W and s for an agglomerate of a fixed size ($N = 30$). The curves represent fixed values of V^* and δ .
3. Figure 4.16 shows plots of surface wetness with respect to N . Each subplot is for a fixed value of s and the curves represent a fixed value of V^* . The parameter along the curves is δ .
4. Figure 4.17 plots the wet agglomerate surface area A_{binder}^* against N for $s = 0$ and $s = 0.2R$. Each curve represents a fixed V^* value.
5. Figure 4.18 plots the total agglomerate surface area A_{total}^* against N for $s = 0$ and $s = 0.2R$. Each curve represents a fixed V^* value.

Figures 4.14 and 4.15 were obtained by using sorting the dataset by particle size N and then using the Matlab `contour` command on each of these portions. Figures 4.16-4.17 were obtained by interpolating the data for fixed values of V^* and repeating this all the dataset segments (as sorted by size). The 'jitter' in these figures is because a non-constant

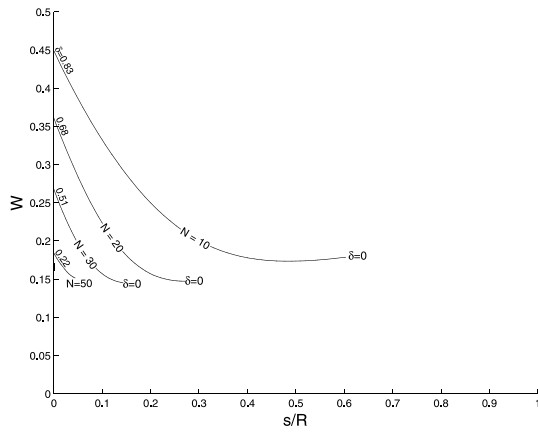
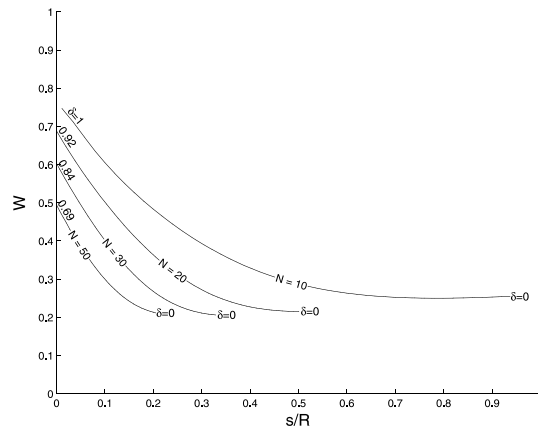
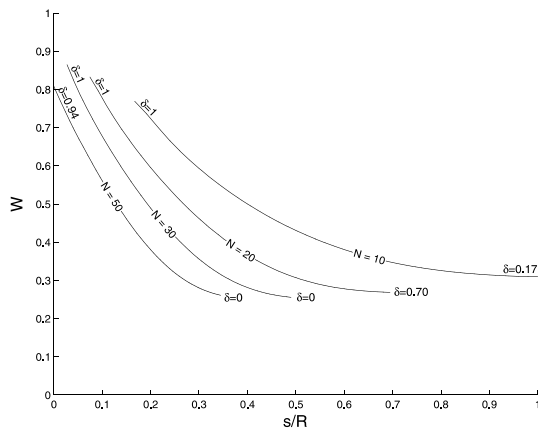
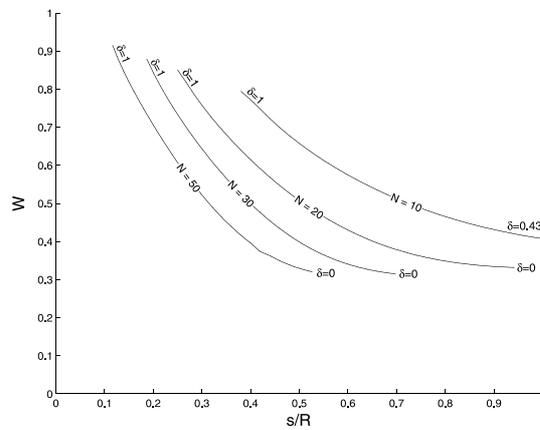
(a) $V^* = 0.3$ (b) $V^* = 0.5$ (c) $V^* = 0.7$ (d) $V^* = 1.0$

Figure 4.14: Plot of surface wetness W with respect to inter-particle separation distance s for agglomerates composed of 10, 20, 30 and 50 primary particles. Values of V^* used in this figure are $V = 0.3, 0.5, 0.7$ and 1.0 .

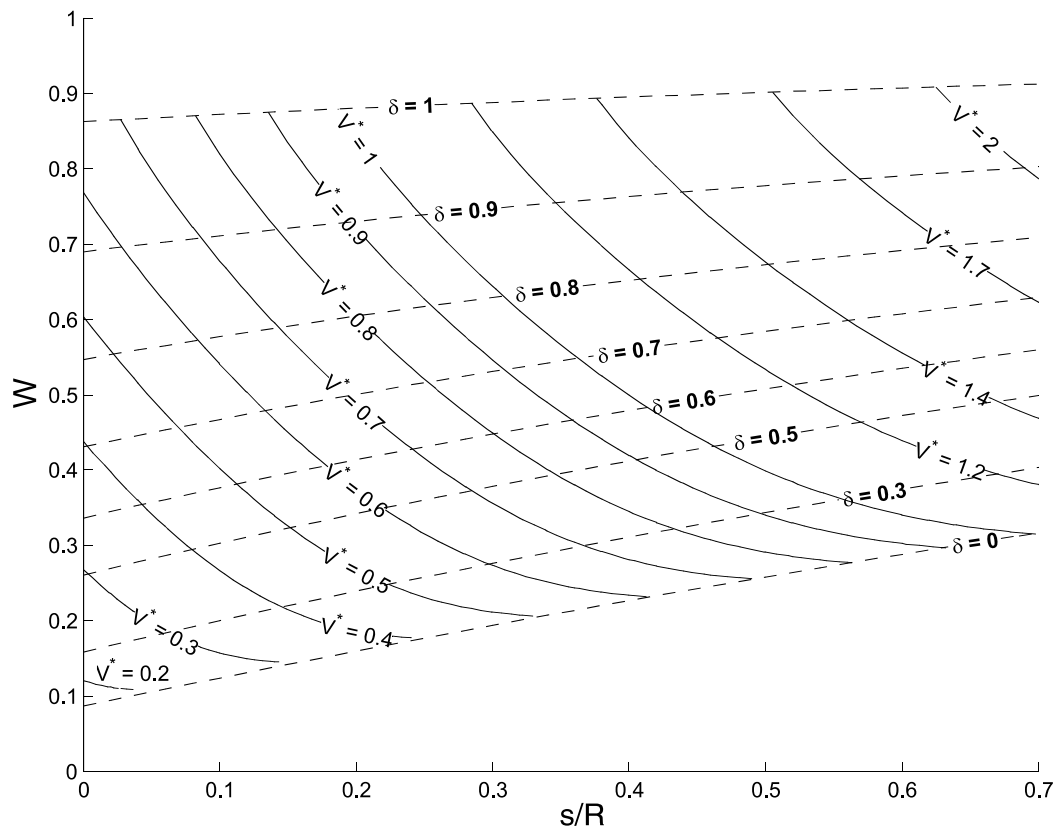
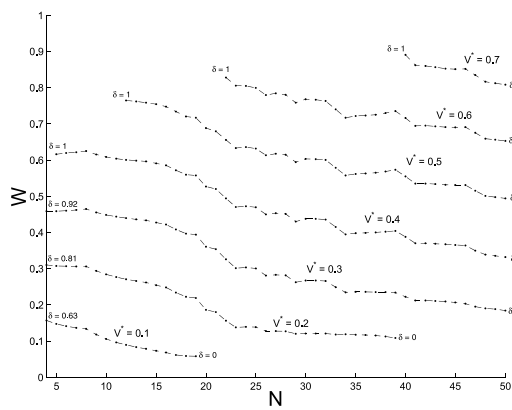
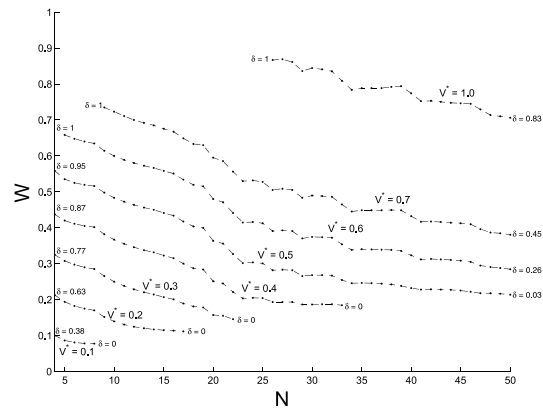


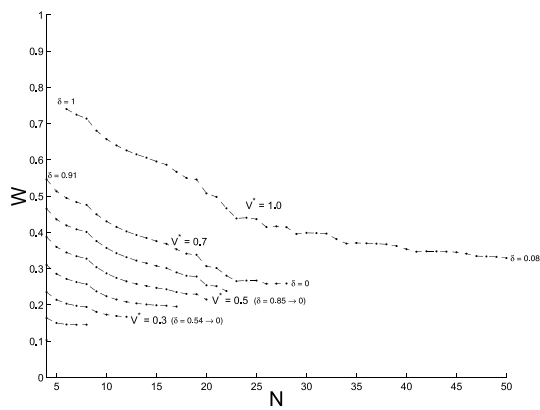
Figure 4.15: Volume contour plot of surface wetness W with respect to separation distance s for an $N = 30$ particle agglomerate. There are two sets of contour labels in this figure. Contour labels on the solid blue lines are the fluid to solid volume ratio \bar{V} , while bold contour labels (drawn in a dashed red line) are lines of constant δ .



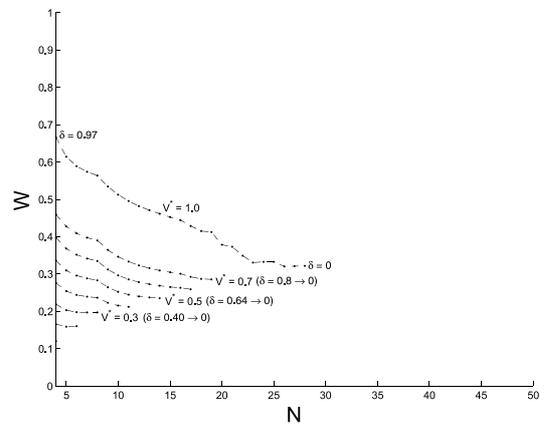
(a) $s = 0$



(b) $s = 0.2R$

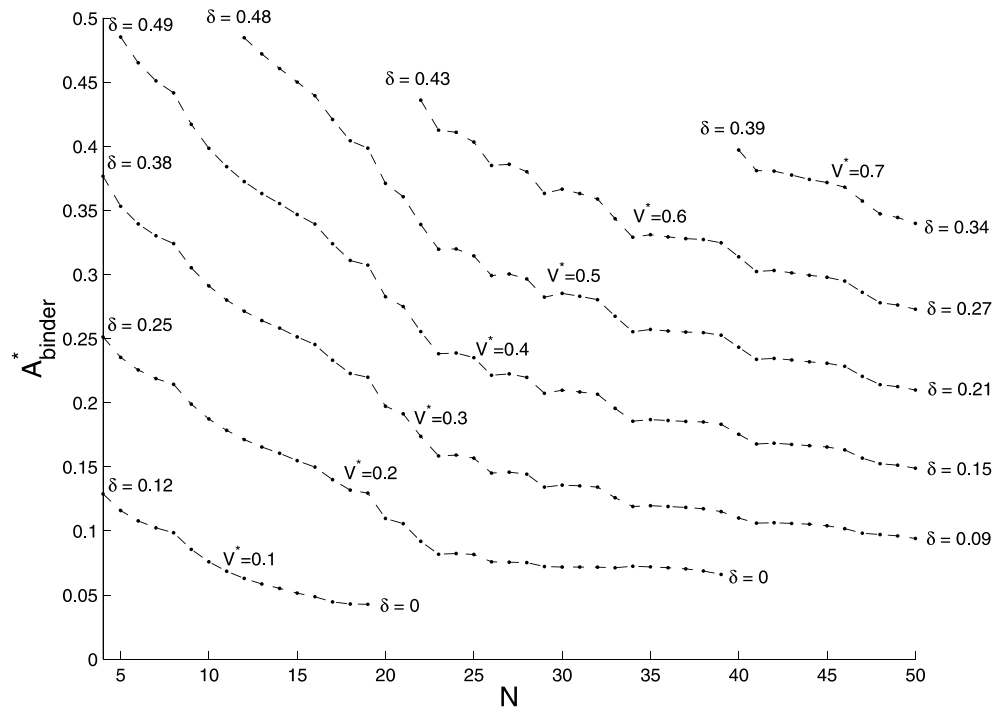
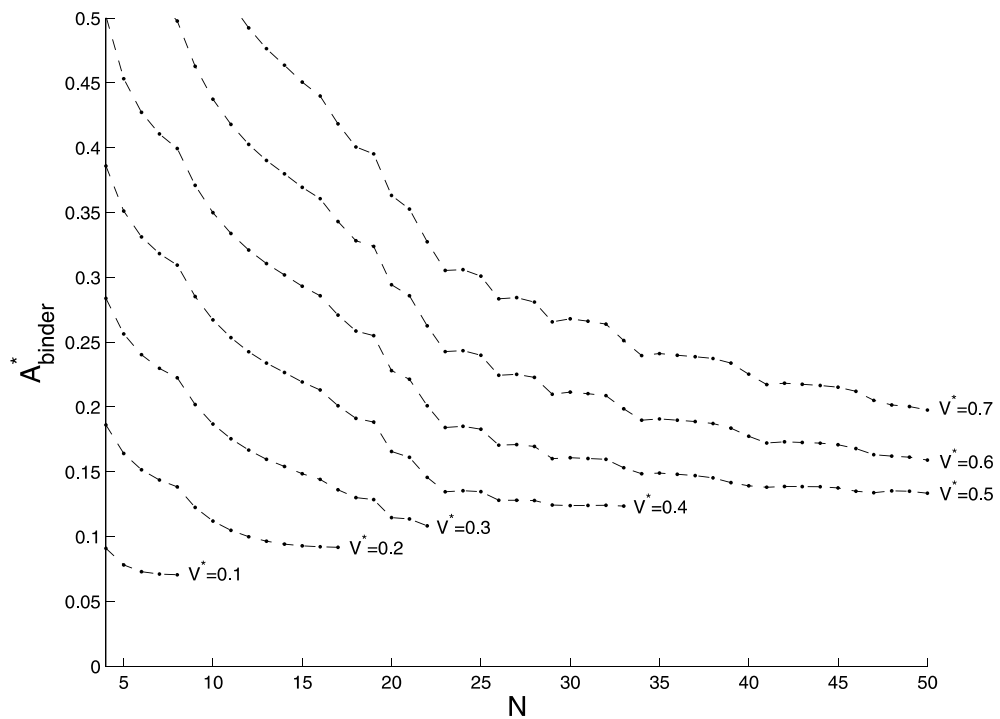


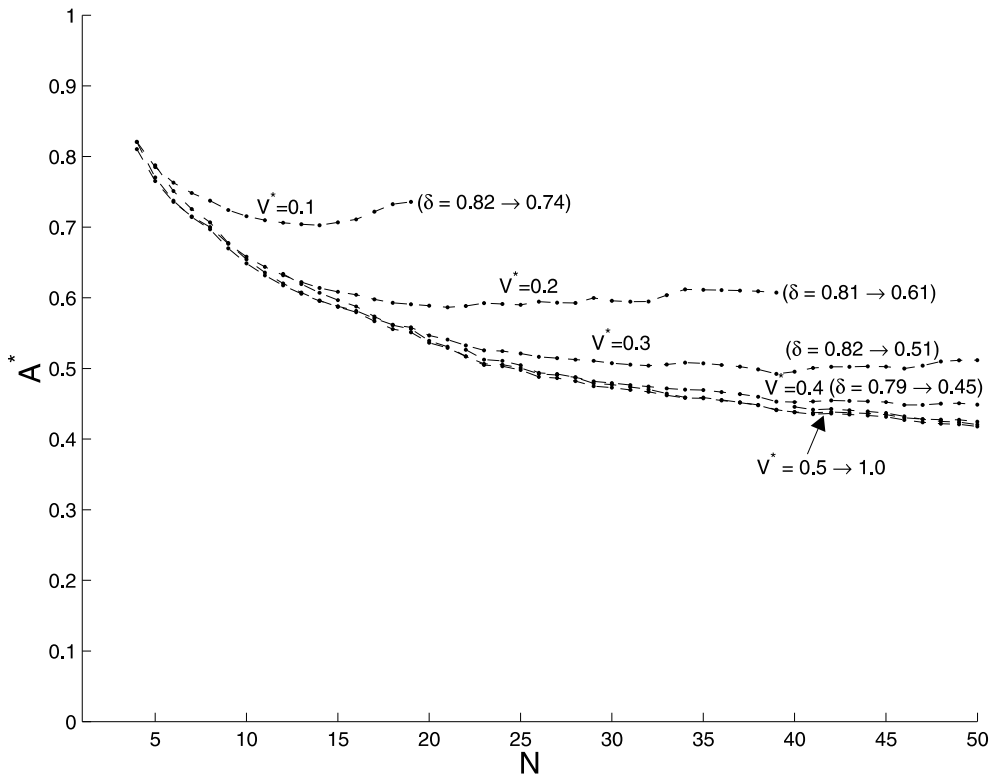
(c) $s = 0.5R$



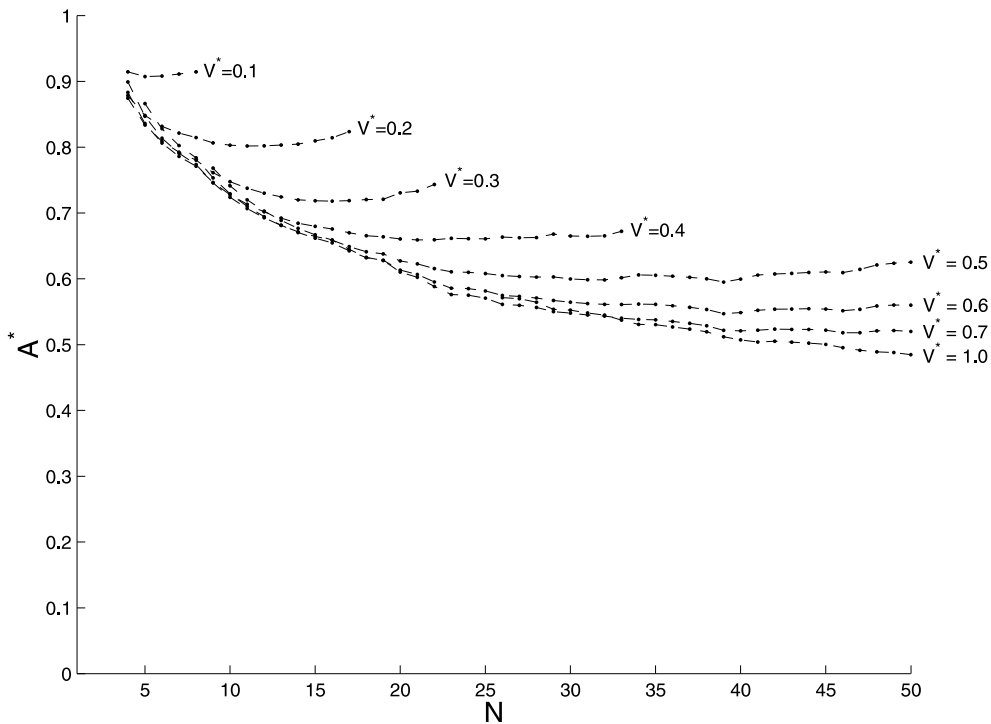
(d) $s = 0.7R$

Figure 4.16: Graphs of wetness W with respect to particle number N for a range of s and a range of fluids to solid ratio values V^* .

(a) $s = 0$ (b) $s = 0.2R$ Figure 4.17: Plot showing the wet area of agglomerates A_{binder}^* with respect to number of particles N .



(a) Plot of A_{total}^* versus N for $s = 0$



(b) Plot of A_{total}^* versus N for $s = 0.2R$

Figure 4.18: Plot showing the total area of agglomerates A_{total}^* with respect to number of particles.

volume of fluid is added with each additional particle. (The volume of binder fluid added depends on the number and placement of the fluid segments.)

The following observations are made from the figures:

Observation(s)	Shown in Figure(s)	Physical Effect
1. W increases as s is decreased for fixed N and fixed V^* . δ increases.	4.14, 4.15	Decreasing s decreases the void space causing liquid to migrate to the surface of the particle.
2. W increases as V^* is increased for fixed N and fixed s . δ increases.	4.15	Fixing N and s fixes the void space. Additional liquid therefore increases the saturation state of the particle.
3. W decreases for increasing size N for fixed V^* and fixed s . δ decreases	4.16	The void space of the agglomerate increases with N . For fixed V^* , W and δ therefore decreases.
4. The relative wet surface area A_{binder}^* decreases for increasing size N for fixed V^* and s . δ decreases.	4.17	The relative void space of the particle increases with increasing size N . The fluid moves to this space which decreases the fluid surface area.
5. The relative total surface area A_{total}^* decreases for increasing size N for fixed V^* and s . δ decreases.	4.18	As above.
6. For V^* values below the random packing limit (approximately $V^* = 0.42$ for $s = 0$) the total surface area increases with N until no solution can be obtained.	4.18(a)	The fluid occupies the increased void space due to increasing N . This exposes portions of the spheres which proportionally have a higher surface area. No solution can be obtained when the binder volume is less than the void space.

The observation made in item 1 supports the theory of Wauters *et al.* [21], described in Section 1.2.2, where particles increase in surface wetness as consolidation occurs.

The surface wetness curves in Figure 4.16 are a function of N , V^* and s so that $W =$

$W(N, V^*, s)$. The extended population balance model in Section 5.2 requires a relationship of the form $W = W(N, V^*)$ for the probability of particle coalescence. The original approach taken was to find the value of s , for a given V^* value, such that the particle had minimum wet binder surface area A_{binder} . However, particles with high s and low δ values were predicted which had a physically unrealistic appearance. The cause of this is due to the use of the approximate binder fluid surface. The case subsequently investigated was $s = 0$ which corresponds to the case of maximum consolidation. The functions fitted to this case are given below and they used in the population balance simulation.

4.10 Fitting Functions for $s = 0$

Functions are now to be fitted to the curves shown in Figures 4.16(a) and 4.17(a). These functions are used in the population balance model which is presented in Chapter 5.

Surface Wetness W

The surface wetness curve W for $s = 0$ shown in Figure 4.16(a) is a function of N and V^* . To fit a suitable family of curves, the following observations were made: (i) the curves are approximately linear with respect to V^* , (ii) a peak or ‘hump’ occurs for $N \lesssim 20$ and (iii) the curves do not pass through the origin. Item (ii) was initially modelled using a $\frac{1}{N}$ curve but a $\frac{1}{N^2}$ curve was found to be more suitable since it decreases more rapidly. A curve fit was obtained to the following family of curves:

$$W(N, V^*) = \frac{k_1}{N^2 + k_4} + k_2 V^* + k_3 \quad (4.31)$$

where k_1 , k_2 , k_3 and k_4 are constants.

The constants k_1 and k_4 in Equation (4.31) control the height and width of the function modelling the ‘hump’, k_2 controls the spacing of the V^* curves and k_3 gives the vertical intercept. The constants k_1 , k_2 and k_3 are linear but k_4 is non-linear. For given k_4 the constants k_1 , k_2 and k_3 may be determined using a linear least-squares solver in Matlab. The use of full non-linear optimisation was able to be avoided by repeating the linear regression and finding the (approximate) k_4 corresponding to a minimum residual.

The problem was setup using vectors W_i , N_i and V_i^* corresponding to the datapoints in Figure 4.16(a). The datapoints were labelled such that $i = 1$ corresponds to the datapoint $V_1^* = 0.1$ and $N_1 = 4$ and $i = I$ to the datapoint at $i = I$ to $V_I^* = 0.7$ and $N_I = 50$. The intermediate datapoints were labelled such that $1 \leq i \leq I$. The following matrix system

was then formed:

$$\begin{bmatrix} \frac{1}{N_1^2+k_4} & V_1^* & 1 \\ \frac{1}{N_2^2+k_4} & V_2^* & 1 \\ \vdots & \vdots & \vdots \\ \frac{1}{N_i^2+k_4} & V_i^* & 1 \\ \vdots & \vdots & \vdots \\ \frac{1}{N_I^2+k_4} & V_I^* & 1 \end{bmatrix} \begin{bmatrix} k_1 \\ k_2 \\ k_3 \end{bmatrix} = \begin{bmatrix} W_1 \\ W_2 \\ \vdots \\ W_i \\ \vdots \\ W_I \end{bmatrix} \quad (4.32)$$

which we write as

$$A\hat{k} = \hat{W}. \quad (4.33)$$

The system was solved for \hat{k} using matrix left division in Matlab with the command $\hat{k} = \text{mldivide}(A, \hat{W})$. The residual was then calculated as $|A\hat{k} - \hat{W}|$. As discussed above the least-squares solution was repeated for different k_4 values using $k_4 = 0$ (50) 2000. The value resulting in the smallest residual was $k_4 = 900$. For this case the linear constants were calculated as $k_1 = 376$, $k_2 = 1.62$ and $k_3 = -0.42$. The curve fit was therefore

$$W(N, V^*) = \frac{376}{N^2 + 900} + 1.62 V^* - 0.42 \quad (4.34)$$

Since the wetness measures the wet fraction of the agglomerate it is necessary to restrict the curve fit such that $0 \leq W \leq 1$. This yields the following function:

$$W(N, V^*) = \begin{cases} 0 & \text{for } V^* \leq 0.26 - \frac{232}{N^2+900} \\ 1 & \text{for } V^* \geq 0.88 - \frac{232}{N^2+900} \\ \frac{376}{N^2+900} + 1.62 V^* - 0.42 & \text{otherwise} \end{cases} \quad (4.35)$$

The curve fit is shown superimposed on the original data in Figure 4.19.

Wet Binder Surface Area A_{binder}

Figure 4.17(a) shows a plot of A_{binder}^* against N for $s = 0$ and Figure 4.20 shows logarithm plots of these variables. For each V^* the function $\log A_{\text{binder}}$ was found to be approximately linear in $\log N$ [§]. It is observed that the spacing between the curves in Figure 4.20 decreases with increasing V^* and that the curves do not pass through the origin. This suggests a fit to the following family of curves:

$$\log A_{\text{binder}}^* = k_1 \log N + k_2 (V^*)^{k_3} + k_4 \quad (4.36)$$

where k_1 , k_2 , k_3 and k_4 are constants. The slope of the curve fit is k_1 , k_3 controls

[§]More complex functions can be used to model the curves in Figure 4.20. However, the overall curve fit, shown in Figure 4.21, was found to be similar (when compared to a linear fit of $\log A_{\text{binder}}^*$ against $\log N$). The linear curve fit was therefore used as it resulted in a simpler formula for $A_{\text{binder}}^* = A_{\text{binder}}^*(N, V^*)$.

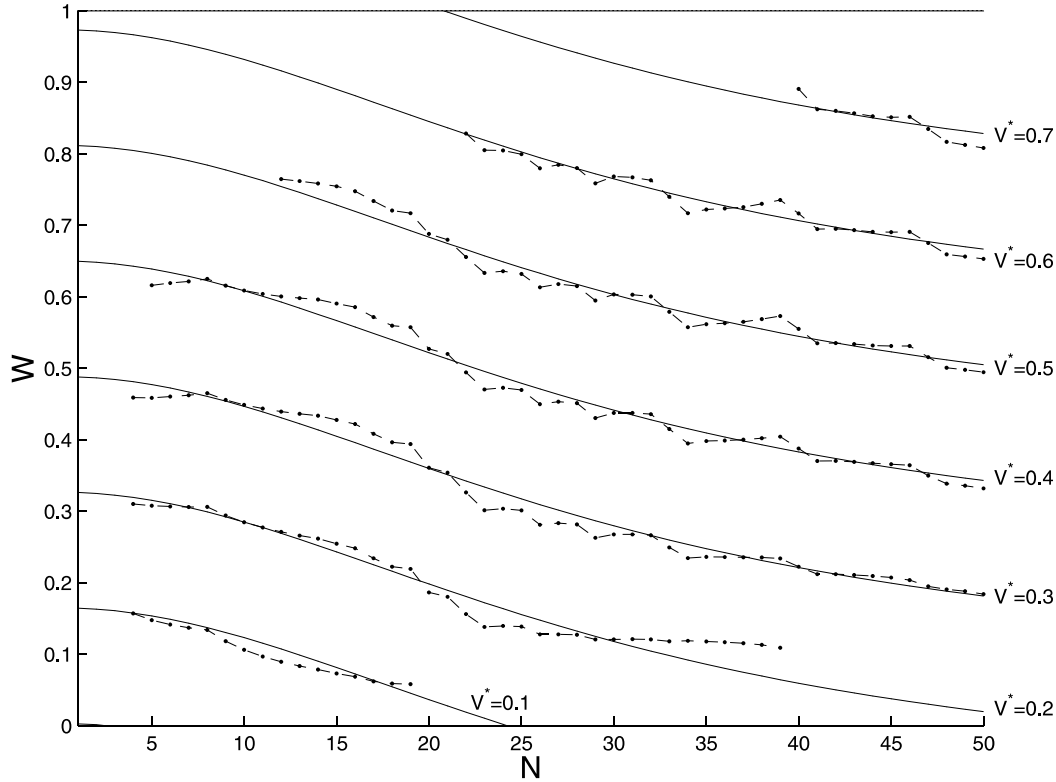


Figure 4.19: The curve fit for $W = W(N, V^*)$ for $s = 0$.

the spacing of the V^* curves, k_2 is the constant of proportionality between $(V^*)^{k_3}$ and $\log A_{\text{binder}}^*$ and k_4 is the vertical intercept. The terms k_1 , k_2 and k_4 are linear while k_3 is non-linear.

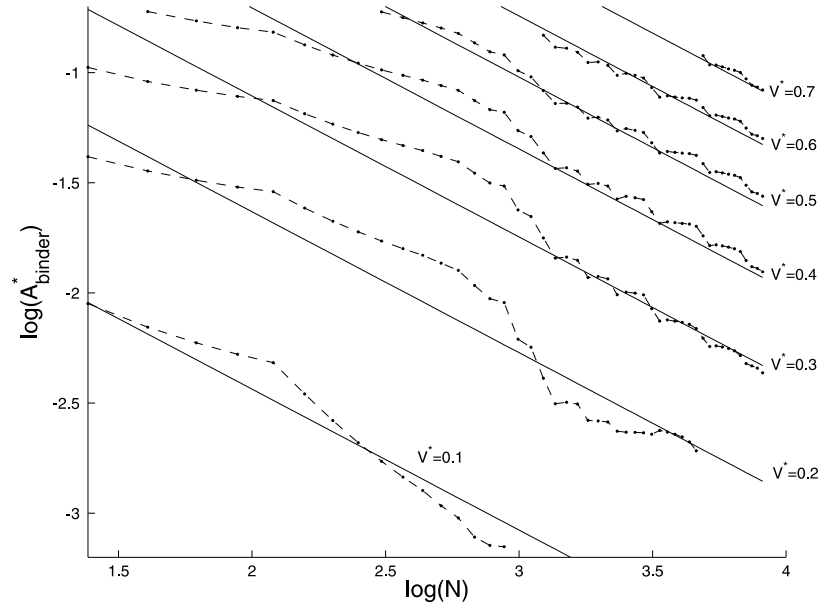
The constants in Equation (4.36) are determined by using the same approach as fitting curves to the surface wetness plot W . Using the datapoints from Figure 4.17, vectors W_i , N_i and V_i^* are formed where $1 \leq i \leq I$. The non-linear term k_3 is determined by repeating the linear least-squares solution to find the k_3 value which gives the smallest residual.

The matrix system formed is:

$$\begin{bmatrix} \log N_1 & V_1^* & 1 \\ \vdots & \vdots & \vdots \\ \log N_i & V_i^* & 1 \\ \vdots & \vdots & \vdots \\ \log N_I & V_I^* & 1 \end{bmatrix} \begin{bmatrix} k_1 \\ k_2 \\ k_4 \end{bmatrix} = \begin{bmatrix} \log (A_{\text{binder}}^*)_1 \\ \vdots \\ \log (A_{\text{binder}}^*)_i \\ \vdots \\ \log (A_{\text{binder}}^*)_I \end{bmatrix} \quad (4.37)$$

which we write as

$$A\hat{k} = \hat{L}. \quad (4.38)$$

Figure 4.20: Plot of $\log A_{\text{binder}}^*$ versus $\log N$.

Matrix left division in Matlab was used to solve Equation (4.38) for \hat{k} . The residual $|A\hat{k} - \hat{L}|$ was calculated for $k_3 = 0.1(0.1)1$ and found to be a minimum for $k_3 = 0.2$. For this case, the linear constants were calculated to be $k_1 = -0.64$, $k_2 = 8.59$ and $k_4 = -6.57$. Therefore, from Equation (4.36),

$$\log A_{\text{binder}}^* = -0.64 \log N + 8.59(V^*)^{0.2} - 6.57 \quad (4.39)$$

or

$$A_{\text{binder}}^* = N^{-0.64} e^{[8.59(V^*)^{0.2} - 6.57]} \quad (4.40)$$

The function from Equation (4.40) is shown superimposed on the original datapoints in Figure 4.21. The figure shows that $A_{\text{binder}}^* = 0.5$ is an upper bound for the data. The curve fit is accordingly defined as

$$A_{\text{binder}}^* = \min \left(N^{-0.64} e^{[8.59(V^*)^{0.2} - 6.57]}, 0.5 \right). \quad (4.41)$$

The population balance model in Chapter 5 uses A_{binder} to calculate the rate of binder drying. Since $A_{\text{binder}} = NA_{\text{solid}}A_{\text{binder}}^*$, it follows, for $R = 1$, that

$$A_{\text{binder}} = \min \left(4\pi N^{0.36} e^{[8.59(V^*)^{0.2} - 6.57]}, 2\pi \right). \quad (4.42)$$

Equations (4.35) and (4.42) are used in the population balance model of Chapter 5.

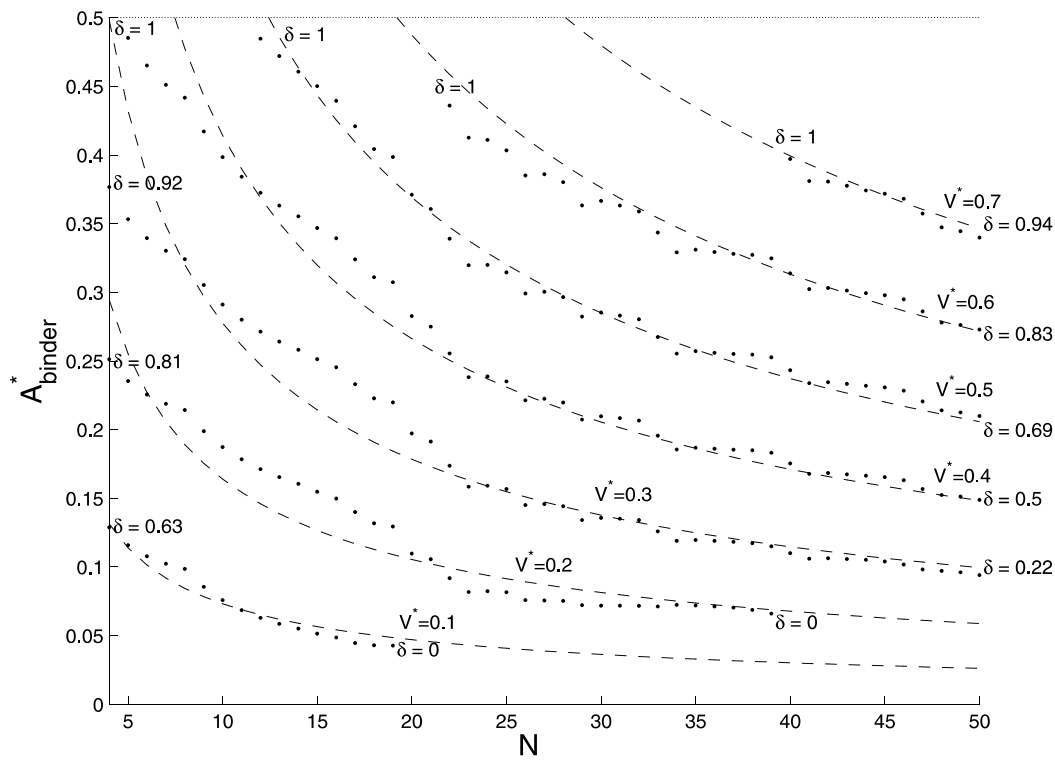


Figure 4.21: Plot of A_{binder}^* versus N .

4.11 Future Work

Images of wet granules taken under microscope could also be compared with the shape and fluid surface of agglomerates predicted by this model as shown in Figure 4.12.

Population Balance Modelling

5.1 Introduction

In 1917 Smoluchowski [48] developed a mathematical model for the coalescence of particles. He was studying the coalescence of liquid particles in a colloidal suspension. However, his model has since become established as the fundamental equation for population modelling of particle agglomeration and has been used in numerous studies such as the coalescence of aerosols, liquid droplets, snowflake formation, and the formation of planets and stars [57–59]. In this chapter the Smoluchowski model is extended to include the effects of binder fluid by adding a system of differential equations. These extensions to the model are new.

The Smoluchowski model is a population balance or flow-box model [11]. That is, only the number of particles of each size is recorded. The essence of the model is to track the flow of particles as they coalesce from one size to another. In contrast, simulations based on the distinct element method (DEM) use additional information, such as the position, velocity, and energy of the particles, in order to determine the criteria for particle coalescence [47, 60].

The Smoluchowski model is based on the following assumptions:

1. The total number of particles N is large.
2. Each particle is an agglomeration of an integer number of primary particles. Primary particles are of equal mass. Units are used so that the mass of a primary particle is 1. (An agglomerate formed by i primary particles is abbreviated as an ‘ i particle’.)

3. The particles are incompressible.
4. It is a continuous population model: positions, velocities, shapes, and the constitution of individual particles are disregarded. The only dependent variable is the real number $n_i(t)$ of particles of size i . The mass of particles of size i is denoted $m_i(t) = i n_i(t)$. The independent variables are particle size i (a positive integer) and time t (a non-negative real number).
5. Only two-particle (binary) collisions are possible.
6. Collisions occur continuously between particles of size i and j at a rate determined by $i, j, n_i(t)$ and $n_j(t)$.
7. For fixed particle sizes i and j , each i particle has an equal chance of colliding with a j particle.
8. Particles stick together when they collide.
9. Particles do not break apart.

Using the assumptions above the differential equations which govern the evolution of $n_i(t)$ are now derived.

Firstly the collision rate between i and j particles is determined. A different number of collisions occur depending on whether $i \neq j$ or $i = j$. When $i \neq j$, using assumption 7, each i particle may collide with a j particle to result in $n_j(t)$ collisions. Since there are $n_i(t)$ i particles the total number of collisions possible is $n_i(t) n_j(t)$. When $i = j$, collisions occur between particles in the same size category and care must be taken to avoid double counting. For $n_i(t)$ particles, the number of unique collisions is given by

$$(n_i - 1) + (n_i - 2) + \dots + 1 = \sum_{i=1}^{n_i-1} (n_i(t) - i) = \frac{1}{2} n_i(t) (n_i(t) - 1) \approx \frac{1}{2} n_i(t)^2 \quad (5.1)$$

because the ‘first’ particle may collide with $(n_i - 1)$ particles and the ‘second’ particle with $(n_i - 2)$ particles and so on. The approximation $n_i(t) - 1 \approx n_i(t)$ follows from assumption 1.

Using assumption 6, and the discussion above, the collision rate between i and j particles is $K_{i,j} n_i(t) n_j(t)$ when $i \neq j$ and $\frac{1}{2} K_{i,i} n_i(t)^2$ when $i = j$. The rate constants $K_{i,j}$ should depend smoothly on i and j and must obey $K_{i,j} = K_{j,i}$ and $K_{i,j} \geq 0$. The function K is called the coalescence kernel and it is determined by the modelling of physical processes [11]. Table 5.1 provides a list of kernels in the literature where K_0 is a constant.

<i>Name of the kernel</i>	<i>Physical application</i>	<i>Kernel</i>
Size-independent (random) [44,61]	Droplet coalescence Granulation	K_0
Product	Polymers	$K_0 ij$
Cross-sectional area (CSA)	Granulation	$K_0(i^{\frac{1}{3}} + j^{\frac{1}{3}})^2$
Equi-partition of kinetic energy (EPKE)	Granulation	$K_0(i^{-\frac{1}{2}} + j^{-\frac{1}{2}})$
Brownian motion [48]	Aerosols	$K_0(i^{\frac{1}{3}} + j^{\frac{1}{3}})(i^{-\frac{1}{3}} + j^{-\frac{1}{3}})$
Gravitational settling [62]	Aerosols	$K_0(i^{\frac{1}{3}} + j^{\frac{1}{3}})^2 i^{\frac{1}{3}} - j^{\frac{1}{3}} $ for $i^{\frac{1}{3}} > 50\mu m$ $K_0(i^{\frac{1}{3}} + j^{\frac{1}{3}})^2 i^{\frac{2}{3}} - j^{\frac{2}{3}} $ for $i^{\frac{1}{3}} < 50\mu m$
Polymerisation	Branched polymers	$K_0(i+c)(j+c)$ where c is a constant.
Kapur [63]	Granulation	$K_0 \frac{(i+j)^a}{(ij)^b}$ where a, b are constants.
Sastry [64]	Granulation	$K_0 \frac{(i^{\frac{2}{3}} + j^{\frac{2}{3}})}{\frac{1}{i} + \frac{1}{j}}$
Adetayo <i>et al.</i> [65]	Granulation	K_0 for $t \leq t_1$ $K_0 a(i+j)$ for $t > t_1$: a is constant.
Adetayo and Ennis [66]	Granulation	K_0 for $w \leq w^*$ 0 for $w > w^*$ where $w^* = \frac{(ij)^a}{(i+j)^b}$: a, b are constants.

Table 5.1: Table of coalescence kernels in the literature.

Smoluchowski took $K_{i,j} \equiv K_0$ so that all particles have an equal chance of colliding together. In this case the resulting equations of agglomeration can be solved analytically along with some simple size dependent kernels. In general, however, a numerical solution is required.

Above a flow-box model was discussed with particles leaving sizes i and j and entering size $i+j$. A differential equation for $n_l(t)$ is now derived by examining the rate at which particles enter and leave size l . Particles leave size l when collisions occur with any particle of size $m \geq 1$. When $m \neq l$, each l particle coalesces with a m particle and the rate of loss from size l is $K_{l,m}n_l(t)n_m(t)$. When $m = l$, $\frac{1}{2}K_{l,l}n_l(t)^2$ collisions occur but two particles leave size l for each collision. Therefore the rate of loss is $2 \times \frac{1}{2}K_{l,l}n_l(t)^2 = K_{l,l}n_l(t)^2$. The terms from both cases are the same which allows the total rate of particle loss from size l to be written as $n_l(t) \sum_{m=1}^{\infty} K_{l,m}n_m(t)$.

Particles enter size l when m and $(l-m)$ particles coalesce. The coalescence rate depends on whether l is even or odd. Two cases occur when l is even: (i) $m \neq l-m$ and (ii) $m = l-m$. For $m \neq l-m$, which occurs for $1 \leq m \leq \frac{l}{2} - 1$, the sizes m and $l-m$ differ and the rate of coalescence is $\sum_{m=1}^{\frac{l}{2}-1} K_{m,l-m}n_m(t)n_{l-m}(t)$. When $m = l-m$, or $m = \frac{l}{2}$, particles of the same size coalesce at the rate of $\frac{1}{2}K_{\frac{l}{2},\frac{l}{2}}n_{\frac{l}{2}}(t)^2$ (from above). When l is odd, coalescence occurs for $m \neq l-m$, or $1 \leq m \leq \frac{l-1}{2}$, and the rate of coalescence is $\sum_{m=1}^{\frac{l-1}{2}} K_{m,l-m}n_m(t)n_{l-m}(t)$.

From the discussion above, the differential equations for the even case are:

$$\frac{dn_l}{dt} = \frac{1}{2}K_{\frac{l}{2}, \frac{l}{2}} n_{\frac{l}{2}}(t)^2 + \sum_{m=1}^{\frac{l}{2}-1} K_{m, l-m} n_m(t) n_{l-m}(t) - n_l(t) \sum_{m=1}^{\infty} K_{l,m} n_m(t), \quad (5.2)$$

and, for the odd case,

$$\frac{dn_l}{dt} = \sum_{m=1}^{\frac{l-1}{2}} K_{m, l-m} n_m(t) n_{l-m}(t) - n_l(t) \sum_{m=1}^{\infty} K_{l,m} n_m(t). \quad (5.3)$$

Equations (5.2) and (5.3) may be combined into a single differential equation by use of the symmetry property of the kernel, $K_{m, l-m} = K_{l-m, m}$. For the even case, the first sum in Equation (5.2) may be written

$$\begin{aligned} \sum_{m=1}^{\frac{l}{2}-1} K_{m, l-m} n_m(t) n_{l-m}(t) &= \sum_{m=\frac{l}{2}+1}^{l-1} K_{l-m, m} n_{l-m}(t) n_m(t) \\ &= \frac{1}{2} \sum_{m=1}^{l-1} K_{m, l-m} n_m(t) n_{l-m}(t). \end{aligned} \quad (5.4)$$

Similarly, for odd l , from Equation (5.3),

$$\begin{aligned} \sum_{m=1}^{\frac{l-1}{2}} K_{m, l-m} n_m(t) n_{l-m}(t) &= \sum_{m=\frac{l+1}{2}}^{l-1} K_{l-m, m} n_{l-m}(t) n_m(t) \\ &= \frac{1}{2} \sum_{m=1}^{l-1} K_{m, l-m} n_m(t) n_{l-m}(t). \end{aligned} \quad (5.5)$$

Combining Equation (5.4) with Equation (5.2) and Equation (5.5) with Equation (5.3) gives a system of ordinary differential equations which we call the Smoluchowski equations:

$$\frac{dn_l}{dt} = \frac{1}{2} \sum_{m=1}^{l-1} K_{m, l-m} n_m(t) n_{l-m}(t) - n_l(t) \sum_{m=1}^{\infty} K_{l,m} n_m(t). \quad (5.6)$$

We solve these equations subject to the initial condition of $N_0 \equiv n_1(0)$ and $n_i(0) = 0$ for $i > 1$ where N_0 denotes the initial number of particles.

Proposition 5.1 Equation (5.6) conserves total mass $M = \sum_{l=1}^{\infty} l n_l$.

Proof: We prove this by showing that $\frac{dM}{dt} = 0$.

Now

$$\begin{aligned} \frac{dM}{dt} &= \frac{d}{dt} \left(\sum_{l=1}^{\infty} m_l(t) \right) \\ &= \frac{d}{dt} \left(\sum_{l=1}^{\infty} l n_l(t) \right) \\ &= \sum_{l=1}^{\infty} \left(\frac{l}{2} \sum_{m=1}^{l-1} K_{m,l-m} n_m(t) n_{l-m}(t) - l n_l(t) \sum_{m=1}^{\infty} K_{l,m} n_m(t) \right). \end{aligned} \quad (5.7)$$

The first sum adds diagonal entries of K while the second sums along rows of K . The summation order of the first sum may be changed to match that of the second by introducing new indices p and q where $p = m$ and $q = l - m$. Then

$$\begin{aligned} \sum_{l=1}^{\infty} \sum_{m=1}^{l-1} l K_{m,l-m} n_m(t) n_{l-m}(t) &= \sum_{m=1}^{\infty} \sum_{l=m+1}^{\infty} l K_{m,l-m} n_m(t) n_{l-m}(t) \\ &= \sum_{p=1}^{\infty} \sum_{q=1}^{\infty} (p+q) K_{p,q} n_p(t) n_q(t). \end{aligned} \quad (5.8)$$

Substituting Equation (5.8) into Equation (5.7) gives

$$\frac{dM}{dt} = \sum_{p=1}^{\infty} \sum_{q=1}^{\infty} \frac{p+q}{2} K_{p,q} n_p(t) n_q(t) - \sum_{p=1}^{\infty} \sum_{q=1}^{\infty} p K_{p,q} n_p(t) n_q(t). \quad (5.9)$$

But now

$$\begin{aligned} \sum_{p=1}^{\infty} \sum_{q=1}^{\infty} p K_{p,q} n_p(t) n_q(t) &= \sum_{p=1}^{\infty} \sum_{q=1}^{\infty} q K_{q,p} n_q(t) n_p(t) \\ &= \frac{1}{2} \left(\sum_{p=1}^{\infty} \sum_{q=1}^{\infty} p K_{p,q} n_p(t) n_q(t) + \sum_{p=1}^{\infty} \sum_{q=1}^{\infty} q K_{q,p} n_q(t) n_p(t) \right) \\ &= \sum_{p=1}^{\infty} \sum_{q=1}^{\infty} \frac{p+q}{2} K_{p,q} n_p(t) n_q(t). \end{aligned} \quad (5.10)$$

Substituting Equation (5.10) into Equation (5.9) gives the result. ■

Due to particle coalescence the total number of particles in the system N is not conserved. However, it can be shown that N decays, and, when $K_{l,m} \equiv K_0$, the total number of particles may be calculated.

Proposition 5.2 *Let $N = \sum_{l=1}^{\infty} n_l$ be the total number of particles. Then $\frac{dN}{dt} \leq 0$.*

Proof:

$$\begin{aligned}
\frac{dN}{dt} &= \frac{d}{dt} \left(\sum_{l=1}^{\infty} n_l \right) = \sum_{l=1}^{\infty} \frac{dn_l}{dt} \\
&= \sum_{l=1}^{\infty} \left(\frac{1}{2} \sum_{m=1}^{l-1} K_{m,l-m} n_m(t) n_{l-m}(t) - \sum_{m=1}^{\infty} K_{l,m} n_l(t) n_m(t) \right) \\
&= \frac{1}{2} \sum_{p=1}^{\infty} \sum_{q=1}^{\infty} K_{p,q} n_p(t) n_q(t) - \sum_{l=1}^{\infty} \sum_{m=1}^{\infty} K_{l,m} n_l(t) n_m(t) \\
&= - \sum_{p=1}^{\infty} \sum_{q=1}^{\infty} \frac{1}{2} K_{p,q} n_p(t) n_q(t) \\
&\leq 0. \quad \blacksquare
\end{aligned} \tag{5.11}$$

Corollary 5.3 *For the size-independent kernel, $K_{l,m} \equiv K_0$, the total number of particles is given by*

$$N(t) = \frac{2N_0}{K_0 N_0 t + 2}. \tag{5.12}$$

Proof: From Equation (5.11), for $K_{p,q} \equiv K_0$,

$$\begin{aligned}
\frac{dN}{dt} &= -\frac{K_0}{2} \sum_{p=1}^{\infty} \sum_{q=1}^{\infty} n_p(t) n_q(t) \\
&= -\frac{K_0}{2} \left[\sum_{p=1}^{\infty} \left(n_p(t)^2 + 2n_p(t) \sum_{q=1}^{p-1} n_q(t) \right) \right] \\
&= -\frac{K_0}{2} \left(\sum_{p=1}^{\infty} n_p(t) \right)^2 \\
&= -\frac{K_0}{2} N^2.
\end{aligned} \tag{5.13}$$

Integrating Equation (5.13) gives Equation (5.12). \blacksquare

Corollary 5.4 *The mean particle size \bar{i} is increasing.*

Proof: Now

$$\bar{i} = \frac{M}{N} = \frac{\sum_{l=1}^{\infty} l n_l}{\sum_{l=1}^{\infty} n_l}.$$

The total mass $M = \sum_{l=1}^{\infty} l n_l$ is constant. From Proposition 5.2, N is decreasing and the result follows. ■

To illustrate how the predictions of the model depend on the coalescence kernel, Equation (5.6) was solved using (i) the size-independent kernel $K_{l,m} \equiv K_0 = 4$ and (ii) the cross-sectional area dependent kernel $K_{l,m} \equiv (l^{\frac{1}{3}} + m^{\frac{1}{3}})^2$. Both kernels are discussed below. (Since the values of $K_{1,1}$ are equal the kernels may be compared.) The initial condition used was $N_0 \equiv n_1(0) = 1000$. Figure 5.1 plots the change in number of particles, with respect to time, for $K_{l,m} = K_0 \equiv 4$. The total number of particles N and the evolution of particles in the first four size categories (n_1, n_2, n_3 and n_4) are shown. The N curve was evaluated numerically using Matlab and analytically using Equation (5.12). Agreement was obtained with both solutions.

Figure 5.2 shows number distribution plots with respect to size for different times t . The corresponding mass distributions, where $m_i = i n_i$, are shown in Figure 5.3.

From these graphs the following features and comparisons are noted:

1. The mean particle size \bar{i} of the distributions is observed to be increasing. (This observation was proved by Corollary 5.4.) The variance in the distributions is observed to be increasing.
2. The total number of particles N is observed to be decreasing because the area under the N curve in Figure 5.1 decreases with time. (This observation was proved by Proposition 5.2.)
3. By numerically evaluating the area under the mass curves in Figure 5.3, it was found that the total mass M is constant. (This observation was proved by Proposition 5.1.)
4. Coalescence occurs at a faster rate for the $K_{l,m} \equiv (l^{\frac{1}{3}} + m^{\frac{1}{3}})^2$ kernel because $K_{l,m} \equiv 4 \leq K_{l,m} \equiv (l^{\frac{1}{3}} + m^{\frac{1}{3}})^2$ for all l and m . By comparing the area under the number density curves in Figure 5.2, the decay rate of total particles N is higher for the cross-sectional area kernel. This also causes the shape of the two distributions to differ; for instance, a peak develops in the mass distribution for $K_{l,m} \equiv (l^{\frac{1}{3}} + m^{\frac{1}{3}})^2$ but not for $K_{l,m} \equiv K_0 = 4$.

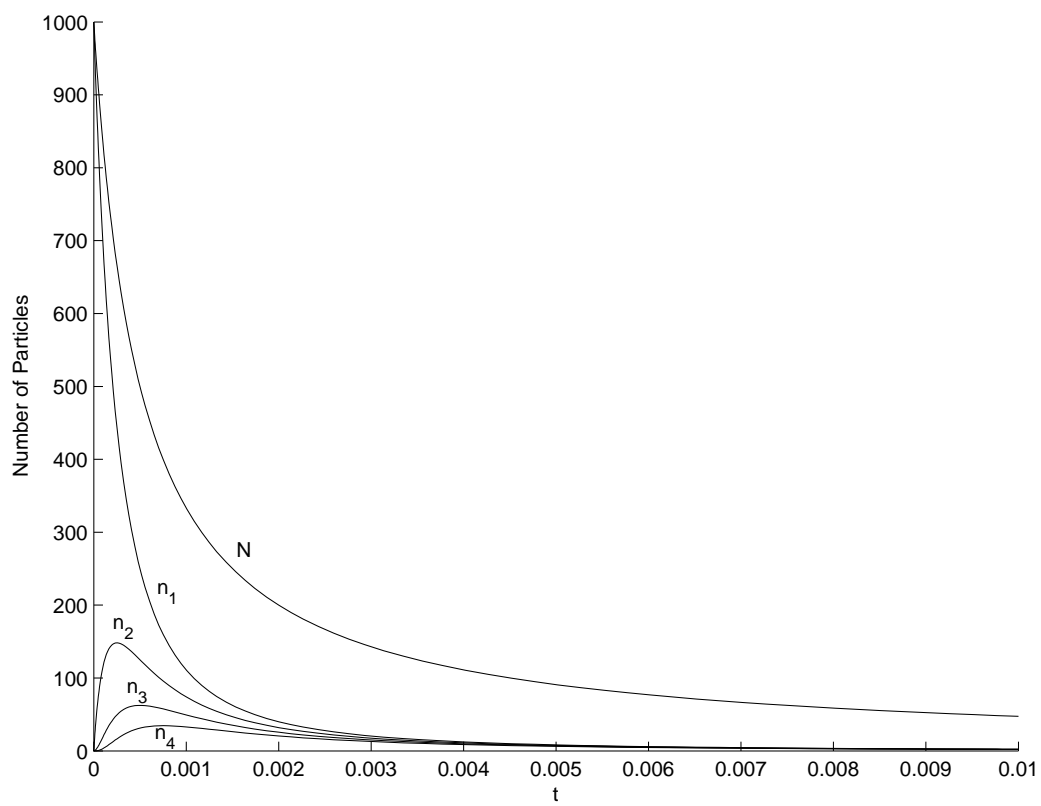


Figure 5.1: Plot showing the change in the number of particles for $K_{l,m} \equiv K_0 = 4$ using the initial condition $N_0 \equiv n_1(0) = 1000$. N refers to the total number of particles and n_1, n_2, n_3 and n_4 to the first four size categories.

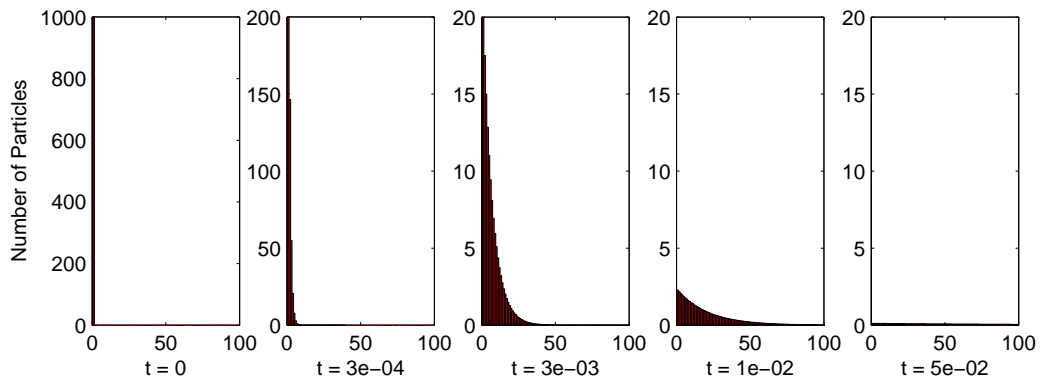
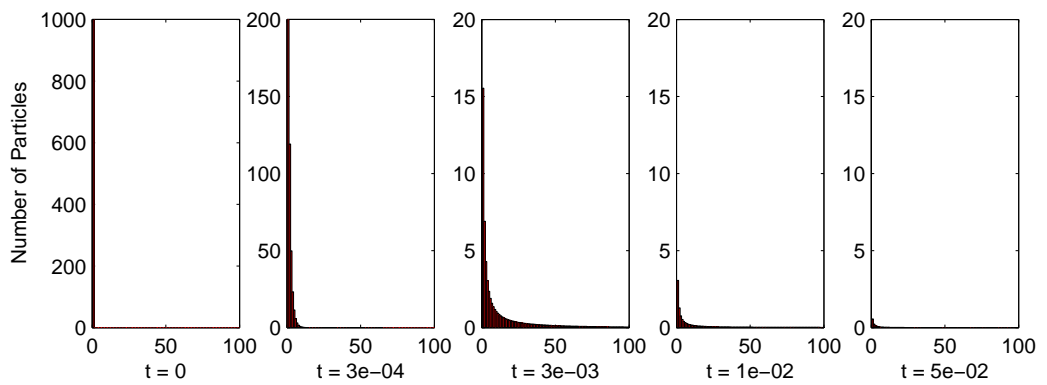
(a) $K_{l,m} \equiv K_0 = 4$.(b) $K_{l,m} \equiv (l^{\frac{1}{3}} + m^{\frac{1}{3}})^2$

Figure 5.2: Plots showing the evolution of numbers of particles for (a) $K_{l,m} \equiv K_0 = 4$ and (b) $K_{l,m} \equiv (l^{\frac{1}{3}} + m^{\frac{1}{3}})^2$. Size is plotted on the horizontal axis. Figure 5.3 shows the corresponding mass distribution plots, where $m_i = in_i$, with respect to particle size. Note that the vertical axis scale changes with time.

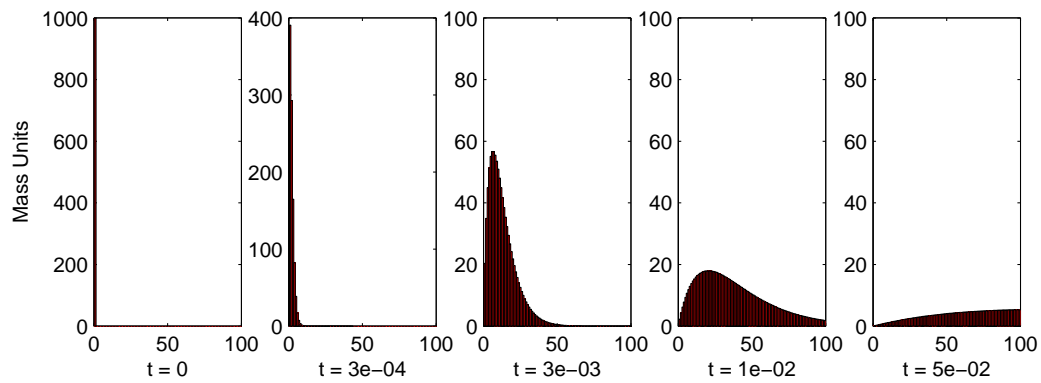
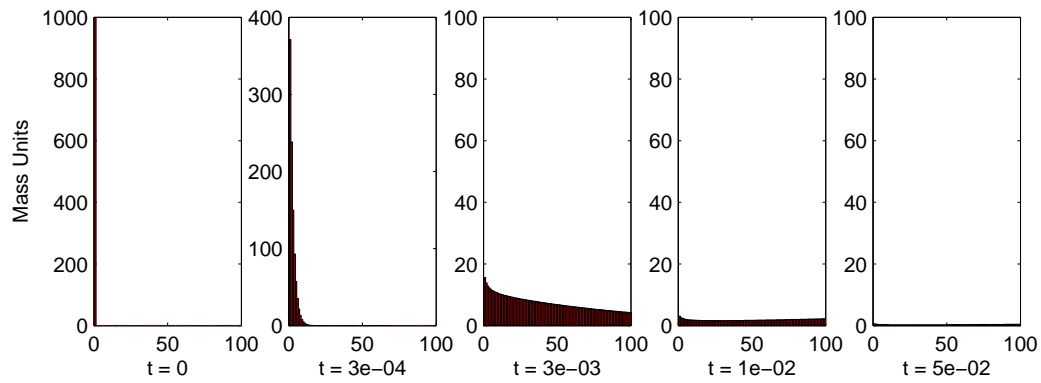
(a) $K_{l,m} \equiv K_0 = 4$.(b) $K_{l,m} \equiv (l^{\frac{1}{3}} + m^{\frac{1}{3}})^2$

Figure 5.3: Plots showing the evolution of the mass distribution for (a) $K_{l,m} \equiv K_0 = 4$ and (b) $K_{l,m} \equiv (l^{\frac{1}{3}} + m^{\frac{1}{3}})^2$. The relationship between mass and particle number is $m_i = in_i$. Note that the vertical axis scale changes with time.

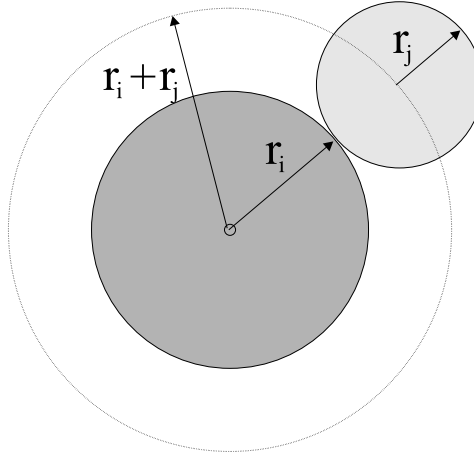


Figure 5.4: Particles of size i and j colliding, where $r_i \propto i^{\frac{1}{3}}$ and $r_j \propto j^{\frac{1}{3}}$, for the cross-sectional area kernel $K_{i,j} = K_0(i^{\frac{1}{3}} + j^{\frac{1}{3}})^2$.

To conclude this section, we now provide several examples to illustrate how the coalescence kernels $K_{l,m}$ may be derived:

1. Product

This kernel applies to the coalescence of thin, straight-line (one dimensional) polymers undergoing motion in \mathbb{R}^3 . The size of the particles is given by the number of monomer units. As two particles come nearby their relative motion may be traced out by a ribbon. If the ribbon self-intersects then the particles collide. The chance of intersection is proportional to each of the lengths separately. The chance of coalescence is therefore proportional to their product. Therefore $K_{i,j} \equiv K_0 ij$.

2. Cross-Sectional Area (CSA)

For this kernel the chance of coalescence is determined by the effective cross-sectional area of particles. In Figure 5.4 non-deformable particles i and j are considered with respective radii r_i and r_j . If particles of different sizes also have similar shapes, then, from assumptions 2 and 3, $r_i \propto i^{\frac{1}{3}}$ and $r_j \propto j^{\frac{1}{3}}$. A rest frame is used where the i particle is motionless. The particles touch if the centre of the j particle, at the closest approach of the centre of mass of the arrangement, lies within in the circle $r_i + r_j$. The coalescence kernel is therefore given by $K_{i,j} \equiv K_0(r_i + r_j)^2 = K_0(i^{\frac{1}{3}} + j^{\frac{1}{3}})^2$.

3. Equi-Partition of Kinetic Energy (EPKE)

This kernel applies to distributions where the kinetic energy is distributed evenly amongst the particles. An i particle at velocity v_i has kinetic energy $E = \frac{1}{2}iv_i^2$ and therefore $v_i \propto i^{-\frac{1}{2}}$. Similarly $v_j \propto j^{-\frac{1}{2}}$. If it is assumed that the mutual velocities of colliding particles add together then $K_{i,j} = K_0(i^{-\frac{1}{2}} + j^{-\frac{1}{2}})$.

5.2 Modelling the Effects of Binder Fluid

We now extend the Smoluchowski model to model the presence of a binder fluid. The additional assumptions for the extended model are as follows:

1. Adapting assumption 4 from the model in Section 5.1, a new dependent variable $b_i(t)$ (a real number) is added to represent the total wet binder mass of particles of size i . Particles of the same size are assumed to contain the same amount of binder. Therefore each i particle contains $B_i(t) = \frac{b_i(t)}{n_i(t)}$ units of binder.
2. Wet binder is assumed to dry into solid binder which then remains to form solid bridges between particles. Solid binder is not tracked in the model. The rate of drying of i particles depends only on i and $b_i(t)$. Therefore particles of the same size dry at the same rate.
3. Each collision has a chance of sticking which depends only on $i, j, B_i(t)$ and $B_j(t)$.
4. Binder is transferred only when particles coalesce.
5. If either particle in a binary collision becomes more wet then the chance of sticking can not decrease.
6. Binder combines (or adds) together as particles coalesce.
7. Two completely dry particles can not stick.

The coalescence kernel is now modified to incorporate the above assumptions into the extended model. From assumption 3, the *sticking efficiency function* is introduced as

$$\Phi_{i,j} = \Phi(i, j, B_i(t), B_j(t)) \quad (5.14)$$

where $0 \leq \Phi_{i,j} \leq 1$. This function gives the probability that i and j particles coalesce together following a collision. (The original Smoluchowski model corresponds to $\Phi_{i,j} \equiv 1$ because all particles coalesce upon collision.) In developing the extended model, we also separate the size-independent K_0 and size-dependent $K_{i,j}$ components of the coalescence kernel, writing the effective coalescence kernel as

$$\hat{K}_{i,j} \equiv K_0 K_{i,j} \Phi_{i,j}. \quad (5.15)$$

The product $K_0 K_{i,j}$ is called the *collision rate function*. Substituting $\hat{K}_{i,j}$ from Equation (5.15) into Equation (5.6) gives

$$\begin{aligned} \frac{dn_l}{dt} &= \frac{1}{2} \sum_{m=1}^{l-1} \hat{K}_{m,l-m} n_m(t) n_{l-m}(t) - n_l(t) \sum_{m=1}^{\infty} \hat{K}_{l,m} n_m(t) \\ &= \frac{K_0}{2} \sum_{m=1}^{l-1} K_{m,l-m} \Phi_{m,l-m} n_m(t) n_{l-m}(t) - K_0 n_l(t) \sum_{m=1}^{\infty} K_{l,m} \Phi_{l,m} n_m(t). \end{aligned} \quad (5.16)$$

To eliminate an overall time scaling factor from the model, we now divide Equation (5.16) by K_0 to give

$$\frac{dn_l(t)}{d(K_0 t)} = \frac{1}{2} \sum_{m=1}^{l-1} K_{m,l-m} \Phi_{m,l-m} n_m(t) n_{l-m}(t) - n_l(t) \sum_{m=1}^{\infty} K_{l,m} \Phi_{l,m} n_m(t). \quad (5.17)$$

Equation (5.17) is the system of differential equations for the movement of particles in the extended model. We now derive associated differential equations for the movement of wet binder fluid. To do this, consider the binary coalescence of m and $(l-m)$ particles. From assumption 1, these particles contain, respectively, $B_m(t)$ and $B_{l-m}(t)$ units of binder. If these particles coalesce, then, from assumption 4, $B_m(t)$ units of binder depart size m , $B_{l-m}(t)$ units of binder depart size $l-m$ and $B_m(t) + B_{l-m}(t)$ units of binder enter into size l . From assumption 2, the rate of drying of particles of size l depends on l and $b_l(t)$. The *drying rate* is defined as $D_0 D_l(b_l(t))$ where D_0 is the size-independent component of the drying function and $D_l(b_l(t)) \geq 0$ is the size-dependent portion.

Since binder is transferred as particles coalesce, it follows, from Equation (5.17), and the discussion above, that

$$\begin{aligned} \frac{db_l(t)}{d(K_0 t)} &= \frac{1}{2} \sum_{m=1}^{l-1} K_{m,l-m} \Phi_{m,l-m} n_m(t) n_{l-m}(t) [B_m(t) + B_{l-m}(t)] \\ &\quad - n_l(t) B_l(t) \sum_{m=1}^{\infty} K_{l,m} \Phi_{l,m} n_m(t) - \frac{D_0}{K_0} D_l(b_l(t)). \end{aligned} \quad (5.18)$$

After simplification, Equation (5.18) becomes

$$\begin{aligned} \frac{db_l(t)}{d(K_0 t)} &= \frac{1}{2} \sum_{m=1}^{l-1} K_{m,l-m} \Phi_{m,l-m} [n_{l-m}(t) b_m(t) + n_m(t) b_{l-m}(t)] \\ &\quad - b_l(t) \sum_{m=1}^{\infty} K_{l,m} \Phi_{l,m} n_m(t) - \frac{D_0}{K_0} D_l(b_l(t)). \end{aligned} \quad (5.19)$$

The active parameter $\frac{D_0}{K_0}$ is called the *drying-to-collision ratio*.

Equations (5.17) and (5.19) are the system of equations for the extended model. They provide a powerful and flexible means for the modelling of wet granulation.

Proposition 5.5 *If there is no drying ($D_l(b_l(t)) = 0$ for all l) then the total wet binder mass $\bar{B} = \sum_{l=1}^{\infty} b_l$ is conserved by Equation (5.19).*

Proof:

$$\begin{aligned}
\frac{d\bar{B}}{dt} &= \frac{d}{dt} \left(\sum_{l=1}^{\infty} b_l(t) \right) = K_0 \sum_{l=1}^{\infty} \frac{db_l(t)}{d(K_0 t)} \\
&= K_0 \left(\frac{1}{2} \sum_{l=1}^{\infty} \sum_{m=1}^{l-1} K_{m,l-m} \Phi_{m,l-m} [n_{l-m} b_m + n_m b_{l-m}] - \sum_{l=1}^{\infty} \sum_{m=1}^{\infty} K_{l,m} \Phi_{l,m} n_m b_l \right) \\
&= K_0 \left(\frac{1}{2} \sum_{m=1}^{\infty} \sum_{l=m+1}^{\infty} K_{m,l-m} \Phi_{m,l-m} [n_{l-m} b_m + n_m b_{l-m}] - \sum_{l=1}^{\infty} \sum_{m=1}^{\infty} K_{l,m} \Phi_{l,m} n_m b_l \right) \quad (5.20) \\
&= K_0 \left(\frac{1}{2} \sum_{p=1}^{\infty} \sum_{q=1}^{\infty} K_{p,q} \Phi_{p,q} [n_q b_p + n_p b_q] - \sum_{p=1}^{\infty} \sum_{q=1}^{\infty} K_{p,q} \Phi_{p,q} n_q b_p \right) \\
&= 0 \quad \blacksquare
\end{aligned}$$

Corollary 5.6 *If there is drying ($D_0 D_l(b_l(t)) \neq 0$ for all l) then the total wet binder mass $\bar{B} = \sum_{l=1}^{\infty} b_l$ decreases.*

Proof: Using Equation (5.19),

$$\begin{aligned}
\frac{d\bar{B}}{dt} &= \frac{d}{dt} \left(\sum_{l=1}^{\infty} b_l(t) \right) = K_0 \sum_{l=1}^{\infty} \frac{db_l(t)}{d(K_0 t)} \\
&= K_0 \left[\frac{1}{2} \sum_{l=1}^{\infty} \sum_{m=1}^{l-1} K_{m,l-m} \Phi_{m,l-m} [n_{l-m} b_m + n_m b_{l-m}] - \sum_{l=1}^{\infty} \sum_{m=1}^{\infty} K_{l,m} \Phi_{l,m} n_m b_l \right] \\
&\quad - D_0 \sum_{l=1}^{\infty} D_l(b_l(t)) \quad (5.21)
\end{aligned}$$

From Equation (5.20) the term in square brackets in Equation (5.21) is equal to zero. Therefore

$$\frac{d\bar{B}}{dt} = -D_0 \sum_{l=1}^{\infty} D_l(b_l(t)) \quad (5.22)$$

and the result follows. \blacksquare

To investigate solutions to the agglomeration model, functions $K_{i,j}$, $\Phi_{i,j}$ and D_i are required to close Equations (5.17) and (5.19). To achieve this, two different models are

proposed: ‘Model 1’ is based on a minimal set of assumptions and uses only the variables introduced so far in this chapter while ‘Model 2’ uses functions derived from the geometric model of Chapter 4 and makes use of additional variables. Both models are investigated for the collision rate functions (a) $K_{l,m} \equiv lm$ (product), (b) $K_{l,m} \equiv (l^{\frac{1}{3}} + m^{\frac{1}{3}})^2$ (cross-sectional area, CSA), (c) $K_{l,m} \equiv 1$ (size-independent) and (d) $K_{l,m} \equiv (i^{-\frac{1}{2}} + j^{-\frac{1}{2}})$ (equi-partition of kinetic energy, EPKE).

Model 1

The following assumptions determine $\Phi_{i,j}$ and D_i :

1. The stickiness of an i particle is proportional to $B_i(t)$.
2. The stickiness of an i particle is inversely proportional to size i .
3. The stickiness of particles is additive in a binary collision.
4. The drying rate of i particles is proportional to $B_i(t)$.
5. The drying rate of i particles is inversely proportional to size i .
6. The drying rate of i particles is proportional to surface area.

Assumption 1 is a minimal assumption where the stickiness of a particle is determined by the amount of binder it contains. For assumption 2, an i particle containing a fixed amount of binder fluid $B_i(t)$ was considered. It was estimated that if the size of the particle was doubled to $2i$ then it was reasonable for the stickiness of the particle to approximately halve. Similar reasoning was used to obtain assumption 5.

From assumptions 1-3 the sticking efficiency function is

$$\Phi_{i,j} = \min \left\{ \Phi_0 \left(\frac{B_i}{i} + \frac{B_j}{j} \right), 1 \right\} \quad (5.23)$$

where Φ_0 is a constant. The results presented in Section 5.4 take $\Phi_0 \equiv 1$.

From assumptions 4-6 the drying rate of i particles is inversely proportional to the relative wet fraction of i particles and proportional to the particle surface area. Therefore

$$\begin{aligned} D_i(B_i) &= \frac{B_i(t)}{i} i^{\frac{2}{3}} \\ &= i^{-\frac{1}{3}} B_i(t). \end{aligned} \quad (5.24)$$

Model 2

This model uses functions derived from the geometric model, presented in Chapter 4, for the maximum consolidated case of $s = 0$ (c.f. Section 4.10).

The following assumptions determine $\Phi_{i,j}$ and D_i :

1. Particles have the same shape and properties as those generated by the geometric model for the case of $s = 0$.
2. The stickiness of an i particle is given by the surface wetness of an i particle, W_i .
3. Particles have a probability of coalescence unless they are both dry at the point of contact.
4. The rate of drying of an i particle, $D_i(b_i(t))$, is proportional to the wet agglomerate surface area $(A_{\text{binder}})_i$.
5. Internal drying of the binder does not occur.

For assumption 1, from Equation 4.35, the surface wetness of particles, as a function of the fluid-to-solid ratio V^* for $s = 0$, is given by

$$W(i, V^*) = \begin{cases} 0 & \text{for } V^* \leq 0.26 - \frac{232}{i^2+900} \\ 1 & \text{for } V^* \geq 0.88 - \frac{232}{i^2+900} \\ \frac{376}{i^2+900} + 1.62 V^* - 0.42 & \text{otherwise.} \end{cases} \quad (5.25)$$

To convert B_i (in mass units) to the fluid-to-solid volume ratio V^* , the formula

$$V^* = \frac{b_i/\rho_b}{i/\rho_p} = B_i \frac{\rho_p}{\rho_b} \quad (5.26)$$

is applied where ρ_p and ρ_b are the particle and binder densities. For the results in Section 5.4, the values $\rho_p = \rho_b = 1$ were used.

For assumptions 2 and 3, the following function, which permits coalescence from wet-wet and wet-dry particle collisions, but not from dry-dry collisions, is proposed for the sticking efficiency function $\Phi_{i,j}$:

$$\begin{aligned} \Phi_{i,j}(B_i(t), B_j(t)) &= W_i W_j + (1 - W_j) W_i + W_j (1 - W_i) \\ &= 1 - (1 - W_i)(1 - W_j). \end{aligned} \quad (5.27)$$

(The conversion from B to V^* using Equation (5.26) is implied when using Equation (5.27).)

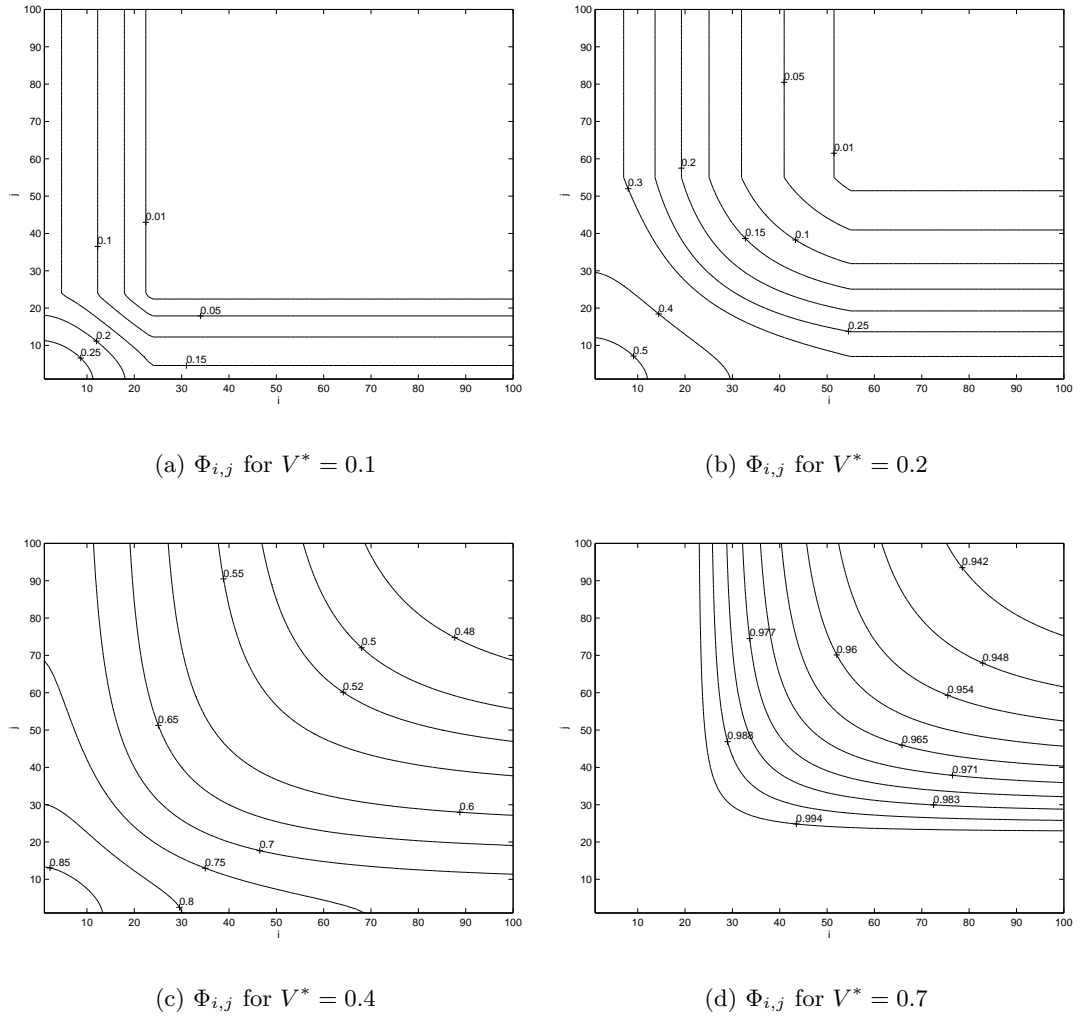


Figure 5.5: Contour plot of $\Phi_{i,j}$ for Model 2 for colliding particles of size i and j . The values on the contours are values of $\Phi_{i,j}$. Individual plots correspond to different values of the fluid-to-solid ratio V^* .

Figure 5.5 shows plots of $\Phi_{i,j}$ for colliding particles of size i and j . The values on the contours are values of $\Phi_{i,j}$. The individual plots (a)-(d) correspond to different values of the fluid-to-solid ratio V^* . (Straight lines occur in plots (a) and (b) because we limit W_i such that $0 \leq W_i \leq 1$ from Equation (5.25).)

From assumption 4, the rate of drying is proportional to the wet surface area of agglomerates A_{binder} . From Equation (4.42), the drying function is given by

$$D_l(b_l(t)) = \min \left\{ 4\pi l^{0.36} e^{[8.59(V_l^*)^{0.2} - 6.57]}, 2\pi \right\}. \quad (5.28)$$

The results from Models 1 and 2 are presented in Section 5.4.

5.3 Numerical Solution

The steps taken to solve Equations (5.17) and (5.19) numerically are now discussed.

The maximum particle size is restricted to a finite limit of s_{\max} (a positive integer). Following this, Equations (5.17) and (5.19) are written as

$$\frac{dn_l}{d(K_0 t)} = \frac{1}{2} \sum_{m=1}^{l-1} K_{m,l-m} \Phi_{m,l-m} n_m(t) n_{l-m}(t) - n_l(t) \sum_{m=1}^{s_{\max}} K_{l,m} \Phi_{l,m} n_m(t) \quad (5.29)$$

and

$$\begin{aligned} \frac{db_l(t)}{d(K_0 t)} = & \frac{1}{2} \sum_{m=1}^{l-1} K_{m,l-m} \Phi_{m,l-m} [n_{l-m}(t) b_m(t) + n_m(t) b_{l-m}(t)] \\ & - \sum_{m=1}^{s_{\max}} K_{l,m} \Phi_{l,m} n_m(t) b_l(t) - \frac{D_0}{K_0} D_l(b_l(t)) \end{aligned} \quad (5.30)$$

where $1 \leq l \leq s_{\max}$.

Introducing the finite limit on particle size breaks mass conservation near the s_{\max} boundary. To illustrate, consider particles of size k and l where $k \leq s_{\max}$, $l \leq s_{\max}$ but $k + l > s_{\max}$. In this case, particles can leave sizes k and l but no balancing entry term occurs because size $k + l$ does not exist. This mass loss is permitted, however, because if collisions are restricted based on the arbitrary choice of s_{\max} , boundary effects are introduced into the equations, which causes the profile and properties of the distributions to change with the choice of s_{\max} . In practice a suitable value of s_{\max} is required to minimise the mass loss.

The populations reach steady-state when all the wet binder dries into solid binder (as given by assumption 2 of Section 5.2). The loss of wet binder, due to drying, is given by $\frac{\bar{B}(t)}{M(t)}$ where $\bar{B}(t)$ and $M(t)$ denote, respectively, the total binder and particle mass in the simulation at time t . Binder loss due to particles exceeding s_{\max} does not affect $\frac{\bar{B}(t)}{M(t)}$, because each pair of coalescing particles of size k and l , where $k + l > s_{\max}$, depart the simulation with a net total of $B_k(t) + B_l(t)$ units of binder (by Equation (5.19)). This proportionally decreases $\bar{B}(t)$ and $M(t)$ such that $\frac{\bar{B}(t)}{M(t)}$ remains constant. The steady-state termination condition is therefore

$$\frac{\bar{B}(t)}{M(t)} \leq \epsilon \quad (5.31)$$

where $\epsilon > 0$ is a numerical tolerance. The results presented in Section 5.4 used $\epsilon = 0.01$ corresponding to drying of $\geq 99\%$ of the wet binder at the steady-state condition.

The results in Section 5.4 present a solution space where the fluid-to-solid ratio V^* and the drying-to-collision ratio $\frac{D_0}{K_0}$ are parameters. For given values of V^* and $\frac{D_0}{K_0}$, the following solution technique was used to obtain a steady-state mass distribution:

1. Initial mass and binder distributions were supplied as vectors $\vec{n}(t)$ and $\vec{b}(t)$, of length s_{\max} , where

$$\vec{n}(t) = (n_1(t), n_2(t), \dots, n_{s_{\max}}(t))$$

and

$$\vec{b}(t) = (b_1(t), b_2(t), \dots, b_{s_{\max}}(t)).$$

The results presented in Section 5.4 used the initial conditions $N_0 \equiv n_1(0) = 1000$, $n_i(0) = 0$ for $i > 1$, $b_1(0) = V^*n_1(0)$ and $b_i(0) = 0$ for $i > 1$ where V^* denotes the fluid-to-solid ratio.

2. The Matlab `ode45` integrator was used to integrate the system of equations in Equations (5.29) and (5.30). At each time step, `MeX` code (compiled C++ code) was called from the `ode45` script file to evaluate the vectors $\frac{d\vec{n}}{dt}$ and $\frac{d\vec{b}}{dt}$. This technique was used because evaluation of these vectors requires double `for` loops (since the sums in Equations (5.29) and (5.30) must be calculated for each size l where $1 \leq l \leq s_{\max}$). Completing the required loops using C++ was found to be significantly faster than using Matlab.
3. The Matlab event handler was used to monitor the drying of the binder and terminate integration upon reaching the steady-state condition. (See Section 2.3 for a discussion of the use of zeros-crossing functions in Matlab.) From Equation (5.31), the zeros-crossing function Z was defined as

$$Z = \overline{B}(t) - \epsilon M(t) \tag{5.32}$$

where $\epsilon = 0.01$. Integration was terminated if the event in Equation (5.32) was detected.

5.4 Model Results

Steady-state mass distributions for models 1 and 2 are shown in Figures 5.6 and 5.8 using the initial conditions of $N_0 \equiv n_1(0) = 1000$ and $b_1(0) = V^*n_1(0)$. The corresponding times taken to reach steady-state K_0t , the mean particle size \bar{i} and the standard deviation σ are shown in Figures 5.7 and 5.9. For both models, the collision rate functions compared are (a) $K_{l,m} \equiv lm$ (product), (b) $K_{l,m} \equiv (l^{\frac{1}{3}} + m^{\frac{1}{3}})^2$ (cross-sectional area, CSA), (c) $K_{l,m} \equiv 1$ (size-independent) and (d) $K_{l,m} \equiv (i^{-\frac{1}{2}} + j^{-\frac{1}{2}})$ (equi-partition of kinetic energy, EPKE). In Figures 5.6 and 5.8, the individual plots, for a given kernel, correspond to different fluid-to-solid ratio V^* and drying-to-collision $\frac{D_0}{K_0}$ values. (The $\frac{D_0}{K_0}$ values differ between different cases because the kernels and models have different time-scales. The values presented have been chosen so that the bulk portion of the mass distributions, at steady-state, occur within in the first 100 sizes.) The distinguishing features of the different kernels and models are now discussed.

Firstly the profile of the steady-state mass distributions are discussed. For model 1, the product collision rate function $K_{l,m} \equiv lm$ predicts the strongly monotonic distribution, centred on size 1, as shown in Figure 5.6(a). The cross-sectional area (CSA) collision rate function $K_{l,m} \equiv (l^{\frac{1}{3}} + m^{\frac{1}{3}})^2$ predicts a less strongly monotonic distribution, also centred on size 1, as shown in Figure 5.6(b). The function $K_{l,m} \equiv 1$ predicts the peaked distribution shown in Figure 5.6(c) while the equi-partition of kinetic energy (EPKE) collision rate function $K_{l,m} \equiv (l^{-\frac{1}{2}} + m^{-\frac{1}{2}})$ predicts the less strongly peaked distribution shown in Figure 5.6(d). This progression is due to the order maintained by the collision rate functions where (a) the product kernel favours large-large particle collisions, (b) the CSA kernel favours large particle collisions, but less strongly, (c) the random kernel is independent of size and (d) the EPKE kernel favours collisions between small particles. The graphs of mean particle size \bar{i} and standard deviation σ in Figure 5.7 support these observations. Comparing the limiting cases of the product and the EPKE kernel, the product kernel predicts a tight, skewed distribution (where mass is spread rapidly but thinly across large sizes) while distributions obtained using the EPKE kernel have the largest mean particle size \bar{i} and the broadest steady-state mass distributions. Distributions obtained using the product kernel reach steady-state in the shortest time while distributions obtained from the EPKE kernel reach steady-state in the longest time. Properties of distributions obtained using the CSA and the size-independent kernel occur, in order, between these two cases.

For Model 2, the effects described above are present, along with an additional effect due to the sticking efficiency function $\Phi_{i,j}$. As shown in Figure 5.5, $\Phi_{i,j}$ decreases for collisions between large particles, for a given V^* , causing the coalescence rate to decrease

for large particles. For the CSA and product kernels, the competing effect of a collision rate that favours large particle collisions and a sticking efficiency function which favours coalescence with small particles is shown as the introduction of a second peak in Figure 5.8.

Both models show that increasing V^* for fixed $\frac{D_0}{K_0}$ widens the mass distribution. This is due to coalescence being promoted by the presence of more binder. For this case, Figures 5.7 and 5.9 show that the times taken to reach steady-state increase because there is more wet binder to dry. Both models also exhibit scaling with respect to V^* . For instance, the steady-state distributions in Figures 5.6 and 5.8 appear similar when viewed along the diagonals for increasing V^* and $\frac{D_0}{K_0}$ and have comparable steady-state times. This suggests that an increased drying rate compensates for larger values of the fluid-to-solid ratio V^* .

For a particular model and kernel, fixing V^* , but increasing $\frac{D_0}{K_0}$, narrows the size distribution and decreases the time taken to reach steady-state. For a particular granulator and batch, K_0 is fixed, so increasing $\frac{D_0}{K_0}$ corresponds to an increased drying rate. The limiting case $\frac{D_0}{K_0} \rightarrow \infty$ corresponds to all of the wet binder drying at $t = 0$. In this case, the steady-state distribution is given by that of the initial particle distribution. For $\frac{D_0}{K_0} = 0$ (no drying) the system maintains a constant V^* as proved by Equation (5.20). In this case, steady-state distributions do not occur as particle coalescence is not restricted.

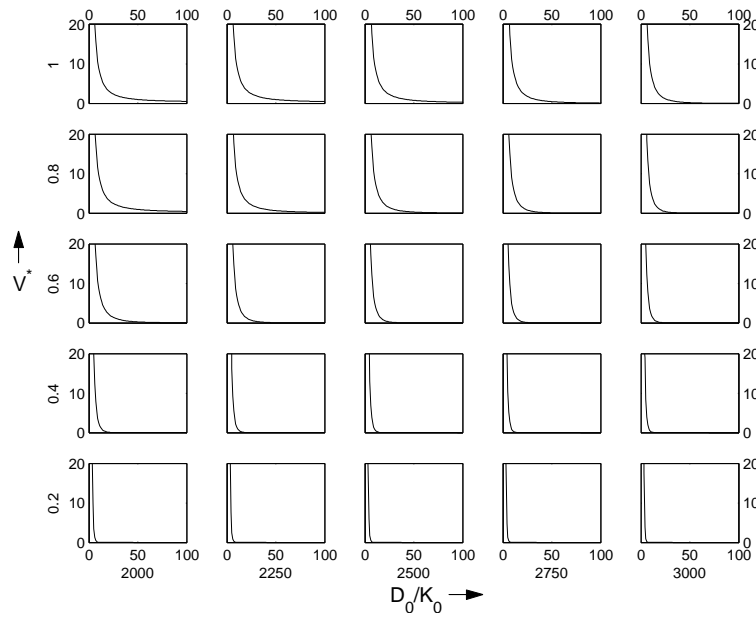
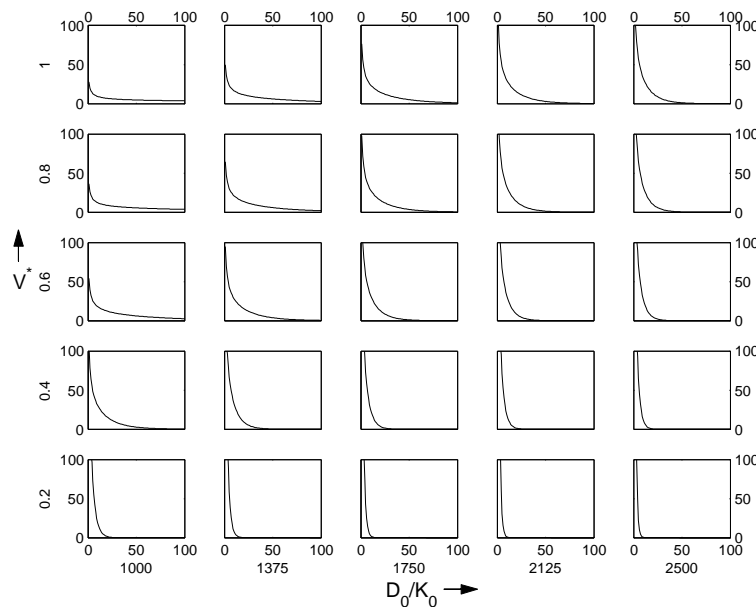
(a) $K_{l,m} \equiv lm$.(b) $K_{l,m} \equiv (l^{\frac{1}{3}} + m^{\frac{1}{3}})^2$.

Figure 5.6: Steady-state mass distributions for Model 1. Mass units are plotted on the vertical axis and size on the horizontal axis. Note that the vertical axis scale differs between figures (a) and (b).

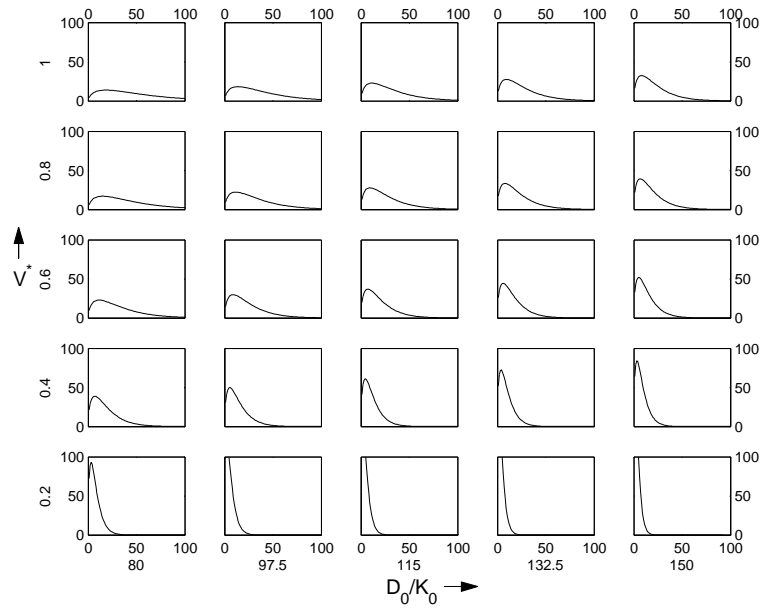
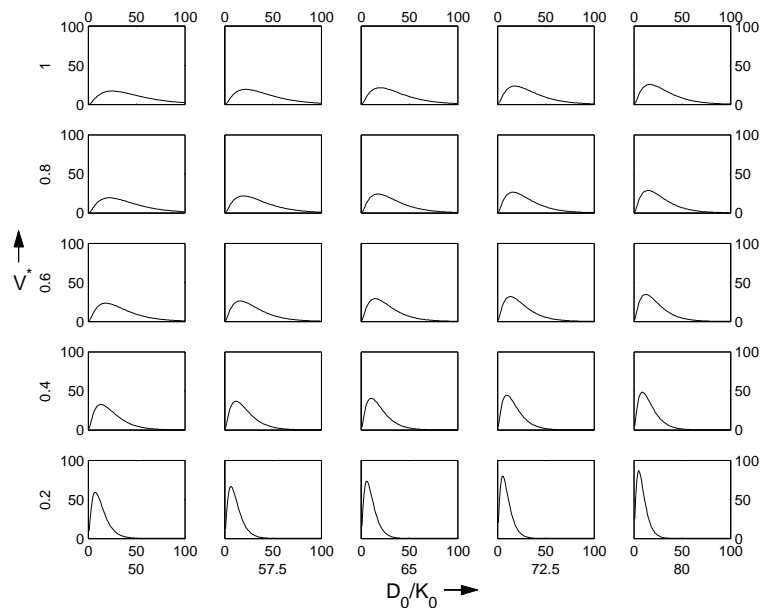
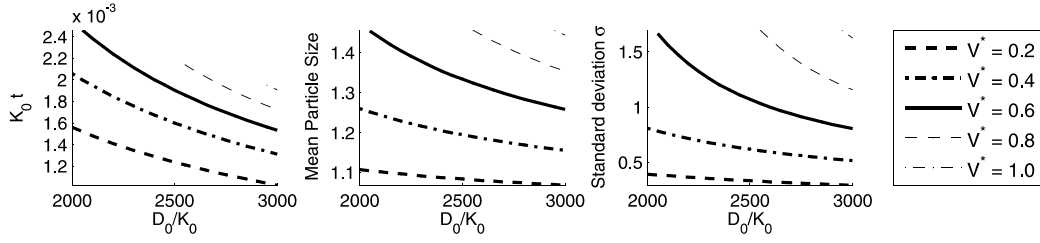
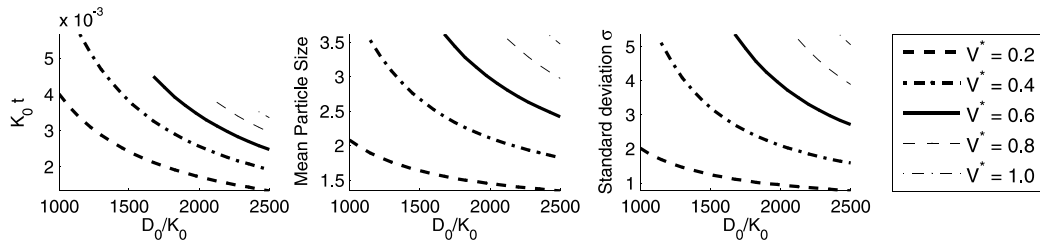
(c) $K_{l,m} \equiv 1$.(d) $K_{l,m} \equiv (l^{-\frac{1}{2}} + m^{-\frac{1}{2}})$.

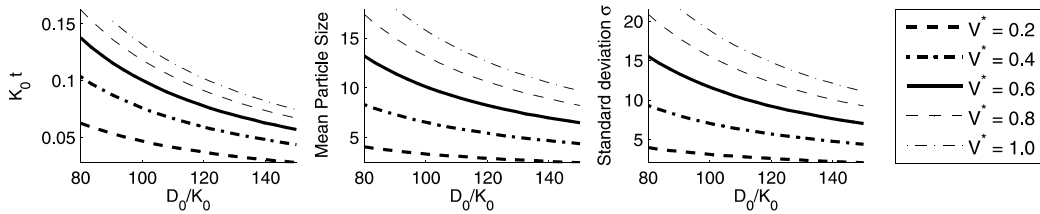
Figure 5.6: Steady-state mass distributions for Model 1 (continued).



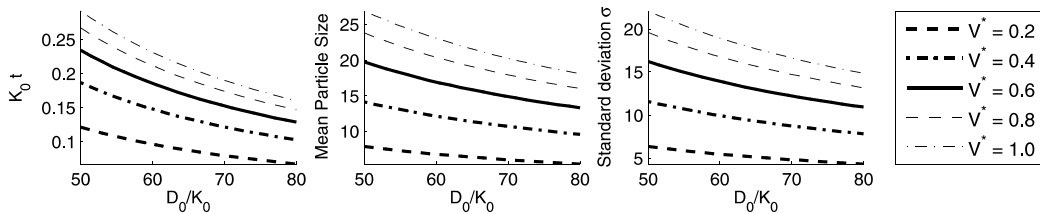
(a) $K_{l,m} \equiv lm$.



(b) $K_{l,m} \equiv (l^{1/3} + m^{1/3})^2$.



(c) $K_{l,m} \equiv 1$.



(d) $K_{l,m} \equiv (l^{-1/2} + m^{-1/2})$.

Figure 5.7: Plots showing the time taken to reach steady-state $K_0 t$, the mean particle size \bar{v} and the standard deviation σ at steady-state for Model 1. The mass distributions at steady-state are shown in Figure 5.6.

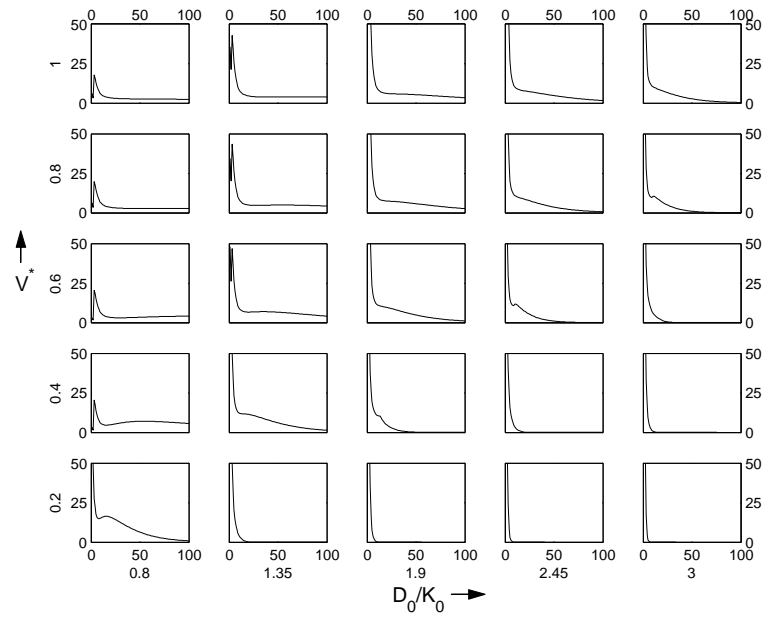
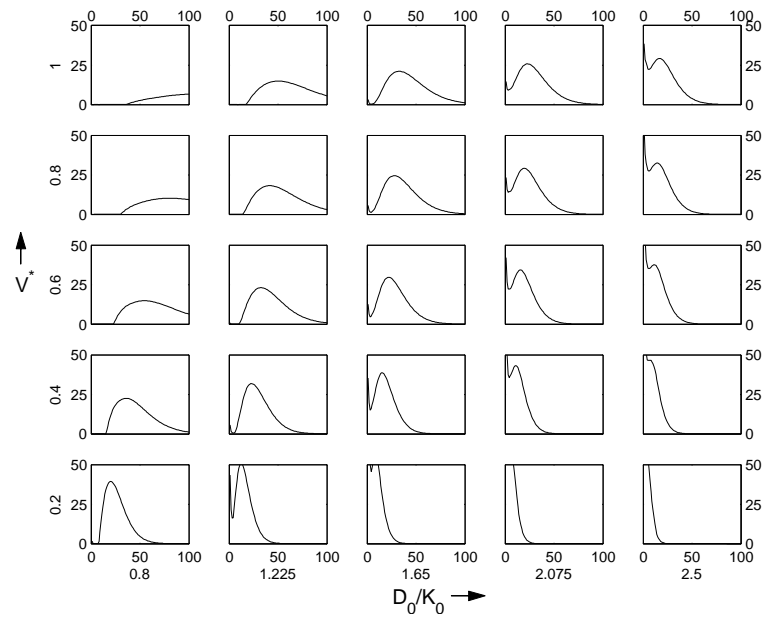
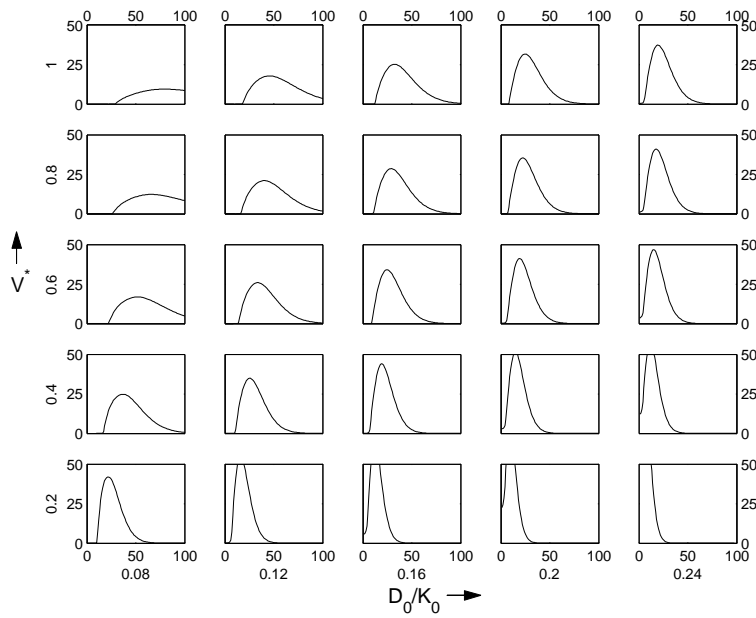
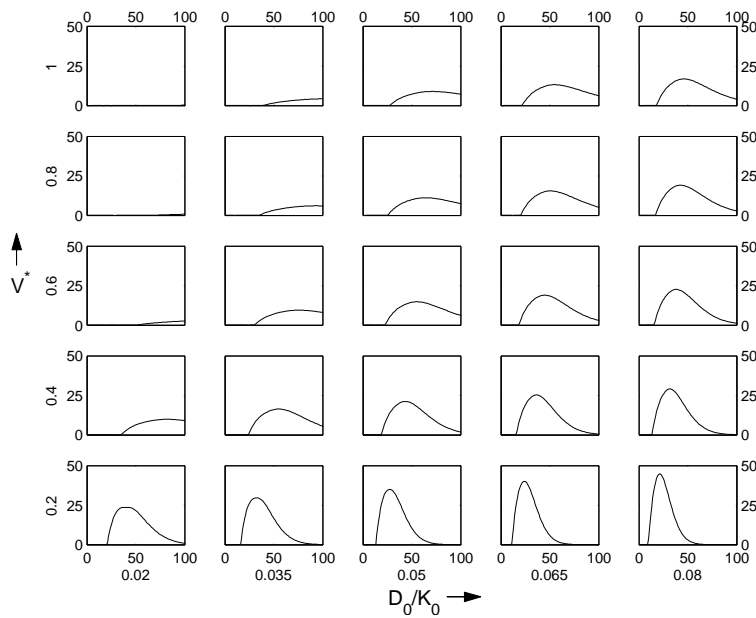
(a) $K_{l,m} \equiv lm$.(b) $K_{l,m} \equiv (l^{\frac{1}{3}} + m^{\frac{1}{3}})^2$.

Figure 5.8: Steady-state mass distributions for Model 2. Mass units are plotted on the vertical axis and size on the horizontal axis.

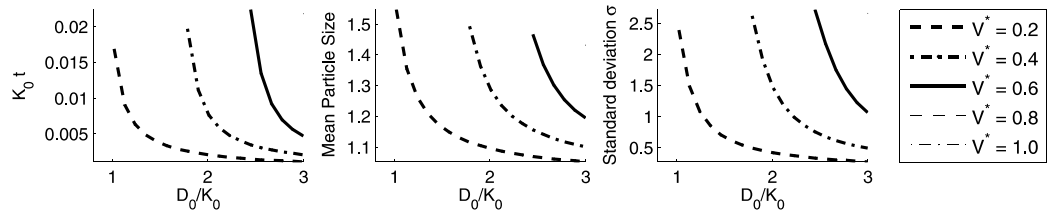


(c) $K_{l,m} \equiv 1$.

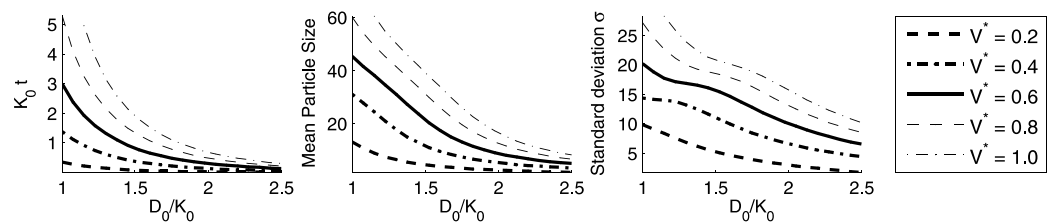


(d) $K_{l,m} \equiv (l^{-\frac{1}{2}} + m^{-\frac{1}{2}})$.

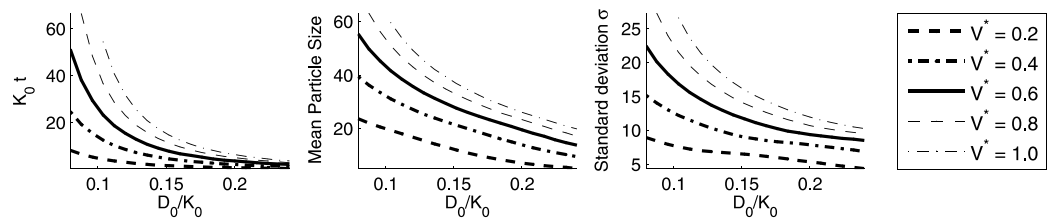
Figure 5.8: Steady-state mass distributions for Model 2 (continued).



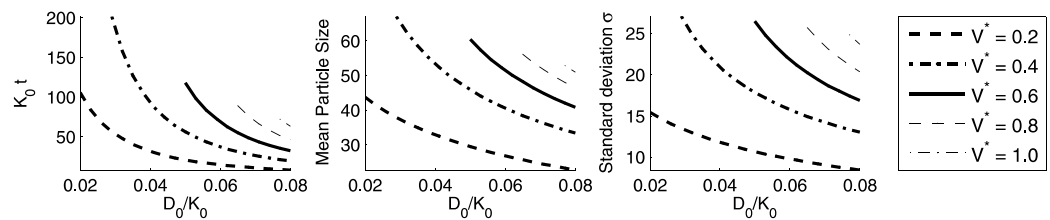
(a) $K_{l,m} \equiv lm$.



(b) $K_{l,m} \equiv (l^{\frac{1}{3}} + m^{\frac{1}{3}})^2$.



(c) $K_{l,m} \equiv 1$.



(d) $K_{l,m} \equiv (l^{-\frac{1}{2}} + m^{-\frac{1}{2}})$.

Figure 5.9: Plots showing the time taken to reach steady-state $K_0 t$, the mean particle size \bar{i} and the standard deviation σ at steady-state for Model 2. The mass distributions at steady-state are shown in Figure 5.8.

5.4.1 Recommendations for verifying the model

To verify the sticking efficiency and drying models the “ideal” experiment would monitor the position and size of all particles in a granulator and, in the presence of a binder, determine the fraction of collisions that result in coalescence as the drying rate is varied. Similarly, the collision rate function would be verified by finding the collision rate of particles, as a function of size, in the absence of a binder. At present, however, techniques are not available to perform these experiments. (Positron emission particle tomography (PEPT) has been used to monitor the movements of an individual tracer particle in low and high-shear granulators [67, 68]. This method continually monitors the decay of a radioactive tracer particle to determine its position in a system. However, this method monitors only the motion of one particle which is not sufficient to determine the characteristics of an ensemble.)

Currently, the best method to verify the models would be to perform experimental work to obtain steady-state size distributions. The profile and properties of these distributions may be used to compare the results with the theoretical predictions made in Section 5.4. To experimentally investigate a particular model component, the appropriate operating variables should be varied while the others remain fixed. The value of $\frac{D_0}{K_0}$, for instance, may be investigated by varying the agitation intensity of the granulator while the fill-level and binder delivery rate remain fixed. The resulting changes in the size distributions may be used to determine the model parameters and hence establish whether the models proposed are valid.

Summary, Conclusions and Suggestions for Future Work

6.1 Summary and Conclusions

This thesis presented micro and macro-level scale studies of agglomeration. Chapter 1 provided a comprehensive review of wet granulation where the mechanisms of granule growth, micro-level liquid bridge models and the various types of simulations were discussed. The topics subsequently investigated were (i) liquid bridges between two and three particles in Chapters 2 and 3, (ii) an approximate model to estimate the stickiness of moderately large agglomerates in Chapter 4 and (iii) a population balance model, extended to model the effects of binder fluid, in Chapter 5. The details and findings of each of these studies are now summarised.

The work presented in Chapter 2 concerned a mathematical study of liquid bridges between two particles. The chapter was divided into two parts with Sections 2.2-2.5 studying the static case and Section 2.6 studying the dynamic case. The static case solved the non-dimensional Young-Laplace equation numerically and analytically. The numerical solution enabled liquid bridge properties, such as the inter-particle binding force, to be calculated. Results were presented showing the variation of these properties in terms of a fixed fluid volume. This extends the work of Lian [35] who assumed particles of the same radius. Section 2.5 presented a new analytic parametric solution and obtained a phase portrait which related the height and the slope of the fluid surface together. Generic results were obtained due to scaling of the pressure difference parameter. The phase portrait predicted (theoretically) six distinct types of static liquid bridges. Section 2.6 presented a simplified solution of a dynamic liquid bridge between two particles using the Navier-Stokes equations and the low Reynolds number approximation. The numerical solution obtained showed the motion of the particles to be damped by the liquid bridge

viscosity.

Static liquid bridges between three equally sized primary particles were investigated in Chapter 3. This is the first time the Young-Laplace equation has been solved for this arrangement. Due to symmetry, and an innovative choice of coordinates, the complete fluid surface was obtained by numerically solving for 1/12 of the entire surface. Partial differential equations for constant mean curvature and boundary conditions were analytically derived and then numerically solved on a 15×15 mesh to calculate liquid bridge properties including the volume, surface area and inter-particle force. Independent experimental work was conducted and visual agreement with the numerical work was obtained.

Chapter 4 presented a novel geometric model for the placement of primary particles and liquid bridges in moderately sized agglomerates. No comparable work exists in the literature. The approximate fluid surface was formed from a union of tetrahedral fluid segments. The model had two parameters which represented the consolidation state of the particle and the saturation state of the fluid. Computational geometry was used to calculate agglomerate properties including their stickiness and wet and dry surface area. Results were obtained and functions fitted to the data for the maximum consolidated case of $s = 0$.

In Chapter 5 population balance modelling work was presented. Smoluchowski's model was independently derived in the discrete setting and was extended to include the effects of binder fluid by adding a further set of equations for the binder fluid. This extension is novel. Sample collision rate functions were derived. The approach taken to solve the equations numerically was discussed. Results were presented for a range of collision rate functions using two models for the coalescence and drying rate of particles. The results presented showed the effects of changing the ratio between the drying and collision rates.

6.2 Suggestions for Future Work

Suggestions for extending the work presented in this thesis are:

1. Obtain experimental data for the inter-particle force for a static liquid bridge between three particles and compare this to the predictions of the model in Chapter 3.
2. Obtain a parametric solution to the three particle model developed in Chapter 3.
3. Solve the Young-Laplace equation for the four and five particle cases using the method detailed in Chapter 3.

-
4. Calculate the surface wetness \overline{W} , as defined in Chapter 4 for the two and three particle arrangements and compare them with the predictions of the large agglomerate model in Chapter 4. This will require the parameters s and δ to be defined in Chapters 2 and 3.
 5. Extend the number of particles in the Chapter 4 agglomerate model (e.g. to 500 primary particles). This could be used to determine whether the curve fits presented for $s = 0$ are accurate.
 6. Confirm the collision, drying and sticking models used in the population balance model experimentally as discussed in Chapter 5.

Bibliography

- [1] Sherrington P J; Oliver R (1981). Granulation. Heyden and Son Limited, London.
- [2] Iveson S M; Litster J D; Hapgood K P; Ennis B J (2001). Nucleation, growth and breakage phenomena in agitated wet granulation processes: A review. *Powder Technology*, 117:3–39.
- [3] Kristensen H G; Schaefer T (1987). Granulation; A review on pharmaceutical wet-granulation. *Drug Development and Industrial Pharmacy*, 13(4-5):803–872.
- [4] Ennis B J; Tardos G I; Pfeffer R (1991). A microlevel based characterisation of granulation phenomena. *Powder Technology*, 65:257–272.
- [5] Leuenberger H (2001). New trends in the production of pharmaceutical granules: Batch versus continuous processing. *European Journal of Pharmaceutics and Biopharmaceutics*, 52(3):289–296.
- [6] Vonk P; Guillaume C P F; Ramaker J S; Vromans H; Kossen N W F (1997). Growth mechanisms of high-shear pelletisation. *International Journal of Pharmaceutics*, 157:93–102.
- [7] Kristensen H G (1996). Particle agglomeration in high shear mixers. *Powder Technology*, 88:197–202.
- [8] Murakami H; Yoneyama T; Nakajima K; Kobayashi M (2001). Correlation between loose density and compactibility of granules prepared by various granulation methods. *International Journal of Pharmaceutics*, 216(1-2):159–164.
- [9] Davidson J F; Harrison D (1971). Fluidisation. Academic press, Florida.
- [10] Knight P C (1993). An investigation of the kinetics of granulation using a high shear mixer. *Powder Technology*, 77:159–169.
- [11] Snow R H; Allen T; Ennis B J; Litster J D (1997). Size reduction and size enlargement. Chapter in Perry's Chemical Engineers' handbook (Editors Perry R H and Green D W). McGraw-Hill, New York, 7th edition.
- [12] Kristensen H G; Schaefer T (1987). A review on pharmaceutical wet-granulation. *Drug Development and Industrial Pharmacy*, 13(4-5):803–872.

- [13] Aulton M E; Banks M (1981). Fluidized bed granulation: Factors influencing the quality of the product. *International Journal of Pharmaceutical Technology and Product Manufacture*, 2(4):24–29.
- [14] Schaefer T; C C M (1996). Melt pelletization in a high shear mixer: IX Effects of binder particle size. *International Journal of Pharmaceutics*, 139:139–148.
- [15] Hapgood K P (2000). Nucleation and Binder Dispersion in Wet Granulation. Ph.D. thesis, Department of Chemical Engineering, University of Queensland.
- [16] Wildeboer W J (2002). Design and Operation of Regime Separated Granulators. Ph.D. thesis, Department of Chemical Engineering, University of Queensland.
- [17] Batchelor G K (1967). An introduction to fluid dynamics. Cambridge University Press, Cambridge.
- [18] Ayala R E; Casassa E Z; Parfitt G D (1987). A study of the applicability of the capillary rise of aqueous solutions in the measurement of contact angles in powder systems. *Powder Technology*, 51(1):3–14.
- [19] Schaefer T; Mathiesen C (1996). Melt pelletization in a high shear mixer: VIII Effects of binder viscosity. *International Journal of Pharmaceutics*, 139:125–138.
- [20] Lister J D; Hapgood K P; Michaels J N; Sims A; Roberts M; Kameneni S K; Hsu T (2001). Liquid distribution in wet granulation: Dimensionless spray flux. *Powder Technology*, 114:29–32.
- [21] Wauters P A L; Jakobsen R B; Litster J D; Meesters G M H; Scarlett B (2002). Liquid distribution as a means to describing the granule growth mechanism. *Powder Technology*, 123:166–177.
- [22] Iveson S M; Litster J D (1998). Growth regime map for liquid-bound granules. *American Institute of Chemical Engineers'*, 44:1510–1518.
- [23] Ouchiyama N; Tanaka T (1975). The probability of coalescence in granulation kinetics. *Industrial and Engineering Chemistry: Process Design and Development*, 14:286–289.
- [24] Simons S J R; Seville J P K; Adams M J (1994). An analysis of the rupture energy of pendular liquid bridges. *Chemical Engineering Science*, 49(14):2331–2339.
- [25] Thornton C; Ning Z (1998). A theoretical model for the stick/bounce behaviour of adhesive, elastic-plastic spheres. *Powder Technology*, 99:154–162.

- [26] Liu L X; Litster J D; Iveson S M; Ennis B J (2000). Coalescence of deformable granules in wet granulation processes. *American Institute of Chemical Engineers'*, 46:529–539.
- [27] Lian G; Thornton C; Adams M J (1998). Discrete particle simulation of agglomerate impact coalescence. *Chemical Engineering Science*, 53:3381–3391.
- [28] Iveson S M; Wauters P A L; Forrest S; Litster J D; Meesters G M H; Scarlett B (2001). Growth regime map for liquid-bound granules: further development and experimental validation. *Powder Technology*, 117:83–97.
- [29] Tardos G I; Irfan K M; Mort M; Paul R (1997). Critical parameters and limiting conditions in binder granulation of fine powders. *Powder Technology*, 94(3):245–258.
- [30] Newitt D M; Conway-Jones J M (1958). A contribution to the theory and practice of granulation. *Food and Bioproducts Processing: Transactions of the Institution of Chemical Engineers'*, 36:422.
- [31] Bisschop F R E D; Rigole W J L (1982). A physical model for liquid capillary bridges between adsorptive solid spheres: The nodoid of plateau. *Journal of Colloid and Interface Science*, 88:117–128.
- [32] Fisher R A (1926). The capillary forces in an ideal soil; correction of the formulas given by W. B. Haines. *Journal of Agricultural Science*, 16:492–503.
- [33] Erle M A; Dyson D C; Morrow N R (1974). Liquid bridges between cylinders, in a Torus, and between spheres. *American Institute of Chemical Engineers'*, 17:115–121.
- [34] Hotta K; Takeda K; Inoya K (1974). Capillary binding force of a liquid bridge. *Powder Technology*, 10:231–242.
- [35] Lian G (1994). Computer simulation of moist agglomerate collisions. Ph.D. thesis, Birmingham, Aston University. Department of Civil Engineering.
- [36] Hsu H P (1984). Applied vector analysis. Harcourt Brace Jovanovich, Florida.
- [37] van Brunt B (2004). The Calculus of Variations (Editors S Axler, F W Gehring and K A Ribet). Springer-Verlag, New York.
- [38] Urso M E D; Lawrence C J; Adams M J (1999). Pendular, funicular and capillary Bridges: Results for two dimensions. *Journal of Colloid and Interface Science*, 220:42–56.
- [39] Love A E H (1944). A treatise on the mathematical theory of elasticity. Dover Publications Incorporated, New York, 4th edition.

- [40] Barnocky G; Davis R H (1998). Elastohydrodynamic collision and rebound of spheres: Experimental verification. *Physics of Fluids*, 31(6):1324–1329.
- [41] Johnson K L (1987). Contact Mechanics. Cambridge University Press, New York.
- [42] Adams M J; Perchard V (1985). The cohesive forces between particles with interstitial liquid. *Institution of Chemical Engineers' Symposium Series*, 91:147–160.
- [43] M M G; Kraft M (2004). Simulation of coalescence and breakage: an assessment of two stochastic methods suitable for simulating liquid-liquid extraction. *Chemical Engineering Science*, 59(18):3865–3881.
- [44] Wauters P A L (2001). Modelling and mechanisms of granulation. Ph.D. thesis, Technische Universiteit Delft, Netherlands.
- [45] Hounslow M J; Ryall R L; Marshall V R (1988). A discretized population balance for nucleation, growth, and aggregation. *American Institute of Chemical Engineers'*, 34(11):1821–1832.
- [46] Liu Y; Cameron I T (2003). A new wavelet-based adaptive method for solving population balance equations. *Powder Technology*, 130(1-3):181–188.
- [47] Cundall P A; Strack O D L (1979). A discrete numerical model for granular assemblies. *Geotechnique*, 29(1):47–65.
- [48] Smoluchowski M V (1917). Mathematical theory of the kinetics of the coagulation of colloidal solutions. *International Journal for Research in Physical Chemistry and Chemical Physics*, 92:129–168.
- [49] Finney R; Weir M; Giordano F (2001). Thomas' calculus. Addison Wesley Publishing Company, New York, 10th edition.
- [50] Gradshteyn I S; Ryzhik I M (1980). Tables of integrals, series and products. Academic Press, Florida.
- [51] Hughes W F; Gaylord E W (1964). Basic equations of engineering science. McGraw-Hill, New York.
- [52] Struik D J (1988). Lectures on classical differential geometry. Dover Publications Incorporated, New York, 2nd edition.
- [53] Simons S J R; Fairbrother R J (2000). Direct observations of liquid binder-particle interactions: the role of wetting behaviour in agglomerate growth. *Powder Technology*, 110:44–58.

- [54] Conway J H; Sloane N J A (1993). Sphere packings, lattices, and groups. Springer-Verlag, New York, 2nd edition.
- [55] O'Rourke J (1994). Computational geometry in C. Cambridge University Press, New York.
- [56] Veres S M (2000). Reference of the geometric bounding toolbox (GBT) version 7. Available in electronic form at www.sysbrain.com. Southampton, United Kingdom.
- [57] Golovin A M (1963). The solution of the coagulation equation for raindrops, taking condensation into account. *Soviet Physics*, 8(2):191–193.
- [58] Drake R L (1972). A general mathematical survey of the coagulation equation (Editors G M Hidy and J R Brock). Chapter in Topics in Current Aerosol Research (Part 2), Volume 3 of International Reviews in Aerosol Physics and Chemistry. Pergamon Press, New York.
- [59] Silk J; White S D (1978). The development of structure in the expanding universe. *Astrophysical Journal*, 223:59–62.
- [60] Cundall P A (1971). A computer model for simulating progressive large-scale movements in block rock mechanics. *Proceedings of the International Symposium on Rock Mechanics*, Paper II-8.
- [61] Kapur P C; Fuerstenau D W (1969). Coalescence model for granulation. *Industrial and Engineering Chemistry Process Design and Development*, 8:56–62.
- [62] Berry E X (1967). Cloud droplet growth by collection. *Journal of Atmospheric Science*, 24:688–701.
- [63] Kapur P C (1972). Kinetics of granulation by non-random coalescence mechanism. *Chemical Engineering Science*, 27(10):1863–1869.
- [64] Sastry K V S (1975). Similarity size distribution of agglomerates during their growth by coalescence in granulation or green pelletization. *International Journal of Mineral Processing*, 2:187–203.
- [65] Adetayo A A; Litster J D; Pratsinis S E; Ennis B J (1995). Population balance modeling of drum granulation of materials with wide size distribution. *Powder Technology*, 82(1):37–49.
- [66] Adetayo A A; Ennis B J (1997). Unifying approach to modelling granule coalescence mechanisms. *American Institute of Chemical Engineers'*, 43:927–934.

- [67] Hoffmann A C; Dechsiri C; van de Wiel F; Ghione A; Dehling H G; Paans A M J (2003). Tracking individual particles in a fluidized bed using a medical PET-camera. *Proceedings of the 3rd World Conference on Industrial Process Tomography, Banff, Canada.*
- [68] Knight P C; Seville J P (2001). Prediction of impeller torque in high shear powder mixers. *Chemical Engineering Science*, 56(15):4457–4471.